A Measurement of Solar Neutrinos and the Development of Reconstruction Algorithms for the SNO+ Experiment

by

Jie Hu

A thesis submitted in partial fulfillment of the requirements for the degree of

Doctor of Philosophy

Department of Physics

University of Alberta

Abstract

This thesis presents a measurement of the flux of Boron-8 (^{8}B) solar neutrinos. The measurement is based on a dataset of 190.33 live days acquired during the SNO+ water physics commissioning. To analyze the data, an event reconstruction framework was developed to evaluate the orientation of the incoming neutrino's momentum vector and the position of the event it induces. A multivariate analysis was applied to reduce the number of background events in the analysis dataset. By analyzing the data within an energy range from 5 to 15 MeV, an observed elastic scattering flux assuming no neutrino flavor transformation is obtained as $\Phi_{\mathrm{ES}} = (2.07 \pm 0.206(stats.)^{+0.0527}_{-0.0454}(syst.)) \times 10^6\ \mathrm{cm}^{-2}\mathrm{s}^{-1}$ while the total ^{8}B solar neutrino flux is evaluated as $\Phi_{^8\mathrm{B}} = (4.62 \pm 0.459(stats.)^{+0.126}_{-0.104}(syst.)) \times 10^6\ \mathrm{cm}^{-2}\mathrm{s}^{-1}$. These fluxes are consistent with the previous measurement done by SNO+[1], and from the other experiments, such as Super Kamiokande[2]. The systematics were obtained by reconstructing and analyzing the calibration datasets from an Nitrogen-16 calibration source.

Currently, the SNO+ experiment has completed the water phase commission and is filled with the liquid scintillator. It turns from a Water Cherenkov detector into a 780-tonne liquid scintillator detector. Tellurium-130 isotopes will be loaded into the detector to fulfill the ultimate physics goal of SNO+: to search for the neutrinoless double beta decay. The other parts of this thesis discuss the reconstruction framework for the partial-fill and scintillator phases. For the scintillator phase, the event reconstruction gives a high position resolution down to about 65 mm.

Acknowledgements

Contents

Abstract iii

Acknowledgements iv

Contents v

List of Figures x

List of Tables xvi

1 Introduction 1

2 Neutrino physics 5

2.1 Overview 6

2.2 Neutrino Interactions 8

2.2.1 Neutrino-Electron Elastic Scattering 8

2.3 Neutrino Flavor Transformation 12

2.3.1 Vacuum Oscillation 12

2.3.2 Matter Effect 16

2.4 Solar Neutrinos 18

2.4.1 Kamiokande and Super-Kamiokande 21

2.4.2 SNO 22

2.4.3 KamLAND 23

2.4.4 Borexino . . . 24
2.4.5 More Studies on Solar Neutrino and Future Experiments . . . 24
2.5 Neutrinoless Double Beta Decay . . . 26

3 The SNO+ Experiment **31**
3.1 Overview . . . 31
3.2 SNO+ Physics Phases . . . 32
3.2.1 Water Phase . . . 33
3.2.2 Scintillator Phase . . . 35
3.2.3 Partial-fill Phase . . . 35
3.3 Detection Media . . . 36
3.3.1 Cherenkov Radiation . . . 36
3.3.2 Scintillation from Organic Scintillator . . . 37
3.3.3 Liquid Scintillator for SNO+ . . . 40
3.3.4 Water-based Wavelength Shifter (Proposal) . . . 41
3.3.5 Relative Light Yield Measurements of the Te-loaded Liquid Scintillators 46
3.4 SNO+ Electronics . . . 55
3.5 Calibration . . . 57
3.5.1 The ^{16}N Calibration Source . . . 58
3.6 Monte Carlo Simulation and RAT Software . . . 61

4 Event Reconstruction **62**
4.1 An Overview of the Reconstruction Algorithms in SNO+ . . . 62
4.2 Multi-path Vertex and Direction Reconstructions for the Water Phase . . . 65
4.2.1 Vertex Reconstruction . . . 65
4.2.2 Direction Reconstruction . . . 68
4.2.3 Effective Group Velocity . . . 70
4.2.4 Fitter Pull and Drive Correction . . . 73
4.2.5 PMT Selectors for the Reconstruction . . . 76

4.2.6 Position Figure of Merit . . . 79
4.2.7 Performances of the Water Vertex Reconstruction . . . 80
4.2.8 Performances of the Water Direction Reconstruction . . . 84
4.2.9 Test on Gamma Events . . . 87
4.3 Vertex and Direction Reconstruction for the Water-based Wavelength-shifter 88
4.4 Vertex Reconstruction for the Partial-fill . . . 92
4.4.1 Partial-fill . . . 92
4.4.2 Making Timing PDFs . . . 97
4.4.3 Partial Fitter Performances . . . 99
4.4.4 Test on Bi-Po Simulations . . . 105
4.4.5 Discussions for the Partial Fitter . . . 106
4.5 Vertex Reconstruction for the Scintillator Phase . . . 109
4.5.1 Performance of the Vertex Reconstruction . . . 109
4.6 Multi-path Fitter Structure for Multiple SNO+ Physics Phases . . . 112
4.7 Energy Reconstruction . . . 114
4.7.1 Energy Figure of Merit . . . 115
4.7.2 Energy Reconstruction in Partial-fill Phase . . . 116
4.8 Machine Learning and Deep Learning . . . 117
4.9 Conclusion . . . 117

5 Calibration **118**
5.1 ^{16}N Calibration Scans in the Water Phase . . . 119
5.2 High Level Cuts for the Water Phase . . . 120
5.2.1 Effects of the High-level Cuts . . . 121
5.3 Reconstruction Evaluations from ^{16}N Calibration Scans in the Water Phase 122
5.3.1 Position Reconstruction Evaluation . . . 123
5.3.2 Direction Reconstruction Evaluation . . . 134
5.3.3 β_{14} and Its Systematic . . . 138
5.3.4 Energy Reconstruction Evaluation . . . 140

6 Solar Neutrino Analysis in the SNO+ Water Phase **151**

6.1 Backgrounds 152

6.1.1 Internal backgrounds 152

6.1.2 External backgrounds 153

6.2 Solar neutrino Analysis in Open Dataset 153

6.3 Likelihood Fits for Solar Neutrino Candidate Events 156

6.3.1 Maximum Likelihood Fit 156

6.3.2 Ensemble Test 157

6.3.3 Kullback–Leibler Divergence for High Level Cuts 160

6.3.4 Signal-background Discrimination Based on TMVA 162

6.3.5 TMVA Outputs 169

6.3.6 Discussions on TMVA Results 172

6.3.7 Fitting Whole Low Background Dataset 172

6.3.8 Evaluating ^{8}B Solar Neutrino Flux 173

6.3.9 Systematics Evaluation 177

6.3.10 A Summary of Results 181

6.3.11 Limitations of this Study 183

7 Conclusions **185**

A Details for the MultiPath Fitter **186**

A.1 Create a Random Vertex 186

A.2 Levenberg-Marquardt Method 187

A.3 Calculations of Derivatives of Likelihood Functions 190

A.4 Inversion of Hessian Matrix 191

A.5 Likelihood Surfaces 192

A.6 Detailed Light Path Calculations in the `MP Partial Fitter` 192

B Information for ^{16}N Scan Runs **197**

B.1 Information for ^{16}N Scan Runs 197

C Bi-Po Analysis **203**

C.1 Uranium chain and Bi-Po Analysis 203

References **205**

List of Figures

2.1 Feynman diagrams for the elastic scattering interaction in different channels at tree level. 9

2.2 A diagram of the $\nu + e^-$ elastic scattering in the lab frame, modified from Ref. [3]. 10

2.3 All reactions in the three PP chains. 19

2.4 All reactions in the CNO bicycle. 19

2.5 Solar neutrino energy spectrum. 21

2.6 Feynman diagrams for $2\nu\beta\beta$ and $0\nu\beta\beta$. 27

2.7 Energy spectrum of the ^{130}Te $2\nu\beta\beta$ decay and the hypothetical $0\nu\beta\beta$ decay. 29

2.8 Natural abundance vs. Q-values for different $2\nu\beta\beta$ isotopes, from Ref. [4]. . 30

3.1 The SNO+ detector labeled with main structures. 33

3.2 A Jablonski diagram for the organic scintillator. 38

3.3 Structural formulae of LAB and PPO. 42

3.4 Absorption length of SNO+ optical components. 43

3.5 Time profiles for liquid scintillators in different SNO+ phases. 44

3.6 Initial stages of the TeBD compound formation, modified from Ref. [5]. . . 45

3.7 A vial of the test sample and the measurement setup. 47

3.8 A diagram shows the light yield measurement setup. 48

3.9 A typical triggered waveform. 50

3.10 Measured LAB-PPO energy spectrum with and without coincidence cut . . 51

3.11 The 2D energy spectrum of the counting measurements. 52
3.12 The single p.e. peak fitted with an asymmetric Gaussian function. 54
3.13 Two dimensional spectrum of LAB-PPO sample with coincidence cut. . . . 54
3.14 The SNO+ Source Manipulator System. 59
3.15 ^{16}N calibration source geometry. 60
3.16 ^{16}N main decay scheme 60

4.1 Straight light path calculation in the water geometry. 66
4.2 The PMT response time profile as the timing PDF for the vertex reconstruction. 67
4.3 Diagrams of position in the SNO+ water phase geometry. 68
4.4 PMT angular distribution as the angular response PDF for direction reconstruction. 69
4.5 Refractive index vs wavelength. 70
4.6 A cartoon shows effects of tuning the effective group velocity. 71
4.7 Group velocity vs. radial bias for the `MPW fitter`. 72
4.8 ^{16}N central run for evaluating the average group velocity. 73
4.9 A cartoon shows fitter pull effect. 74
4.10 A diagram illustrates the drive correction. 75
4.11 Drive correction parameter p_0 (left) and p_1 (right) as a function of energy. . 76
4.12 Radial biases of the simulated e^- events as a function of energy. 77
4.13 The PMTs are grouped by dividing the PSUP sphere with latitudes and longitudes. 79
4.14 The position biases projected on the x, y and z axes. 81
4.15 The position biases against the position FoMs. 82
4.16 The `MPW fitter` fit position biases ($\mu_{x,y,z}$) as a function of energy. 83
4.17 The `MPW fitter` fit position resolutions ($\sigma_{x,y,z}$) as a function of energy. . . 84
4.18 The `MPW fitter` fit position biases ($\mu_{x,y,z}$) as a function of energies. 85
4.19 The `MPW fitter` position resolutions ($\sigma_{x,y,z}$) as a function of energies. . . . 85

4.20 The biases between the fitted and MC directions. 86
4.21 Direction resolutions as a function of radius. 87
4.22 Position distributions of hit PMTs (in zenith and azimuth angles). 89
4.23 The energies of simulated electrons as a function of mean NHits. 89
4.24 The timing PDF for the wbWLS. 90
4.25 Fitted x position. 91
4.26 Light path calculation for the `MP scint-water fitter fitter`. 93
4.27 Line-sphere intersections. 94
4.28 Timing PDFs used by the `MP scint-water fitter fitter`. 96
4.29 Timing PDFs built for various PPO concentrations based on the Oxford bench-top measurements. 98
4.30 Tuning the effective group velocities in the scintillator and water. 99
4.31 Reconstructed positions and fit biases of the 3-MeV e^- events in the scintillator region. 101
4.32 Effects of the $scaleLogL$ cut on the reconstructed positions and fit biases. . 102
4.33 Reconstructed positions and fit biases of the 3-MeV e^- events in the water region. 103
4.34 Fit position biases against the PPO concentrations. 104
4.35 Fit position resolutions against the PPO concentrations. 105
4.36 Distributions of NHits for the tagged ^{214}Po and ^{214}Bi events. 107
4.37 Fit position biases for tagged ^{214}Bi and ^{214}Po 108
4.38 The fit position biases projected on the x, y and z axes, for 2.5-MeV e^- in full scintillator simulations. 110
4.39 The Gaussian biases (μ) of the `MP scint fitter` fit position biases as a function of radius, for the x, y, and z axes. 111
4.40 The Gaussian resolutions (σ) of the `MP scint fitter` fit position biases as a function of radius, for the x, y, and z axes. 111

4.41 The Gaussian biases (μ) of the `MP scint fitter` fit position biases as a function of energy, for the x, y, and z axes. 112
4.42 The Gaussian resolutions (σ) of the `MP scint fitter` fit position biases as a function of energy, for the x, y, and z axes. 112

5.1 The deployed source positions of the ^{16}N scan runs. 119
5.2 Position biases vs ITR (top) and β_{14} (bottom) for the ^{16}N central run-107055. 122
5.3 Position biases ($|\vec{X}_{fit} - \vec{X}_{MC}|$) vs $scaleLogL$ for the ^{16}N central run-107055. 123
5.4 Reconstructed energy vs $scaleLogL$ for the ^{16}N central run-107055. 124
5.5 A cartoon shows the ^{16}N source. 125
5.6 Spatial distributions of ^{16}N first γ-rays interaction position projected on x axis. 126
5.7 Distributions of the reconstructed position projected on x axis. 127
5.8 The fitted values of μ_P and σ_P along x, y and z scans. 129
5.9 Relative differences of σ_P ($\sigma_{p,\delta}$) as a function of the ^{16}N source position. . . 131
5.10 Vertex shifts of μ_P ($\mu_{p,\delta}$) as a function of the ^{16}N source position. 132
5.11 Vertex shifts along x, y, z axes and fitted with linear functions. 133
5.12 Angular distributions extracted from the data and MC. 135
5.13 Fitted direction resolution parameters β_M, β_S for the source scans in x, y, z-axes respectively. 137
5.14 Relative differences of β_M and β_S as a function of the ^{16}N source position. . 138
5.15 Distributions of β_{14} for the ^{16}N central run-107055. 139
5.16 A comparison of the β_{14} for the data and the MC in run-107055. 139
5.17 β_{14} systematic along x, y, z scans. 140
5.18 ^{16}N central-run 107055, U_{test} vs. E_{fit}/5.1 MeV. 141
5.19 ^{16}N central-run 107055, G_{test} vs. E_{fit}/5.1 MeV. 141
5.20 ^{16}N central-run 107055, Z_{factor} vs. E_{fit}/5.1 MeV. 142
5.21 Reconstructed energy spectrum from the ^{16}N central run-106925 and 107055. 143
5.22 NHit spectrum for the ^{16}N central run-107055. 144

5.23 Simulated ^{16}N energy spectrum for different processes. 144
5.24 E_{fit} vs β_{14} for the data and MC. 145
5.25 Converting number of photons to effective electron spectrum. 146
5.26 The reconstructed energy spectrum fitted with resolution function. 147
5.27 Fitted energy scales (δ_E) as a function of the source radial manipulation position. 148
5.28 Fitted energy resolutions (b) as a function of the source radial manipulation position. 148
5.29 Smeared reconstructed energy spectrum of ^{16}N central run-107055. 149
5.30 Smeared reconstructed energy spectrum of ^{16}N central run-107055. 150

6.1 Reconstruction results for the candidate events, projected onto PMT sinusoidal maps. 155
6.2 The $\cos\theta_{sun}$ distribution of solar ν_e used as a PDF function. 157
6.3 Real data from run-200004 to 203602 (half-dataset), after the beforehand cuts.158
6.4 An example of the $\cos\theta_{sun}$ distribution from a fake dataset fitted with (N_{sig}, N_{bkg}).159
6.5 N_{sig} fit biases for 5000 fake datasets. 160
6.6 N_{sig} fit pulls for 5000 fake datasets. 160
6.7 The $-2\ln L$ distribution of the best fit results from the 5000 fake datasets. 161
6.8 Angular distributions of the MC events in run-by-run simulations. 162
6.9 Energy spectrum of events from different simulations. 164
6.10 Multiple variables as the inputs for the TMVA analysis, for the $4 < E < 15$ MeV dataset. 166
6.11 TMVA outputs for signal/background separations by different methods, for the $4 < E < 15$ MeV testing dataset. 167
6.12 TMVA outputs for signal/background separations by different methods . . 168
6.13 BDT and MLP outputs for the $\cos\theta_{sun}$, with $4 < E_{fit} < 15$ MeV. 170
6.14 BDT outputs from one random fake dataset, with $5 < E_{fit} < 15$ MeV. . . . 171

6.15 Event number fractions from BDT outputs on 5000 fake datasets, with $5 < E_{fit} < 15$ MeV. 171
6.16 Poisson fit results for the $5 < E_{fit} < 15$ MeV. 173
6.17 The MSW survival probability curves as functions of MC energies. 174
6.18 The MC $\cos\theta_{sun}$ distributions used as PDFs for the flux calculations, for $5 < E_{fit} < 15$ MeV after the BDT selections. 175
6.19 A fit on the total ^{8}B flux. 176
6.20 Fitting with the spectrum of elastic scattering. 177
6.21 Smearing effects on the $\cos\theta_{sun}$ PDF. 180
6.22 A comparison of the ES flux measured recently by three independent experiments (after BDT selection). 182

A.1 Likelihood surface of an ^{16}N event projected on X-Y, Y-Z, X-Z planes. . . . 193
A.2 Likelihood surface of an ^{16}N event projected on x, y, z, t-axis respectively. . 194
A.3 Derivatives of $\ln L$ of an ^{16}N event projected on x, y, z, t-axis respectively. The analytical derivatives (blue) are overlaid with numerical derivatives (red). They basically match with each other. 195
A.4 Layouts for the scintillator light paths inside the AV sphere. 195
A.5 Layouts of the scintillator light paths inside the neck cylinder. 196

C.1 A flow chart for Bi-Po tagging. 204

List of Tables

2.1 Neutrino interactions in the $\mathcal{O}$(0.1-10 MeV) energy region, modified from Ref. [6]. 8

2.2 Neutrino experiments for studying flavor transformation. 15

2.3 The main reactions producing solar neutrinos. 20

3.1 Number of photons calculated by Charge weighted photon number method. 55

3.2 A list of SNO+ radioactive sources. 57

4.1 Direction resolutions for the reconstruction of the 5-MeV e^- events. 87

4.2 Reconstruction performances for the 2.2-MeV and 4.4-MeV γ events. 88

4.3 A comparison of quantitative estimates for the angular resolution for the SNO heavy water, SNO+ wbWLS and the SNO+ pure water cases. 91

4.4 Time constants and amplitudes measured by Ref. [7]. Here the relative light yield is with respect to the LAB+2 g/L PPO case (11900 photons/MeV). . 97

4.5 Relative light yield (RLY) measured by Ref. [7]. 98

4.6 Tuned effective group velocities for different PPO concentrations. 99

4.7 Fit position biases and resolutions for the ^{214}Bi-^{214}Po tagging. 106

5.1 Position resolution parameters for the `MPW fitter` (x-axis). 128

5.2 The `MPW fitter` position resolution systematic uncertainties in x, y and z axes. Unit: mm. 130

5.3 Vertex shifts for the reconstructed positions in x, y and z axes. Unit: mm. . 133

5.4 Vertex shifts for the reconstructed positions in x, y and z axes. Unit: mm. . 134

5.5 Direction resolutions. 135

6.1 Candidate events in the open dataset. 154

6.2 Candidate events in the open dataset searched by the `MPW fitter`. 154

6.3 Datasets of MC simulations. 163

6.4 Ratios of the signal event numbers to the background event numbers. . . . 164

6.5 Testing results from different TMVA methods. 169

6.6 Fit results for the whole dataset ($5 < E < 15$ MeV). 174

6.7 Systematics for the solar ν_e analysis in the water phase. 178

6.8 Systematics for the fitted flux scale f_s. 181

6.9 Average results. 183

A.1 Optimized fitter setting parameters for different physics phases. 190

B.1 198

B.2 199

B.3 200

B.4 201

B.5 202

Chapter 1

Introduction

Among state-of-the-art neutrino experiments, SNO+ aims to search for an extremely rare process called neutrinoless double-beta decay ($0\nu\beta\beta$). This search will explore and attempt to resolve a key question as to the nature of the neutrino: is it a Majorana or a Dirac particle. A discovery that the $0\nu\beta\beta$ process occurs would unravel the masses of neutrinos and test new physics theories.

Regarding its physics targets, the SNO+ experiment goes through three major stages, mainly determined by the working medium inside the SNO+ detector. First, the detector was filled with water and operated as a water Cherenkov detector. During this water phase, over 300 live days of data have been collected. Calibration sources were also deployed for measuring the detector properties. Based on the first 114.7 live days of data, SNO+ published a measurement of the fluxes of Boron-8 neutrinos from the Sun. The results are consistent with the other solar neutrino experiments and also demonstrate extremely low background levels for the analysis[1].

As of the time of writing this thesis, the water phase stage has been completed, and liquid scintillator has replaced the water. During the scintillator filling, there were several long intervals during which the water/scintillator interface level remained stable at a fixed height (z) inside the detector. Collectively these stable (albeit) transitional stages are named the "partial-fill phase", during which detector data are used to analyze the properties and estimate the backgrounds of the liquid scintillator for the two physics phases to follow.

Once the detector is fully filled with the liquid scintillator, the detector will be operated during the "scintillator phase". A 6-month data-taking interval is planned, to establish the background levels of the liquid scintillator and to measure solar neutrinos, reactor antineutrinos and geoneutrinos[8]. After this scintillator phase, tellurium isotopes will be loaded into the liquid scintillator and once the mixture (or "cocktail") is stable, the search for the $0\nu\beta\beta$ signal will commence.

Event reconstruction is crucial for the physics analysis. In this thesis, a framework of reconstruction algorithm, called the "multiple-path fitter" (`MP fitter`), was developed for multiple SNO+ physics phases. This framework was first developed by the author's supervisor, Dr. A. L. Hallin, to reconstruct and investigate the data taken during the "partial-fill water", which was an early stage of the experiment when the detector was only *partially* filled with water (the residual volume being air) in December, 2014[9]. Drs. K. Singh and D. J. Auty (U. Alberta) further developed this fitter to accommodate the wavelength shifter and analyse water events ([10, 11, 12, 13]), while Dr. J. Tseng (U. Oxford) restructured the framework using more flexible and efficient C++ code logic, and implemented it into the SNO+ software[14]. I was first involved in testing and optimizing the `MP fitter` on simulations and data. Then I extended its usage by developing an `MP partial fitter` for the partial-fill phase and an `MP scint fitter` for both the scintillator phase and tellurium phase. With these extensions, the `MP fitter` framework is ready for multiple SNO+ physics phases. The principles, optimizations, and performances of these fitters are described in Chapter 4 and Appendix A. The key research results presented in this thesis stem from application of the `MP water fitter` to calibration data taken during the SNO+ water phase and to the 190.3 live days of water phase data. Based on these data, a measurement of the Boron-8 solar neutrino flux was performed.

The thesis is organised as follows. In Chapter 2, basic neutrino properties and the phenomena of neutrino flavor transformation and neutrinoless double beta decay are introduced, along with the relevant theories and experiments. Chapter 3 is an overview of the

SNO+ experiment, covering how the SNO+ detector works and reads the physics data; optical properties of liquid scintillators and the detector calibrations, which are crucial to the reconstruction; and a bench-top light yield measurement for a tellurium-loaded liquid scintillator. The latter measurement shows a light yield shift due to the humidity content of the tellurium-loaded scintillator in addition to (an expected) light yield sensitivity to tellurium concentration. Since the light yield of the scintillator is crucial to event reconstruction, this study is helpful for the detector running in realistic situations.

As mentioned above, Chapter 4 describes the principle of event reconstruction and focuses on the `MP fitter`. The other reconstruction algorithms, for example the energy reconstruction, are also introduced. Chapter 5 focuses on the calibration during the SNO+ water phase. The `MP water fitter` was applied to the calibration data and simulations. Among the reconstructed quantities, the position and direction results were based on the MultiPath water fitter, while the energy and classifier results were extracted using the SNO+ official algorithms. However, these results (energy, event type) depend on the position and direction results provided by `MP water fitter`. By comparing simulations and data, I obtained the reconstruction resolutions and uncertainties, following procedures suggested by the collaboration. This chapter also discusses the calibration during the partial-fill phase. The `MP partial fitter` was applied. Based on the calibration data, analysis for extracting the Cherenkov signals from the scintillation lights is discussed.

The results of Chapter 5 underpin an analysis (in Chapter 6) of solar neutrinos during the SNO+ water phase. The `MP water fitter` was applied to the water phase physics data and simulations. Based on the simulations, I applied a machine learning analysis to optimize the signal and background separation. Then the optimized separation parameters were applied to the data to extract the solar neutrinos from the backgrounds. I evaluated the solar neutrino rates and the background rates from the dataset. The systematics and uncertainties from Chapter 5 were evaluated and included in the results. Finally, a ^{8}B solar neutrino flux was evaluated.

Note: unless otherwise stated or cited in the text, the analyses of simulations and data from Chapters 4 to 6 are my own work, performed under the supervision of Drs. A. L. Hallin, J.-P. Yañez Garza, and C. B. Krauss.

Chapter 2

Neutrino physics

This chapter introduces the properties of neutrinos and their interactions, focusing on the weak interactions, neutrino mass and flavor transformations. Existence of the particle (or class of particles) now known as the neutrino was first proposed by Pauli, to explain the (otherwise incomprehensible) spread of the electron energy spectrum in radioactive beta-decay. Since the first (indirect) *observations* of the neutrino, decades later in the 1950s, various types of neutrino experiments have measured and studied neutrinos produced from different sources: the core of the Sun, Earth's mantle and crust, the atmosphere, fission reactors, accelerator beams, and astrophysical objects such as supernovae. To state the obvious, these sources produce (in turn): solar neutrinos, geoneutrinos, atmospheric neutrinos, reactor antineutrinos, accelerator neutrinos and supernova/astrophysical neutrinos. Experiments focused on solar neutrinos have unraveled the phenomenon of neutrino flavor transformation in matter. The solar neutrino experiments relevant to the analysis presented in Chapter 6 are introduced. The last section of this chapter introduces the major physics goal for SNO+, i.e. neutrinoless double beta decay, and covers experiments relevant to that goal.

2.1 Overview

A neutrino is a neutral, spin-1/2 fermion that interacts (*with other fermions or fermionic fields*) only via the weak interaction and gravity. Its basic properties and interactions are described by the Standard Model (SM), a theory describing the properties of all elementary particles currently observed and their interactions based on *three* fundamental forces: the strong, weak, and electromagnetic forces. Notably the gravitational force, though equally deserving the adjective 'fundamental', is not included in the Standard Model, and a long-standing effort to unify the four forces is ongoing.

The SM has successfully explained and predicted phenomena in particle physics since the latter half of the 20th century. An important triumph achieved by the SM is the discovery of the predicted Higgs bosons in 2012. However, there are still open issues in the SM. Besides the question of accommodating gravity, some of the unsolved questions relate to the mysterious properties and behaviour of neutrinos: What are the masses of neutrinos? How do neutrinos obtain their masses? Why are their masses so small compared to those of the other elementary particles? Are neutrinos their own antiparticles? Still further questions about neutrinos are likely to emerge. Were any of these questions to be answered, a door would open to new physics theories beyond the SM.

Since neutrinos weakly interact with other particles and fields, they can penetrate through massive matter or travel a long way through space without being interrupted. Neutrinos produced in the core of the Sun, in Supernovae, or in the galactic core of the Milky Way can carry original information of these astrophysics objects and easily bring these information to the detectors on the Earth. This property enables neutrinos as a probe to study the status of astrophysics objects.

The interesting facts mentioned above put the researches of neutrinos under the spotlight.

The existence of neutrinos was first put forward by Wolfgang Pauli in the 1930s to solve the observed contradicts in β-decay process. In 1914, James Chadwick found that the electrons emitted in β-decay (called the "β-electrons") have a continuous energy spectrum[15].

However, since nuclei have discrete energy levels, the energy spectrum of β-electrons should be discrete and equal to the difference between the final and initial states of nuclei. This indicates that the energy and momentum are not conserved if only nuclei and β-electrons present in the β-decay products. Pauli then introduced a charge-neutral, spin-1/2, and nearly massless particle to the β-decay products. This particle was later called "neutrino" (the small neutral one) by Enrico Fermi. The neutrinos take away a part of energies and then cause the broad energy spectrum of β-electrons, thus the problem was solved.

In 1934, Fermi developed the four-fermion vertex interaction theory to describe the weak interactions relating to neutrinos. Soon after that, Bethe and Peierls suggested direct neutrino detection can be made via a neutrino-induced interaction, called the inverse beta decay (IBD): $\bar{\nu}_e + p \rightarrow e^+ + n$. Their calculation showed that the IBD cross-section was in the order of $\mathcal{O}(10^{-44}\ \mathrm{cm}^2)$, which was difficult for detection[16]. Though the task to detect neutrinos was difficult, in 1956, Fred Reines and Clyde Cowan made the first discovery of the antineutrinos from nuclear reactors. They measured the cross-section as 6.3×10^{-44} cm^2, which was consistent with Bethe's calculation[17].

In 1962, Lederman, Schwartz, and Steinberger demonstrated that more than one type of neutrino exists by detecting the interactions of the muon neutrino (ν_μ)[18]. The tauon neutrino (ν_τ) was proposed after the discovery of the τ lepton and was observed in 2000 by the DONUT collaboration[19]. The decay width of the Z^0 boson measured by the ALEPH collaboration implied that based on the SM, the number of light neutrino species is three[20].

Currently, there are three flavor neutrinos described in the SM. Neutrinos mostly participate in the weak interaction, while the other interactions are negligible. Via weak interaction, a neutrino ν_x is generated with a definite leptonic flavor, accompanied by one of the three charged leptons: electron (e), muon (μ) or tauon (τ), from which it is identified as an electron neutrino (ν_e), a muon neutrino (ν_μ), or a tauon neutrino (ν_τ). By observing the produced secondary charged particles, neutrinos can be detected.

Table 2.1: Neutrino interactions in the $\mathcal{O}$(0.1-10 MeV) energy region, modified from Ref. [6].

ES	IBD	Nuclear Interactions
$\overset{(-)}{\nu}_x + e^- \rightarrow \overset{(-)}{\nu}_x + e^-$	$\bar{\nu}_e + p \rightarrow n + e^+$	$\nu_e + (N, Z) \rightarrow (N-1, Z+1) + e^-$
$\overset{(-)}{\nu}_x + p \rightarrow \overset{(-)}{\nu}_x + p$		$\bar{\nu}_e + (N, Z) \rightarrow (N+1, Z-1) + e^+$
		$\nu_x + A \rightarrow \nu_x + A^*$
		$\nu_x + A \rightarrow \nu_x + A$

2.2 Neutrino Interactions

In the SM, the weak interaction is described by the electroweak theory based on the Glashow-Weinberg-Salam (GWS) model, as fermions exchanging three types of gauge bosons, the weak force carriers: the charged $W^\pm$, and the neutral Z^0. The theory requires the lepton number and lepton flavor conservation and allows only the chiral left-handed neutrino (ν_L) and right-handed antineutrino ($\bar{\nu}_R$) to participate in weak interactions. Neutrino interactions include the neutrino-electron scattering, neutrino-nucleon scattering and hadron decays [3].

This thesis studies solar neutrinos in the energy range $E_\nu \sim \mathcal{O}$(0.1-10 MeV), a range in which the most completely understood interactions are neutrino elastic scattering on electrons, protons and nuclei [6], see Table. 2.1. Elastic scattering can proceed via the charged weak current (CC) process entailing an exchange of the $W^\pm$ bosons, or via the neutral weak current (NC) process wherein the Z^0 boson is exchanged. In particular the elastic scattering interaction $\nu + e^-$ ES: $\nu_x + e^- \rightarrow \nu_x + e^-$ $(x = e, \mu, \tau)$ plays an important role in the detection of solar neutrinos, and will be discussed in the next section.

2.2.1 Neutrino-Electron Elastic Scattering

The $\nu + e^-$ ES process is a pure leptonic process and can be precisely described by the electroweak theory in the SM. This process has no energy threshold, and is sensitive to all neutrino flavors. It is valid for both neutrino and antineutrino.

The amplitude for this process has contributions from both NC and CC interactions. Fig. 2.1 shows the tree-level Feynman diagrams (without radiative corrections) for the CC

ES (Fig. 2.1(a)) and the NC ES (Fig. 2.1(b)) interactions.

It is a characteristic of the charged vertex that lepton generation does not change, thus, although the ν_e can undergo both the CC ES and NC ES interactions, the ν_μ and ν_τ may interact only through the NC ES interaction[1] . In other words for the CC channel the charged lepton in the final state must belong to the same lepton generation as the (incoming) neutrino, this being required by (the theory of) the weak interaction. In this case, since the rest masses of muon and tau leptons are much larger than the masses of solar neutrinos, specifically $m_\mu \approx 105.6$ MeV and $m_\tau \approx 1.78$ GeV [21], evaluation of the elastic scattering via the CC channel requires energy thresholds larger than 10.9 GeV for the ν_μ and 3089 GeV for the ν_τ, which is impossible for solar neutrinos. On the other hand, for the NC ES, the Feynman diagram is the same for all flavors $\bar{\nu}_x$[3, 22].

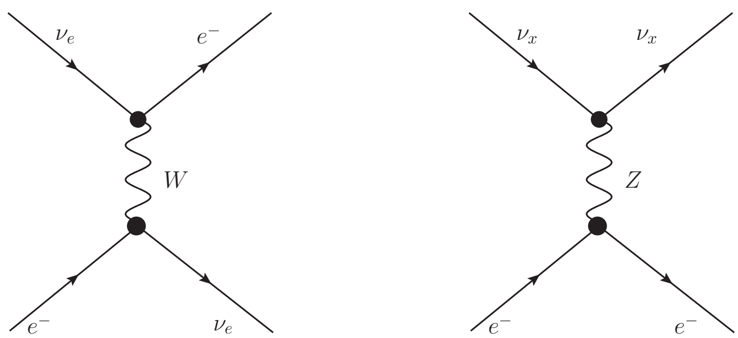

(a) CC ES.

(b) NC ES.

Figure 2.1: Feynman diagrams for the elastic scattering interaction in different channels at tree level. (a): CC ES for ν_e; (b): NC ES for all flavors ν_x ($x = e, \mu, \tau$).

In a particle detector, the 'target' electron is normally an atomic electron of the detector medium, and is considered to be at rest in the laboratory frame. The incoming solar neutrinos interact with these electrons via the $\nu + e^-$ ES, and these electrons are scattered, as shown in Fig 2.2.

In the laboratory frame, the kinetic energy of a recoil electron from the $\nu + e^-$ ES process

[1]For $\bar{\nu}_e$, the Feynman diagram of the CC ES is a s-channel diagram rather than the t-channel presented in Fig 2.1(a)

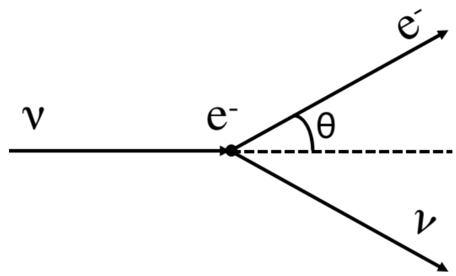

Figure 2.2: A diagram of the $\nu + e^-$ elastic scattering in the lab frame, modified from Ref. [3].

is [3]:

$$T_e = \frac{2m_e c^2 E_\nu^2 \cos^2\theta}{(m_e c^2 + E_\nu)^2 - E_\nu^2 \cos^2\theta}, \tag{2.1}$$

where the scattering angle θ is defined (Fig. 2.2) as the deviation of the outgoing (scattered) electron's path and the path of the incoming neutrino (Eqn. 2.1 follows directly from conservation of relativistic 4-momentum, if one neglects the mass of the neutrinos). The recoil electron has maximum energy

$$T_{max} = \frac{2E_\nu^2}{2E_\nu + m_e c^2} \tag{2.2}$$

when it scatters along the direction of the incident neutrino (i.e. when $\theta = 0$ or $\theta = \pi$).

The direction of the scattered electron is strongly correlated with the direction of the incident neutrino. For solar neutrinos, the scattering angle (relative to the axis between the Snoplus detector and the sun's position) is denoted as "solar angle" (θ_{sun}) in this thesis. It is one of the crucial parameters for measuring solar neutrinos, which will be discussed in Chapter 6 for analyzing solar neutrinos in the SNO+ water phase. By rearranging Eqn. (2.1) we obtain

$$\begin{aligned} \cos\theta_{sun} &= \sqrt{\frac{T_e(m_e c^2 + E_\nu)^2}{2m_e c^2 E_\nu^2 + T_e E_\nu^2}}, \\ &= \left(1 + \frac{m_e c^2}{E_\nu}\right) \frac{1}{\sqrt{1 + \frac{2m_e c^2}{T_e}}}. \end{aligned} \tag{2.3}$$

The differential cross-section of the $\nu + e^-$ ES in the lab frame (without radiative corrections) is given by[3, 22, 23]:

$$\frac{d\sigma}{dT_e}(E_\nu, T_e) = \frac{G_F^2 m_e}{2\pi}\left[(c_V + c_A)^2 + (c_V - c_A)^2\left(1 - \frac{T_e}{E_\nu}\right)^2 - (c_V^2 - c_A^2)\frac{m_e T_e}{E_\nu^2}\right], \qquad (2.4)$$

where G_F is the Fermi coupling constant in the weak interaction; the coupling parameters $c_V = 2\sin^2\theta_W \pm \frac{1}{2}$, $c_A = \pm\frac{1}{2}$, and the "+" sign is for the $\nu_e + e^-$ case while "−" sign is for the $\nu_{\mu,\tau} + e^-$ cases; the Weinberg angle $\sin\theta_W$ is given by $\sin^2\theta_W = 0.23$. The cross-section is $\sigma^{ES}(\nu_e + e^-) = 9.52 \times 10^{-44}$ $(E_\nu/10$ MeV$)$ cm^2 and the expected solar neutrino rate is (see [23]):

$$R = A\int_{T_{thresh}}^{T_{max}} \frac{d\sigma}{dE}\frac{dN}{dE_\nu}\,dE_\nu\ . \qquad (2.5)$$

The shape of the recoil electron energy spectrum and the directionality are utilized by the experiments to tag solar neutrinos in real-time [23]. These experiments will be introduced in Sect. 2.4.

For the solar neutrino case, $E_\nu \gg m_e c^2$, the total cross-section of $\nu_e + e^-$ ES and $\nu_x + e^-$ ES ($x = \mu$ or τ) can safely be approximated as [22]:

$$\sigma^{ES}(\nu_e + e^-) = \frac{2G_F^2}{\pi}m_e E_\nu\left[(1 + c_L)^2 + \frac{1}{3}(c_R)^2\right], \qquad (2.6)$$

$$\sigma^{ES}(\nu_x + e^-) = \frac{2G_F^2}{\pi}m_e E_\nu\left[(c_L)^2 + \frac{1}{3}(c_R)^2\right], \qquad (2.7)$$

where $x = \mu$ or τ, $c_L = \frac{(c_V + c_A)}{2}$ and $c_R = \frac{(c_V - c_A)}{2}$. Then the ratio of $\sigma^{ES}(\nu_{\mu,\tau} + e^-)$ to $\sigma^{ES}(\nu_e + e^-)$ is [22]:

$$\frac{\sigma^{ES}(\nu_x + e^-)}{\sigma^{ES}(\nu_e + e^-)} = \frac{3(c_L)^2 + (c_R)^2}{3(1 + c_L)^2 + (c_R)^2} \approx 0.155\ . \qquad (2.8)$$

Thus the cross-section for CC ES is about 6.5 times larger than that for NC ES. It follows that *if* at the detector the fluxes of ν_e (Φ_{ν_e}) and of ν_μ **or** ν_τ (Φ_{ν_x}) *were equal*, the expected number of ν_e detected would be about 6.5 times greater than the sum of the ν_μ and ν_τ events. This theory-based expectation was an input in the solar neutrino simulations, which will be discussed in Sect. 6.3.8, Chapter 6.

2.3 Neutrino Flavor Transformation

Neutrino flavor transformation is a quantum mechanical interference phenomenon [24]. It was first discovered in 1998, based on the analysis of atmospheric neutrino fluxes measured by the Super-Kamiokande (Super-K) experiment to solve the "atmospheric neutrino anomaly" [25]. It is the first direct evidence showing that neutrinos have finite masses and that the SM is incomplete.

2.3.1 Vacuum Oscillation

For neutrino flavor oscillation experiments, neutrinos are detected in certain flavor eigenstates via weak interaction. A neutrino flavor state vector can be taken as a linear superposition of the mass eigenstates. For three-flavor neutrino mixing, we have[2] [21]:

$$|\nu_f\rangle = \sum_{j=1}^{3} U^*_{fj}|\nu_j\rangle, \tag{2.9}$$

where $f = (e, \mu, \tau)$ and $j = (1, 2, 3)$. The unitary matrix U^*_{fj}, known as the Pontecorvo–Maki– Nakagawa– Sakata (PMNS) matrix, U_{PMNS}, can be parameterized as[3] :

$$U_{PMNS} = \begin{pmatrix} 1 & 0 & 0 \\ 0 & c_{23} & s_{23} \\ 0 & -s_{23} & c_{23} \end{pmatrix} \begin{pmatrix} c_{13} & 0 & e^{-i\delta_{CP}}s_{13} \\ 0 & 1 & 0 \\ e^{-i\delta_{CP}}s_{13} & 0 & c_{13} \end{pmatrix} \begin{pmatrix} c_{12} & s_{12} & 0 \\ -s_{12} & c_{12} & 0 \\ 0 & 0 & 1 \end{pmatrix}, \tag{2.10}$$

where $c_{jk} \equiv \cos\theta_{jk}$ and $s_{jk} \equiv \sin\theta_{jk}$ $(j, k = 1, 2, 3)$. In the PMNS matrix, there are four parameters: the three mixing angles θ_{12}, θ_{13}, θ_{23} and the charge-parity (CP) violation parameter of the lepton sector, δ_{CP}. The unknown value of δ_{CP} is related to leptogenesis, the hypothetical physical process that produced an asymmetry between leptons and anti-leptons in the very early universe [26].

Now consider the propagation of a neutrino in the vacuum. Suppose that a neutrino is generated at time $t_0 = 0$ (in the lab frame) by some mechanism (source), and that it is in

[2]The reader is asked to be alert for two distinct usages of i — as both $i = \sqrt{-1}$ and as an *index*. Short of invoking unusual symbols, such conflicts are hard to avoid. Hopefully no confusion will arise.

[3]Here we ignore the Majorana CP violation phases, which cancel out and do not affect the calculation of flavor transformation probability. They will be introduced in Sect. 2.5.

flavor state

$$|\nu(0)\rangle = |\nu_\alpha\rangle = \sum_j U^*_{\alpha j}|\nu_j\rangle \ . \tag{2.11}$$

The energy of the initial state is a linear combination of the energies $E_j = \sqrt{p_j^2 + (m_j c^2)^2}$ of the mass eigenstates (where p_j is the 3-momentum). The neutrino then propagates in vacuum with a speed close to the speed of light (ultra-relativistic) for a distance L and is finally detected at time t in a detector.

Now assume that the 3-momentum vector is oriented along the vector separating source and detector, with a single non-zero component. Via the 1D Schrödinger equation, the amplitude for the flavor eigenstate $|\nu_\beta\rangle$ in the detector at (L, t) is (using the natural units: $\hbar = c = 1$) [27]:

$$\mathcal{A}(\nu_\alpha \to \nu_\beta; L, E) = \sum_j U^*_{\alpha j} e^{-iE_j t + ip_j L}\langle\nu_\beta|\nu_j, p_j\rangle = \sum_j U^*_{\alpha j} U_{\beta j} e^{-iE_j t + ip_j L} \ . \tag{2.12}$$

Then the probability that the neutrino ν_α at time $t_0 = 0$ transforms into a ν_β at time t is:

$$\begin{aligned} &P(\nu_\alpha \to \nu_\beta; L, E) = |\mathcal{A}|^2 \ = \ \mathcal{A}\mathcal{A}^* \ = \\ &(U^*_{\alpha 1}U_{\beta 1}e^{-iE_1 t + ip_1 L} + U^*_{\alpha 2}U_{\beta 2}e^{-iE_2 t + ip_2 L} + ...)(U_{\alpha 1}U^*_{\beta 1}e^{+iE_1 t - ip_1 L} + U_{\alpha 2}U^*_{\beta 2}e^{+iE_2 t - ip_2 L} + ...) = \\ &\sum_j |U_{\alpha j}|^2|U_{\beta j}|^2 + \sum_{j>k}(U^*_{\alpha j}U_{\beta j}U_{\alpha k}U^*_{\beta k})\exp\{-i(E_j - E_k)t + i(p_j - p_k)L\} + (j \leftrightarrow k), \end{aligned} \tag{2.13}$$

where $(j \leftrightarrow k)$ stands for the second term exchanging the j, k indices.

For the second term in Eqn. 2.13, in the ultra-relativistic case, $p_j \simeq p_k \equiv p \simeq E \gg m$, where E is the average energy[4] . Then $E_j = \sqrt{p_j^2 + m_j^2} \simeq p + \frac{m_j^2}{2E}$ and thus [21, 27]

$$E_j - E_k \simeq \frac{m_j^2 - m_k^2}{2E} \equiv \frac{\Delta m_{jk}^2}{2E} \ . \tag{2.14}$$

Here Δm_{jk}^2 is a set of parameters called the 'mass square differences', and they feature in the flavor transition probability[5] . With the further simplification that $L \simeq ct = t$ $(c \equiv 1)$,

[4]Note: here and elsewhere in the thesis factors of c or c^2 (etc.) will be dropped – but are understood to be necessary for dimensional homogeneity.

[5]Viewed as a matrix or rank-2 tensor, the quantity $\frac{\Delta m_{jk}^2}{2E}$ has zeros along the diagonal. It is anti-symmetric in its indices.

we obtain

$$\exp\{-i(E_j - E_k)t + i(p_j - p_k)L\} \simeq \exp\{-i\frac{\Delta m_{jk}^2}{2E} L\} \ .$$

In addition,

$$\begin{aligned} U_{\alpha k}^* U_{\beta j} U_{\alpha k} U_{\beta k}^* &= |U_{\alpha j}^* U_{\beta j} U_{\alpha k} U_{\beta k}^*| \ \exp\{i\phi_{\alpha\beta;jk}\} \ , \\ &= |U_{\alpha j}^* U_{\beta j} U_{\alpha k} U_{\beta k}^*| \ \{\cos\phi_{\alpha\beta;jk} + i \sin\phi_{\alpha\beta;jk}\} \end{aligned}$$

where

$$\begin{aligned} \phi_{\alpha\beta;jk} &= \mathrm{Arg}(U_{\alpha j}^* U_{\beta j} U_{\alpha k} U_{\beta k}^*) \ , \\ \phi_{\alpha\beta;jk} &= -\phi_{\alpha\beta;kj} \ . \end{aligned}$$

Then combining the second term (of Eqn. 2.13) and the corresponding ($j \leftrightarrow k$) term, Eqn. 2.13 can be written as [27]:

$$P_{\nu_\alpha \to \nu_\beta}(L, E) = \sum_j |U_{\alpha j}|^2 |U_{\beta j}|^2 + 2 \sum_{j>k} |U_{\alpha j}^* U_{\beta j} U_{\alpha k} U_{\beta k}^*| \cos(\frac{\Delta m_{jk}^2}{2E} L - \phi_{\alpha\beta;jk}), \tag{2.15}$$

where (recall) L is distance from source to detector, and E is the energy of the neutrino *averaged along the path.*

Because the matrix U is unitary the second term in Eqn. 2.15 expands as

$$\begin{aligned} &|U_{\alpha j}^* U_{\beta j} U_{\alpha k} U_{\beta k}^*| \{\cos(\phi_{\alpha\beta;jk}) \cos(\frac{\Delta m_{jk}^2}{2E} L) + \sin(\phi_{\alpha\beta;jk}) \sin(\frac{\Delta m_{jk}^2}{2E} L)\} = \\ &\Re(U_{\alpha j}^* U_{\beta j} U_{\alpha k} U_{\beta k}^*)(1 - 2\sin^2 \frac{\Delta m_{jk}^2 L}{4E}) + \Im(U_{\alpha j}^* U_{\beta j} U_{\alpha k} U_{\beta k}^*) \sin \frac{\Delta m_{jk}^2 L}{2E}, \end{aligned} \tag{2.16}$$

and when $t = L = 0$, Eqn. 2.15 becomes

$$P_{\nu_\alpha \to \nu_\beta} = \delta_{\alpha\beta} = \sum_j |U_{\alpha j}|^2 |U_{\beta j}|^2 + 2 \sum_{j>k} \Re(U_{\alpha j}^* U_{\beta j} U_{\alpha k} U_{\beta k}^*) \ . \tag{2.17}$$

We can now eliminate the first term in Eqn. 2.15, and upon doing so we obtain the important and widely cited 'vacuum neutrino oscillation equation'[21, 27]:

$$\begin{aligned} P_{\nu_\alpha \to \nu_\beta}(L, E) = \delta_{\alpha\beta} \quad &- \quad 4 \sum_{j>k} \Re[U_{\beta j} U_{\alpha j}^* U_{\alpha k} U_{\beta k}^*] \sin^2 \frac{\Delta m_{jk}^2 L}{4E} \\ &+ \quad 2 \sum_{j>k} \Im(U_{\beta j} U_{\alpha j}^* U_{\alpha k} U_{\beta k}^*) \sin \frac{\Delta m_{jk}^2 L}{2E} \ . \end{aligned} \tag{2.18}$$

Choosing a set of units commonly used by experiments and with dimensional transformation, we have [21]:

$$X_{jk} \equiv \frac{\Delta m_{jk}^2 L}{4E} = \frac{1.267\Delta m_{jk}^2[\mathrm{eV}^2]L[\mathrm{m}]}{E_\nu[\mathrm{MeV}]}. \tag{2.19}$$

Maximum oscillation occurs when $X_{jk} \sim \pi$, which gives an effective length $L^{osc}(\Delta m_{jk}, E_\nu) = 4\pi E/|\Delta m_{jk}^2|$.

Currently, the four parameters in the PMNS matrix ($\theta_{12}, \theta_{13}, \theta_{23}$ and δ_{CP}), as well as the two squared-mass differences: $\Delta m_{21}^2 = m_2^2 - m_1^2$ and $\Delta m_{32}^2 = m_3^2 - m_2^2$, have been measured by neutrino oscillation experiments.

These experiments can be classified by the neutrino sources they use: the sun, nuclear reactors, muons generated in the atmosphere by cosmic rays, particle accelerators, and, astronomical sources in deep space. Table 2.2 lists the energy scale of the neutrino source as well as the example experiments.

Table 2.2: Neutrino experiments for studying flavor transformation.

type	source	E_ν	example
solar	the Sun	MeV scale	SNO
reactor	reactor	MeV scale	DayaBay
atmospheric	cosmic-ray	GeV scale	SuperK
accelerator	ν beam from accelerator	GeV scale	T2K
astronomical	astronomical objects	GeV-EeV scale	IceCube

Currently, the sign of Δm_{32}^2 is still not determined. If it is positive, the neutrino masses are in a 'normal hierarchy' (NH, $m_3 > m_2 > m_1$); otherwise they are in an inverted hierarchy (IH, $m_3 < m_1 < m_2$) [21].

For Δm_{21}^2 and θ_{12}, a combined analysis of the measurements from the reactor experiment KamLAND (Kamioka Liquid Scintillator Antineutrino Detector) and the solar neutrino experiment SNO (Sudbury Neutrino Observation) gave $\Delta m_{21}^2 = 7.59^{+0.21}_{-0.21} \times 10^{-5}$ eV^2 and $\tan^2\theta_{21} = 0.47^{+0.06}_{-0.05}$ [28]. Details will be discussed in Sect.2.4.

Accelerator neutrino experiments as well as atmospheric neutrino experiments have measured Δm_{32}^2 and θ_{23}. The most recent results from Super-K show that assuming a normal mass hierarchy, $\Delta m_{32}^2 = 2.5^{+0.13}_{-0.20} \times 10^{-3}\,\mathrm{eV}^2$ and $\sin^2\theta_{23} = 0.588^{+0.031}_{-0.064}$ [29].

In 2012, the reactor neutrino experiment Daya Bay reported the discovery of non-zero θ_{13} with a significance of 5.2σ. In 2016, Daya Bay reported that $\sin^2 2\theta_{13} = 0.0841 \pm 0.0027(stat.) \pm 0.0019(syst.)$. This high-precision result makes $\sin^2 2\theta_{13}$ the best measured mixing angle [30, 31].

In the case of antineutrino flavor oscillation, we have $|\bar{\nu}_\alpha\rangle = \sum_i U_{\alpha i}|\bar{\nu}_i, p_i\rangle$. By a calculation analogous to that summarized above, a similar oscillation probability equation can be obtained, but with the final term (in 2.18) being negative [27]:

$$\begin{aligned} P_{\bar{\nu}_\alpha \to \bar{\nu}_\beta}(L,E) = \delta_{\alpha\beta} \quad &- \quad 4\sum_{j>k} \Re[U_{\beta j}U^*_{\alpha j}U_{\alpha k}U^*_{\beta k}] \sin^2 \frac{\Delta m^2_{jk} L}{4E} \\ &- \quad 2\sum_{j>k} \Im(U_{\beta j}U^*_{\alpha j}U_{\alpha k}U^*_{\beta k}) \sin \frac{\Delta m^2_{jk} L}{2E} \,. \end{aligned} \tag{2.20}$$

This provides a measure of CP violation [27],

$$\mathcal{A}_{CP} = P_{\nu_\alpha \to \nu_\beta}(L,E) - P_{\bar{\nu}_\alpha \to \bar{\nu}_\beta}(L,E) = 4\sum_{j>k} \Im(U_{\beta j}U^*_{\alpha j}U_{\alpha k}U^*_{\beta k}) \sin \frac{\Delta m^2_{jk} L}{2E}, \tag{2.21}$$

where δ_{CP} is examined by the experiments which measure the difference between neutrino and antineutrino oscillation probabilities $P(\bar{\nu}_\alpha \to \bar{\nu}_\beta)$ and $P(\nu_\alpha \to \nu_\beta)$ [22]. In 2019, the Tokai-to-Kamioka (T2K) experiment in Japan claimed confidence intervals for δ_{CP} with three standard deviations (3σ): [-3.41,-0.03] (NH) or [-2.54,-0.32] (IH). This result indicates that leptons exhibit CP violation [32].

2.3.2 Matter Effect

The matter effect is caused by neutrinos interacting with ambient electrons and nucleons in dense matter such as the Sun or the Earth. In this case, at the MeV energy scale, the $\nu + e^-$ ES is dominant. As explained in Sect. 2.2.1, a ν_e may interact electrons via either the charged current (CC) or the neutral current (NC) mechanism, while ν_μ and ν_τ interact only by the NC. Thus the $\nu_e + e^-$ ES has an additional potential, $V_{CC} = \sqrt{2}\, G_F\, n_e$, where n_e is the number density of electrons in the matter encountered. This term alters the oscillation probabilities for neutrinos propagating in matter relative to the situation in the vacuum, an effect which is called the Mikheyev-Smirnov-Wolfenstein (MSW) mechanism [33, 34].

In vacuum two-flavor mixing, the Schrödinger equation can be written (in natural units) [22]:

$$i\frac{d}{dt}\begin{pmatrix}\nu_e\\ \nu_\mu\end{pmatrix} = H_0^f \begin{pmatrix}\nu_e\\ \nu_\mu\end{pmatrix}, \tag{2.22}$$

where

$$\begin{aligned} H_0^f = \frac{1}{2E}&\begin{pmatrix} m_1^2\cos^2\theta + m_2^2\sin^2\theta & (m_2^2-m_1^2)\sin\theta\cos\theta \\ (m_2^2-m_1^2)\sin\theta\cos\theta & m_1^2\sin 2\theta + m_2^2\cos^2\theta \end{pmatrix} = \\ &\frac{\Delta m_{21}^2}{4E}\begin{pmatrix} -\cos 2\theta & \sin 2\theta \\ \sin 2\theta & \cos 2\theta \end{pmatrix} + \frac{(m_1^2+m_2^2)}{4E}\begin{pmatrix} 1 & 0 \\ 0 & 1 \end{pmatrix}, \end{aligned} \tag{2.23}$$

and $\Delta m_{21}^2 = (m_2^2 - m_1^2)$.

To simplify the calculation, we can drop the second unitary term of H_0^f that is irrelevant to the neutrino flavor transformation. Including the matter effect

$$H_m = \begin{pmatrix} -\frac{\Delta m_{21}^2}{4E}\cos 2\theta + \sqrt{2}G_F n_e & \frac{\Delta m_{21}^2}{4E}\sin 2\theta \\ \frac{\Delta m_{21}^2}{4E}\sin 2\theta & \frac{\Delta m_{21}^2}{4E}\cos 2\theta \end{pmatrix}. \tag{2.24}$$

By analogy with mixing in vacuum, a mixing angle in matter, θ_m is defined as

$$\tan 2\theta_m = \frac{\Delta m^2 \sin 2\theta}{\Delta m^2\cos 2\theta - 2\sqrt{2}EG_F n_e}, \tag{2.25}$$

and an effective squared-mass difference in matter, Δm_m^2 is defined as:

$$\Delta m_m^2 = \sqrt{(\Delta m^2\cos 2\theta - 2\sqrt{2}EG_F n_e)^2 + (\Delta m^2 \sin 2\theta)^2}. \tag{2.26}$$

Thus we can write the mixing equation relating the energy eigenstates in matter (ν_{1m}, ν_{2m}) to the flavor eigenstates by a unitary matrix:

$$\begin{pmatrix}\nu_e\\ \nu_\mu\end{pmatrix} = \begin{pmatrix} \cos\theta_m & \sin\theta_m \\ -\sin\theta_m & \cos\theta_m \end{pmatrix}\begin{pmatrix}\nu_{1m}\\ \nu_{2m}\end{pmatrix}. \tag{2.27}$$

The probability of flavor transformation in matter is:

$$P_{\nu_e\to\nu_\mu} = \sin^2(2\theta_m)\sin^2\Big(\frac{\Delta m_m^2 L}{4E}\Big). \tag{2.28}$$

The denominator in equation (2.25) implies a resonance condition:

$$V(n_e) = \sqrt{2} G_F n_e = \frac{\Delta m^2 \cos 2\theta}{2E}. \tag{2.29}$$

From this condition, for a given E, there is a resonance density n_e^{res} while for a given n_e, there is a resonance energy E^{res}. When the resonance condition is satisfied, $\theta_m = \frac{\pi}{4}$ and two flavor neutrinos are maximally mixed, even if the vacuum mixing angle θ is small. This is called matter enhanced neutrino oscillation [33, 35]. The matter effect was first observed by measuring the solar neutrino fluxes, which will be discussed in the next section.

2.4 Solar Neutrinos

In the 1930s, Gamow, von Weizsäcker and Bethe et al. explained that the Sun's energy is derived from a series of nuclear reactions [36]. Our current knowledge of these nuclear reactions has been summarized in the Standard Solar Model (SSM).

The SSM is a modern and broadly accepted theory for tracing the evolution of the Sun from its beginning, which is based on contemporary data from theories and experimental measurements, including an equation of state describing the balance between the gravitational and pressure forces; the cross-sections of the nuclear reactions; and the modern Sun's mass, age, radius, luminosity, etc. [37]. According to the SSM, the energy in the Sun is mainly produced by two sets of reactions: the proton-proton (pp) chain, which is dominant and contributes $\sim 98.6\%$ of the energy released, and the Carbon-Nitrogen-Oxygen (CNO) cycle, which contributes $\sim 1.4\%$ [6]. Fig. 2.3 shows all the reactions in the pp chain, and Fig. 2.4 shows the reactions in the CNO cycle.

Via these nuclear reactions, hydrogen is eventually fused into helium, and the net nuclear transformation is $4p + 2e^- \rightarrow {}^4\text{He} + 2\nu_e + Q$, where the released energy $Q = 26.73$ MeV is mostly in the form of the kinetic energy of the photons, with a small fraction carried by neutrinos [6, 39].

The electron neutrinos ν_e produced in the solar nuclear reactions are called "solar neutrinos" and they can be detected on the Earth. Due to the branching ratios and unterminated

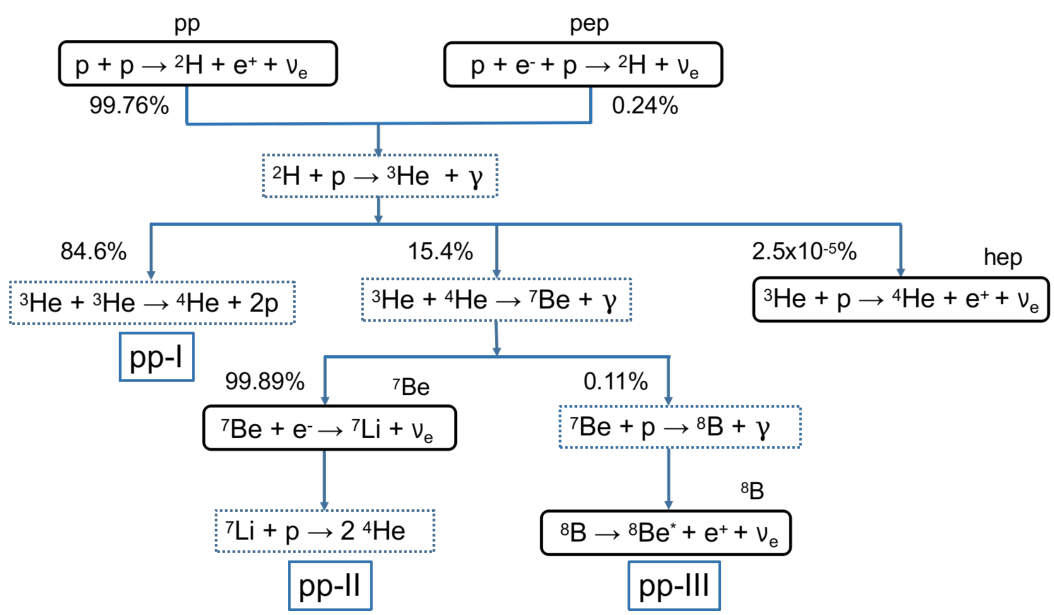

Figure 2.3: All reactions in the three PP chains: PP-I, PP-II, PP-III. The reactions producing neutrinos are labeled in the solid frames. Modified from [38].

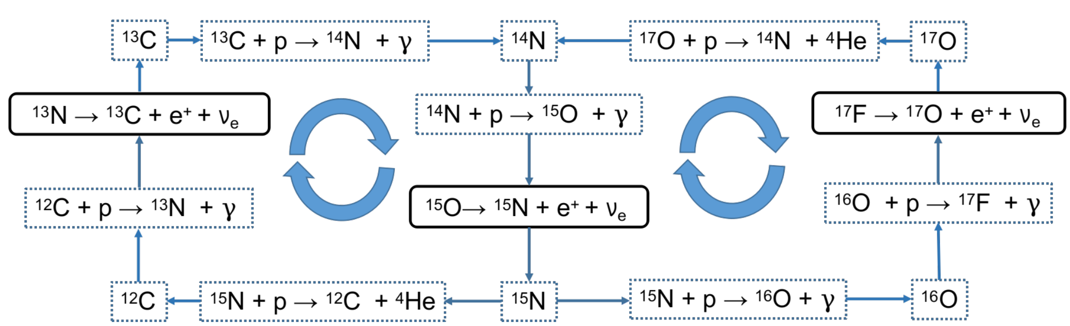

Figure 2.4: All reactions in the CNO bicycle. The reactions producing neutrinos are labeled in the solid frames. Modified from [38].

chains in the pp chain and CNO cycle, the solar neutrinos come from different reactions, as shown in Fig. 2.3 and Fig. 2.4. They are named after the corresponding reactions, as shown in Table. 2.3.

Table 2.3: The main reactions producing solar neutrinos in pp chain (a) and CNO cycle (b).

(a) pp chain

solar ν_e	reaction
pp	$p + p \rightarrow {}^2\text{H} + e^+ + \nu_e$
pep	$p + e^- + p \rightarrow {}^2\text{H} + \nu_e$
hep	${}^3\text{He} + p \rightarrow {}^4\text{He} + e^+ + \nu_e$
^{7}Be	${}^7\text{Be} + e^- \rightarrow {}^7\text{Li} + \nu_e$
^{8}B	${}^8\text{B} \rightarrow {}^8\text{Be}^* + e^+ + \nu_e$

(b) CNO cycle

solar ν_e	reaction
CNO	${}^{13}\text{N} \rightarrow {}^{13}\text{C} + e^+ + \nu_e$
	${}^{15}\text{O} \rightarrow {}^{15}\text{N} + e^+ + \nu_e$
	${}^{17}\text{F} \rightarrow {}^{17}\text{O} + e^+ + \nu_e$

The average energy of a solar electron neutrino (ν_e) is calculated by summing over the energies $E^i_{\nu_e}$ from the i^{th} reaction chain with a flux of $\Phi^i_{\nu_e}$ and dividing by $\Phi^{tot}_{\nu_e}$[6]:

$$\langle E_{\nu_e} \rangle = \sum_i E^i_{\nu_e} \frac{\Phi^i_{\nu_e}}{\Phi^{\text{tot}}_{\nu_e}} \approx 0.265 \text{ MeV}. \tag{2.30}$$

For every MeV of released energy, there are about two ν_e generated. Then the solar ν_e flux at the Earth's surface can be estimated via the measured solar radiation energy on the Earth surface:

$$\Phi_{\nu_e} \simeq \frac{\mathcal{L}_\odot}{4\pi D^2_\odot} \frac{2}{Q - 2\langle E_{\nu_e} \rangle} \simeq 6.40 \times 10^{10} \ \nu_e/\text{cm}^2/\text{s}, \tag{2.31}$$

where the solar constant $G_{sc} = \mathcal{L}_\odot/(4\pi D^2_\odot) \simeq 0.136$ W/cm^2 [40].

The SSM can predict the fluxes and energies of the solar neutrinos coming from different reactions, as shown in Fig. 2.5 [37].

In 1964, J. Bahcall and R. Davis proposed the first experiment to detect solar neutrinos [41, 42]. Davis designed an experiment that used a 380 m^3 tank filled with Perchloroethylene (C_2Cl_4), a dry-cleaning fluid rich in chlorine. Solar neutrinos were expected to change ^{37}C1 to ^{37}Ar via the endothermic reaction: $\nu_e + {}^{37}\text{Cl} \rightarrow {}^{37}\text{Ar} + e^-$, and the resulting ^{37}Ar atoms were extracted and counted (a 'radiochemical' method). The neutrino energy threshold (E_{min}) of the experiment was 0.814 MeV, which allowed a measurement mostly of the

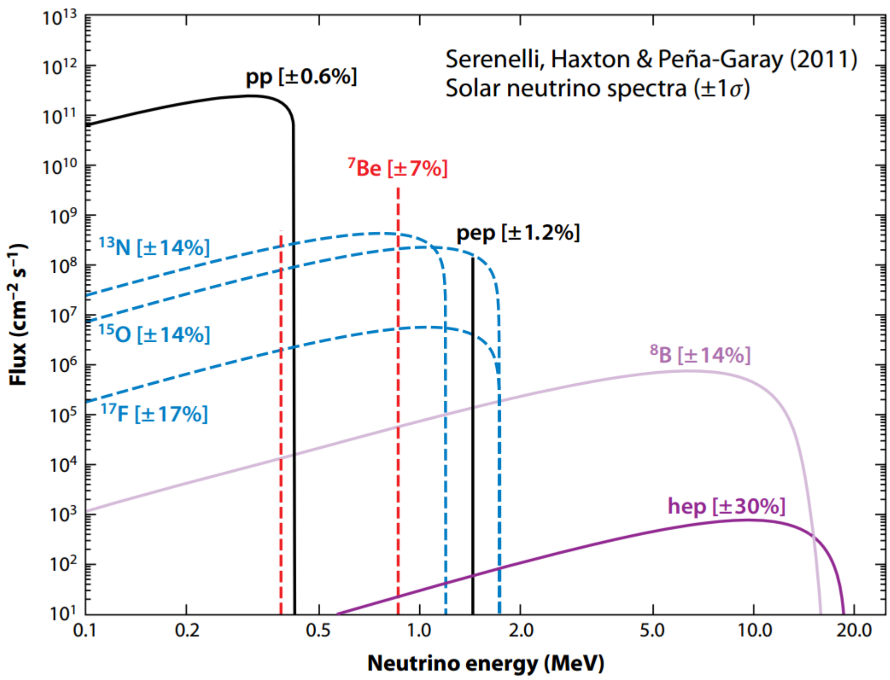

Figure 2.5: Solar neutrino energy spectrum (E_ν vs. flux) along with the SSM uncertainties, from Ref. [37].

^{8}B solar ν_e flux but also including some lower energy neutrinos [42]. Their first results, announced in 1968, showed that only about one-third of the predicted radioactive argon atoms were measured[43]. This pioneering experiment raised a problem of the "missing" solar neutrinos, the "solar neutrino problem."

2.4.1 Kamiokande and Super-Kamiokande

The solar neutrino problem was later confirmed by the Kamiokande-II experiment in 1988 [44]. As the successor of the Kamiokande, Super-K uses a 50-kilotonne water Cherenkov detector to measure the solar neutrinos via the $\nu + e^-$ elastic scattering. By utilizing the pattern of Cherenkov light produced by the recoil electrons (see Sect. 3.3.1, Chapter 3), the direction of the incoming neutrino can be traced and thus neutrinos produced specifically by the sun can be selected. Unlike the radiochemical method, this enables real-time measurements of the solar neutrinos.

In 2000, Super-K reported the observed solar neutrino flux to be only about 45% of the flux expected according to the SSM, and with more than a 99.9% confidence level. This suggest there had been a flavor transformation of solar neutrinos, and limited the oscillation parameters (Δm_{21}^2, θ_{12}) [44].

Super-K continues to measure solar neutrinos with more precision and higher statistical accuracy, and the energy threshold has been lowered to 3.5 MeV to enable a search for ^{8}B solar neutrinos. The fourth phase of Super-K (Super-K-IV) took data from 2008 to 2014, and by utilizing this 1664 live-day data, Super-K-IV reported a measurement of the elastic scattering flux as: $\Phi_{ES} = (2.308 \pm 0.020(stat.)^{+0.039}_{-0.040}(syst.)) \times 10^6\ \mathrm{cm}^{-2}\mathrm{s}^{-1}$[2]. Combined with the previous three phases, it gives $\Phi_{ES} = (2.345 \pm 0.014(stat.) \pm 0.036(syst.)) \times 10^6\ \mathrm{cm}^{-2}\mathrm{s}^{-1}$[2]. In Chapter 6 these values will be compared to the Snoplus measurements of this thesis.

2.4.2 SNO

The Sudbury Neutrino Observatory (SNO) experiment finally resolved the solar neutrino problem and first confirmed that the missing solar neutrinos are due to the neutrino flavor transformation $\nu_e \to \nu_{\mu,\tau}$, along with the matter effect mentioned in Sect. 2.3.2.

SNO used a 1-kilotonne heavy water (D_2O) Cherenkov detector to distinguish the flavors of solar neutrinos. The SNO detector was sensitive to the ^{8}B solar neutrinos via three interactions: (1) the charged current (CC) on deuteron (d): $\nu_e + d \to p + p + e^-$, (2) the neutral current (NC): $\nu_x + d \to p + n + \nu_x$, and (3) the elastic scattering (ES): $\nu_x + e^- \to \nu_x + e^-$. The CC channel was sensitive only to ν_e while the NC channel was independent of the neutrino type ("flavor-blind"), which provided a measurement of the total solar neutrino flux regardless of neutrino flavors. The ES channel was also sensitive to all flavors but with reduced sensitivities to ν_μ and ν_τ [45]. As mentioned in Sect. 2.2.1, from Eqn. 2.8 the ES cross-section of ν_e is 6.5 times larger than that of $\nu_{\mu,\tau}$ (combined).

In 2002, SNO reported that the measured total ^{8}B solar neutrino flux via the NC channel (Φ_{NC}) was consistent with the SSM while the ν_e component of the flux (Φ_e) was about one-third of the total flux[45]:

$$R = \Phi_{CC}/\Phi_{NC} = \Phi_e/\Phi_{tot} = 0.34 \pm 0.04. \tag{2.32}$$

A combined analysis of SNO data acquired from 1999 to 2006 gave the measured total flux of ^{8}B solar neutrinos as $\Phi_{^8\mathrm{B}} = 5.25 \pm 0.16(stat.)^{+0.11}_{-0.13}(syst.)$ cm^{-2}s^{-1}. Based on a two-flavor neutrino oscillation analysis, SNO implied that $\Delta m^2_{21} = (5.6^{+1.9}_{-1.4}) \times 10^{-5}$ eV^2 and $\tan^2\theta_{12} = 0.427^{+0.033}_{-0.029}$ [46].

2.4.3 KamLAND

As mentioned in Sect. 2.3.1, reactor antineutrino experiments study the neutrino flavor transformation by measuring $\mathcal{O}$(MeV) $\bar{\nu}_e$ produced by nuclear reactors. If the distance between the reactor and the detector is long enough (according to Eqn. 2.19, $L \sim \mathcal{O}(100$ km$)$), such experiments can probe the Δm^2_{12} and θ_{12} parameters, or the flavor transformation parameters in the solar sector. KamLAND is able to study the solar sector due to its long baseline of 180 kilometers (the average value of the distances to the various reactors). It is a 1-kilotonne liquid scintillator detector, located in Gifu Prefecture, Japan, under Mount Ikenoyama at a depth of about 2700 metres water equivalent ($m.w.e$) [28]. KamLAND measures the $\bar{\nu}_e$ via the inverse beta-decay (IBD) process $\bar{\nu}_e + p \to n + e^+$, utilizing the prompt (light) signal produced by annihilation of the positron e^+, along with the delayed coincidence with the signal due to the γ emitted by neutron capture on a nucleus after thermalization [21]. KamLAND provided best fit values of [47]: $\Delta m^2_{21} = 7.50^{+0.19}_{-0.20} \times 10^{-5}$ eV^2 and $\tan^2\theta_{12} = 0.452^{+0.035}_{-0.033}$. This value for $\tan^2\theta_{12}$ matches well with the solar neutrino measurements, but for the Δm^2_{21} there is a $< 2\sigma$ level tension, which may be attributable to statistical fluctuation or some minor effect, such as the day/night matter effect.

Assuming CPT invariance, the KamLAND and solar neutrino data can be combined by including solar ν_e and reactor $\bar{\nu}_e$ data to obtain the oscillation parameters. These values have been given in Sect. 2.3.1.

2.4.4 Borexino

Borexino is a liquid scintillator neutrino detector with a target mass of about 300 tonnes. It is located at the Gran Sasso National Laboratory (LNGS) in central Italy, under an overburden of rock with 3800 water equivalent meter (m.w.e) to suppress the cosmogenic backgrounds. It is the first experiment to have made real-time measurements of low energy (< 1 MeV) solar neutrinos, thanks to the high light yield of the liquid scintillator [48].

Unlike a water Cherenkov detector, although a liquid scintillator provides more (detectable) photons per unit of neutrino energy deposited, it cannot be used to measure the event direction (see Sect. 3.3.2, Chapter 3). Borexino mainly measures the energy spectrum of the recoil electrons from the $\nu + e^-$ ES, a method that is termed 'spectroscopic' [48]. Precise measurements of the energy spectrum can identify different types of solar neutrinos and separate backgrounds.

Borexino has measured the ^{7}Be, pep, pp and ^{8}B solar neutrino fluxes [49]. In 2020 it reported the first observation of CNO neutrinos with an interaction rate of $7.2^{+3.0}_{-1.7}$ counts per day per 100 tonnes of target at 68% C.L., and this result gives an estimate of the CNO neutrino flux at the Earth as $7.0^{+3.0}_{-2.0} \times 10^8$ cm^{-2} s^{-1} [50]. An improved measurement of the ^{8}B solar neutrino was reported in 2020, with the elastic scattering flux (integrated over energy range $3.2 < E_\nu < 17$ MeV) determined as $\Phi_{ES} = (2.57^{+0.17}_{-0.18}(stat.) \pm 0.07(syst.)) \times 10^6$ cm^{-2} s^{-1} [48].

2.4.5 More Studies on Solar Neutrino and Future Experiments

There are at least the following three avenues for future solar neutrino research: (1) precision measurements of solar neutrino fluxes, (2) sub-leading-order effects on the phenomenology from both standard and nonstandard physics, and (3) new detection techniques [6].

Currently, *hep* neutrinos have not been measured yet due to the weakness of their flux. On the other hand, although most 'species' of low energy solar neutrinos have been discovered (i.e. measured), more precise measurements would help to probe the details of matter effects, measure the oscillation parameters in the solar sector more precisely to resolve the tensions between reactor- and solar-source experiments, and could unveil new physics such as nonstandard neutrino interactions (NSI) by observing sub-leading effects [51]. Among the low energy neutrinos, pep neutrinos enjoy the distinction of being mono-energetic (with E_ν=1.442 MeV), and their flux is well predicted by the Standard Solar Model [**?**]. A precise measurement of the pep neutrinos will give more information on the matter effect in neutrino oscillations.

Solar metallicity (Z) is the abundance of elements heavier than ^{4}He (called "metal" elements in the context of astronomy). It is poorly constrained and the predictions from different solar models vary. Since the sub-dominant CNO neutrino flux depends linearly on the metallicity of the solar core, a precise measurement of the CNO neutrinos can determine the abundance of ^{12}C, ^{13}N and ^{15}O in the Sun and thus determine the solar metallicity [**?**].

Several new experiments using various detection techniques are being planned, to precisely measure the solar neutrinos in the near future. These experiments include:

Large-scale water Cherenkov detectors, such as Hyper-Kamiokande (Hyper-K). Hyper-K is the next generation of Super-K, and it is designed to have a fiducial mass of 187 kilotonnes, about 8× larger than that of Super-K. With a 4.5-MeV energy threshold, it will measure the ^{8}B solar neutrinos, and it expects to observe 130 $\nu + e^-$ elastic scattering events per day. With such a high count rate, the oscillation parameters in the solar sector can be precisely measured. Hyper-K also has a potential to detect the *hep* neutrinos[52].

A liquid argon neutrino detector, such as DUNE (Deep Underground Neutrino Experiment), can provide two channels for detecting solar neutrinos: ν_e+^{40}Ar→ e^-+^{40}K* and the $\nu + e^-$ ES process: $\nu_x + e^- \rightarrow \nu_x + e^-$. Similar to Hyper-K, DUNE aims for precise measurements of ^{8}B neutrinos, and also searches for *hep* neutrinos [53].

Large-scale liquid scintillator detectors with $\mathcal{O}(10)$ kilotonne fiducial mass, such as ASDC (Advanced Scintillation Detector Concept)-THEIA [54], JUNO (Jiangmen Underground) [55], Jinping (Jinping Neutrino Experiment) [56], and LENA (Low Energy Neutrino Astronomy) [57], are expected to be built to measure low energy solar neutrinos. Some new liquid scintillator techniques (such as water-based liquid scintillator) will be implemented to precisely measure neutrino energy and incoming direction. More details of the water-based liquid scintillator will be discussed in Sect. 3.3.4, Chapter 3.

Ton-scale dark matter direct search experiments, such as the DARWIN experiment (DARk matter WImp search with liquid xenoN) can also measure low-energy solar neutrinos. With an energy threshold down to several keV and ultra-low background level, DARWIN will be able to measure the pp and ^{7}Be solar neutrinos [58, 59, 60].

SNO+, one of the operating large-scale liquid scintillator detectors, has measured the ^{8}B solar neutrino flux during its initial water phase [1]. In the following (scintillator) phase, SNO+ is able to measure low energy solar neutrinos ($E_\nu < 2$ MeV), and specifically the CNO and *pep* neutrinos. Due to the depth of SNOLAB, SNO+ is expected to have much lower cosmogenic backgrounds than did Borexino, and thus may obtain more precise measurements [8]. More details will be discussed in Sect. 3.2.2, Chapter 3.

2.5 Neutrinoless Double Beta Decay

The neutrino flavor transformation experiments proved that neutrinos are not massless. However in these experiments mass *differences* rather than absolute masses are measured, so we cannot from these results know the absolute scale of neutrino mass. Currently, there are three main approaches to probing the neutrino masses [39]: (1) Cosmological measurements [61, 62, 63]; (2) Direct measurements of the β-decay spectrum; and (3) A search for the neutrinoless double beta decay ($0\nu\beta\beta$) process, which will be discussed below.

For heavy radioactive isotopes ($A > 70$) whose nuclei have even neutron number and even proton number ("even-even" nuclei), beta decay results in an odd-odd daughter nucleus that is *less* stable. Thus for such isotopes, the β-decay is energetically forbidden. In 1935, M. Goeppert-Mayer pointed out that these isotopes can still decay through a *double* beta decay process: $(Z, A) \to (Z+2, A)+2e^-+2\bar{\nu}_e+Q_{\beta\beta}$, where $Q_{\beta\beta}$ is the released energy. This is called ordinary double beta decay or $2\nu\beta\beta$, which is allowed within the SM. Typically the half-life for isotopes subject to $2\nu\beta\beta$ $T_{1/2} > 10^{19}$ years (yr) [64, 65].

In the SM, neutrinos are neutral (charge 0) fermions. As such, there is no apparent quantum number to distinguish a neutrino and an antineutrino[66]. A neutral fermion that *is* its own antiparticle is named a 'Majorana' particle, in honour of E. Majorana who developed a mathematical modification of the Dirac equation[67].

In 1939 W.H.Furry [68] proposed that *if* neutrinos are Majorana particles (Majorana neutrinos), then a process called neutrinoless double beta decay ($0\nu\beta\beta$) will also be expected to occur: $(Z, A) \rightarrow (Z+2, A) + 2e^- + Q_{\beta\beta}$. In this process, evidently the *lepton number changes* 2, which within the scope of the SM is illegal. Should such a decay be observed, a new paradigm for elementary particle physics will be required. The Feynman diagrams for $2\nu\beta\beta$ and $0\nu\beta\beta$ are compared in Fig. 2.6.

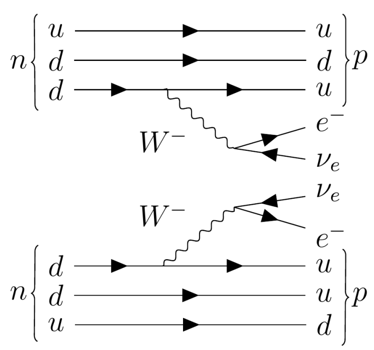

(a) $2\nu\beta\beta$.

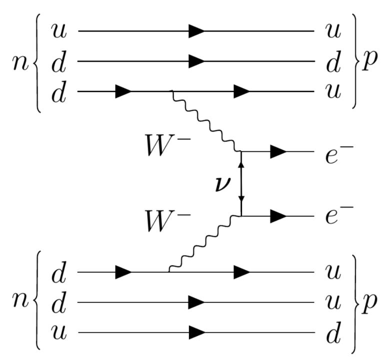

(b) $0\nu\beta\beta$.

Figure 2.6: Feynman diagrams for $2\nu\beta\beta$ (a) and $0\nu\beta\beta$ (b).

For the Majorana neutrino, an effective Majorana mass $\langle m_{ee} \rangle$ is defined as [40, 69]:

$$\langle m_{ee} \rangle = |\sum_{i=1}^{3} U_{ei}^2 m_i| = |c_{13}^2 c_{12}^2 m_1 + c_{13}^2 s_{12}^2 e^{i\alpha_1} m_2 + s_{13}^2 e^{i\alpha_2} m_3|, \quad (2.33)$$

where the values of U_{ei} are the elements of the neutrino mixing matrix for the flavor state ν_e, and m_i are the mass eigenvalues of the mass eigenstates, according to Enq. 2.9; α_1, α_2 are two Majorana CP-violation phase factors ranging from 0 to π, and α_2 can also be taken as $\alpha_2 - \delta_{CP}$.

The neutrino mass eigenvalues m_i can be expressed as the lightest neutrino mass $m_{\nu\text{min}}$

and mass square differences Δm^2_{ij}[40]. For the normal hierarchy (NH),

$$\begin{aligned}
m_{\nu\min} &= m_1 , \\
m_2 &= \sqrt{m^2_{\nu\min} + \Delta m^2_{21}} , \\
m_3 &= \sqrt{m^2_{\nu\min} + |\Delta m^2_{31}|} ,
\end{aligned}$$

while for the IH,

$$\begin{aligned}
m_{\nu\min} &= m_3 , \\
m_1 &= \sqrt{m^2_{\nu\min} + |\Delta m^2_{31}|} , \\
m_2 &= \sqrt{m^2_{\nu\min} + |\Delta m^2_{31}| + \Delta m^2_{21}} .
\end{aligned}$$

In this case, the effective Majorana mass can be derived from $m_{\nu\min}$ and neutrino flavor transformation parameters θ_{ij} and Δm^2_{ij}. A probe of the effective Majorana mass $\langle m_{ee}\rangle$ can thus determine $m_{\nu\min}$ and (in turn) the absolute neutrino masses.

The decay width and the half-life of the $0\nu\beta\beta$ process are calculated as [40, 69]:

$$\Gamma = (T^{0\nu}_{1/2})^{-1} = G_{PS}(Q, Z)\ |M_{Nuc}|^2\ \langle m_{ee}\rangle^2, \tag{2.34}$$

where $G_{PS}(Q, Z)$ is a phase space corresponding to the effective coupling constant, which depends on the endpoint energy Q and the atomic number Z, while $|M_{Nuc}|$ is the nuclear matrix element describing the nuclear transition. The latter can be calculated theoretically, albeit using *approximate methods* based on many-body nuclear models, such as the Nuclear Shell Model (NSM), interacting Boson Model (IBM), etc. Since G_{PS} and $|M_{Nuc}|^2$ can be calculated theoretically, a $0\nu\beta\beta$ experiment measures $T^{0\nu}_{1/2}$ to quantify $\langle m_{ee}\rangle$.

Similar to the β-decay case, the $2\nu\beta\beta$ process will cause a continuous spectrum in the detector. However very significantly, the (hypothetical) $0\nu\beta\beta$ process only has *two electrons in the final state* and so the *sum of the energies of these two electrons is constrained.* These electrons must carry away the total energy released by the decay (the energy from the nuclear recoil is negligible here), and so a spectrum of the (summed) energy released to the outgoing electrons must show a distinct energy peak at the Q-value ($Q_{\beta\beta}$). Taking the isotope ^{130}Te as an example, Fig. 2.7 illustrates the shapes of the energy spectrum from the $2\nu\beta\beta$ and the $0\nu\beta\beta$ decay processes.

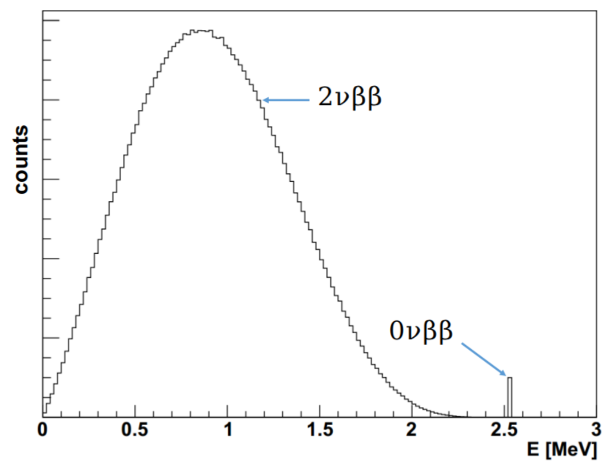

Figure 2.7: Energy spectrum of the ^{130}Te $2\nu\beta\beta$ decay and the hypothetical $0\nu\beta\beta$ decay (sum of the energies of the two outgoing electrons). The SNO+ software package (RAT) was used to produce the simulations for the plot. The package is described in Sect. 3.6.

To determine $T^{0\nu}_{1/2}$, experiments search for events in which the total energy deposited is close to $Q_{\beta\beta}$. For a candidate isotope, the observed number of events in expectation is:

$$N_{event} = \ln 2 \, \frac{N_A}{M_A} \, \frac{\alpha \cdot \epsilon \cdot m \cdot t}{T^{0\nu}_{1/2}}, \tag{2.35}$$

where N_A is the Avogadro's number, α is the abundance of the isotope in the element, M_A is the molar mass of the isotope, m is the target isotope mass in the detector, and t is the measurement time of total exposure.

There are 35 candidate isotopes that can undergo the $2\nu\beta\beta$ decay process, but only a few of them are suitable for the application in direct $0\nu\beta\beta$ search experiments [3]. From the experimental viewpoint, the candidate isotopes are expected to have relatively high natural abundances and high Q-values, be deployable in a large amount with low cost, be atoxic and unharmful to the environment, etc. However, in a realistic situation, no isotope fulfills all these criteria, and trade-offs have to be made for contemporary experiments [70]. Fig. 2.8 shows the Q-values and natural abundances of the candidate isotopes currently selected by the $0\nu\beta\beta$ experiments.

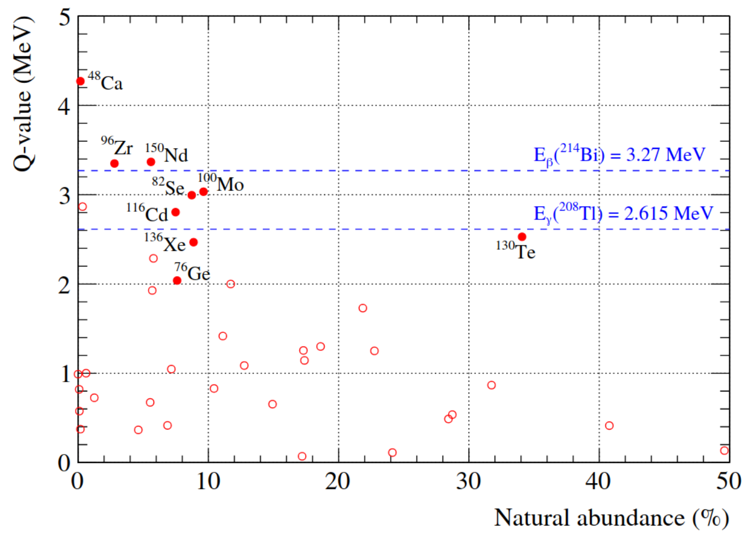

Figure 2.8: Natural abundance vs. Q-values for different $2\nu\beta\beta$ isotopes, from Ref. [4].

Among these isotopes, ^{130}Te has the highest natural abundance of 34% and thus can provide a higher target isotope mass. SNO+ will use Te-loaded liquid scintillator to search for $0\nu\beta\beta$, which will be discussed in Chapter 3.

At the time of this writing, no experiment has found the signal of $0\nu\beta\beta$, while limits on $T^{0\nu}_{1/2}$ and $\langle m_{ee}\rangle$ for various candidate isotopes have been set. Currently, the best limit on $T^{0\nu}_{1/2}$ reported by the experiments is obtained from the KamLAND-Zen (ZEroNeutrino) Experiment, searching for the signal from the ^{136}Xe. Their 2016 results gave a lower limit of $T^{0\nu}_{1/2}(^{136}\mathrm{Xe}) > 1.07 \times 10^{26}$ yr at 90% C.L., and a corresponding upper limit on the effective Majorana mass: $\langle m_{ee}\rangle < (61 - 165)$ meV [71].

For ^{130}Te, the current best limit is from the CUORE experiment (Cryogenic Underground Observatory for Rare Events). In 2018, CUORE placed a lower limit of $T^{0\nu}_{1/2}(^{130}\mathrm{Te}) > 1.5 \times 10^{25}$ yr at 90% C.L., with $\langle m_{ee}\rangle < (110 - 520)$ meV [72].

For ^{76}Ge, the current best limit is from the GERDA experiment (GERmanium Detector Array). In 2019, GERDA reported a lower limit half-life of $T^{0\nu}_{1/2}(^{76}\mathrm{Ge}) > 1.8 \times 10^{26}$ years at 90% C.L. with $\langle m_{ee}\rangle < (79 - 180)$ meV [73].

Future experiments such as the KamLAND2-Zen, LEGEND-1000 and nEXO, coming to fruition within about a decade, are expected to reach $T^{0\nu}_{1/2}$ at $\mathcal{O}(10^{27} - 10^{28})$ years [70].

Chapter 3

The SNO+ Experiment

3.1 Overview

The SNO+ experiment is located at SNOLAB. This deep underground facility sits at Vale's Creighton mine in Sudbury, Ontario, Canada (coordinate: 46°28'19.6"N, 81°11'12.4"W). It provides an environment with extremely low cosmic ray backgrounds. At sea level, an average cosmic muon (μ) flux rate is about 1.44×10^7 $\mu/\mathrm{m}^2/\mathrm{day}$[74]. Cosmic muons with high energies (mostly $\mathcal{O}(\mathrm{GeV})$) can induce spallation backgrounds, such as fast neutrons and lasting isotopes, which are harmful to the low background counting experiments[56]. The SNOLAB has a 2092 ± 6 m flat overburden of rock and it ensures that cosmic muon (μ) flux rate is as low as 0.286 ± 0.009 $\mu/\mathrm{m}^2/\mathrm{day}$, corresponding to 6010 water equivalent meter (m.w.e)[75], which means that every hour only about 1 μ passes through the SNO+ detector.

The SNO+ detector is a refurbishment of the SNO detector. The SNO+ collaboration makes use of the SNO infrastructure and upgraded it to be a liquid scintillator detector. As shown in Fig. 3.1, the detector is inside a barrel-like rock cavity with a diameter of 22 m at its waist and a height of 34 m. The cavity is filled with 7000 tonnes of ultrapure water (UPW) to provide buoyancy for the vessel, and shield radiation backgrounds from the environment, such as the cosmic rays and isotope decays from the rock.

The detector consists of an acrylic vessel (AV) sphere of 12.01 m in diameter and 5.5 cm in thickness. The AV contains detection media (or called target materials) and is held in place by a rope net system including hold-up and hold-down Tensylon ropes. This spherical structure is simple in geometry and reduces the complexities of simulation and event reconstruction. Furthermore, this geometry allows for spherical fiducial volume cuts from the center of the AV to further get rid of external backgrounds, which makes the SNO+ as a graded-shield type detector[76]. On the top of the AV sphere, there is an acrylic neck cylinder with 6.8 m high and 1.46 m inner diameter. The neck connects the AV sphere to the facilities on the deck above the detector. Through the neck, pipes can fill the detection media into the AV and recirculate as well. Calibration sources for internal scans can also be lowered down into the AV through the neck.

The AV sphere is concentric within a stainless steel geodesic dome with an average radius of 8.4 m, which is called the photomultiplier support structure (PSUP). 9394 Hamamatsu 8-inch R1408 photomultipliers (PMTs) were mounted on the PSUP, looking inward to the AV. To increase the light collection efficiency of these PMTs and thus to obtain an extensive photocathode coverage of the detector, each of these PMTs was fitted into a 27 cm diameter reflective bucket (called "concentrator"), which consists of reflective pedals coated with aluminum. The effective photocathode coverage of the detector reaches about 54%[77]. Besides the inward-looking PMTs, 90 PMTs look outward, serving as muon vetos. Furthermore, 4 Hamamatsu R5912 High Quantum Efficiency (HQE) PMTs were also installed for testing the performance of potential SNO+ phases-II[78].

3.2 SNO+ Physics Phases

The SNO+ experiment is designed for multi-purpose measurements of neutrino physics. The detector has been running since December 2016. There are three physics phases of the experiment and each phase has different detection media inside the AV: the water phase, the scintillator phase, and the tellurium phase[77].

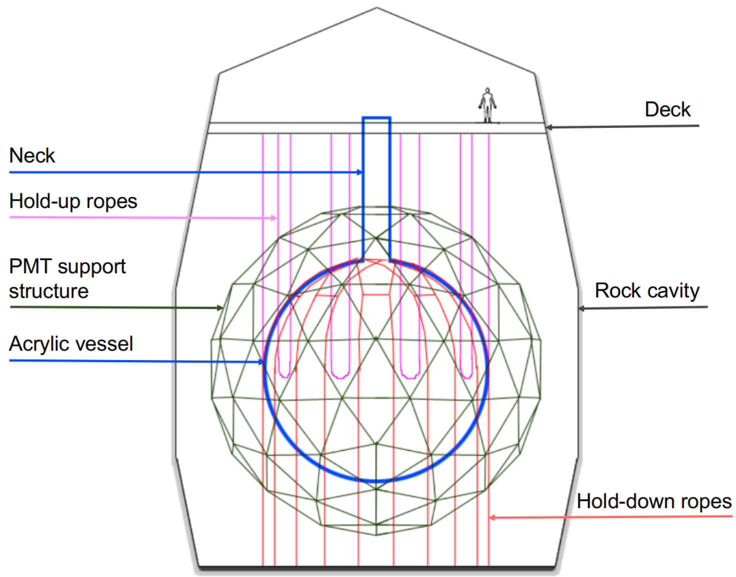

Figure 3.1: The SNO+ detector labeled with main structures, modified from Ref. [79].

3.2.1 Water Phase

In this initial phase, about 905 tonnes of ultrapure water was filled into the AV. The detector collected water physics data from May 2017 to July 2019.

During the data-taking, different types of calibration runs have been taken. The detector timing and energy response, systematics, and backgrounds are studied. Multiple physics analyses of invisible nucleon decay, solar neutrinos, and reactor antineutrinos are ongoing, and relating results have been published[80, 1, 81, 82]. The external backgrounds are also measured, which will be the same as the following two phases.

In this phase, the main physics goal is to search for the invisible nucleon decay, which violates the baryon number and predicts Grand Unified Theory (GUT). A proton or a bound neutron decays away without releasing charged particles in the invisible decay mode, compared to the "visible" decay channels of $p \to e\pi$ and $p \to \nu K$, which has been searched and set limits by the Super-K experiment. In the SNO+ water detector, ^{16}O may decay into ^{15}O* (bound neutron invisible decay) or ^{15}N* (proton invisible decay) excited state. The ^{15}O* has 44% chance to deexcite to produce 6.18-MeV γ ray and 2% chance to produce

7.03-MeV γ; while $^{15}N^{*}$ has 41% to release 6.32 MeV γ and 7.01, 7.03 and 9.93-MeV γ with chances of 2%, 2% and 3% respectively. The experiment has searched for these γ signals and the first publication sets world-leading limits of $\mathcal{O}(10^{29})$ years for both the proton and neutron invisible decay lifetime at 90% Bayesian credibility level[80].

The ^{8}B solar neutrinos were measured with a 69.2 kilo-tonnes·day dataset. By analyzing the solar neutrino elastic scattering events based on the dataset (Chapter 6 will discuss the method in detail), the number of the solar neutrino events were counted in different energy regions. In the first publication[1], by fitting to the non-oscillation solar neutrino model, an observed flux was obtained from the dataset to be $2.53^{+0.31}_{-0.28}(stat.)^{+0.13}_{-0.10}(syst.) \times 10^{6}$ cm^{-2}s^{-1} for the ^{8}B solar neutrinos with energies larger than 5 MeV. In the energy region larger than 6 MeV, the dataset has a background rate of $0.25^{+0.09}_{-0.07}$ events/kilo-tonne·day, which is extremely pure with solar neutrinos. Currently, this background rate is the lowest one compared to the other water Cherenkov detectors[1].

Reactor antineutrinos can be captured by the SNO+ detector and be measured. 40% of these antineutrinos are from one nearby reactor complex in Canada at a 240-km baseline; 20% are from two Canadian complexes at around 350 km; the rest are from the USA and elsewhere with longer baselines[77]. Though the antineutrino event rate in pure water is much lower than in the scintillator, during the water phase, SNO+ still has the potentials to detect reactor antineutrinos due to the low background dataset and relatively high detection efficiency. An Americium-Beryllium (AmBe) calibration source was deployed during the water phase to evaluate the sensitivity for detecting reactor antineutrinos. This source provides neutrons along with 4.4-MeV γs. Neutrons are captured by hydrogen, and 2.2-MeV γs are released. An analysis of delayed coincidence between 4.4-MeV and 2.2-MeV γs can help tag neutrons, which is crucial for tagging the reactor antineutrinos since they are measured by the inverse β-decay process, which produces neutrons with a similar energy scale. In the first publication for the SNO+ water phase, a neutron detection efficiency of 50% was obtained when the AmBe source was deployed at the center of the detector; the neutron-hydrogen capture time constant τ was measured to be $202.35^{+0.87}_{-0.76}$ μs, and from τ, a thermal capture cross-section was calculated to be $336.3^{+1.2}_{-1.5}$ milli-barn (mb)[81].

3.2.2 Scintillator Phase

In this phase, the AV will be filled with 780 tonnes of liquid scintillator, which is a mixture of linear alkylbenzene (LAB) serving as solvent and 2,5-diphenyloxazole (PPO) serving as fluor, with a concentration of 2 gram PPO per liter LAB (2 g/L in short). This LAB-based organic liquid scintillator is denoted as the "unloaded" liquid scintillator (more details in Sect. 3.3.4.1).

As mentioned in Sect. 2.4.5, the main physics goal of the scintillator phase is to measure low energy solar neutrinos: the CNO, pep, and low energy ^{8}B neutrinos. Three kinds of antineutrinos will also be measured: reactor antineutrinos (mentioned before), geoneutrinos (from natural radioactivity in the Earth); and the supernova neutrinos. SNO+ is planned to join the SuperNova Early Warning System (SNEWS), which is an international network of experiments with abilities to provide an early warning of a galactic supernova[75].

3.2.3 Partial-fill Phase

Between the water phase and scintillator phase, the liquid scintillator was gradually filled into the AV and replaced the water. In the AV, the liquid scintillator stayed above the water since it is insoluble in water and its density is less than the water. At some filling stages, the water level and the mixing of LAB and PPO were stable, and these stable stages were kept for a few weeks to take data. These transition stages were denoted as "partial-fill phase". Analyses on the partial-fill phase data are mainly aimed to demonstrate the techniques of liquid scintillator before the scintillator phase, and to test the physics properties of the liquid scintillator, such as the light yield, the background levels, etc. Due to the Pandemic, the partial-fill phase is longer than planned, which accidentally provides chances for physics studies, such as measuring solar neutrinos.

3.2.3.1 Tellurium Phase

In this final phase, 0.5% natural Tellurium (Te) by mass (with 1.3 kilo-tonnes of ^{130}Te) will be loaded into the scintillator, which is denoted as the "Te-loaded" scintillator (more details in Sect. 3.3.4.2). Higher loading concentrations would be possible for a further loading plan[5]. The main purpose of this phase is to search for the $0\nu\beta\beta$ signals in ^{130}Te.

3.3 Detection Media

In the SNO+ detector, charged particles are expected to interact with the detection media and create Cherenkov lights and scintillation lights.

3.3.1 Cherenkov Radiation

For any charged particle traveling in a transparent medium at an ultra-relativistic speed (a speed greater than the local phase speed of light in the medium), a type of electromagnetic radiation, called Cherenkov radiation, can be emitted from the coherent response of the medium under the action of the field of the moving particle[83, 84].

Suppose a charged particle moves in a transparent, isotropic, and non-magnetic medium and creates an electromagnetic wave. The electromagnetic wave propagates with a wavenumber $k = n \cdot \omega / c$, where c is the speed of light in vacuum, n is the real-valued refractive index and ω is the frequency. If the particle travels uniformly along x-axis with a velocity of v, the x-component of the wave vector is $k_x = \omega / v$. For a freely propagating wave, $k > k_x$, therefore $v > v_p = c/n(\omega)$, where v_p is the phase velocity in the medium. Under this condition that the speed of the charged particle is greater than the v_p, the Cherenkov radiation is emitted with a frequency of ω[84].

The Cherenkov angle, θ_c is the angle between the direction of the particle and the direction of Cherenkov emission and it is well-defined by $\cos\theta_c(\omega) = \frac{c}{n(\omega)v}$. The radiation is distributed over a surface of a cone with the half-opening angle θ_c.

Consider the condition $v > v_p = c/n(\omega)$, for the case of e^- traveling in a water detector, if neglecting the dependency on ω, $n_{water} \simeq 1.33$ [21], then $\theta_c \simeq 41.25°$ and $v_p \simeq 2.254 \times 10^8\ m/s$, which corresponds to a kinetic energy of e^-:

$$E_k = (\gamma - 1)mc^2 = 0.264 \text{ MeV},$$

where $\gamma = 1/\sqrt{1 - v_p^2/c^2}$. This is the lowest kinetic energy to create Cherenkov radiation, which is referred to the Cherenkov threshold (E_{thresh}). In the case that the LAB-PPO liquid scintillator is the medium, $n \simeq 1.50$[85], $\theta_c \simeq 48.19°$ and for e^-, $E_{thresh} \simeq 0.175$ MeV.

For a particle with a charge of ze, the number of photons produced by Cherenkov radiation per unit path length and per unit frequency of the photons is given by[86]:

$$\frac{d^2N}{d\omega dx} = \frac{\alpha^2(ze)^2}{c}\sin^2\theta_c = \frac{z^2\alpha}{c}(1 - \frac{1}{\beta^2 n^2(\omega)}), \tag{3.1}$$

where α is the fine structure constant.

Transforming the frequency into the wavelength ($\lambda = 2\pi\omega$) and integrating over the wavelength, the number of photons along the particle track projected on the x-axis is[86]:

$$\frac{dN}{dx} = 2\pi(ze)^2\alpha\sin\theta_c\int_{\lambda_1}^{\lambda_2}\frac{d\lambda}{\lambda^2}, \tag{3.2}$$

For optical photons with wavelengths ranging from 350 to 550 nm (typical PMT detection sensitive range), the above formula changes to[86]:

$$\frac{dN}{dx} = 476(ze)^2\sin^2\theta_c\ photons/cm. \tag{3.3}$$

For the Cherenkov radiation caused by e^- in a water detector, $dN/dx \simeq 207\ photons/cm$; while in the LAB-PPO case, $dN/dx \simeq 264\ photons/cm$. In a realistic measurement, the detection efficiency and the coverage of photon sensors are also required to be taken into account.

3.3.2 Scintillation from Organic Scintillator

Besides the Cherenkov photons described in the previous section, the majority of lights emitted from the organic scintillator are scintillation photons.

The organic liquid scintillator can convert the kinetic energy of charged particles into scintillation photons with wavelengths in the sensitive detection region of PMTs. They are aromatic hydrocarbon compounds with benzene-ring structures. When ionizing radiation happens in the scintillator, the free valence electrons of the molecules are excited and transit to occupy the π-molecular orbitals with the benzene rings. These highly delocalized electrons are called π-electrons, which can occupy a series of energy levels. A Jablonski diagram is generally used to describe molecular absorbance and emission of light. In Fig. 3.2, the diagram illustrates the π-electronic energy levels of an organic scintillator molecule[87, 86]. In the diagram, $S_{0,1,2,3,...}$ are the energy levels of the spin-0 singlet states, where S_0 is

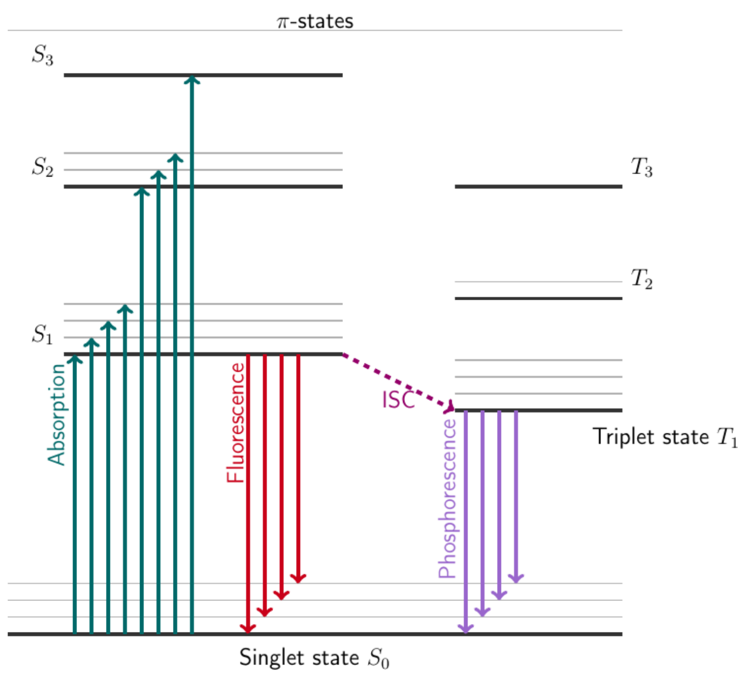

Figure 3.2: A Jablonski diagram for the organic scintillator, modified from Refs. [88, 87].

the ground state and $S^* = S_{1,2,3,...}$ are the excited singlet states. Above the ground state S_0, there are also a set of spin-1 triplet states $T_{1,2,3,...}$, where T_1 is the lowest triplet state. These electron energy levels are labeled with thick black lines. The energy spacings between these levels are $\mathcal{O}$(eV). In each level, there are also fine structure levels that correspond to excited vibration modes of the molecule (labeled with gray lines and can be marked as

$S_{10}, S_{11}, ..., S_{20}, S_{21}, ...$). The energy spacing between these fine levels are $\mathcal{O}(0.15)$ eV[86, 87].

The ionization radiation transfers the energy to the molecules and excites the electron levels as well as the vibrational levels, labeled as the absorption lines (in green). The decays between the excited singlet states (not to the ground state) are almost immediate ($\leq 10\ ps$) without the emission of light. This process is called internal degradation. The decays from the excited singlet state S_1 (as well as the vibrational states $S_{10}, S_{11}, S_{12}, ...$) to the ground state (as well as the vibration states $S_{01}, S_{02}, ...$) happen promptly ($\mathcal{O}$(ns)) and emit lights (labelled as red lines). This process is called $fluorescence$ which contributes to the prompt component of the emission of scintillation light. The probability of S_1 decays into the vibrational states $S_1 \to S_{01}, S_{02}, ...$ among the ground state is more than $S_1 \to S_0$. Since the absorbed energy of $S_0 \to S_1$ is larger than the emitted energy of $S_1 \to S_{01}, S_{02}, ...$, the scintillators have very little self-absorption of the fluorescence and are transparent to their own radiation. The effect of Stokes shift, which refers to the overlap between the optical absorption and emission spectra, is small for the organic scintillator[86, 87].

The transitions between the singlet and triplet states are highly forbidden due to the electron spin-flip is involved[89, 90]. There also exists a relatively rare process called inter-system crossing (ISC), which converts excited singlet states into triplet states. Besides this, 75% of triplet states can be produced by ionization-recombination[89, 91].

For the de-excitation, the similar processes of internal degradation occur among $T_{2,3,...} \to T_1$. T_1 is a relatively stable state and the lifetime of the molecule in the triplet state is in $\mathcal{O}(10^{-4}\ -\ 10)$ s[92]. $T_1 \to S_0$ is highly forbidden. However, the T_1 state can go through an indirect decay process by interacting with another excited T_1 molecule and forms an excited singlet state:

$$T_1 + T_1 \to S^* + S_0 + phonons. \tag{3.4}$$

The S^* will de-excite and emit delayed scintillation light. The process for emitting this delayed scintillation light is called delayed fluorescence or phosphorescence[86]. This process contributes to the delayed component of scintillation light.

For a typical scintillator detector, the time scale of detector response is $\mathcal{O}(1-100)$ ns. In this time region, the emission of the scintillation light contains the primary fluorescence from the de-excitation of the singlet states (prompt component) and the delayed fluorescence from the de-excitation of the indirect triplet states (delayed component)[91]. The time profile of the scintillation light emission is a mixture of prompt and delayed components.

Different charged particles can cause different ionization densities when they deposit energies to the scintillator molecules. The ionization density affects the relative population of the excited singlet and triplet states. Compared to an e^-, an α-particle can cause a high ionization density, which produces a higher ratio of triplet states. Therefore, the time profile for the α-particle has more delayed components or longer tails than the e^-. This enables the organic scintillator to distinguish α with e^- or other lighter charged particles[91, 93].

An empirical formula, called follows Birk's law[94, 88], describes the photon yield along with unit distance by the incident particle:

$$\frac{dY}{dx} = A\frac{dE/dx}{1 + k_B \cdot dE/dx}, \tag{3.5}$$

where A is a normalization constant, k_B is the Birks' constant of the scintillator, which in practice is obtained by fitting the formula to the measured data.

3.3.3 Liquid Scintillator for SNO+

Organic scintillators can release a large number of photons with wavelengths in the sensitive regions of the PMTs and have abilities for particle identification. In addition, since organic liquids are non-polar media, it is hard for ionic impurities to dissolve in. This leads to the lower contamination levels of uranium (U), thorium (Th), and potassium (K) in the organic liquid scintillators. Among the organic scintillators, aromatic organic liquid scintillators have high electron densities and thus they can provide sufficient targets for particle interactions[95]. Due to these advantages, aromatic organic liquid scintillators have been extensively developed as detection media for large particle detectors, especially for neutrino experiments, such as KamLAND, Borexino, Day Bay, and JUNO[93].

SNO+ has developed such kind of liquid scintillators that are compatible with the detector components, especially with the acrylic materials, like the AV sphere. Two kinds of SNO+ liquid scintillators are discussed in the following sub-sections: the unloaded liquid scintillator for the scintillator phase and the Tellurium-loaded liquid scintillator (TeLS) for the tellurium phase.

3.3.4 Water-based Wavelength Shifter (Proposal)

X. Dai et al.[96] made a proposal for adding wavelength shifters (WLS) into a water Cherenkov detector like SNO. Compared to the water Cherenkov detector, a water-based wavelength shifter (wbWLS) detector has a higher light yield (about threefold higher than SNO[96]) and thus can lower down the energy threshold, and then opens opportunity to detect low energy events. At the meantime, it will still keep the directionality from Cherenkov signals compared to a loss of the directionality for the liquid scintillator detector. For studying the directional signals such as solar neutrinos, this directionality can be used to suppress the backgrounds. This technology is being studied by future neutrino experiments, such as the Advanced Scintillation Detector Concept (ASDC)[97], WATCHMAN experiment[98] and Jinping experiment[56].

The U. Alberta group made a proposal of adding wavelength shifter (WLS) into the SNO+ detector in the middle of the water phase. The specific wavelength shifter we considered is PPO, which is a well-studied ingredient of the liquid scintillator used in the SNO+ scintillator phase and Te-loaded phase. It can be dissolved into water by mixing with proper water-surfactant. Although this proposal was not adopted due to the experiment schedule, it is still worthwhile for a conceptual study of a SNO+-like detector that uses water-based wavelength shifter (wbWLS) as the detection medium. In Sect. 4.3, Chapter 4, an event reconstruction algorithm based on the wbWLS is discussed. Based on the algorithm, it shows that comparing the wbWLS to the water, the energy threshold can be pushed down and the event position resolutions can be improved, while the directionality is still kept. This feature will help for measuring low energy solar neutrinos.

3.3.4.1 Unloaded Liquid Scintillator

SNO+ adopts a liquid scintillator cocktail contains two primary components: LAB as solvent and PPO as solute. The LAB is doped with PPO to a concentration of 2 g/L. This mixture of the LAB and 2 g/L PPO is denoted as the unloaded liquid scintillator in the text. Fig. 3.3 shows the chemical structural formulae of LAB and PPO[93].

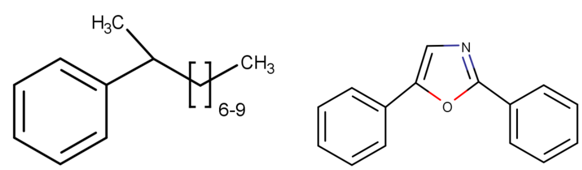

Figure 3.3: Structural formulae of LAB (left) and PPO (right).

LAB is a family of alkylated aromatic organic compounds with a phenyl group attached to a long carbon chain varying from 9 to 14 carbons[99, 93]. It has been used as a biodegradable detergent since the 1960s and it is proved to be relatively non-toxic and bring very low risks for the environment or human health[99]. Due to the long carbon chain, LAB is an effective energy absorber to transfer the deposit energy to lights. It also has a long attenuation length of (72 ± 14) m at 546 nm and thus has a good optical transparency[75]. Fig. 3.4 shows the absorption lengths of SNO+ optical components, comparing the LAB, PPO to the water.

As a wavelength shifter, PPO is usually added and dissolved into the LAB [100]. This wavelength shifter is used as a fluor. Energies are transferred from LAB to PPO via non-radiative Förster resonant energy transfer. It can shift the wavelengths of the scintillation photons to a range of 300-550 nm, which is in the sensitive range of the PMT detection and can also reduce the probability of being the self-absorption of LAB.

The 2 g/L PPO concentration in LAB is optimized by SNO+[77]. The absolute light yield of the LAB+ 2g/L PPO mixture has been well-measured from large particle physics experiments[101, 49], as well as bench-top measurements[101, 102, 103]. The absolute light yield determined by SNO+ is 11900 ± 60 photons/MeV, and it is expected to be increased by

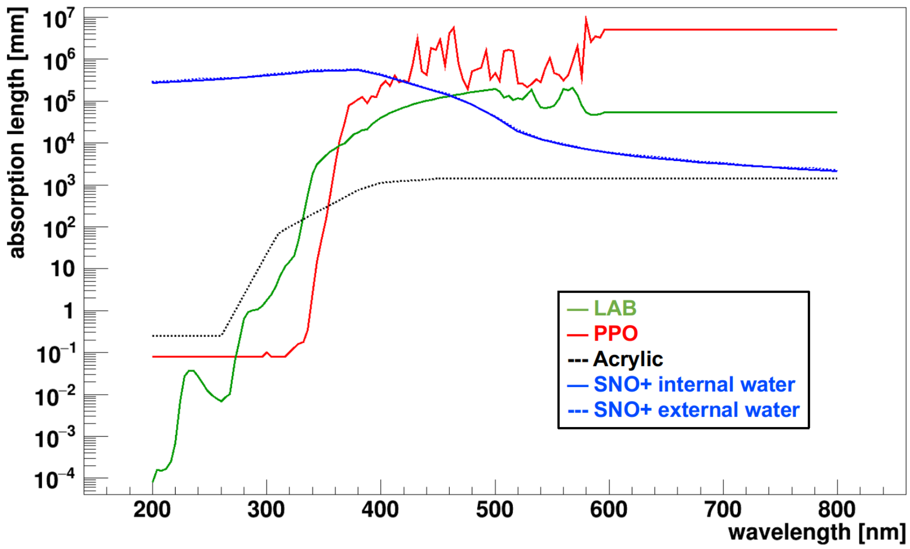

Figure 3.4: Absorption length of SNO+ optical components. The internal (solid blue line) and external water (dashed blue line) absorption curves are based on the measurements of the laserball scans in July 2018 during the SNO+ water phase. The horizontal lines are due to absence of the measurements and they are conservative assumptions.

over 15% after extensive purification process[75, 104]. At the 2 g/L PPO concentration, the emission decay time is about 5 ns, which is good enough for the event vertex reconstruction, and this fast timing enables different timing spectrum for α and β events, which is crucial to the analysis of the α/β discrimination for reducing the backgrounds[75].

During the SNO+ partial-fill phase, the filling amounts of the PPO were at 0.25 g/L, 0.5 g/L and 1 g/L concentrations. When the PPO concentration increases, the PPO transfer efficiency will increase, which can increase the light yield of the liquid scintillator, and also cause a faster scintillation timing response. However, it finds that if the concentration is above 2 g/L, due to the an increase in self-absorption, there is not much to be gained as the light yield reaches a plateau and the timing goes slightly faster (see Sect. 4.4.2.1, Chapter 4 for more details)[75, 93]. In Sect. 4.4.3.1, Chapter 4, I show the effects of the PPO concentrations on the event position reconstruction. It finds that from 0.25 g/L to 2 g/L, the reconstructed position resolution for SNO+ increases by about 90 mm (for 3-MeV electron events); while from 2 g/L to 6 g/L, there is almost no changes, which demonstrates the optimized 2 g/L PPO concentration is proper.

The time profiles of scintillator were obtained from bench-top measurement. An empirical model consists n (n=3 or 4) exponential decays with a common rise time is used to describe the time profiles[105].

A default time profile function is:

$$\sum_{i=1}^{n} A_i \cdot \frac{e^{-\frac{t}{\tau_i}} - e^{-\frac{t}{\tau_{rise}}}}{\tau_i - \tau_{rise}}, \tag{3.6}$$

where the rise time (t_{rise}), timing parameters t_i, and amplitude a_i of a certain liquid scintillator are determined by the measurement results. Fig. 3.5 plots the time profiles based on the measured parameters from the collaboration[106, 107, 108, 109]. It shows the time profiles of 4 different liquid scintillators planned for SNO+, including the LAB + 0.5g/L PPO for the partial-fill phase, which will be discussed in Chapter 4; the LAB + 2g/L PPO for the scintillator phase; the LAB + 2g/L PPO + 0.5% molar concentrations DDA, which will be a transit state before loading the Te; and the LAB + 2g/L PPO + 0.5% molar concentrations Te+0.5% molar DDA for the tellurium phase. For each liquid scintillator, their timing responses to the β^- (solid lines) and α-particles (dashed lines) are also shown. It shows that for the liquid scintillators with 2 g/L PPO, there are obvious differences between the α and β^- timing, while for the 0.5 g/L PPO, it is not. So for the partial-fill phase, it is difficult to distinguish the α/β^- by time profiles.

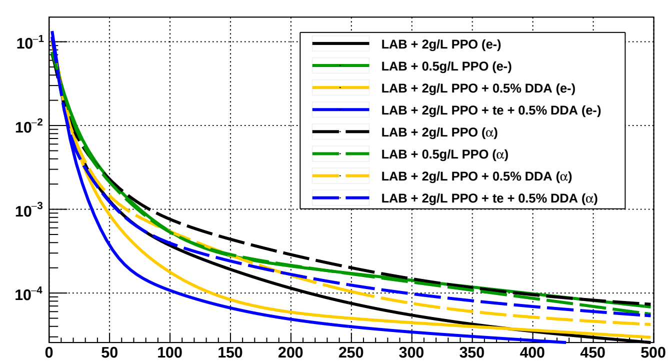

Figure 3.5: Time profiles for liquid scintillators in different SNO+ phases.

The LAB and the PPO used by SNO+ are ultrapure, with very low levels of natural radioactive contaminants such as U, Th and K. The target background levels for the SNO+ LAB are expected to be $\mathcal{O}(10^{-17})$ gram of ^{238}U in per gram LAB (g^{238}U/gLAB), which is equal to be thousands of events per year. While the ^{232}Th and ^{40}K levels are $\mathcal{O}(10^{-17})$ g/gLAB, which is equal to be hundreds of events per year[75, 110]. A liquid scintillator purification plant has been implemented to maintain the optical clarity and radiopurity of the scintillator[75].

3.3.4.2 Tellurium-loaded Liquid Scintillator

To load the ^{130}Te into the liquid scintillator, an organo-metallic compound, called the "Tellurium Butanediol (TeBD)", is formed by condensation (or called "diolization") reactions between telluric acid (TeA) and 1,2-butanediol (BD)[5]. A tertiary amine: N, N-Dimethyldodecylamine (DDA) is added during the reaction to stabilize TeBD compounds and avoid any phase separation[111]. Fig. 3.6 shows initial stages of the process. This compound is then loaded into the liquid scintillator.

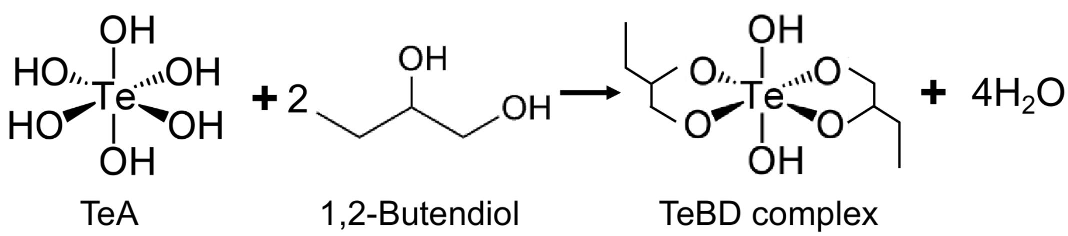

Figure 3.6: Initial stages of the TeBD compound formation, modified from Ref. [5].

Two special synthesis procedures, called the "DDA" and "SOP" procedures (see Refs. [112, 113, 114] for details) are being developed by the SNO+ Te-loading working groups. These methods can keep the optical transparency of the unloaded scintillator after the loading and ensure that the mixture will be stable for a decade. The total light yield of the full cocktail is expected to be 400 NHits/MeV, which is about 65% of the unloaded scintillator light yield.

For the ^{130}Te $0\nu\beta\beta$-decay process, the signature energy peak is at 2.5 MeV[77]. This peak is relatively small and can be immersed in the ubiquitous radioactive decays from natural sources, such as the natural Uranium and thorium decay chains existing in the materials[77]. Therefore, the $0\nu\beta\beta$-decay experiments require a very high energy resolution to distinguish the signal from the backgrounds. For the liquid scintillator, it is expected to create as large amount of light caused by a particle interaction as possible. A quantity of light yield, defined as the number of photons for per MeV energy deposit (photons/MeV) by a particle interaction, is used for describing the detection property of the liquid scintillator.

To meet the low background requirement of the $0\nu\beta\beta$ analysis, the purity of the TeLS cocktail is aimed to $\mathcal{O}(10^{-15})$ g/g level for U and Th.

3.3.5 Relative Light Yield Measurements of the Te-loaded Liquid Scintillators

As mentioned in the previous section, the $0\nu\beta\beta$ analysis requires high purity and a good light yield of the TeLS.

Here I measured the light yield of 0.5% Te-loaded LAB (TeLS) samples relative to the LAB-PPO scintillator (called “relative light yield”, RLT). With tellurium being loaded into the LAB, the light yield of the liquid scintillator will go down since the tellurium atoms can block the photon transmissions to the photosensors. The light yield of the TeLS is crucial for the $0\nu\beta\beta$-decay experiments since it determines the energy resolution of the detector and sensitivity for studying the $0\nu\beta\beta$ process from the ^{130}Te. A few efforts are aimed to develop high light yield Tellurium-loaded scintillators[112].

3.3.5.1 Measurement Setup and Data Acquisition

We first prepared LAB+2 g/L PPO by dissolving PPO into the pure LAB. The LAB-PPO mixture was distilled by heating and flowing with liquid nitrogen to remove humidity and oxygen, affecting the light yield for 48 hours. The distilled LAB-PPO was added into the original 16.5% weight Te-butanediol samples to dilute into the 0.5% TeLS samples. Two Te-butanediol samples synthesized from the DDA and SOP synthesis procedures (described in Ref. [111]) were prepared and were tagged as the TeDDA and TeSOP samples, respectively.

These samples were further transferred into scintillation vials for the measurement, as shown in the left picture of Fig. 3.7. The vials have PTFE caps sealed on the top of the glass cylinders to prevent the humidity exposure from the air. The liquid level for each sample was kept at 30 mm to avoid air bubbles and contamination created by squeezing the vial cap into the liquid.

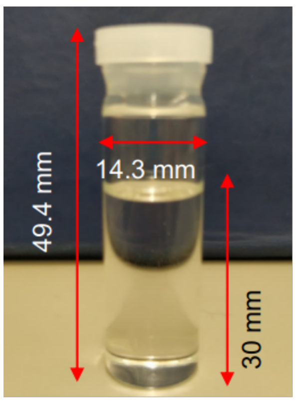

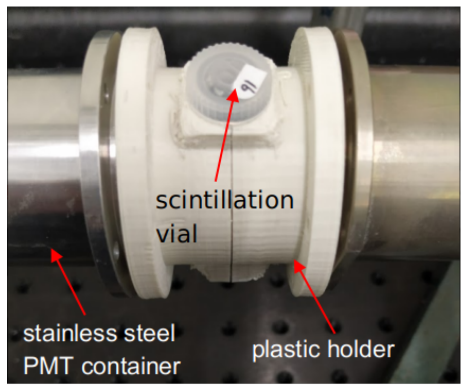

Figure 3.7: A vial of the test sample (left) and the measurement setup (right). Left: The samples were filled into scintillation vials. The dimensions are shown in the picture. Right: two PMTs were aligned to face to the scintillation vial from each side.

Two Hamamatsu R580 PMTs (described by Ref. [115]) were used for detecting the light. The diameter of the PMT round surface is 38.71 mm. These PMTs were housed in stainless steel cylinders (PMT holders), set face to face, looking at the scintillation vial from each side. The PMTs and the vial were aligned by a plastic piece, as shown in the right picture in Fig. 3.7. The plastic piece is cylindrical with a hole on the top to plug in the scintillation vial and a slot at the bottom to attach a radioactive source. Inside the cylinder, there is a button-shaped groove at the bottom to fix the vial plugged in and keep the vial upright. Also, a 2-mm-diameter hole was drilled at the bottom of the piece to allow the radiation rays to pass through the vial from the bottom. The surface inside was polished to reduce the absorption of the material to the photons. The piece is made of plant-based and biodegradable polylactide (PLA) filament and was machined by a 3D printing facility at the University of Alberta[1] .

[1]Shengzhao Yu helped with the machining.

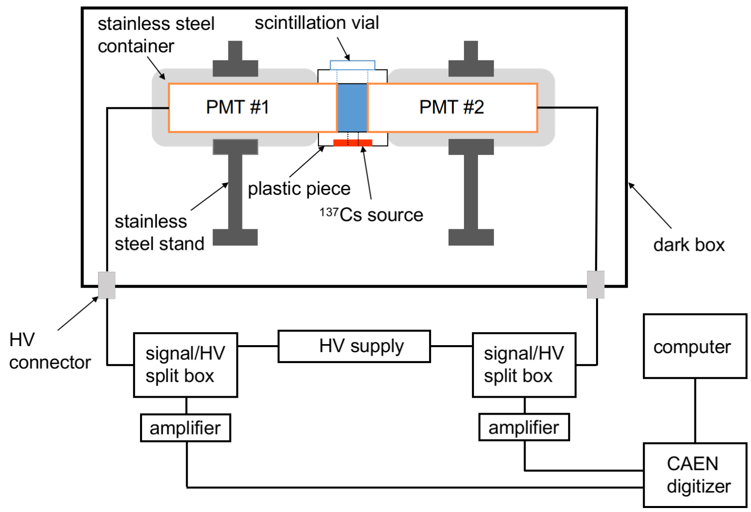

Figure 3.8: A diagram shows the light yield measurement setup. See the text for details.

Fig. 3.8 shows a diagram of the whole measurement setup. The plastic piece held the radioactive source and the scintillation vial. It also aligned two PMTs to face the scintillation vial from each side. The piece can shield lights from outside as well. These setups were placed in a dark box to prevent the lights from the lab. Two RG59/U-type high voltage (HV) cables connected the PMTs to an HV supply outside the dark box. The HV cables were connected to two signal/HV split boxes to separate the HV current and electrical signals. Due to the resistor of the split box, the HV supply was set to 2200 Volts (V) for the PMT operation, while the operation voltage suggested by the Hamamatsu is 1800 V.

The signal cables from the split box were connected to a two-channel Hewlett Packard (HP) amplifier. This amplifier inverted the signals and amplified them by 26 dB. The amplified signals were then input into a two-channel digitizer. The digitizer recorded the data and sent them to a desktop computer.

To obtain and analyze the data, we used a desktop Waveform Digitizer, the DT5751 module provided by the Costruzioni Apparecchiature Elettroniche Nucleari (CAEN). Running at a digital pulse processing mode, the module records the digitized PMT waveforms with a data-taking rate of 1 GHz for each channel[116].

This module was controlled by the `CoMPASS` software provided by CAEN. The software set up the threshold and trigger parameters. Once the triggered event passed the threshold, the software recorded event time, trigger flag, and waveform histograms from the two channels. By integrating the waveforms, the energy of a triggered event was calculated[117].

Each channel recorded the signals from each PMT individually. With the two-PMT setup, we applied coincidence time mode measurements. In the coincidence mode, a coincidence time window between two channels was set to 48 ns. For a certain event, the `CoMPASS` software compares the event time difference between two channels and only records it if the event time difference is less than 48 ns. A smaller window of 10 ns was further applied for analysis.

3.3.5.2 Measurement

The liquid scintillator samples we have measured are LAB-PPO, TeDDA, and TeSOP. The unloaded LAB-PPO sample served as a standard candle.

A Cesium-137 (^{137}Cs) radioactive source was always placed at the bottom of the scintillation vials. The source was made by Radiochemical Centre Amersham. The radioactivity measured on 1st April 1974 was 11.09 $microcurie(\mu Ci)$ on record, with an accuracy of 3.7%. Then the activity was expected to be $11.09 \times (\frac{1}{2})^{\frac{46}{30.08}} = 3.84\ \mu Ci$ in 2020, considering a half-life of 30.08 years for the ^{137}Cs[118].

The ^{137}Cs isotope has a 85.10% chance to emit 0.661 MeV γ-particles[118]. These γ-particles can travel into the liquid scintillator samples in the vial, interact with the samples and create scintillation photon.

For each sample, measurements were taken for a one-minute time duration. Waveforms from the PMT photo-current signals were digitized in a 252 ns time window. Shown in Fig. 3.9 is a typical waveform caused by γ-particles interacting with the LAB-PPO sample. The p.e. signals triggered PMT pulses, and the pulses were digitized as waveforms. For each waveform, the digitizer firmware dynamically calculated the baseline as the mean value of 256 data points inside a moving time window of 252 ns. A threshold was set as 100 units above the baseline. The data point on the 90% leading edge of the pulse was taken as the trigger time ($t_{trigger}$) tag. From this $t_{trigger}$ tag, in the following 80-ns window, the digitizer did not calculate another trigger to avoid introducing another pulse (trigger hold-off). Also, from the $t_{trigger}$ tag, a pre-gate of 8 ns was set. The waveform was integrated into the time gate of $[t_{trigger} - 8, t_{trigger} + 72]$ ns. This gives the integrated charge, which was calculated as an A/D converter (ADC) channel number. If the measurement system can be calibrated, the ADC channel number can be exactly converted into the energy of the particle interaction. Since here we only interested in the photon numbers, we used the ADC channel as the energy. Once the pulse in the waveform passed the threshold and a triggered time tag can be found, the digitizer considered it as a triggered event. A time flow started when the measurement began. Timestamps were recorded as event time when the triggered event happened. The waveform was recorded, and the ADC channel number (energy) of this event was calculated.

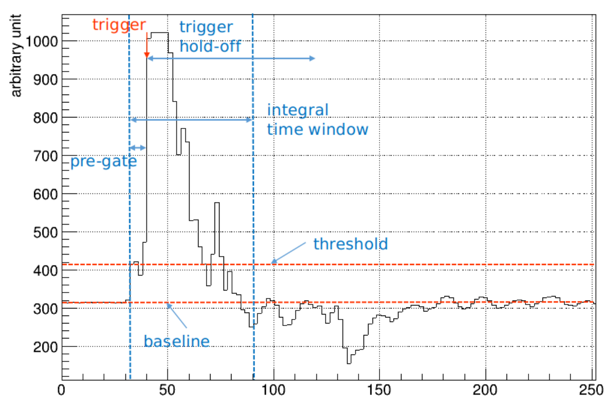

Figure 3.9: A typical waveform triggered by scintillation photons from ^{137}Cs γ-particles interacting with LAB-PPO sample.

In a coincidence time measurement, the event times of the events recorded by each of the two PMTs were compared. If the event time differences between two events from each PMTs were too long, these events were considered random noises rather than the physics events and were not recorded. We optimized a coincidence time cut as 40 ns and set that cut during the digitizer data-taking.

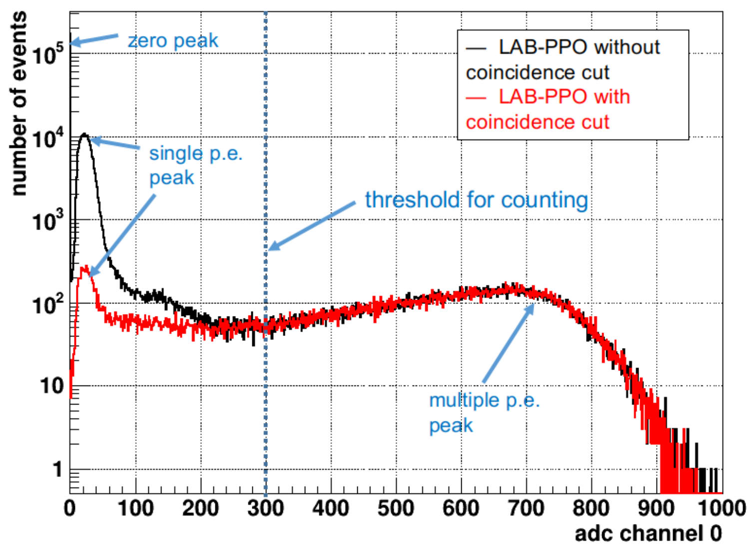

Figure 3.10: Measured LAB-PPO energy spectrum with and without coincidence cut on the ADC channel 0. A threshold for counting is set by comparing the two spectrum.

Fig. 3.10 shows the measured LAB-PPO energy spectrum with and without coincidence time cut (10 ns) on the ADC channel 0. Without the coincidence time cut, there is a zero peak caused by the pulses from random electronic noises or fluctuations of the digitized waveforms. The peak on the left is the single p.e. peak. It is mainly caused by some light sources which are weak enough that the photons only strike out at most one single p.e. inside the PMT[86]. The peak on the right is the multiple p.e. peak, in our case, which is mainly caused by some scintillation photons produced by the γ-ray interacting with the LAB-PPO. In the coincidence time measurement mode, it only records the photons detected by the two PMTs almost simultaneously. Therefore, the zero peaks are removed while the single p.e. peak is suppressed. The multiple p.e. peak is consistent with the non-coincidence measurement. A threshold in energy can be set to count only the scintillation photons emitted from LAB-PPO.

Fig. 3.11 (a) shows the result of a one-minute measurement for the LAB-PPO sample. The data points in the 2D plot represent the triggered event fall in certain ADC channel numbers in each channel. A 10 ns coincidence window cut was applied to cut down noise, single p.e., and background events. The events in the 0 ADC channel, which represent

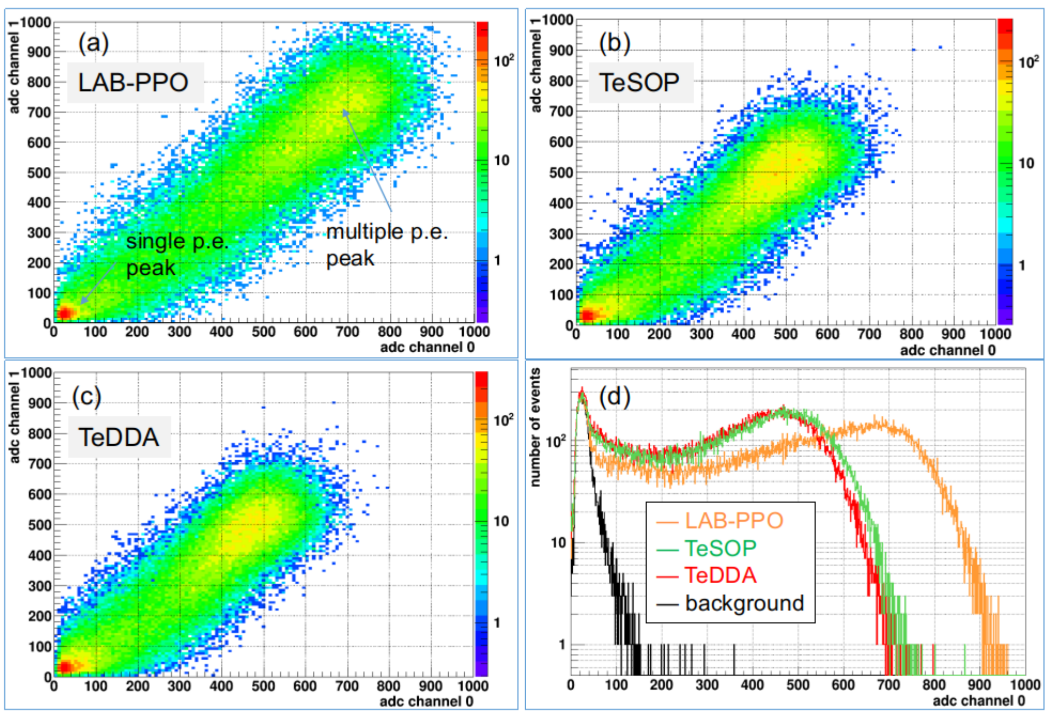

Figure 3.11: The 2D energy spectrum of the counting measurements of LAB-PPO (a), TeSOP (b), and TeDDA (c) samples, projected the 2D plots into one channel (d). The single photo-electron (p.e.) peak is mainly caused by backgrounds while the multiple p.e. peak is from scintillation photons.

noises, were totally cut off after applying the coincidence. Fig. 3.11 (b) and (c) show the results of the TeSOP and TeDDA samples respectively. Compared to the LAB-PPO sample, a shift of the multiple p.e. peak due to the different light yields can be observed clearly.

The 2D plots were projected onto a single channel, as shown in Fig. 3.11 (d). We used an empty vial and let γ-particles from ^{137}Cs source passed through it as a background run (without the coincidence cut). This is to verify the single p.e. peak and noise region, shown as the black background spectrum.

From this plot, the single p.e. peaks for all the samples and the background match together. The multiple p.e. peaks indicate the different light yields of the scintillator samples. Here we can see the multiple p.e. peak of the LAB-PPO occupies the largest ADC channel number, while the channels of TeSOP are slightly larger than the TeDDA.

To quantify the light yield differences between different samples, an analysis method of charge weighted photon number has been applied as the following:

First, from the energy spectrum, the single p.e. peak was fitted with an asymmetric Gaussian function (as f_{asym} in 3.7), as shown in Fig. 3.12. The mean value of the asymmetric Gaussian (p_0) represents the ADC channel number corresponding to the single p.e. peak for the weighting.

$$f_{asym} = c \cdot e^{-\frac{1}{2}(\frac{x-\mu}{\sigma})^2} \cdot Erfc(\xi), \tag{3.7}$$

where $\xi = -\frac{\alpha(x-\mu)}{\sqrt{2}\sigma}, p_0 = \mu, p_1 = \sigma, p_2 = \alpha$, and $p_3 = c$.

Then in the multiple p.e. region, weighting (dividing) the counts of the event in each channel with the single p.e. ADC channel number to calculate the total number of the photons.

To define the multiple p.e. region for the counting, the spectrum projected on each channel with and without coincidence cut are compared to define a threshold of the ADC channel for counting. By integrating from this threshold, the total numbers of events between two spectrum are close to each other. From two channels, we get two thresholds and then define a box cut in the 2D coincidence plot. We weights the events in the box to

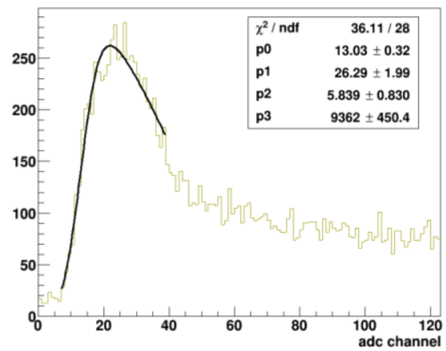

Figure 3.12: The single p.e. peak is fitted with an asymmetric Gaussian function (f_{asym}) to obtain the ADC channel for weighting. The mean value of p0 is used as the adc channel relative to a single p.e. peak.

obtain the total number of photons. Fig. 16 and Fig. 19 show the case of the LAB-PPO sample.

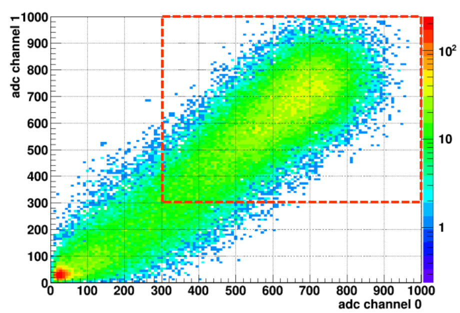

Figure 3.13: Two dimensional spectrum of LAB-PPO sample with coincidence cut. A box cut is defined for multiple PE counting.

Two dimensional (2D) spectrum of LAB-PPO with coincidence cut is shown in Fig. 3.13. A box cut is defined for multiple PE counting.

Once the total number of photons for a certain sample is counted, we can calculate its ratio to the LAB-PPO sample to obtain the relative light yield.

3.3.5.3 Results

Table. 3.1 shows the number of photons calculated by the charge weighted photon number method. Here we quantify the relative light yields of our samples. The light yield of the 0.5% Te by SOP synthesis procedure (TeSOP) is 0.61 and the one of the 0.5% Te by DDA

Table 3.1: Number of photons calculated by Charge weighted photon number method.

Sample	Number of photons ($\times 10^6$)	RLY
LAB-PPO	2.0811	1
TeDDA	1.2652	0.61
TeSOP	1.3976	0.67

procedure is 0.67. The light yield of TeSOP is slightly larger than the TeDDA. In [112], a relative light yield of ~ 0.65 was reported.

3.4 SNO+ Electronics

In this section, the SNO+ electronics system is introduced. The system includes the trigger and readout systems. As mentioned in 3.1, the PMTs as photon sensors are the basic detection elements for the SNO+ detector. The signals from the PMTs are sent to the SNO+ electronics system, which records the PMT time and charges information and then transfers the digitized data to offsite computing systems for data analysis. These steps are detailed in the following.

The photons created from particle interactions in the detector propagate to the PMT sphere and may hit a certain PMT and strike on its photo-cathode, which is a thin cesium bialkali film coated on the inner surface of PMT glass. The photocathode then produces a photo-electron (p.e.) through a photoelectric effect. The photocathode is set at ground voltage while the anode is at a high voltage ranging from +1700 to +2100 V [119, 91]. This forms electric fields inside the PMT. The p.e. is accelerated and focused by the electric field in the PMT and goes through the volume which is under vacuum until it reaches the region of a series of secondary emission electrodes, called dynodes. When the p.e. transfers its energy to the materials in dynodes, a number of secondary electrons escape and form a measurable current which is collected by a custom-made operating circuit (called "PMT base") at the anode[120].

The anode pulse produced from the PMT travels along 35-m-long RG59/U type coaxial cable (with a resistance of 75 Ω) to the front-end electronics which are set up on the deck above the detector. The coaxial cable also carries the high-voltage[119].

To tackle with more than 9000 PMTs in the SNO+ detector, the coaxial cables connected to each PMTs are grouped into bundles. Each bundle is connected to a Paddle Card, which are linked to a PMT Interface Card (PMTIC). The PMTIC supplies high voltages and receives signals from the PMTs. 32 channels (for 32 PMTs) in the PMTIC are plugged into a Front End Card (FEC) that processes, digitizes, and stores PMT signals. 19 crates tackle 9728 PMT channels in total, of which 32 channels are reserved for calibration inputs and labeled as FEC Diagnose (FECD) channels. These FECD channels are mainly used to tag calibration events. The triggered PMTs can be labeled by the logical channel number (lcn) using the map of the PMT to the crates and cards[75, 78]:

$$lcn = 512 \times crate + 32 \times FEC + channel. \tag{3.8}$$

A 10-MHz and a 50-MHz clocks are used to record the time of the triggered event. The universal time of the triggered event is calculated as the time elapsed from a predefined T_{zero}, the midnight of January 1, 2010 (GMT) to the moment when the event happens. A 10-MHz clock used for counting the absolute time started at T_{zero}. It has a 53 bit register and can run for 28.5 years. Its accuracy is maintained by a GPS system. The 50 MHz clock gives more accurate timing. It limits the best time resolution of the GT to 20 ns. This clock has a 43 bit register and rolls over every 2.04 days. The relative time between the events can be used for analyzing specific physics processes, such as radioactive decays[121, 78].

The recorded hit information of the triggered event, including the time and charge information of hit PMTs and the trigger settings, are sent to a Crate Controller Card (XL3) in each crate. These cards were installed for SNO+ to handle higher data transfer rates compared to SNO, with a max rate of 14 MB/s, which is equivalent to approximately 2 million hits per second[122]. They read out the recorded data and wrap them as ethernet packets and send them to the Data Acquisition System (DAQ) and Event Builder system[123]. The Event Builder system writes information into event records based on their GT identification number (GTID) and saves them on storage disk[75]. These raw data are written to the disc and are further processed into ROOT format by high-performance computing clusters.

As a summary, the SNO+ electronic system can measure signals with a nanosecond-level timing resolution and a single-photon level charge resolution. It can handle an event rate of several kHz and even much higher rates for cases such as the burst events from a galactic supernova[75].

3.5 Calibration

Calibration sources with known physics parameters are applied to understand the detector response to the events and thus to make accurate measurements.

Two kinds of calibration sources are used by SNO+: (1) the optical sources to measure the *in-situ* optical properties of the detector media and to calibrate the PMT responses[75, 82]; and (2) the radioactive sources to test the detector energy responses, check the performance of event reconstruction algorithms for reconstructing event position, direction and energy and then determine reconstruction systematic uncertainties. Various types of radioactive sources designed for SNO+ cover the energy range from 0.1 MeV to about 10 MeV, as listed in Table. 3.2[75]. All the calibration sources have been designed to meet the radiopurity required by SNO+ and their materials are compatible with the detection media[75].

Table 3.2: A list of SNO+ radioactive sources. The main energy is given as the total γ energy, modified from Ref. [75].

source	total γ energy [MeV]
^{16}N	6.1
AmBe	4.4
^{46}Sc	2.0
^{48}Sc	3.3
^{137}Cs	0.66
^{57}Co	0.14

Among these radioactive sources, the Nitrogen-16 (^{16}N) calibration source and the Americium Beryllium (AmBe) source have been deployed in the water phase and the partial-fill phase. The ^{16}N source was used to test and optimize the reconstruction algorithm discussed in Chapter 4. It was also used to obtain the reconstruction uncertainties in the water phase, which is the topic of Chapter 5. A detailed description of ^{16}N source is given in Sect. 3.5.1.

The ^{46}Sc, ^{48}Sc, ^{137}Cs and ^{57}Co sources are newly designed by SNO+ to calibrate the energy scale in the scintillator and tellurium-loading phases, especially for the energy region of interest (ROI) in the $0\nu\beta\beta$ study[75].

The detector geometry is not perfectly symmetric due to the presence of the AV neck, ropes, gaps between the PMTs, and the difference in individual PMTs[75]. The deployment of calibration sources at different positions in the detector can help to understand the asymmetries in the detector responses. To realize this, a few fixed optical sources were mounted at different positions on the PSUP. Besides that, a source manipulator system (SMS) was installed, as shown in Fig. 3.14. The sources are attached or detached to the SMS via the Universal Interface (UI), which is a sealed cylinder-shaped glove box on the top of the AV to prevent the air in the lab leaking into the detector. The motion of the deployed sources along the central vertical axis inside the AV is controlled by the Umbilical Retrieval Mechanism (URM) through an umbilical and a central rope, and the off-axis motion is controlled by the side rope manipulator system. The motion of the sources in the external water region between the AV and PSUP is along the calibration guide tubes[75].

The position of the deployed source in the detector can be evaluated by the manipulator system. In addition, a camera system with six underwater cameras already mounted on the PSUP can take photographs of the source and then triangulate its position. An accuracy of several centimeters is achieved. This system is also used to monitor the physical state of the detector, such as the offset of the AV center with respect to the PSUP, the movement of the rope net, the height of the water-scintillator interface during the partial-fill, etc[124, 75].

3.5.1 The ^{16}N Calibration Source

The ^{16}N calibration source is inherit from the SNO experiment and has been well-understood[125, 126, 127]. Fig. 3.15 shows the geometry of the ^{16}N source chamber. The chamber is a stain-

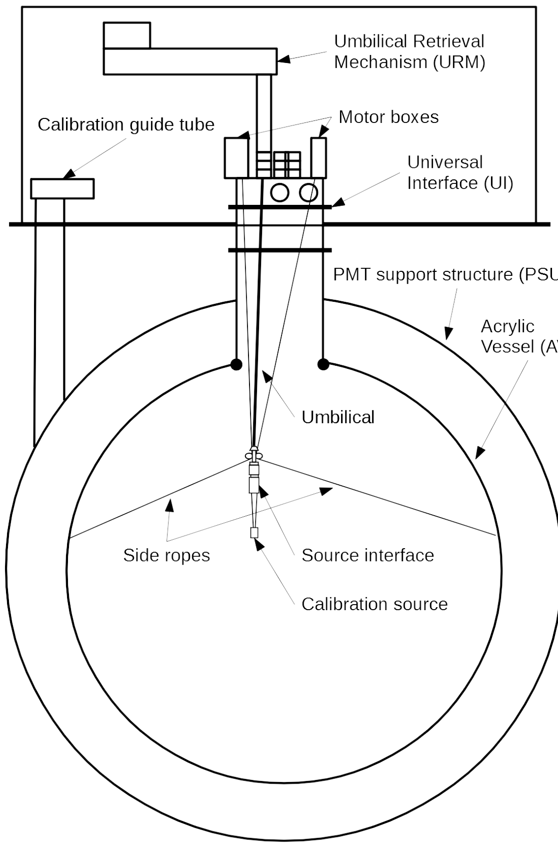

Figure 3.14: The SNO+ Source Manipulator System, from Ref. [75].

less steel cylinder mainly containing a small PMT and a gas decay chamber. The chamber was designed to confine the electrons from ^{16}N decay within the chamber and let them be detected by the PMT inside[125].

Since the ^{16}N isotope has a short half-life of 7.13 s, it must be produced on-site during the calibration runs. A commercial deuterium-tritium (DT) generator was installed in SNOLAB to produce neutrons through the reaction: $D + T \rightarrow n{+}^{4}$He; then the produced 14-MeV neutrons interact with the CO_2 gas streaming through the small diameter capillary tubing and produce the ^{16}N isotopes via the (n,p) reaction: $n{+}^{16}\mathrm{O}{\rightarrow}^{16}\mathrm{N}{+}p$. These ^{16}N isotopes are transferred into the cavity or the detector by the CO_2 gas tubing[126].

The ^{16}N isotope mainly decays through β-decay process: $^{16}\mathrm{N}{\rightarrow}^{16}\mathrm{O}{+}e^{-} + \bar{\nu}_e$. It has a 66.2% chance to emit an electron with $E_{end\ point}$ = 4.29 MeV and a 22.8% chance to an

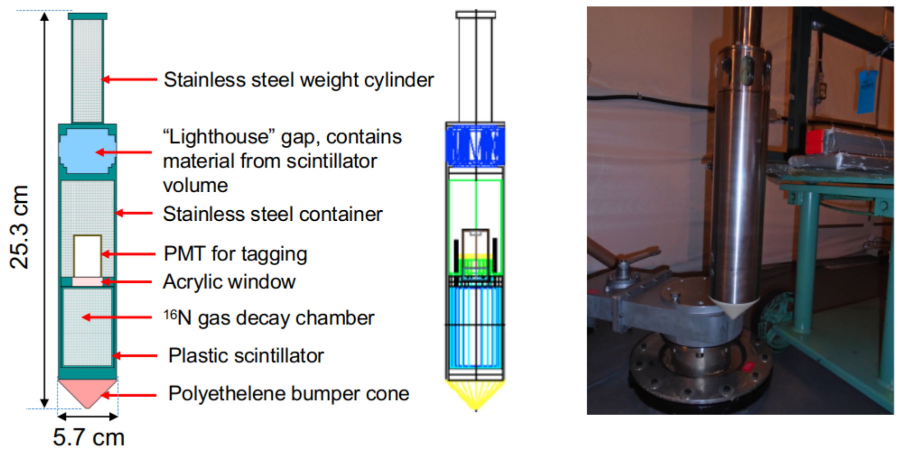

Figure 3.15: ^{16}N calibration source geometry. Left: a detailed diagram of ^{16}N source geometry, modified from Refs. [128, 129]; middle: source geometry implemented in RAT, modified from Ref. [130]; right: a picture of the ^{16}N source, taken from [131].

electron with $E_{end\ point}$ = 10.42 MeV; while the resulting ^{16}O deexcites and produces a cascade of γ-particles. There are mainly 6.13-MeV γ with an intensity of 67.0% and 7.12-MeV γ with an intensity of 4.9%. The intensities of the γ-particles with other energies are all below 1%[118]. A simplified decay scheme is shown in Fig. 3.16.

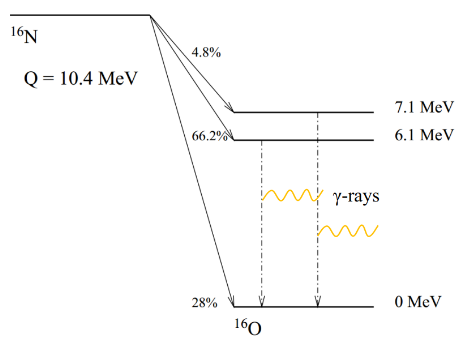

Figure 3.16: ^{16}N main decay scheme, modified from Ref. [126].

The calibration of the ^{16}N source is crucial for the reconstruction. The source was used to test and optimize the reconstruction algorithms, which will be shown in Chapter 4. In Chapter 5, it will show a study of using the source to estimate the reconstruction uncertainties.

3.6 Monte Carlo Simulation and RAT Software

The SNO+ collaboration uses a software package called the Reactor Analysis Tool (`RAT`) for Monte Carlo simulation as well as event-based analysis offline and online. To accomplish these two tasks, `RAT` integrates the `Geant4` simulation toolkit[132] and ROOT data analysis framework[133] for processing and analyzing data. This feature makes it easy to analyze Monte Carlo-generated events and real data in a same framework and data structure.

The software was originally developed by Stan Seibert from the Braidwood Collaboration to simulate a generic KamLAND-like detector[134]. A simulation package called Generic Liquid Scintillator `Geant4` simulation (`GLG4sim`) was developed and implemented in `RAT`[135]. It simulates the scintillation physics processes, the generations of scintillation photons and also the propagation, reflections, refraction, scattering ans absorption of optical photons[91].

The SNO+ version of `RAT` links the existing `ROOT`, `Geant4` and `GLG4sim` packages to minimize the code duplication. The SNO+ `RAT` is being developed by the whole collaboration and evolves with the experiment progress to precisely simulate the SNO+ detector in different physics phases as well as applying multiple analysis tasks. The relative flexible code structure of `RAT` allows the user to introduce their own code into the simulation or analysis process[134]. It can be updated and optimized with the measured parameters from detector calibration; it can be added with more precise descriptions of the physics processes in the detector; it can also be introduced with more advanced analysis tools. The users can apply different analysis tasks, such as different reconstruction algorithms on the same events[134]. Therefore, different versions of `RAT` serving to different SNO+ physics phases may give different outputs. For the work in this thesis, multiple `RAT` versions were used, mainly the versions for the water phase and partial-fill phase. In this case, I will specify the `RAT` version when I discuss a specific analysis.

`RAT` is also used by other astroparticle physics experiments, such as the dark matter experiment DEAP/CLEAN[136].

Chapter 4

Event Reconstruction

4.1 An Overview of the Reconstruction Algorithms in SNO+

A particle interaction that happens in the SNO+ detector can produce Cherenkov or scintillation photons. These photons propagate through the detector, and they can trigger PMTs when they reach the PSUP. As described in the last chapter, if there are enough PMTs triggered within a defined time window, an event is determined by the trigger system, and for the event, the time and charge information measured by the hit PMTs are recorded.

By utilizing the recorded time and charge information, reconstruction algorithms attempt to calculate the physics quantities of an event, including its vertex (position and time), direction, and energy. A few sets of reconstruction algorithms (called "fitters") have been implemented in the SNO+ RAT software or are still being developed. These fitters are based on different methods and can be coordinated and optimized for the different detector situations or physics phases.

According to the physics quantities, the SNO+ fitters can be generally classified as:

- Vertex fitter. A vertex fitter reconstructs the event position and time by utilizing the positions and timing information of the hit PMTs. Currently, vertex fitters have been used to process the data and simulations for the water and partial-fill phases. They are also ready for the scintillator and tellurium-loading phases.

On the other hand, some particular events, such as radioactive background events emitting γ-particles, can create multiple correlated vertices. A multi-site or multi-vertex fitter will be helpful in tagging and removing these events during the $0\nu\beta\beta$ search. This kind of fitter is being developed.

- Direction fitter. A direction fitter reconstructs the event direction by using the directional information from the Cherenkov photons, which cause ring-like patterns formed by the hit PMT positions. The direction fitter has been used in the water phase analysis. For the scintillator and tellurium-loading phases, since the Cherenkov patterns will be submerged in the scintillation photons, it requires other efforts for the direction reconstruction, which is being developed currently.

- Energy fitter. An energy fitter translates the number of photons created from an event to kinetic energy. Similar to the vertex fitters, the energy fitters currently have been used in the water and partial-fill phases, and they are ready for the scintillator and tellurium-loading phases.

- Muon track fitter. This fitter is used to reconstruct the tracks of cosmic muons. It treats a muon track as a straight line, and by dividing the SNO+ detector into several XY-slices along z, it reconstructs the intersection points for each slice by utilizing the positions and timing information of the hit PMTs[137]. It is currently being developed for the scintillator and tellurium-loading phases. It will help to tag and reduce the cosmogenic backgrounds, especially the ^{11}C backgrounds induced by the muon spallation on the liquid scintillators[90].

For a fitter, its performance is first tested on the Monte Carlo simulations of specific physics processes. Then it is tested on both the simulations and data of the calibration runs. Once the algorithm gives good results and is approved by the SNO+ collaboration, it is implemented into the SNO+ RAT software to process the SNO+ simulations and data files.

For a specific SNO+ physics phase, the fitters for reconstructing different physics quantities of an event are integrated. Currently, there are three integrated fitters: the `Water Fitter` for the water phase, the `Partial Fitter` for the partial-fill phase, and the `Scint Fitter` for the scintillator phase and the tellurium loading phase. The fitter parameters, such as the optical parameters, fitter iterations, are coordinated and optimized based on simulations and calibration data from that specific physics phase. In addition, PMT selectors and classifiers are also included in the integrated fitters. The PMT selectors are used to remove the outliers of the hit PMTs for a specific fitter, such as the hit PMT probably triggered by the noises. These selectors can help to make the fitter more accurate or to boost up the fitter speed. The classifiers mainly use the reconstructed results to calculate specific quantities which describe the probability of determining an event as an expected signal or background.

In this chapter, a Multi-path (MP) reconstruction framework and its principles are discussed. It was developed by the University of Alberta group as an additional fitter to provide event vertex and direction reconstructions. In this framework, the fitters can be adapted for all the SNO+ physics phases by switching light path calculations, input parameters such as the optical parameters and the detector state. That is the reason why it is called "multiple paths". It was applied in the water phase to provide alternative information of the event position and direction; it also works as the vertex reconstruction algorithm for the `Partial Fitter`. After re-coordination for the scintillator and tellurium loading phases, I also show the potentials of the vertex fitter being applied in these two future phases.

In addition, the potentials of extracting the directional information from the scintillator phase are also discussed in this chapter.

4.2 Multi-path Vertex and Direction Reconstructions for the Water Phase

In the SNO+ water phase, both the cavity and the AV were filled with ultra-pure water. In this case, the detector geometry is simple since everything inside the PSUP sphere can be simplified as water if omitting the AV shell. Therefore, to explain the reconstruction concepts, I will start with the `MP water fitter` (the `MPW fitter`).

The `MPW fitter` fits for the vertex and direction of a triggered event in the SNO+ water phase. It first fits for the event vertex and then takes the results of the reconstructed position to fit for the event direction.

4.2.1 Vertex Reconstruction

To fit for the vertex with four parameters: x, y, z and t, first the fitter creates a random position inside a sphere with a radius of 10 m (larger than the actual PSUP radius $r_{PSUP} = 8.39\ m$). Meanwhile, a random event time is also generated from a uniform distribution in the range of $[100, 300\ ns]$. The Class Library for High Energy Physics (`CLHEP`) is used for creating pseudo-random numbers. The random position and the random time are combined to form a random event vertex as the trial event vertex $\vec{X}_0$. Details are given in the Appendix. A.1.

For a triggered event, photons are created around the event position and propagate to the hit PMTs. In a simplified detector geometry model that neglects the effects of scattering, reflection, and refraction, these photons are considered as propagating along straight lines connecting the trial event vertex to the hit PMTs. Then the fitter evaluates a timing parameter, called the time residual (t_{res}), which is defined as:

$$t_{res} = t_{\mathrm{PMT}} - t_{transit} - t_{event}, \tag{4.1}$$

where t_{PMT} is the PMT trigger time recorded by the detector, t_{event} is the time when an event occurs (event time), and $t_{transit}$ is the total transit time (or time of flight, TOF)

taken by a photon traveling from the event position ($\vec{X}_{event}$) to the hit PMT ($\vec{X}_{PMT}$) and crossing different materials in the detector.

To calculate the $t_{transit}$, the fitter uses Cherenkov photons in a prompt time window (called "prompt light"), set as $-10 < t_{res} < 10$ ns for the `MPW fitter` and the photons are assumed to propagate in straight lines (straight light paths). By assuming straight light paths, complicated situations of the photon propagation are neglected, including the refraction and reflection when the lights cross boundaries between different detector materials, absorption and scattering from the materials, and the lensing effects caused by the spherical structure of the acrylic vessel. In this case, the TOF can be simply calculated as $t_{transit} = |\vec{X}_{event} - \vec{X}_{PMT}|/v_{water}$, where v_{water} is an average photon group velocity and it is an effective value obtained by tuning on the Monte Carlo simulations. Section 4.2.3 will show the details about the tuning. Based on the reconstruction experiences from the SNO experiment, it found that without these details, the fitter can still produce decent results that are consistent with the case using detailed calculations[138, 79]. Fig. 4.1 shows the straight light paths from the event position to the hit PMT positions.

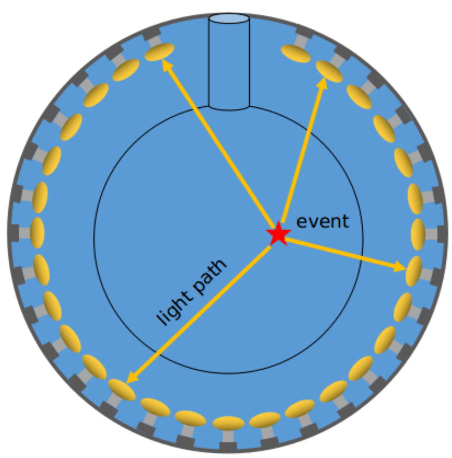

Figure 4.1: A diagram of straight light path for event position reconstruction in the SNO+ water phase geometry.

An one-dimensional (1D) probability density function (PDF) is used for fitting the timing model, as shown in Fig. 4.2. This PDF serves as a model of the timing responses of the triggered PMTs to an event to be fit. It was taken from the bench-top measurement of the individual PMT time profile from SNO[139] and was further tuned according to the measured *in-situ* SNO+ detector responses to the calibration sources[82].

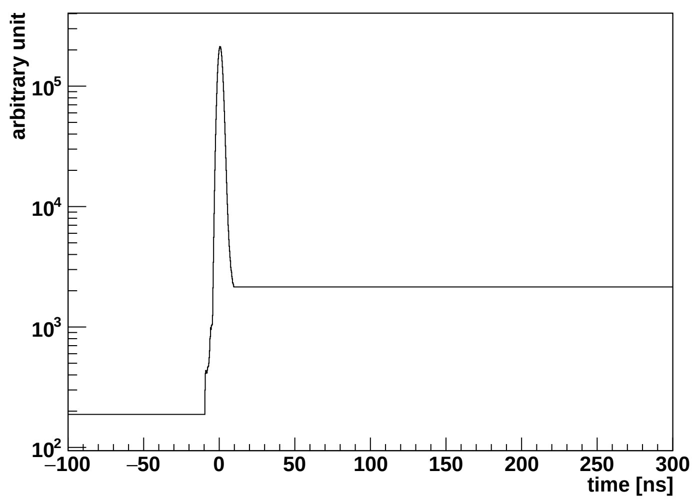

Figure 4.2: The PMT response time profile as the timing PDF for the vertex reconstruction.

For a trial vertex $(\vec{X}_0, t_0)$, the fitter calculates a t_{res} value with respect to each hit PMT. Looping over all the hit PMTs, a likelihood function is built as:

$$\ln \mathcal{L}(\vec{X}_0, t_0) = \sum_{i=1}^{\mathrm{NHits}} \ln P(t^i_{res}), \tag{4.2}$$

where t^i_{res} is the time residual calculated from the i^{th} hit PMT; NHits is the total number of the hit PMTs triggered by an event and $P(t^i_{res})$ is the probability returned by reading the PDF when given a t^i_{res} for the i^{th} hit PMT.

Therefore, the likelihood function starts with a random $(\vec{X}_0, t_0)$ as a seed and calculates the likelihoods and their derivatives for various paths assuming straight-line paths of the prompt Cherenkov light from the trial vertex $(\vec{X}_0, t_0)$ to each of the hit PMTs. The trial vertex is varied until the likelihood function reaches the global maximum when the best-fit vertex is found.

This fitting scheme is tackled by the Levenberg-Marquardt (MRQ) method, which is commonly used for fitting the nonlinear model with multiple parameters. This method is described in detail in the Sect. A.2 and its applications for the `MP fitter` framework are also described. Also see Refs. [140, 141] for details.

As will be shown in the following sections, one of the main tasks for the fitter is to calculate the $t_{transit}$ by evaluating light paths. As mentioned at the beginning, the water phase geometry is the simplest situation. While in the other situations, the AV is filled with the wavelength shifter or scintillator. They are different materials with cavity water, making the light path calculations complicated.

4.2.2 Direction Reconstruction

A direction vector $\vec{u}$ can be determined by two parameters: the zenith angle θ and the azimuth angle ϕ. Then in the Cartesian coordinate system, it can be written as:

$$\vec{u} = (\cos\phi \sin\theta, \sin\phi \sin\theta, \cos\theta). \tag{4.3}$$

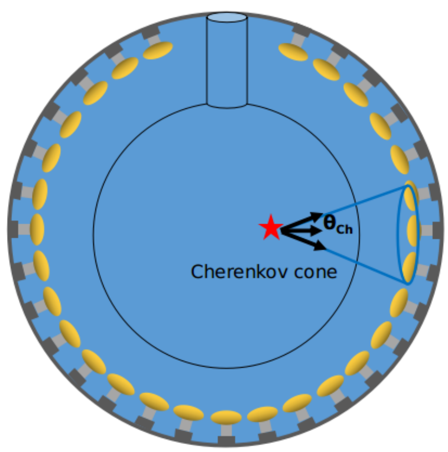

Figure 4.3: Diagrams of position in the SNO+ water phase geometry.

To fit for the direction with 2 parameters: θ and ϕ, similar to the vertex reconstruction, a random trial direction $\vec{u}_0(\phi_0, \theta_0)$ is generated by using `CLHEP`, see Sect. A.1. The direction fitter then evaluates an angular parameter, $\cos\theta_{\text{Ch}}$, which is the angle between $\vec{u}_0$ and $\vec{X}_{\text{diff}} \equiv \vec{X}_{event} - \vec{X}_{PMT}$. Therefore, the direction fitter requires an event position as the input, and it goes after the vertex fitter[1] .

[1] It has been discussed that, instead of fitting in two steps, the vertex and direction can be fit simultaneously by utilizing the MRQ algorithm for fitting six parameters $(x, y, z, t, \theta, \phi)$. However, it shows that the results were worse by using this method.

An 1D PDF is used for fitting the angular model, as shown in Fig. 4.4. This PDF serves as a model of the angular distributions of the triggered PMTs to an event. It was obtained from 10000 MC simulations of 5-MeV e^- events generated at the detector center ($\vec{X}_{MC} = (0,0,0)$), and traveling along the positive side of the x axis, i.e., the direction of the momentum is $\vec{u}_{MC} = (1,0,0)$[2] .

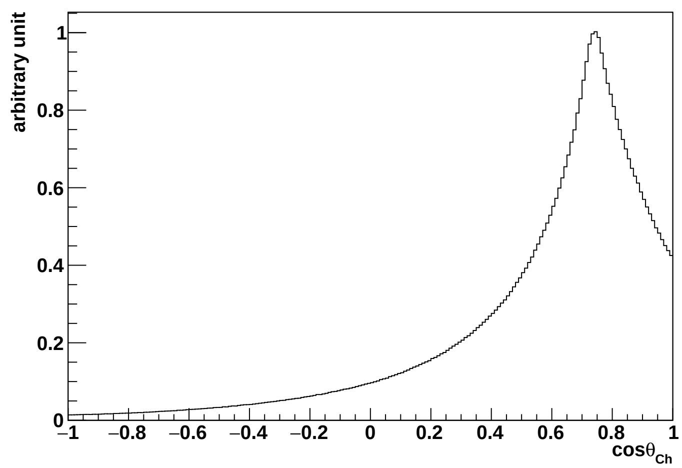

Figure 4.4: PMT angular distribution as the angular response PDF for direction reconstruction.

For the i^{th} hit PMT, $\cos\theta^i_{\mathrm{Ch}} = \vec{u}_0 \cdot \frac{\vec{X}^i_{\mathrm{diff}}}{|\vec{X}^i_{\mathrm{diff}}|}$, then the likelihood function is built as:

$$\ln L(\vec{u}_0) = \sum_{i=1}^{\mathrm{Nhits}} L_i(\cos\theta^i_{\mathrm{Ch}}), \tag{4.4}$$

Finally, the fitter fits for the angular PDF by using the MRQ method to obtain the best-fit direction. There a few optimizations for improving the fitter performances. First, the group velocity used in the $t_{transit}$ calculation is tuned, as shown in Sect. 4.2.3. In Sect. 4.2.4, a drive correction for compensating the pulls in the reconstructed position is discussed. In Sect. 4.2.5, PMT selectors for sending proper PMT information to the fitter are discussed.

[2]Here 5 MeV is a typical energy for the SNO+ water phase analysis. It shows that using the PDFs generated by the other e^- energies does a minor effect on the reconstruction results.

4.2.3 Effective Group Velocity

When photons travel through the detector, their group velocities (v_{gr}) change with different refractive indices of different detector materials. The group velocities also depend on the wavelengths of the photons: $v_{gr} = c/n(\lambda)$. Fig .4.5 shows the measured refractive index (n) as a function of wavelength, obtained from the measurements of the laserball scans in the SNO+ water phase[142]. Furthermore, the v_{gr} can change when the photons are scattered, absorbed, refracted and reflected in the detector.

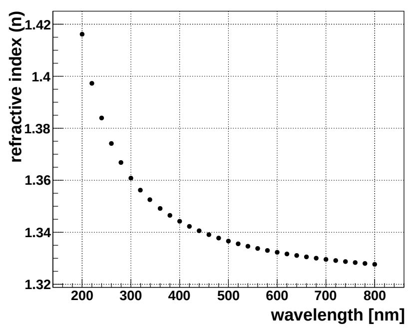

Figure 4.5: Refractive index vs wavelength, reproduced from `RAT`. These values are based on the measurements from laserball calibration scans in the SNO+ water phase[142].

To simplify these complicated situations of v_{gr} for the reconstruction, a tuned value of the v_{gr} is used in the straight line light path calculation. As mentioned in Sect. 4.2, the water vertex fitter calculates the $t_{transit}$ by evaluating the distances from the trial vertex to the hit PMTs: $t_{transit} = |\vec{x}_{event} - \vec{x}_{PMT}|/v_{gr,eff}$, where the v_{water} is replaced by the effective group velocity $v_{gr,eff}$. The value of the $v_{gr,eff}$ set in the fitter can introduce biases in the reconstructed position, which is mainly due to a "complementary" effect of the fitter. Setting a large value of $v_{gr,eff}$ (a fast effective group velocity) will decrease the $t_{transit}$, while according to Eqn. 4.1, the t_{res} will increase. During the reconstruction, when the fitter compares the large t_{res} with the timing PDF, it will attempt to place the trial vertex away from the hit PMTs to increase the $t_{transit}$ and then decrease the t_{res}, as illustrated in Fig. 4.6. On the other hand, if the $v_{gr,eff}$ is set too small (or too slow), the $t_{transit}$ will increase while the t_{res} will decrease, and the fitter will place the trial vertex closer towards the hit PMTs to increase the t_{res}. These effects can be quantified as radial bias (r_{bias}), which is the difference between the reconstructed and true (MC) positions ($\vec{X}_{fit} - \vec{X}_{MC}$), projected along the radial component of the true position (the unit vector $\hat{X}_{MC}$)[143]:

$$r_{bias} \equiv (\vec{X}_{fit} - \vec{X}_{MC}) \cdot \hat{X}_{MC}, \tag{4.5}$$

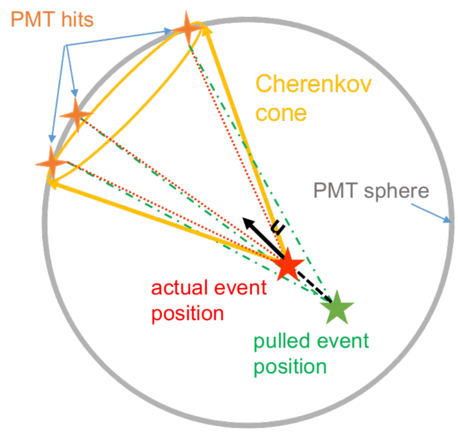

Figure 4.6: A cartoon shows effects of tuning the effective group velocity. In this case, the effective group velocity is faster than expected, the fitted position is dragged back along the direction to increase the $t_{transit}$.

It shows that an overestimated $v_{gr,eff}$ (too fast) brings a positive radial bias to the true event position while an underestimated one (too slow) brings a negative radial bias.

In practice, the $v_{gr,eff}$ is calculated by an effective refractive index n_{eff} (or called RI value): $v_{gr,eff} = c/n_{eff}$. To obtain a reasonable $v_{gr,eff}$ for the water-phase vertex fitter, my first attempt is to obtain the value from linear interpolation based on the MC simulations. First, 500 simulations of 5-MeV e^- were generated uniformly inside the AV and with isotropic momentum directions. Then the `MPW fitter` reconstructed the same MC simulations by using 7 different values of v_{gr}, from 200 to 230 mm/ns (the n_{eff} is from 1.50 to 1.30), with a step of 5 mm/ns. The distributions of radial bias from each reconstruction results were calculated and fitted with Gaussian functions. The mean values of these Gaussian fits were taken as the values of the r_{bias}, and they were plotted against the v_{gr}, as shown in Fig. 4.7. A linear fit was applied on these points and it gives $v_{gr,eff} =$

215.868 ± 5.585 mm/ns ($n_{eff} = 1.3888$) at the point where $r_{bias} = 0$.

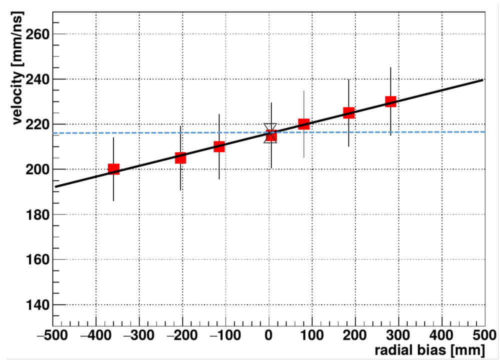

Figure 4.7: Group velocity vs. radial bias for the `MPW fitter`.

Later I turned to a more data-driven approach rather than tuning from the simulations. This approach is to extract an average group velocity by analyzing the ^{16}N calibration source data. As shown in Fig. 4.8, for the ^{16}N central run-100934 and run-107055, the source was deployed almost at the PSUP center where the optical photons were created and propagated to reach the PMTs on the PSUP.

For each event, it supposes that the triggered PMTs were found within a solid angle $\Omega = \pi(L/2)^2/r_{PSUP}^2$, where L is the line segment and $r_{PSUP} = 8390$ mm is the radius of the PSUP, as shown in Fig. 4.8. Since the diameter of the PMT concentrator is 27 cm, the line segment is chosen as $L = 50$ cm ($\theta = \arcsin(\frac{1}{2}L/r_{PSUP}) \approx 0.17°$) to let roughly 2 PMTs be within the Ω. Then the arrival time T_1 was found by calculating $|\vec{X}_{source} - \vec{X}_{PMTin\Omega}|/v_{water}$, where $v_{water} = 217.554$ mm/ns is an effective velocity obtained by the SNO+ for light water[143].

On the other hand, a solid angle Ω' is calculated as opposed to the Ω from the source position. Similarly, the triggered PMTs within the Ω' were found and then the arrival time T_2 is calculated. Thus the average group velocity was calculated as:

$$v_{gr} = \frac{2r_{PSUP}}{(T_1 + T_2)}. \tag{4.6}$$

The final number of the v_{gr} was calculated by averaging the v_{gr} obtained from all the events and triggered PMTs in both the run-100934 and 107055. It finds the $v_{gr} = c/n_{water,eff} = 216.478$ mm/ns, where $n_{water,eff} = 1.38486$.

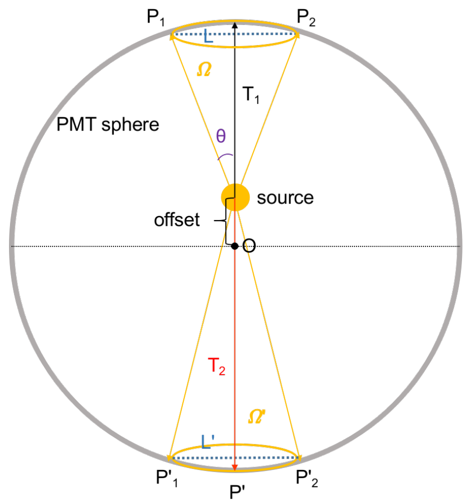

Figure 4.8: ^{16}N central run for evaluating the average group velocity.

The SNO+ collaboration used a more complicated approach to measure actual group velocities in the SNO+ water detector by analyzing a set of laserball calibration runs[144, 82]. This analysis can give a more accurate v_{gr}, while it was not applied here.

For the vertex fitters used in the partial-fill and scintillator phases, since no internal calibration was performed, I adopt the linear interpolation method. It will be discussed in Sect. 4.5.

4.2.4 Fitter Pull and Drive Correction

An effect of "fitter pull" in the event vertex reconstruction utilizing the Cherenkov light was observed in the SNO experiment. The distribution of $(\vec{X}_{fit} - \vec{X}_{MC})/|\vec{X}_{fit} - \vec{X}_{MC}| \cdot \vec{u}_{fit}$ shows a large peak at +1, which indicates that the fitted position $\vec{X}_{fit}$ is prone to be pulled forward from the true position systematically along the event direction$\vec{u}$[145, 146, 143].

Similar to the SNO heavy water case, in the SNO+ ultrapure water, Cherenkov photons created by an event trigger most of the PMT-hits with early timing and these hits are located within the Cherenkov cone; for the same event, there are also a few PMT-hits with later timing. These PMT hits can be caused by the scattered or reflected photons and they are located throughout the detector. For a random PMT hit, it is more probable to be placed outside the Cherenkov cone due to the geometry: consider an event happens at the center of the PSUP, the Cherenkov cone it produced will intersect the PSUP by an area of $2\pi R_{PSUP}^2(1-\cos 41°)$, which occupies about 12% of the total area of the PSUP sphere. Therefore, for a random PMT-hit on the PSUP sphere, it has more than 88% of chance to be placed outside the Cherenkov cone.

For these later timing PMT hits, a similar "complementary" effect mentioned in Sect. 4.2.3 can also happen. When the fitter fits with t_{res}, for the large t_{res} values caused by the later timing hits, it pulls the trial position away from the later timing hits to increase $t_{transit}$ and decrease t_{res}, as illustrated in Fig. 4.9. This effect was also explained as "straighten out delayed photons" by the timing fitter in [145]. Furthermore, the major early hits can also cause small t_{res} values and thus the fitter pulls the trial position closer towards the early hits to decrease $t_{transit}$ and increase t_{res}. Recall that the early hits are located on or around the Cherenkov cone, therefore an overall effect of this "fitter pull" is that the fitted position will be pulled along the axis of the Cherenkov cone and towards the PSUP sphere. This pull direction is coincident with the event direction.

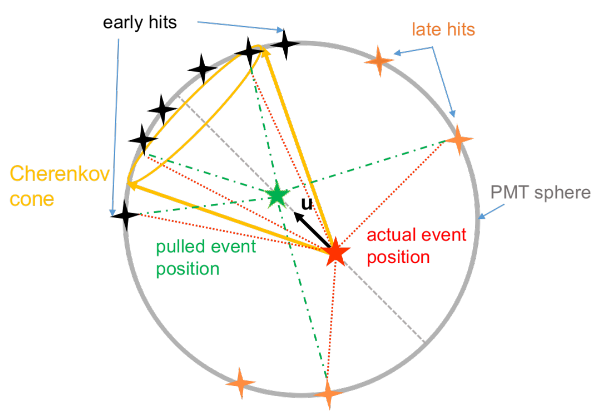

Figure 4.9: A cartoon shows fitter pull effect, modified from Fig. C.2 in Ref. [146] and Fig. 2,3,4 in Ref. [145].

A simple way to eliminate this "fitter pull" effect is to pull back the fitted event position against the event direction. This is called "drive correction".

Once the `MPW fitter` obtains both of the fitted position and direction, the drive correction is applied on the fitted position by $\vec{X}_{\text{corrected}} = p_0\vec{X}_{fit} + p_1\vec{u}_{fit}$, where p_0 and p_1 are the correction parameters, as shown in Fig. 4.10.

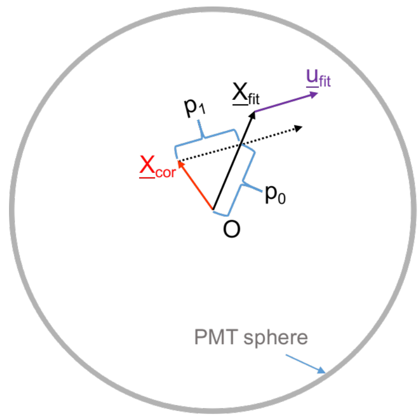

Figure 4.10: A diagram illustrates the drive correction.

To obtain the values of p_0 and p_1, I generated e^- events distributed isotropically inside the AV. The simulations with various e^- energies from 2 to 10MeV by an 1MeV step were produced. Then the `MPW fitter` was applied on each simulations and returned the results of $\vec{X}_{fit}$ and $\vec{u}_{fit}$. Taking the Monte Carlo generated positions $\vec{X}_{MC}$ as the true positions, for all the fitted events, a χ^2 function is calculated by:

$$\chi^2 = \sum_{i=1}^{N_{\text{events}}} [\vec{X}^i_{MC} - (p_0\vec{X}^i_{fit} + p_1\vec{u}^i_{fit})]^2, \tag{4.7}$$

The p_0 and p_1 are obtained by minimizing the χ^2 function. When calculating the χ^2, the fitted events of $|\vec{X}_{fit} - \vec{X}_{MC}| > 3\ m$ are thrown away to improve the χ^2 minimization results.

For the 2 to 10-MeV e^- event simulations (using `RAT` version 6.17.6), the obtained values of p_0 and p_1 are energy or NHit dependent. However, it does not improve the results if using the NHits dependent functions p_0(NHit) and p_1(NHit) as drive corrections. Finally we take the average values from the 5 to 10 MeV electrons simulations and the drive correction is set as:

$$\vec{X}_{\text{corrected}} = 0.9868\vec{X}_{fit} + (-78.417)\vec{u}_{fit}. \tag{4.8}$$

Note that these drive correction parameters were obtained from simulations and changes of the simulation model, especially the optical model of the detector, can affect the $n_{gr,eff}$, mode cut and time residual cut, and then affect the drive correction parameters. However, the drive correction parameters can be re-coordinated with the changes in the simulation.

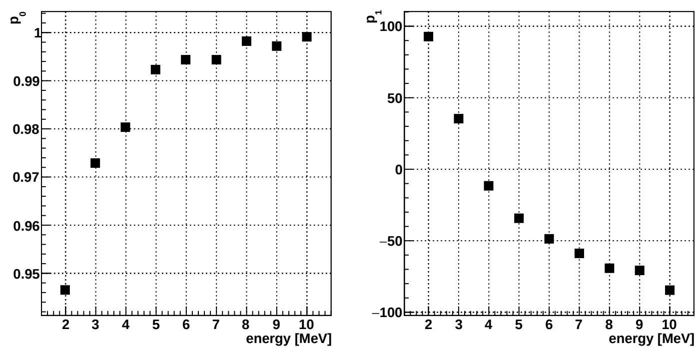

Figure 4.11: Drive correction parameter p_0 (left) and p_1 (right) as a function of energy.

To check the effects of the drive correction, 1000 simulations of the 5-MeV e^- were generated at the detector center with momentum direction at (1,0,0). It shows that the drive effect in the reconstruction causes a +50 mm bias from the detector center in the x axis (i.e., the pull in +x). The drive correction reduces this pull down to ∼+0.2 mm in the x axis. The resolution of the r_{bias} distribution is also improved by ∼20 mm. With the same simulation settings, various energies of e^- from 2 to 10 MeV (with a 1-MeV step) were generated to check the effects before and after the drive correction, as shown in Fig. 4.12. The pull is quantified by the radial bias mentioned in Sect. 4.2.3. The distributions of the r_{bias} in each simulation were fitted with Gaussian functions, and the Gaussian means were used as the pull. It shows that, with higher energy, the pull effect is larger. The drive corrections correct the radial biases by about 55 mm. The drive correction is also applied in the `Rat water fitter`, and their results are also shown.

4.2.5 PMT Selectors for the Reconstruction

PMT selectors were developed to selecting proper PMTs for the reconstruction algorithm from all the recorded PMTs triggered by an event. The purpose is to optimize the fitter

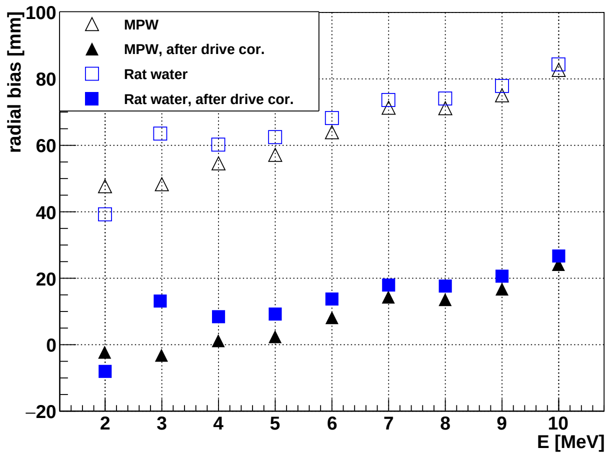

Figure 4.12: Radial biases of the simulated e^- events before (unfilled triangles) and after the drive correction (filled triangles), as a function of energy. The results from the official `RAT water fitter` are also shown here, with the unfilled blue squares for biases before the correction and filled ones after the correction.

results and boosting up the fit speed. The PMT selectors used by the `MP fitter` are:

- Straight Light Path Time Residual Cut Selector

  This selector is used for the direction reconstruction for the SNO+ water phase. It was first developed by Kalpana Singh[13]. In the selector, the value of time residual (t_{res}) is calculated for each hit PMTs from an event and the PMT returning a t_{res} value within the prompt time window of $[-10.0, 120.0]$ ns is selected for the fitter. The selector calculates the t_{res} by using straight line light paths, which is the same as the `MPW fitter`. The selector mostly removes the PMTs triggered by late timing photons, such as the photons reflected off the detector elements (called "late light"), and then keeps the possible Cherenkov ring hit pattern clear for the direction reconstruction. Removing the irrelevant PMTs can potentially boost up the fit speed.

- Mode Cut Selector

  This selector was developed by the SNO+ collaboration for all fitters. It checks the hit time (t_{PMT}) distributions of all the hit PMTs and finds a mode value of the hit time (t_{mode}). If t_{mode} fails to be found, it calculates a median value (t_{median}) instead[147].

Then it selects the PMT with $t_{\text{PMT}} \in [t_{mode} + t_{low}, t_{mode} + t_{high}]$ ns. This selector is used to remove thePMTs triggered by noise and light light from reflection. The values of t_{low}, t_{high} are optimized for different scintillators. For the `MPW fitter`, I found that the optimized window is $[t_{mode} - 50, t_{mode} + 100]$ ns by checking with the fit biases and resolutions for the ^{16}N central run data in the water phase, while for the `MP partial fitter` and `MP scint fitter` the optimized window is $[t_{mode} - 100, t_{mode} + 100]$ ns based on checking with the simulations.

- Uniform PMT Selector

  I implemented this selector and the Earliest Hit Selector mentioned below for the partial-fill and scintillator phases when a single event can trigger many PMTs due to high light yields of the liquid scintillator. In this case, the fit speed for each event becomes slow, which can challenge the data processing. These selectors can reduce the number of the hit PMTs to a designated number (n_{select}) to boost up the fit speed while still keep acceptable results of the fit bias and resolution.

  For the Uniform PMT Selector, when an event triggers N calibrated PMTs, the selector goes through these recorded PMTs and uniformly picks up one PMT by an interval of $\lceil N/n_{select} \rceil$. If $N \leq n_{select}$, the selector does nothing. By doing this, the selector uniformly reduces the number of the PMTs for the fitter without an obvious bias.

- Earliest Hit PMT Selector

  This selector first groups the PMTs by their positions in the PSUP sphere. Taking the centre of the sphere as the origin of the coordinate, the sphere is divided by the azimuth angle ϕ (as longitude) and zenith angle θ (as latitude). The PMT positions are projected to $\phi \in [-\pi, \pi]$ and $\cos\theta \in [-1, 1]$ on the sphere, each is uniformly divided into n intervals. Thus, the PMTs are grouped into $n \times n$ panels by ϕ and $\cos\theta$: $\text{PMT}(\phi_i, \cos\theta_j) \in [i \cdot \phi/n, j \cdot \cos\theta/n]$, $(i, j = 1, 2, .., n)$, see Fig. 4.13.

  In each panel, the selector first removes the hit PMTs which are triggered too early

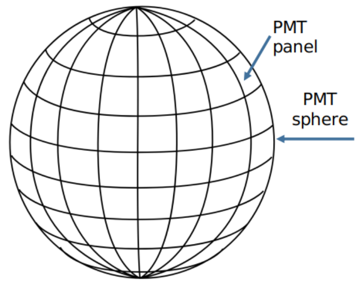

Figure 4.13: The PMTs are grouped by dividing the PSUP sphere with latitudes and longitudes.

($t_{\mathrm{PMT}} < 100$ ns, where 100 ns is set as a default threshold). These PMTs could be triggered by noises, such as the pre-pulsing from thermal noises. Then in the rest of the hit PMTs, the selector picks up one PMT which has the earliest t_{PMT} in the panel. Thus the number of the hit PMTs is reduced to $n \times n$ for the fitter, i.e., $n_{select} = n \times n$. If NHits $\leq n_{select}$, the selector does nothing.

The other timing parameters can also be used for selecting the PMT in each panel, such as the t_{mode} or the t_{median}. However, tests on the simulations for the scintillator phase show that using the earliest hit time t_{PMT} gives fewer fit biases and better fit resolutions.

Tests on the 10-MeV e^- simulations in the scintillator phase show that applying this selector with $n_{select} = 16 \times 16$, the fit speed was reduced from 1.2 s/event to 0.4 s/event.

4.2.6 Position Figure of Merit

A quantity called scaled $\log L$ ($scaleLogL$) is used as the position reconstruction FoM ($posFoM$): $scaleLogL = \ln L/\mathrm{NHit}_{selected}$. This quantity utilizes the best log-likelihood returned by the `MP fitter` for a successfully reconstructed event vertex, and then it is scaled by the "selected" NHit ($\mathrm{NHit}_{selected}$), which is the number of the PMTs actually used by the fitter for the event vertex reconstruction, after the PMT selections mentioned in Sect. 4.2.5. This $posFoM$ quantity can remove a few mis-reconstruct events and then improve the results of the reconstruction.

4.2.7 Performances of the Water Vertex Reconstruction

By using the RAT (version 6.17.6) package, simulations of 10000 e^- events were generated at the detector center (in the PSUP coordination) with isotropic directions, i.e., the event momentum directions were generated randomly and uniformly over all directions. Default detector trigger settings in the SNO+ water phase were used (N100Hi=21.0, N100Med=16.0 and N100Lo=11.0). With these settings, some events may fail to trigger the detector, especially those with lower energies ($E < 3$ MeV), and thus the number of the reconstructed events can be lower than the simulated events.

The average fit speed of the event vertex reconstruction for the 5-MeV e^- simulations is 0.005 second/event and the direction reconstruction is 0.002 second/event, which are very fast and acceptable for the data processing in the SNO+ water phase. Fig. 4.2.7 shows the position reconstruction results and performances for the 5-MeV e^- events. The biases between the fitted and MC positions: $\vec{X}_{fit} - \vec{X}_{mc} = (x_{fit} - x_{MC}, y_{fit} - y_{MC}, z_{fit} - z_{MC})$, were projected on the x, y, and z axes respectively and their distributions were fitted with Gaussian functions. The mean of the fitted Gaussian (μ) is taken as the fit position bias while the Gaussian sigma (σ) is taken as the fit position resolution.

In Fig. 4.2.7, there are a few events with position biases larger than 2000 mm, which are considered as mis-reconstruct events. Some of these events are due to relatively lower log-likelihood values and can be tagged by the $posFoM$ mentioned in Sect. 4.2.6. As shown in Fig. 4.2.7, a cut of $scaleLogL > 10$ can remove a few mis-reconstructed events. The rest of them can be caused by the straight light path calculation in the `MP fitter`, since this calculation omits the complicated situations with the refraction and reflection light paths, as mentioned in Sect. 4.2.1. However, the fraction of these mis-reconstruct events is low, about 0.1% and thus it is acceptable.

A more generic situation is that the events happen everywhere inside the AV. To simulate this, e^- events were generated at random positions uniformly distributed inside the AV

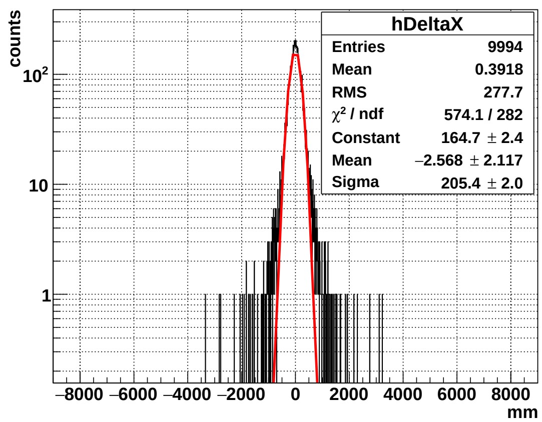

(a) $x_{fit} - x_{mc}$

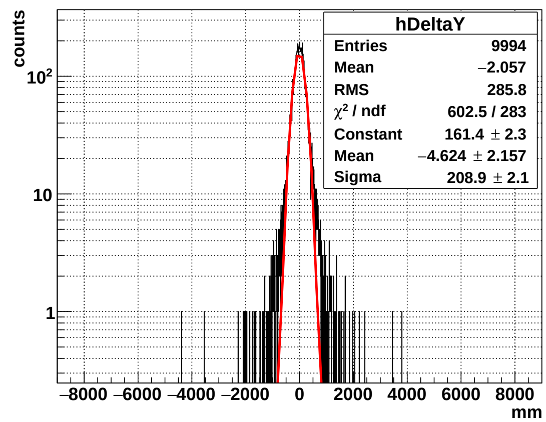

(b) $y_{fit} - y_{mc}$

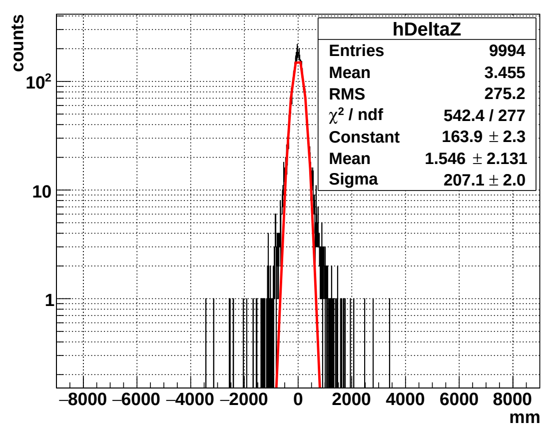

(c) $z_{fit} - z_{mc}$

Figure 4.14: The position biases projected on the x, y and z axes. The distributions were fitted with Gaussian functions. The MC generated 10000 5-MeV e^- particles at the detector center with isotropic directions.

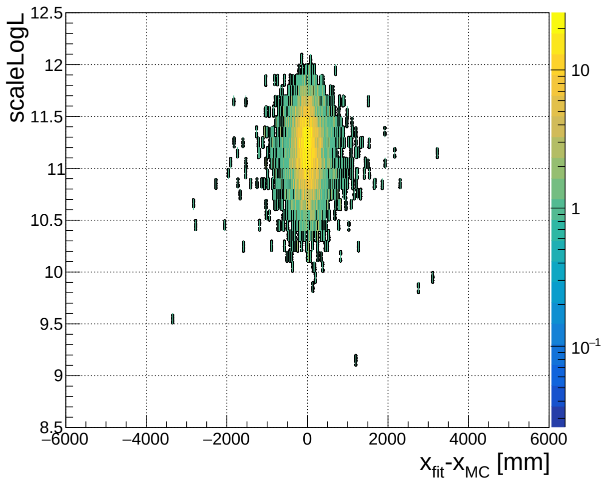

(a) $x_{fit} - x_{mc}$ vs. $scaleLogL$.

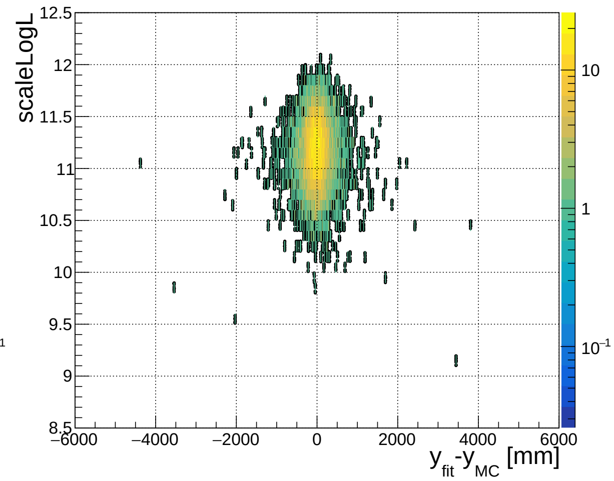

(b) $y_{fit} - y_{mc}$ vs. $scaleLogL$.

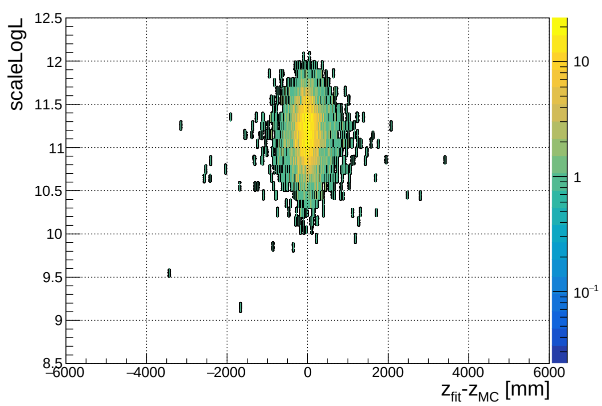

(c) $z_{fit} - z_{mc}$ vs. $scaleLogL$.

Figure 4.15: The position biases against the position FoMs. The MC generated 10000 5-MeV e^- particles at the detector center with isotropic directions.

volume and with isotropic directions. Various e^- energies were also simulated, from 2 to 15 MeV with a 1-MeV step. Fig. 4.16 and Fig. 4.17 show the fit position biases ($\mu_{x,y,z}$) and resolutions ($\sigma_{x,y,z}$) respectively.

These results show that the fit position biases $\mu_{x,y,z}$ are stable across different energies and for $E \leq 5$ MeV, the biases are within 10 mm. The resolutions $\sigma_{x,y,z}$ decrease from about 350 mm to 120 mm and the average is 180 mm. More photons are produced by the e^- events with higher energy, thus triggering more PMTs. With a larger NHits value, more information is provided for the fitter, and it can return better position resolutions. As I will show in the following section, the position resolution can also be improved by using a decent detection medium that can produce more photons for the same event..

With a larger value of NHits, more information is provided for the fitter, and it can return better position resolutions. As I will show in the following section, the position resolution can also be improved by using a decent detection medium that can produce more photons for the same event.

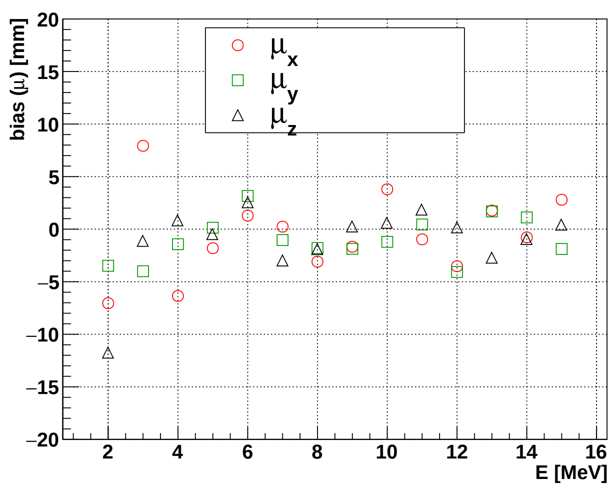

Figure 4.16: The `MPW fitter` fit position biases in x(red circle), y (green square), and z (black triangle) axes as a function of energy.

To check the radial dependence of the reconstruction performance, simulations of the 5-MeV e^- were generated in 11 thin shells, with isotropic directions. The centers of these

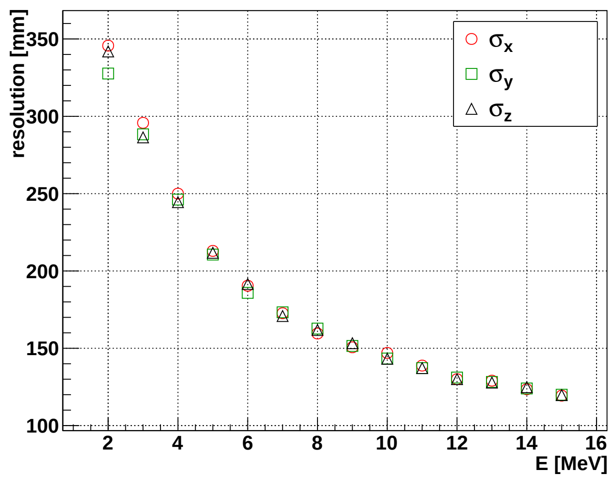

Figure 4.17: The `MPW fitter` fit position resolutions in x (red circle), y (green square), and z (black triangle) axes as a function of energy.

shells are at the AV center, and their radii are at r m and $r + 0.001$ m, where r is from 0.5 m to 5.5 m, with a step of 0.5 m. Fig. 4.18 and Fig. 4.19 show the fit position biases and resolutions respectively. The results show that the fit position biases are stable across the different radii of the AV, while the resolutions become worse when the events are close to the AV, or $R > 5$ m. This is called the "near AV effect", which was observed in SNO. For the position close to the AV, the AV can serve as a lens and distort the light path[146]. A few complicated calculations to tackle this effect and the technique called "Near AV cut" were discussed in Refs. [143, 79], but they are not applied in this thesis.

4.2.8 Performances of the Water Direction Reconstruction

The bias between the true event direction $\vec{u}_{MC}$ and the reconstructed direction $\vec{u}_{fit}$ is described by the angle θ_e, and $\cos\theta_e \equiv \vec{u}_{fit} \cdot \vec{u}_{MC}$.

To describe the distribution of $\cos\theta_e$, an empirical function for the angular resolution was adopted by SNO[138] and it is defined as a combination of two exponential components:

$$P(\cos\theta_e) = \alpha_M \frac{\beta_M \exp[-\beta_M(1-\cos\theta_e)]}{1-\exp(-2\beta_M)} + (1-\alpha_M)\frac{\beta_s \exp[-\beta_s(1-\cos\theta_e)]}{1-\exp(-2\beta_s)}, \tag{4.9}$$

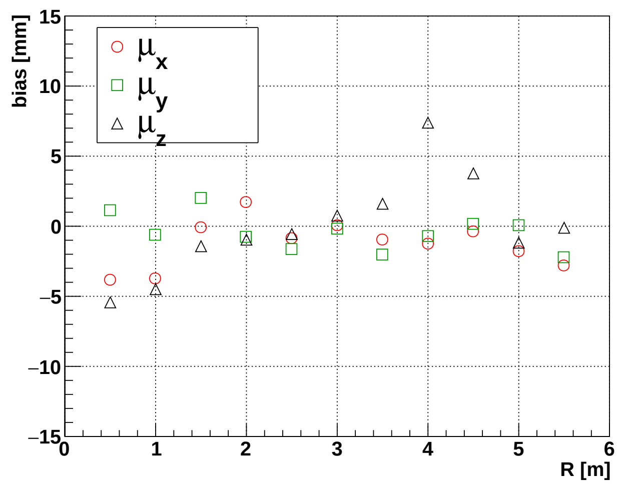

Figure 4.18: The `MPW fitter` fit position biases of x (red circle), y (green square), and z (black triangle) axes as a function of radius.

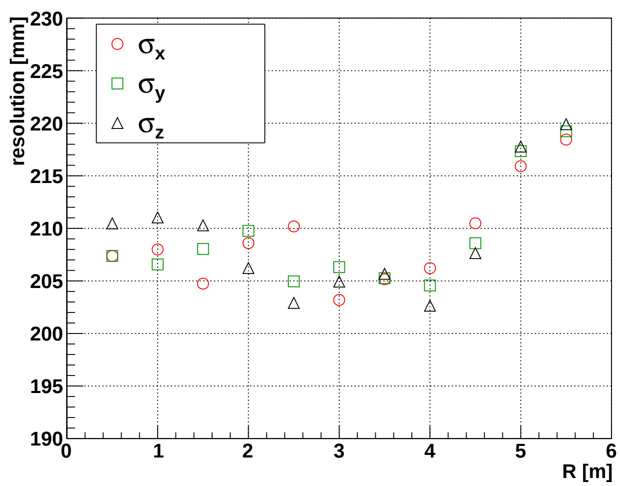

Figure 4.19: The `MPW fitter` position resolutions of x (red circle), y (green square), and z (black triangle) axes as a function of radius.

where the parameters: β_M and β_S are the "decay" constants or the "slopes" of the two exponential components; α_M is the fraction between two exponential components. The first component, the main peak is due to the single scattering of the electrons and is the true angular resolution of the detector, while the second component which has a broad tail is mainly due to the multiple scattering of electrons; there are also back scattering electrons on the detector components and the poorly reconstructed events in the tails[138]. Fig. 4.2.8 shows the $\cos\theta_e$ distribution of the 5-MeV e^- particles generated at the detector center and with isotropic directions.

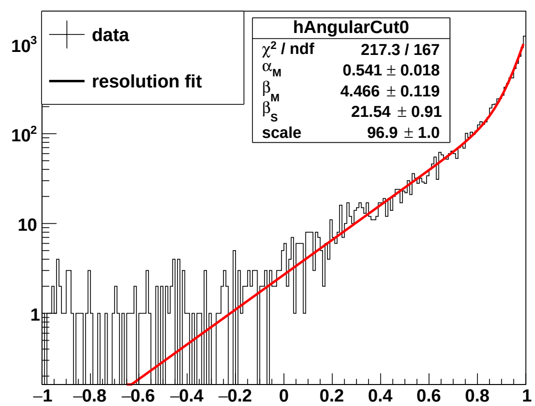

Figure 4.20: The biases between the fitted and MC directions, fitted with the resolution function $P(\cos\theta_e)$ (plotted in red). The MC generated 10^4 5-MeV e^- at the detector center.

Another way to quantify the reconstruction performance based on the $\cos\theta_e$ distribution is to calculate the angles that contain 50%, 80% or 90% of the reconstructed events, denoted by $\cos\theta_{0.5}$, $\cos\theta_{0.8}$ and $\cos\theta_{0.9}$ respectively[143]. Their values are solved numerically from the Eqn. 4.10:

$$\frac{\int_{\cos\theta_a}^{1} P(\cos\theta_e)d\cos\theta_e}{\int_{-1}^{1} P(\cos\theta_e)d\cos\theta_e} = a \times 100\%, \tag{4.10}$$

where $P(\cos\theta_e)$ is the direction resolution function with the best fitted parameters. A larger $\cos\theta_a$ means the $\cos\theta_e$ distribution is more peaked around +1 and a better direction reconstruction. The results of the direction resolutions are listed in Table. 4.1.

These results are slightly better than the SNO fitter results for the 5-MeV e^- in the

Table 4.1: Direction resolutions for the reconstruction of the 5-MeV e^- events.

β_M	β_S	$\cos\theta_{0.5}$	$\cos\theta_{0.8}$	$\cos\theta_{0.9}$
4.47±0.12	21.54 ±0.91	0.978	0.777	0.624

heavy water, with $\beta_M = 3.348 \pm 0.08119, \beta_S = 19.3 \pm 0.6929$[138].

To check the radial dependence of the direction reconstruction performance, the similar tests in Sect. 4.2.7 Fig. 4.21 shows the direction resolutions β_M (left plot) and β_S (right plot) as a function of the radius.

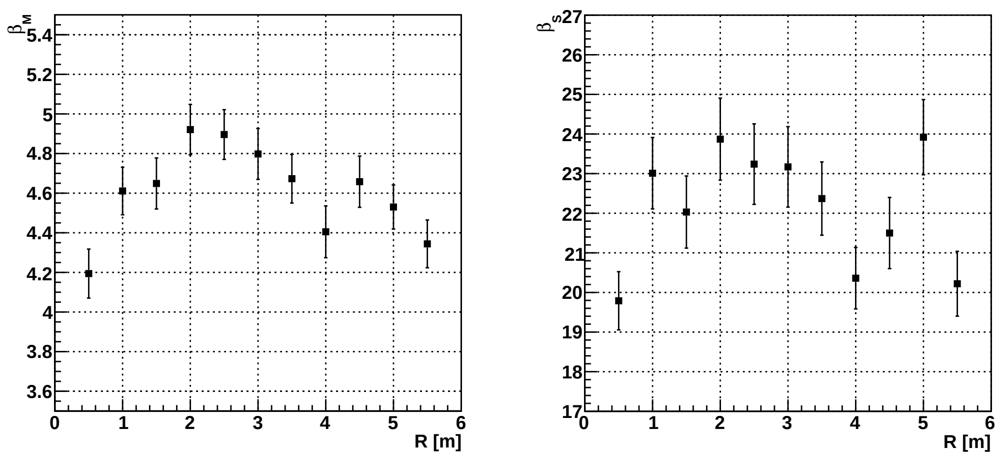

Figure 4.21: Direction resolutions as a function of radius. The MC generated 10000 5-MeV e^- inside the AV with isotropic directions.

4.2.9 Test on Gamma Events

The γ-events with energies of 2.2 MeV and 4.4 MeV are crucial for analyzing the AmBe calibration data. A realistic trigger setting for the antineutrino analysis (run-106904) was also simulated. With this trigger setting in simulations, about 53% of the low energy 2.2-MeV γ events were triggered. So I doubled the simulations to 2×10^4.

Table. 4.2 shows the reconstruction performances.

Table 4.2: Reconstruction performances for the 2.2-MeV and 4.4-MeV γ events.

simulation	$\Delta x \pm \sigma_x$ [mm]	$\Delta y \pm \sigma_y$ [mm]	$\Delta z \pm \sigma_z$ [mm]
2.2-MeV	2.278 ± 626.927	-5.663 ± 608.182	-10.523 ± 626.034
4.4-MeV	-6.964 ± 364.725	-2.804 ± 368.752	-1.342 ± 368.398

4.2.9.1 Test on ^{16}N Calibration Source Events

In a more realistic situation, the data collected from the runs of the calibration sources were used to evaluate the fitter performances as well as the reconstruction uncertainties. Chapter 5 will discuss the analyses of the ^{16}N calibration source in detail. For these tests, a position resolution function including the distributions of the initial interaction positions, rather than the Gaussian function was used, while the same direction resolution function was used.

4.3 Vertex and Direction Reconstruction for the Water-based Wavelength-shifter

A reconstruction algorithm was developed to investigate the proposal for the water-based wavelength-shifter, as mentioned in 3.3.4.

Figure 4.22 shows the position distributions of hit PMTs for MC simulated 5 MeV electrons traveling along $+x$ direction in the AV. The left panel shows the case when the detector is filled with pure water while the right panel is for water plus 0.1 ppm PPO. For the same electrons, the number of hit PMTs (NHits) in wbWLS is about 2.4 times greater than the pure water one. Although there is extra isotropic light emitted, the Cherenkov ring can still be seen clearly, allowing reconstruction of the directionality.

Figure 4.23 shows the energies of simulated electrons as a function of the mean value of the NHit distribution (mean NHits). In pure water, a 1 MeV electron simulation does not trigger any PMTs while in wbWLS case we have a mean NHits of 20.

In the wbWLS case, since the WLS absorbs and re-emits photons, the reconstruction mentioned in section 4.2 is slightly modified to build the MP WLS Fitter. According to

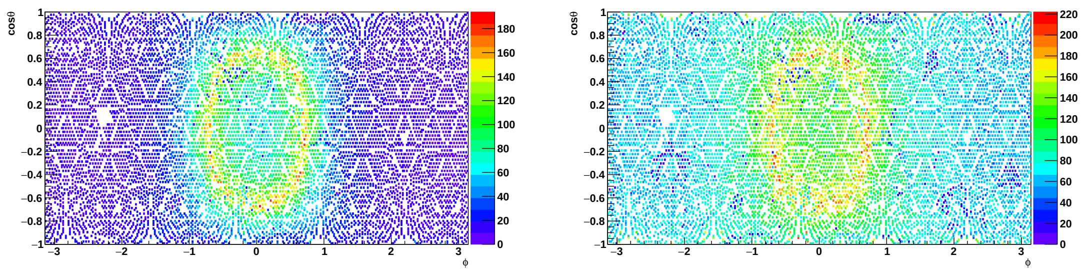

Figure 4.22: Position distributions of hit PMTs (in zenith and azimuth angles) for 5 MeV electrons traveling along $+x$ direction in the pure water (left) and the water plus 0.1 ppm PPO (right).

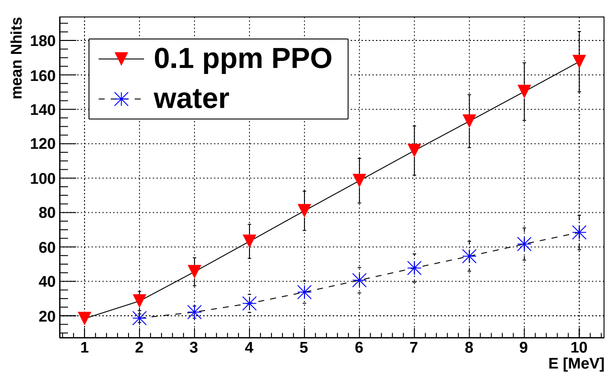

Figure 4.23: The energies of simulated electrons as a function of mean NHits. The values in the 0.1 ppm PPO (solid line with inverted triangle) are compared with the water (dashed line with star).

the optical property of PPO, the prompt light emitted from an event has a probability of $\sim$0.6 to be absorbed by the WLS and then re-emitted at a shifted vertex along the particle direction $\hat{n}$. Then the fitter returns a shifted vertex, $\vec{X}_{0,shifted} = \vec{X}_0 + \text{offset} \cdot \hat{n}$. The offset we set in the fitter is 100 mm obtained from simulations. Figure 4.24 shows the timing PDF for the wbWLS, which is the PMT response time modified to photon propagation time in the wbWLS.

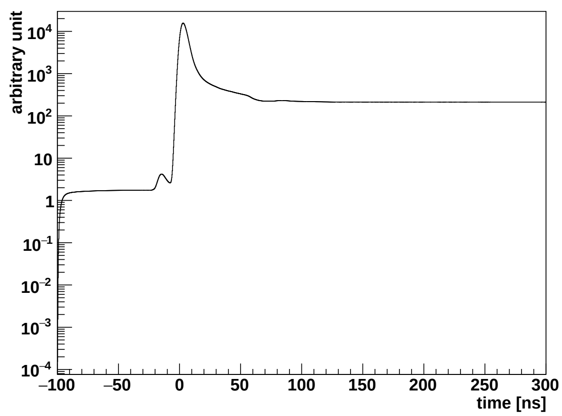

Figure 4.24: The timing PDF for the wbWLS.

To reconstruct the direction, besides the angular distribution of Cherenkov photons, $\cos\theta_{Ch}$, we also consider the fraction of the re-emitted and wavelength shifted photons that cause a flat angular distribution.

To test the performance of the `MP WLS Fitter`, 5 MeV e^- were simulated at the center of the AV filled with wbWLS and traveling along +x direction. As a comparison, the same simulation was done for the AV filled with pure water and the simulated events were reconstructed by the water fitter.

Fig. 4.3 shows the performance of the WLS fitter reconstructed positions of the MC simulations compared to the pure water case. For the fit position distribution of 5-MeV e^- in the wbWLS, we get a root mean square (RMS) of 201 mm and a bias to the center (the mean of histogram) of 29 mm. Compared to the pure water case, the fit bias is about 19 mm better and the RMS is 188 mm better.

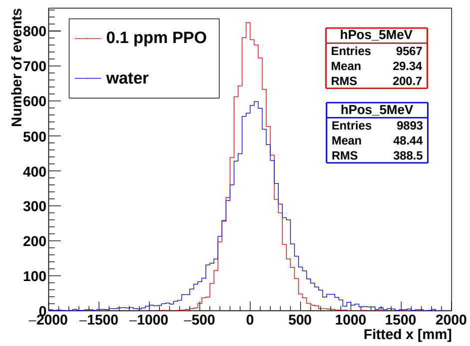

Figure 4.25: Fitted x position. The `MP WLS fitter` reconstructed x positions of the 5-MeV e^- events in the wbWLS (red) are compared to the ones in the water (blue).

Similar to Sect. 4.2.8, $\cos\theta_a$ in Eqn. 4.10 is used to quantify the performances in direction reconstruction. Table. 4.3 shows the results of $\cos\theta_a$ for SNO heavy water data[138] and simulations for SNO+ pure water and wbWLS. It shows that the SNO+ pure water gives the best direction reconstruction, while the wbWLS is about 30% off in $\cos\theta_{0.9}$ compared to the SNO+ pure water.

Table 4.3: A comparison of quantitative estimates for the angular resolution for the SNO heavy water, SNO+ wbWLS and the SNO+ pure water cases.

medium	$\cos\theta_{0.9}$	$\cos\theta_{0.8}$	$\cos\theta_{0.5}$
SNO heavy water	0.50	0.71	0.92
SNO+ water	0.62	0.78	0.98
wbWLS	0.37	0.63	0.90

Comparing a pure water SNO+ detector and the wbWLS one, using the `MP WLS fitter` for physics events gives a better position resolution without a significant loss in the performance of the direction reconstruction. This `MP WLS fitter` was also applied in a study of the potential for measuring the reactor antineutrinos in the wbWLS-filled SNO+ detector, see Ref. [148] for details.

4.4 Vertex Reconstruction for the Partial-fill

The following two sections discuss about the vertex reconstruction relating to the liquid scintillator. The vertex reconstructions for the partial-fill and scintillator phases are very similar. Both of them tackle with two detection media: the water and the scintillator, and calculate the light paths in these two regions. I will first describe the calculations in the partial-fill case, since its geometry is more complicated while the full scintillator case can be considered as a simplified version.

4.4.1 Partial-fill

In the partial-fill geometry, the SNO+ detector can be described as a composition of three parts: the neck cylinder filled with the scintillator; the AV sphere, which is split by a water-scintillator interface (plane) inside, and above this plane is the scintillator and below is the water; and the PSUP sphere outside the neck and the AV, filled with the water.

Omitting the acrylic and other detector materials, photons mainly pass through two different media: the water and the scintillator. As shown in Fig. 4.26, assuming a straight light path from a vertex to a hit PMT position, its total length is $|\vec{l_p}| = |\vec{X}_{\mathrm{PMT}} - \vec{X}_0|$. The `MP scint-water fitter fitter` evaluates the length of the $|\vec{l_p}|$ in the scintillator: d_{sp} and then the length in the water is $|\vec{l_p}| - d_{sp}$. Since photons travel at different speeds in these two media: $v_{gr,scint}$ and $v_{gr,water}$, the `MP scint-water fitter fitter` evaluates the time of flight, $t_{transit}$ by:

$$t_{transit} = \frac{|\vec{l_p}| - d_{sp}}{v_{gr,water}} + \frac{d_{sp}}{v_{gr,scint}}, \tag{4.11}$$

and thus the time residual, t_{res} is calculated. Once the t_{res} is obtained, the following fitting procedure is the same to the `MP water fitter`.

Therefore, the crucial part here is to calculate the d_{sp}. The light path $\vec{l_p}$ is considered as a ray with a direction (rather than a line without direction). The ray intersects with three geometry objects: the neck cylinder, the AV sphere and the water-scintillator interface plane. As illustrated in Fig. 4.26, a detailed calculation of d_{sp} includes the evaluations of (1) $\vec{l_p}$ and neck (ray-cylinder) intersection; (2) $\vec{l_p}$ and the AV (ray-sphere) intersection and (3)

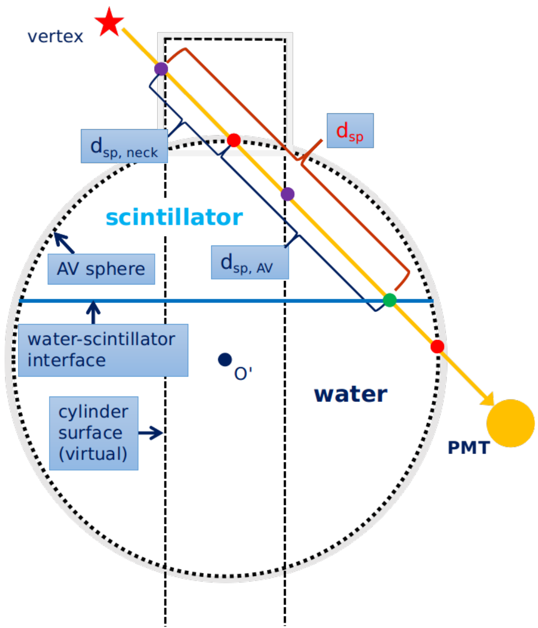

Figure 4.26: Light path calculation for the `MP scint-water fitter fitter`. In the figure, a light path intersects with the neck cylinder surface, the AV sphere as well as the water-scintillator interface. The total length of the path in the scintillator region (scintillator path, d_{sp}) includes the paths in the neck ($d_{sp,neck}$) and in the AV ($d_{sp,AV}$). Calculations of the ray-cylinder, ray-plane and ray-sphere intersections are applied.

$\vec{l}_p$ and the water-scintillator interface (ray-plane) intersection. The d_{sp} is further separated into the path lengths in the neck ($d_{sp,neck}$) and in the AV ($d_{sp,AV}$).

For a trial position $\vec{X}_0 = (x_0, y_0, z_0)$ and a hit PMT position $\vec{X}_{\text{pmt}} = (x_{\text{pmt}}, y_{\text{pmt}}, z_{\text{pmt}})$, define the ray vector as $\vec{l}_0 \equiv \vec{X}_0 + a \cdot \vec{u}$, where a is the distance between vertex and intersection point and it is the parameter to be determined; $\vec{u} = \frac{\vec{X}_{\text{pmt}} - \vec{X}_0}{|\vec{X}_{\text{pmt}} - \vec{X}_0|}$ is the direction of the ray vector. It is a unit vector pointing from the $\vec{X}_0$ to the $\vec{X}_{\text{pmt}}$. The following goes through the three intersection cases:

- Ray-sphere intersection

  In the ray-sphere intersection case (ray vector passes through the AV sphere), the intersection points on the $\vec{l}_0$ satisfy the sphere equation $(\vec{X} - \vec{O}_{av})^2 = r_{AV}^2$, where $\vec{O}_{AV}$ is the origin of the AV sphere and $\vec{O}_{AV} = (0, 0, 108)$ mm in the PSUP coordinate; $r_{av} = 6005$ mm. Thus the intersection equation is: $(\vec{l}_0 - \vec{O}_{av})^2 = r_{AV}^2$.

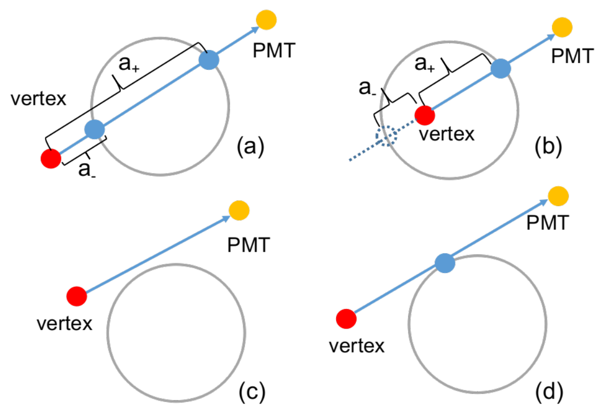

Figure 4.27: Line-sphere intersections. (a) the ray vector intersects the sphere with 2 points; (b) the ray vector intersects the sphere with 1 point; (c) and (d): the ray vector never passes through the sphere.

Let $\Delta \equiv [(\vec{X}_0 - \vec{O}_{av}) \cdot \vec{u}]^2 - (\vec{X}_0 - \vec{O}_{av})^2 + r_{av}^2$, if $\Delta > 0$, solve the equation and get:

$$a_{\pm} = -(\vec{X}_0 - \vec{O}_{av}) \cdot \vec{u} \pm \sqrt{\Delta},\ if\ \Delta > 0. \tag{4.12}$$

In this case, both a_+ and a_- exist and their values are different. If $a_+ > a_- > 0$, the length of the path inside the sphere is $a_+ - a_-$, as illustrated in Fig. 4.27 (a). Due to this geometry, the event position should be outside the AV, the condition $|\vec{X}_0| \geq r_{AV}$ is automatically met. If $a_+ > 0 > a_-$, a_- determines the intersection point along the opposite direction of the ray vector. Thus the ray vector actually does not pass that point (different to the line intersection with no direction). Thus the length of the path inside the sphere is a_+, as illustrated in Fig. 4.27 (b). Also, the condition $|\vec{X}_0| < r_{AV}$ is automatically met.

If $\Delta \leq 0$, there is no intersection point or only one intersection point (when $\Delta = 0$) at the AV, the ray vector never passes through the AV sphere, as illustrated in Fig. 4.27 (c) and (d).

- Ray-plane intersection

For the ray-plane intersection, the z components of the intersection points on $\vec{l}_0$ satisfy the plane equation $z = Z_{split}$, where Z_{split} is the water level, i.e., the z position of the water-scintillator intersection. Thus the intersection equation is: $l_{0,z} = Z_{split}$, where $l_{0,z} = z_0 + a \cdot u_z$.

If $u_z = z_{\mathrm{pmt}} - z_0 = 0$, the ray is parallel to the plane and never intersects the plane.

If $u_z \neq 0$, solve the equation, we have: $a = (Z_{split} - z_0)/u_z = (Z_{split} - z_0)$. Let:

$$a_3 \equiv a = \frac{(Z_{split} - z_0)|\vec{X}_{\mathrm{pmt}} - \vec{X}_0|}{z_{\mathrm{pmt}} - z_0} \quad (if\ z_{\mathrm{pmt}} - z_0 \neq 0), \tag{4.13}$$

Similar to the case of ray-sphere intersection, if $a_3 < 0$, the ray-plane intersection point is on the extended line along the opposite direction to the ray; $a_3 \geq 0$ ensures the ray hits the interface. Note that here we consider the plane is infinitely large. Later we will combine with the calculations of the other geometries to cut it off.

- Ray-cylinder intersection

For the ray-cylinder intersection, the x and y components of the intersection points on the $\vec{l_0}$ satisfy the intersection equation: $l_{0,x}^2 + l_{0,y}^2 = r_{neck}^2$, where r_{neck} is the radius of the neck cylinder ($r_{neck} = 785\ mm$).

To solve the equation, let: $\Delta' \equiv [x_0 \cdot (x_{PMT} - x_0) + y_0 \cdot (y_{PMT} - y_0)]^2 - (x_0^2 + y_0^2 - r_{neck}^2) \cdot [(x_{PMT} - x_0)^2 + (y_{PMT} - y_0)^2]$, and then we get:

$$a'_{\pm} = |\vec{X}_{PMT} - \vec{X}_0| \cdot \frac{-[x_0 \cdot (x_{PMT} - x_0) + y_0 \cdot (y_{PMT} - y_0)] \pm \sqrt{\Delta}'}{(x_{PMT} - x_0)^2 + (y_{PMT} - y_0)^2},\ if\ \Delta' > 0, \tag{4.14}$$

Similar to the ray-sphere case, if $a'_+ > a'_- > 0$, the length of the path inside the cylinder is $a'_+ - a'_-$. Due to this geometry, the event position should be outside the cylinder, the condition $(x_0^2 + y_0^2) \geq r_{neck}$ is automatically met. If $a'_+ > 0 > a'_-$, the event position should be inside the cylinder and the ray-vector intersects the cylinder with one point (while the other point is along the opposite direction). Thus the length of the path inside the cylinder is a'_+. If $\Delta' \leq 0$, the ray vector never passes through the neck cylinder. Also note that here we consider the cylinder is infinitely long. This will also be cut off by the combined calculations of the other geometries. In addition, since only the neck region inside the PSUP is valid for the fitter, we should also ensure $z < 8390$ mm (in the PSUP coordination).

To evaluate the length of the $|\vec{l_p}|$ in the scintillator region (d_{sp}), the above three geometries needs to be combined carefully. The following two procedures go through all the possible situations. First combine the evaluations of the ray-sphere and the ray-plane intersections to calculate the light path in the AV scintillator region ($d_{sp,AV}$). Then combine the evaluations of the ray-sphere and the ray-cylinder intersections to calculate the light path in the neck scintillator region ($d_{sp,neck}$). Detailed algorithms are shown in Appendix. A.6.

Since the valid fit requires the events inside the PSUP sphere, only the neck region inside the PSUP sphere (with $6108 < z_{neck} < 8390$ mm) needs to be considered. The neck path calculation is also allowed to be turned off, while a worse fit result is expected. Detailed calculations are shown in Appendix. A.6.

If $d_{sp} = 0$, the light path is always in the water. In this case, the fitter is the same to the `MP water fitter`. It fits the vertex with the `MP water fitter` PDF. Once the light path passes through the scintillator region, the fitter fits with a scintillator timing PDF, in which the PMT time response was modified to photon propagation time in scintillator, as shown in Fig. 4.28.

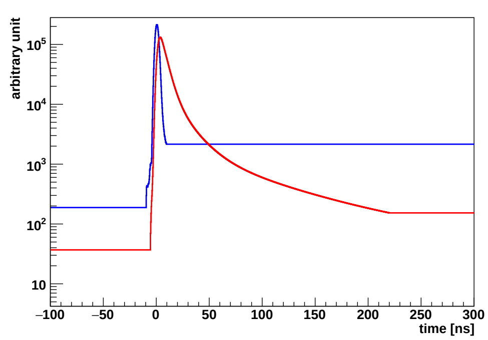

Figure 4.28: Timing PDFs used by the `MP scint-water fitter fitter`. Blue: the timing PDF used by the `MPW fitter`; red: the scintillator timing PDF.

The next section will discuss the timing PDFs used by the fitter.

4.4.2 Making Timing PDFs

4.4.2.1 Different PPO Concentrations during the Filling

During the partial-fill phase, the water level and the concentration of the PPO were changing. The PPO was gradually added into and mixed with the LAB, and for the relative stable partial-fill stages which were used for taking and analyzing data, the PPO concentrations dissolved in the LAB were 0.25 g/L (earlier stage from 2019 to 2020) or 0.5 g/L (later stage from 2020 to 2021). The planned concentration of the PPO in the scintillator phase is 2 g/L.

An understanding of the characteristic photon emission response is crucial for building the timing PDF for the reconstruction. The Oxford group from the SNO+ collaboration did several bench-top measurements to obtain the time constants and relative light yields of the LAB sample dissolved with the following PPO concentrations: 0.25, 0.5, 1.0, 2.0 and 6.0 g/L[149, 7].

The emission time profile model used by the Oxford group is[7]:

$$f_{optics}(t) = \sum_{i=1}^{3}(A_i \frac{e^{-\frac{t}{\tau_i}} - e^{-\frac{t}{\tau_{rise}}}}{\tau_i - \tau_{rise}}) + A' \frac{e^{-\frac{t}{\tau_{rise}}}}{\tau_{rise}}, \tag{4.15}$$

where A_i is the fraction of scintillation light emitted in the i^{th} component, τ_i is the decay constant in the i^{th} component, τ_{rise} is the rise time of scintillator.

The measured parameters are listed in Table. 4.4.2.1 and Table. 4.4.2.1.

Table 4.4: Time constants and amplitudes measured by Ref. [7]. Here the relative light yield is with respect to the LAB+2 g/L PPO case (11900 photons/MeV).

PPO [g/L]	τ_{rise} [ns]	τ_1 [ns]	τ_2 [ns]	τ_3 [ns]	A_1 [%]	A_2 [%]	A_3 [%]	A' [%]
0.25	1.25	8.1	25.0	68.2	29.2	53.1	13.9	3.8
0.5	1.12	7.2	18.7	49.1	43.5	40.4	12.6	3.5
1.0	1.18	5.5	13.3	40.9	45.6	37.5	13.3	3.6
2.0	1.06	4.2	11.7	48.9	57.9	27.8	8.9	5.4
6.0	0.94	2.5	9.3	46.0	63.7	17.0	8.6	10.7

These Oxford-measured time profiles were convolved with the PMT time response profile mentioned in Sect. 4.2.1, Fig. 4.2, to make the timing PDF for the partial-fill vertex

Table 4.5: Relative light yield (RLY) measured by Ref. [7].

PPO [g/L]	RLY
0.25	0.57
0.5	0.65
1.0	0.9
2.0	1.0
6.0	0.93

reconstruction.

$$f(t)_{PDF} = f_{optics}(t) \otimes f_{PMT\ response}(t - t'), \tag{4.16}$$

I wrote a python tool to create the timing PDFs to re-coordinate the partial fitter for the different PPO concentration cases[150], as shown in Fig. 4.29[3] .

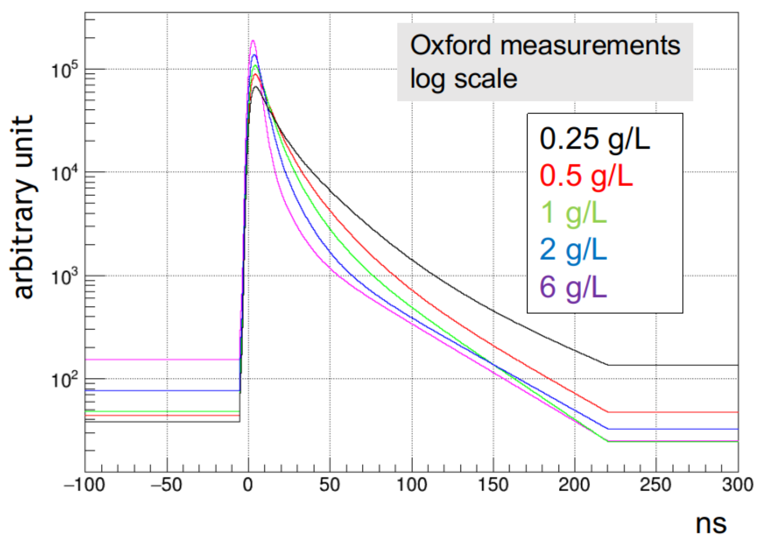

Figure 4.29: Timing PDFs built for various PPO concentrations based on the Oxford bench-top measurements.

Following the same method of tuning the $v_{gr,eff}$ in Sect. 4.2.3, the effective group velocity in the scintillator ($v_{gr,scint}$) is obtained based on the simulations of 500 3-MeV e^- generated uniformly and with isotropic directions in the full scintillator geometry. The `MP scint fitter`, which will be discussed in Sect. 4.5, was used to reconstruct the same simulation

[3] For other potential phases, the PDF can also be built by using the timing spectrum described in Sect. 3.3.4.1.

data with different values of v_{gr}. Once the $v_{gr,scint}$ was obtained, it was fixed in the `MP scint-water fitter fitter`. Then the $v_{gr,water}$ was tuned by simulating 500 3-MeV e^- in the water region of the partial-fill geometry with the water level set at z = 3000 mm in the AV coordination. Fig. 4.30 shows the $v_{gr,scint}$ (a) and the $v_{gr,water}$ (b) obtained from the linear interpolation in the LAB+0.5 g/L PPO scintillator case. Table. 4.6 lists the effective group velocities and n_{eff} values for the liquid scintillator with different PPO concentrations.

Figure 4.30: Tuning the effective group velocities in the scintillator (a) and water (b).

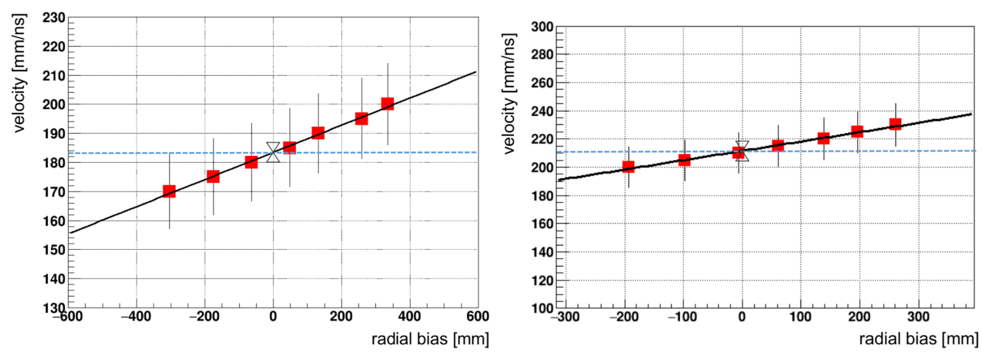

(a) Tuning the $v_{gr,scint}$. (b) Tuning the $v_{gr,water}$.

Table 4.6: Tuned effective group velocities for different PPO concentrations.

PPO [g/L]	$V_{gr,scint}$ [mm/ns]	$n_{eff,scint}$	$V_{gr,water}$ [mm/ns]	$n_{eff,water}$
0.25	184.068±5.153	1.629	211.871±5.731	1.415
0.5	183.467±5.159	1.634	211.587±-5.773	1.417
1.0	182.93±5.193	1.639	211.393±5.805	1.418
2.0	183.045±5.184	1.638	211.629±5.767	1.417
6.0	184.218±5.135	1.627	211.173±5.843	1.420

4.4.3 Partial Fitter Performances

The performance of the `MP scint-water fitter fitter` was studied with MC simulations. During the partial-fill phase, the filling and mixing of the liquid scintillator was stable at several water levels for data taking and data analysis. A typical water level is at 3 m in the AV coordination and a typical PPO concentration is 0.5 g/L. With these two settings in the partial-fill geometry, 5000 3-MeV e^- were simulated inside the scintillator region and the water region respectively to test the partial fitter performances.

The average fit speed of the vertex reconstruction of the events in the scintillator region is 0.2 second/event, which is acceptable for the data processing during the partial-fill phase. For the events in the water region, the average fit speed is 0.05 s/event, which is similar to the `MPW fitter`. Fig. 4.31 and Fig. 4.33 show the results of the `MP scint-water fitter fitter` reconstructed positions in the scintillator and water regions respectively. The subfigures (a) are the reconstructed positions projected on $\rho = \sqrt{x^2+y^2}$ and z while the subfigures (b), (c) and (d) are the position biases between the reconstruction and MC, projected on x, y and z axes respectively. The distributions of the position biases were fitted with Gaussian functions and the values of the Gaussian mean ($\mu_{x,y,z}$) and sigma ($\sigma_{x,y,z}$) are used to quantify the fit biases and resolutions.

For the events in the scintillator region, it shows that the resolutions $\sigma_{x,y,z}$ reach about 150 mm, and the biases in x and y axes: $\mu_{x,y}$ are within 1.5 mm while the μ_z is about -29 mm. The larger bias in z is mostly caused by the events mis-reconstruct in the water region. The main reason for the mis-reconstruction is caused by the fitter omitting the calculations relating to the reflection and refraction light paths happen in the water-scintillator interface or boundaries, as mentioned before. Since the refraction index of the liquid scintillator is larger than the water, there are some chances that the light is reflected off the water-scintillator interface. The additional reflection light path will cause the event with a longer $t_{transit}$, but the event is still created in the scintillator region. While the fitter doesnot tackle with the reflection light path, it will pull the event into the water region a little far away from the actual position to get the longer $t_{transit}$, which causes the event to be mis-reconstruct in the water region. This explains the mis-reconstruct events with $z_{fit}-z_{MC} < 0$ in Fig. 4.31 (d). A discussion for improving the fitter will be shown in Sect.4.4.5. Some of these mis-reconstruct events can be removed by applying the $posFoM$ cut.

Fig. 4.32 (a) shows the $z_{fit}-z_{MC}$ against the $posFoM$ quantity $scaleLogL$ mentioned in Sect. 4.2.6. It shows that applying a $scaleLogL > 9.8$ cut can remove more than 1/3 of the

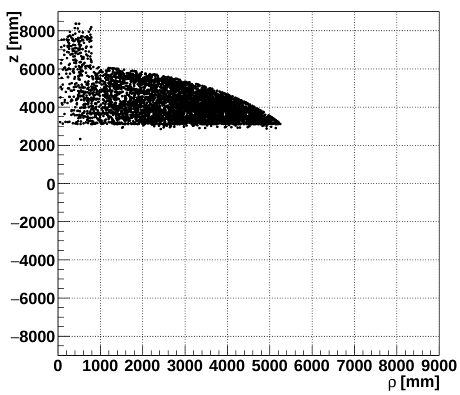

(a) $\rho = \sqrt{x_{fit}^2 + y_{fit}^2}$ vs. z_{fit}.

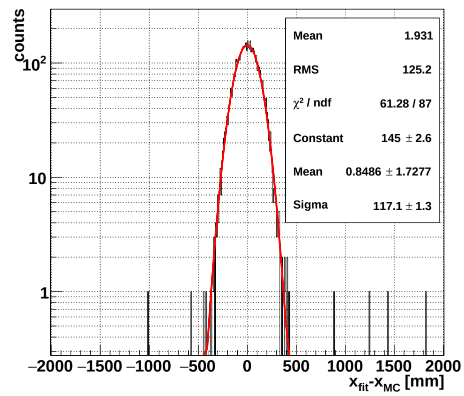

(b) $x_{fit} - x_{mc}$.

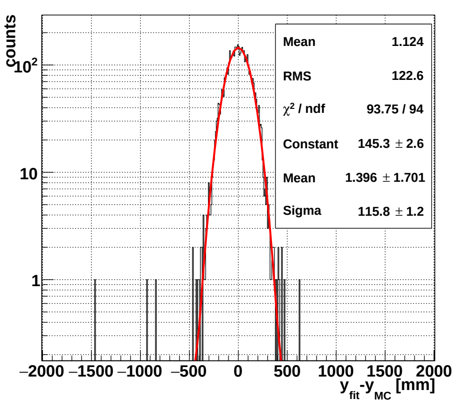

(c) $y_{fit} - y_{mc}$.

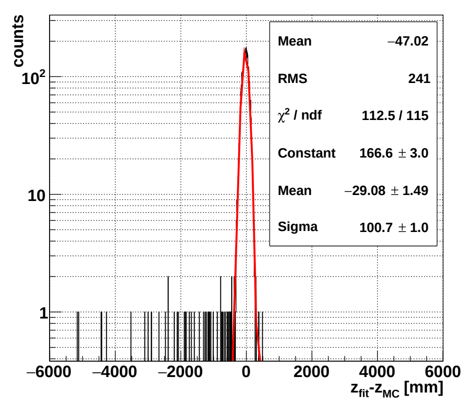

(d) $z_{fit} - z_{mc}$.

Figure 4.31: Reconstructed positions and fit biases of the 3-MeV e^- events in the scintillator region.

mis-reconstructed events with $|\vec{X}_{fit} - \vec{X}_{MC}| > 1000$ mm. In Fig. 4.32 (b), the fit position bias in z ($z_{fit} - z_{MC}$) after the cut is plotted in red, overlaid with the distribution before the cut in black. By fitting with the Gaussian function, it shows that the cut removes a few mis-reconstruct events in the tail of the distribution, and then improves the resolution by about 1.5 mm and reduces the bias in z by about 1.9 mm, compared to the plot in Fig. 4.31 (d). As shown in Fig. 4.32 (c), this cut removes most of the outliers observed in the ρ vs z plot in Fig. 4.31 (a).

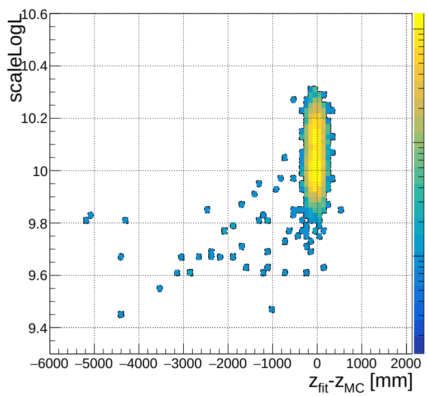

(a) $z_{fit} - z_{MC}$ vs. $scaleLogL$.

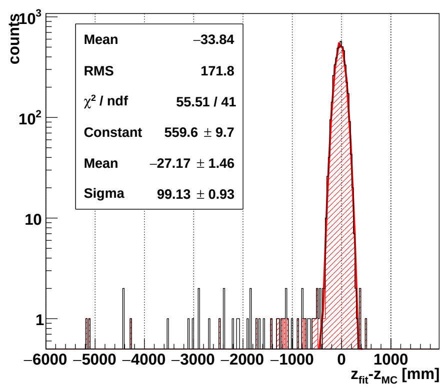

(b) $z_{fit} - z_{mc}$, before (black) and after (red) the $scaleLogL > 9.8$ cut.

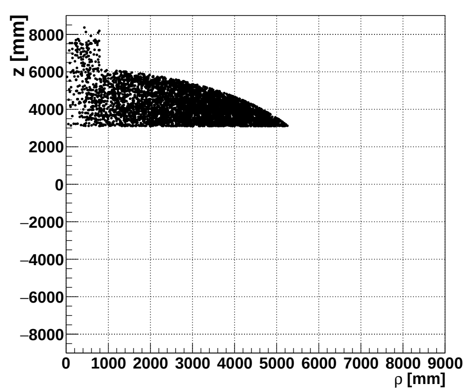

(c) ρ_{fit} vs. z_{fit}, with $scaleLogL > 9.8$.

Figure 4.32: Effects of the $scaleLogL$ cut on the reconstructed positions and fit biases.

For the events in the water region, the fit position biases in x and y ($\mu_{x,y}$) are comparable to the results of the `MPW fitter` shown in Sect. 4.2.7, while the μ_z is about 50 mm worse and the resolutions $\sigma_{x,y,z}$ are about 100 mm worse. This is due to the same effects from the water-scintillator interface and boundaries mentioned previously. These boundary effects are more obvious and worse compared to the scintillator region, as shown in the ρ vs. z plot in Fig. 4.33 (a). This is due to the lower NHits in the water, or less information of triggered PMTs is provided for the fitter. However, the relatively worse reconstruction performance for the water events is insignificant for the partial-fill analysis, since the analysis is focused on studying the liquid scintillator, the events in the water region are less interested and they are mostly removed by the NHits cut (NHits$>$ 40 was applied on the data processing during the partial-fill) and fiducial volume cut in the analyses.

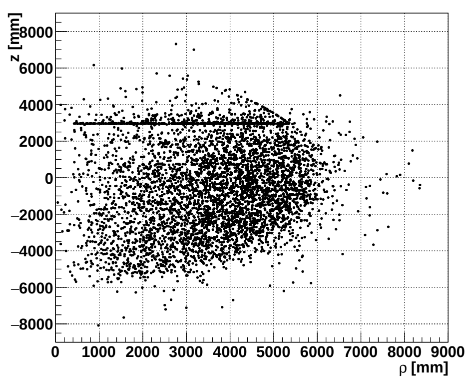

(a) $\rho = \sqrt{x_{fit}^2 + y_{fit}^2}$ vs. z_{fit}.

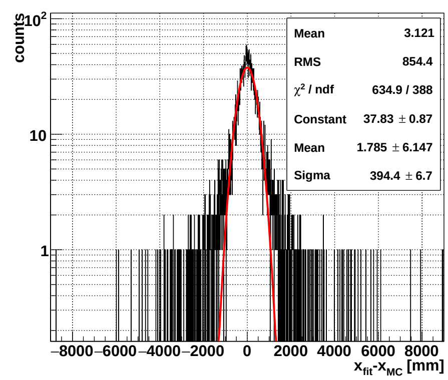

(b) $x_{fit} - x_{mc}$.

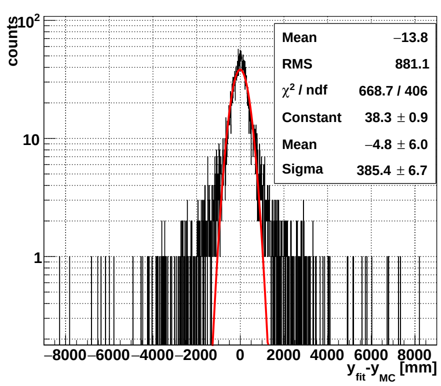

(c) $y_{fit} - y_{mc}$.

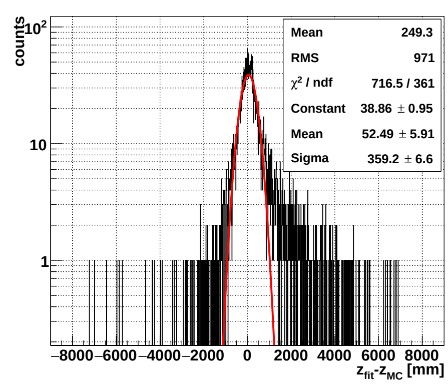

(d) $z_{fit} - z_{mc}$.

Figure 4.33: Reconstructed positions and fit biases of the 3-MeV e^- events in the water region.

4.4.3.1 Test on Different PPO Concentrations

To study the effects of different PPO concentrations, in the partial-fill geometry, the water level was set at 3 m, and the PPO concentrations were set to 0.25, 0.5, 1, 2, and 6 g/L respectively. Simulations of 5000 3-MeV e^- were generated in the scintillator region with uniformly distributed positions and isotropic directions. The `MP scint-water fitter fitter` uses the effective velocities and PDFs re-coordinated to the simulation geometries with corresponding PPO concentrations. The distributions of the position biases between the reconstruction and MC in x, y, and z axes were fitted with Gaussians to obtain the fit position biases ($\mu_{x,y,z}$) and resolutions ($\sigma_{x,y,z}$).

Fig. 4.34 and Fig. 4.35 show the $\mu_{x,y,z}$ and $\sigma_{x,y,z}$ against PPO concentrations. It shows that the values of $\mu_{x,y,z}$ are stable in the [-15,15] mm region, while the values of $\sigma_{x,y,z}$ decrease from about 150 mm to about 60 mm as the concentration increases. The light yield of the liquid scintillator goes up as the PPO concentration increases, which gives larger NHits and more PMT information for the fitter. However, the differences between the 2 g/L and 6 g/L cases are small, which indicates a saturation effect for the PPO concentration above 2 g/L.

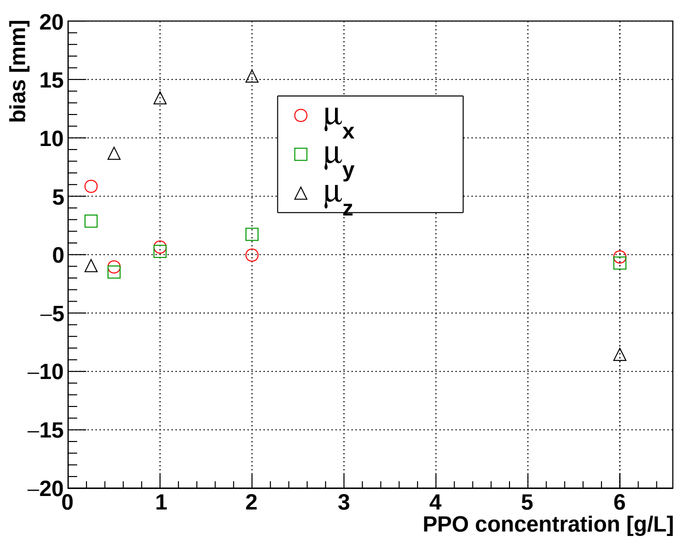

Figure 4.34: Fit position biases against the PPO concentrations.

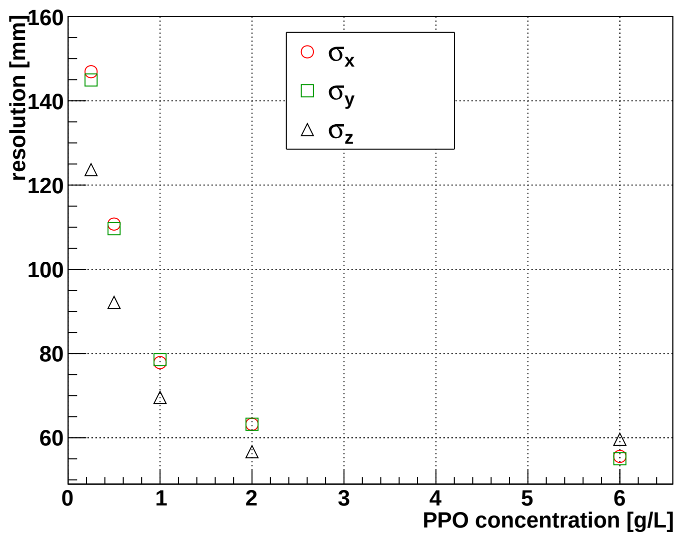

Figure 4.35: Fit position resolutions against the PPO concentrations.

If using a timing PDF with the wrong PPO concentration for the reconstruction, the effect on reconstruction is small[151]. I simulated 3-MeV e^- uniformly distributed in the LAB+0.25 g/L PPO scintillator with isotropic directions, and then reconstructed the events by using the timing PDF of 0.5, 1 and 2 g/L PPO (higher concentrations) respectively. All of these reconstructions give the fitted positions closed to the correct reconstruction using the 0.25 g/L timing PDF, with fit biases about 5 mm in the three axes. On the other hand, I did the same simulations in the LAB+2 g/L PPO and then reconstructed by using the timing PDFs of 0.25, 0.5 and 1 g/L PPO (lower concentrations) respectively. The fit biases are also about 5 mm. It shows that the `MP scint-water fitter` is invulnerable to the changes caused by different PPO concentrations. Therefore, if the actual PPO concentration in the detector is slightly different to the nominal value, the effect on the reconstruction is not significant.

4.4.4 Test on Bi-Po Simulations

Thorium-232 (^{232}Th) and Uranium-238 (^{238}U) are the two major internal backgrounds in the liquid scintillator. The amounts of these two backgrounds can be evaluated by a technique called “Bi-Po analysis”, which refers to tag the ^{212}Bi-^{212}Po event pairs from the ^{232}Th decay chain and to the ^{214}Bi-^{214}Po event pairs from the ^{238}U decay chain. This analysis is one of the crucial physics studies during the partial-fill phase. Here I tested the `MP scint-water fitter fitter` on the simulations of ^{214}Bi-^{214}Po in the detector with the LAB+0.5 g/L PPO and water level at 4.5 m. In the ^{238}U decay chain, ^{214}Bi goes through β^- decay, which can trigger a prompt event[118]; its daughter ^{214}Po, with a half-life of 164.3 μs, goes through α decay, and it can trigger a delayed event. Applying proper cuts of the position and time differences between the prompt and delayed events can tag these $\beta-\alpha$ event pairs from the ^{214}Bi-^{214}Po and then evaluate the ^{238}U level. The optimized algorithm was developed by the collaboration[109], and a flowchart for picking up the event pairs is shown in Fig. C.1 in Appendix. C.1. The tagging algorithm was applied to the reconstructed event vertices. Fig. 4.36 shows the distributions of NHits for the tagged ^{214}Po and ^{214}Bi events. A clear single peak shows the α events from the ^{214}Po, and a continuous spectrum shows the e^- events from the ^{214}Bi. Fig. 4.37 shows the biases between the MC and the reconstructed positions, projected in the z-axis. The biases in the three axes were fitted with Gaussian to obtain the biases and resolutions, which are listed in Table. 4.7. These results indicate that the fitter performance is acceptable for the Bi-Po analysis in the partial-fill.

Table 4.7: Fit position biases and resolutions for the ^{214}Bi-^{214}Po tagging.

Tagged isotope	$\mu_x \pm \sigma_x$	$\mu_y \pm \sigma_y$	$\mu_z \pm \sigma_z$
^{214}Bi	-7.657±127.2	-2.071± 129.6	2.041±114.5
^{214}Po	-0.695± 128.5	-0.1355±129.3	-22.21±103.0

4.4.5 Discussions for the Partial Fitter

Suggested by the SNO+ collaboration, I attempted to use the `MP scint-water fitter fitter` to fit the water level[152]. In this case, the water level (Z_{water}) is considered as a fit parameter and the `MP fitter` fits for 5 parameters: (x, y, z, t, Z_{water}). The bias between the true Z_{water} and the reconstructed one is fitted with a Gaussian, which gives a bias of 40 mm and a resolution of 492 mm. The fit resolution is much larger than the event position

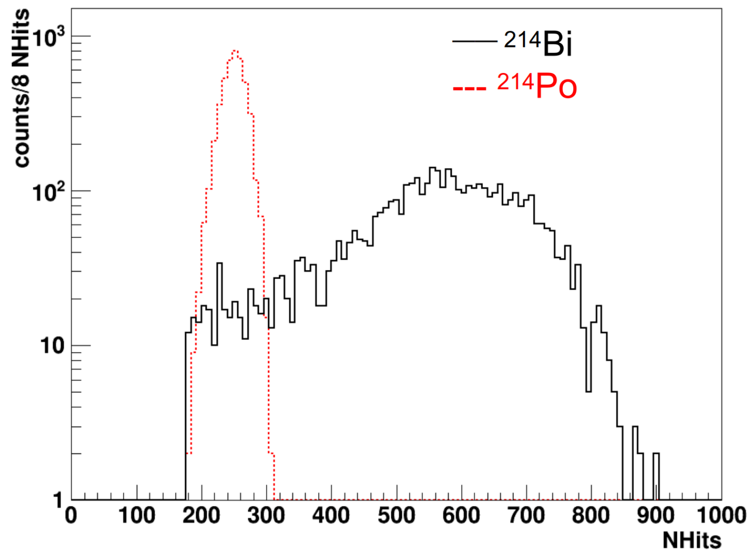

Figure 4.36: Distributions of NHits for the tagged ^{214}Po (dashed red line) and ^{214}Bi (solid black line) events.

resolution, so this method is not good enough to be applied on the analysis.

The reconstructed vertices of certain events, such as the ^{214}Bi^{214}Po event pairs, can be used to calculate the time residual distribution, which is taken as the time profile caused by the e^- or α particles in the liquid scintillator. By extracting the time constants from the time profile, the quality and optical properties of the liquid scintillator can be obtained. This analysis has been applied by the collaboration on the partial-fill data[153, 154].

To process the partial-fill data, the water level set in the `MP scint-water fitter fitter` is intentionally moved down by 150 mm (a few centimeter larger than the resolution at 3-MeV) from the nominal water level. This is to include some events mis-reconstructed in the water region, and then to include more events for a conservative background estimation for the liquid scintillator.

To improve the performance of the `MP scint-water fitter fitter`, two points have been suggested by the collaboration. These implements are not applied and tested in this thesis, but they are worthwhile to be checked in the future:

- The timing PDFs used by the `MP scint-water fitter fitter` is obtained from the bench-top measurement and is always calculated numerically. However, the PDFs

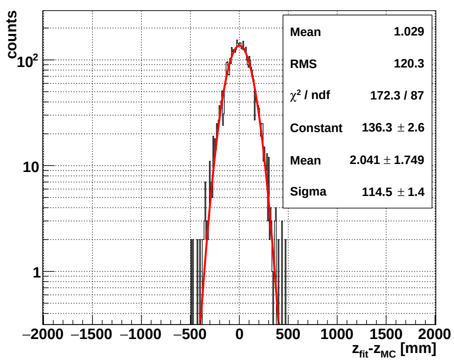

(a) $z_{fit} - z_{MC}$ for tagged ^{214}Bi.

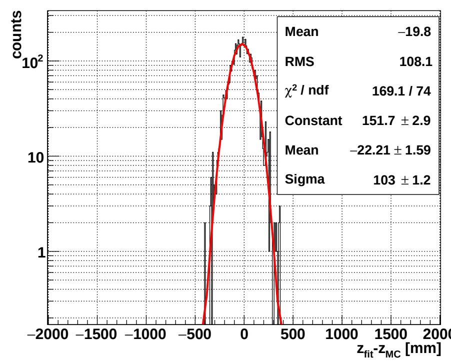

(b) $z_{fit} - z_{MC}$ for tagged ^{214}Po.

Figure 4.37: Fit position biases for tagged ^{214}Bi (left) and ^{214}Po (right).

can be expanded and fitted with Chebyshev polynomials to obtain an analytic approximation function to describe the PDF[141]. Then the analytical function can give proper and smooth analytical derivatives, which may reduce the time cost of calculating the likelihoods using the numerical methods.

- To implement the refraction and reflection calculations. To simplify the calculations, the `MP scint-water fitter fitter` assumes straight light paths from the event position to the hit PMTs and neglects all the possibilities of the refraction and reflection light paths. It is more realistic to count for these light paths since the interface between the two different optical media: the water and the liquid scintillator can cause the reflection and refraction. The Fresnel equations can be used for calculating the possibilities of these light paths[9], while the calculations are complicated. Also, the 5-cm thick AV was totally omitted. To take this into account, the calculations of the refraction and reflection light paths will become more complicated. A trade-off between the accuracy & precision of the reconstruction and the CPU time complexity may be considered. This implementation can also help for the `MP scint fitter` discussed in the next section.

4.5 Vertex Reconstruction for the Scintillator Phase

As mentioned in the previous section, the vertex reconstruction for the scintillator phase is similar to the partial-fill case, while no water-scintillator interface is considered here since the AV is fully filled with liquid scintillator. Only the ray-sphere and ray-cylinder intersections are calculated and thus the major code of the `MP scint fitter` was modified directly from the `MP scint-water fitter fitter` by removing the ray-plane intersection calculations.

4.5.1 Performance of the Vertex Reconstruction

Since the 2.5-MeV event is the major interested signal in the scintillator and tellurium-loading phases, a few tests were focused on this energy. Simulations of 10000 2.5-MeV e^- events were generated at random positions inside the AV and with isotropic directions. Fig. 4.38 shows the distributions of the position biases between the reconstruction and MC. These distributions were fitted with Gaussians to obtain the mean (μ) and resolution (σ). It shows that the fit position biases are within $[-2, 2]$ mm region and the resolutions are less than 70 mm in x, y and z axes ($\mu_{x,y,z} \in (-2, 2)$ mm and $\sigma_{x,y,z} < 70$ mm).

A radial dependence test was performed, similar to the tests in the Sect. 4.2.7. Simulations of 2.5-MeV e^- were generated in 11 thin shells. Fig. 4.39 and Fig. 4.40 show the biases (μ) and resolutions (σ) as a function of radius respectively.

For other energies (from 1 to 10 MeV), the Gaussian means and resolutions of the fit position biases were shown in Fig. 4.41 and Fig. 4.42. For the 1 MeV e^- event, the $\sigma_{x,y,z}$ are below 85 mm. These resolutions are slightly better than the Borexino spatial resolution of $\sigma_{x,y,z} \sim 110$ mm for the 1 MeV e^- at the detector center[50].

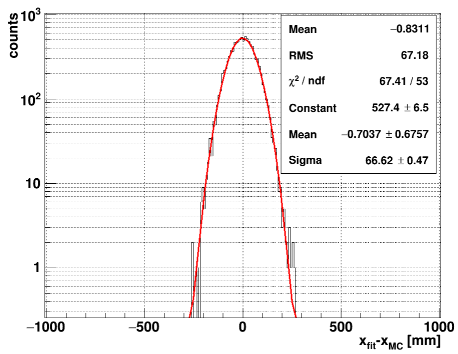

(a) $x_{fit} - x_{mc}$

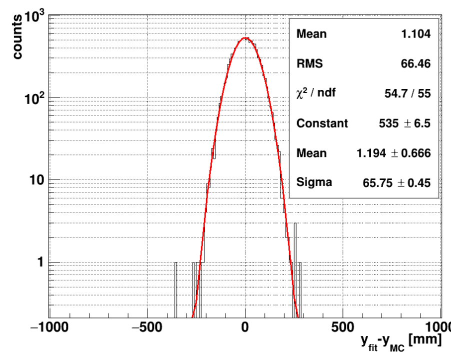

(b) $y_{fit} - y_{mc}$

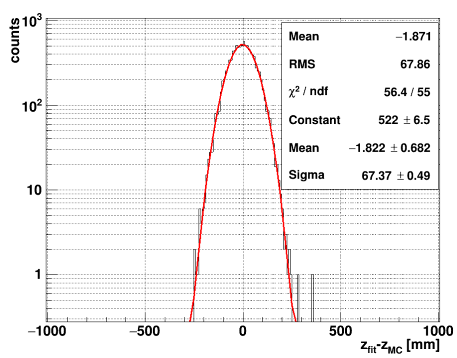

(c) $z_{fit} - z_{mc}$

Figure 4.38: The fit position biases projected on the x, y and z axes, for 2.5-MeV e^- in full scintillator simulations. The distributions were fitted with Gaussian functions.

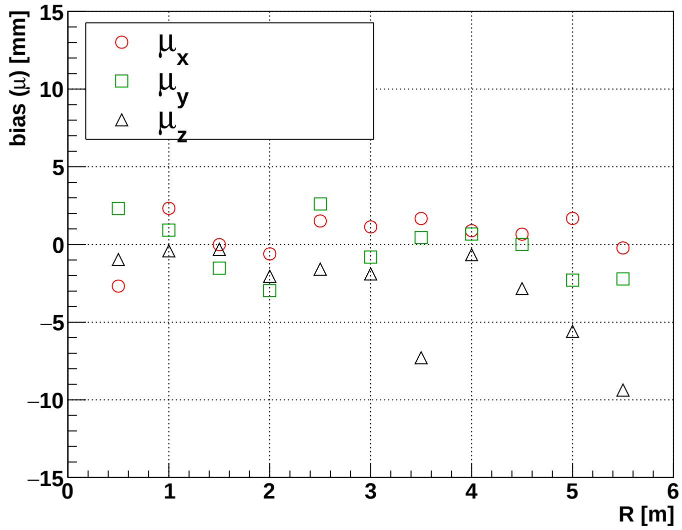

Figure 4.39: The Gaussian biases (μ) of the fit position biases as a function of radius, for the x (red circle), y (green square), and z (black triangle) axes.

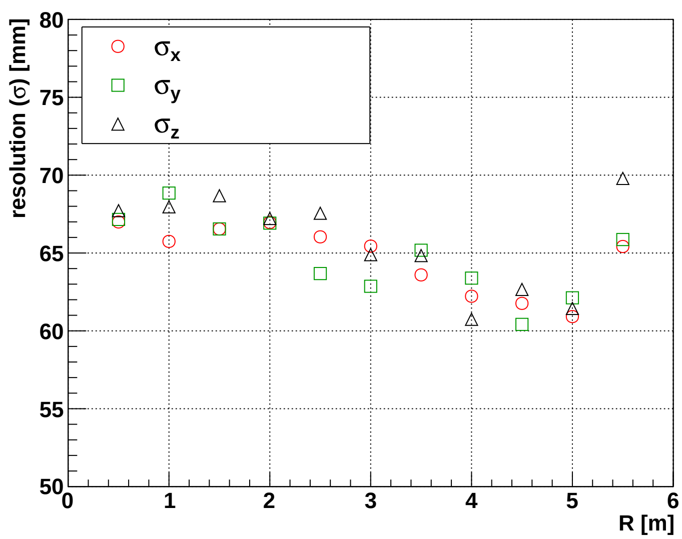

Figure 4.40: The Gaussian resolutions (σ) of the fit position biases as a function of radius, for the x (red circle), y (green square), and z (black triangle) axes.

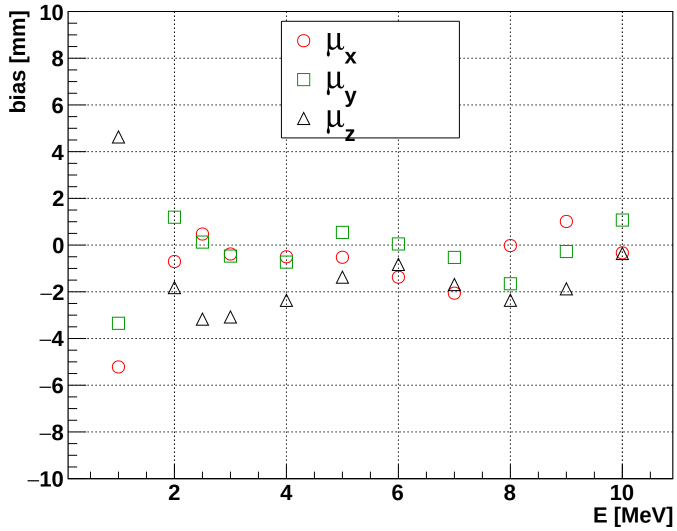

Figure 4.41: The Gaussian resolutions (μ) of the fit position biases as a function of energy, for the x (red circle), y (green square), and z (black triangle) axes.

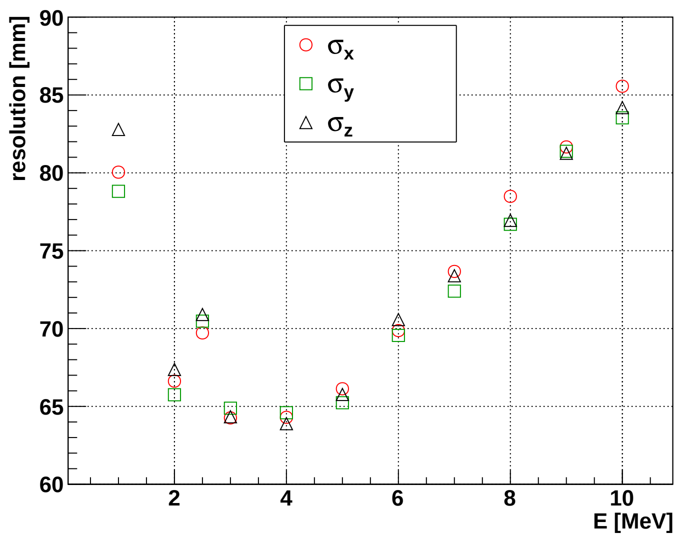

Figure 4.42: The Gaussian resolutions (σ) of the fit position biases as a function of energy, for the x (red circle), y (green square), and z (black triangle) axes.

4.6 Multi-path Fitter Structure for Multiple SNO+ Physics Phases

The `MP fitter` has already been implemented into the `RAT` software for data processing and analyzing. Following the `RAT` event reconstruction structure, the `MP fitter` is feasible to tackle with multiple SNO+ physics phases.

The `MP fitter` first loads the fitter database. The database contains the parameters used by the fitter, including the physics constants (e.g., speed of light), detector geometry parameters (e.g., r_{PSUP}, length of neck, water level), fitter setting parameters (e.g., the effective group velocity, fitter iteration number, etc.) and PDFs. It is included in the `RAT` database (ratdb) in a `JSON` format[155] and contains tables which are tagged by different indices to indicate specific physics phases or detection medium. For example, for the partial-fill phase with a PPO concentration of 0.5 g/L, the fitter extracts the PDFs and fitter setting parameters under the index of "`labppo_0p5_scintillator`". These fitter setting parameters and PDFs were optimized for the 0.5 g/L PPO partial-fill geometry.

Then the `MP fitter` goes through the event-by-event reconstruction. For a triggered event, it calls PMT selectors and sends the information of the selected PMTs to a `Likelihood Calculation Class`. Section 4.2.5 will give the details about the PMT selectors. In the `Likelihood Calculation Class`, there are mainly 4 likelihood calculation functions[4] : the `WaterVertex` and `WaterDirection` for the event vertex and direction reconstruction in the water phase; the `ScintWaterVertex` for the vertex reconstruction in the partial-fill phase; and the `ScintVertex` for the vertex reconstruction in scintillator and tellurium-loading phases.

Reading the detector geometry settings and the assigned index of detection medium, the fitter selects proper likelihood functions to construct the likelihood functions and to calculate the likelihoods and their derivatives by evaluating fit parameters based on different light path calculations in different detector geometries. The calculated likelihoods and derivatives are sent to the MRQ method class to maximize the likelihood and find the best-fit values. The MRQ method class does not care about how the likelihood functions are constructed and how the likelihoods and derivatives are calculated.

A `Dump Likelihood Class` stores the trial fit parameters with respect to their likeli-

[4]The `AirWaterVertex` for the early partial water fill test in 2014 and the `WavelengthShifterVertex` for the conceptual wavelength-shifter test, as mentioned in the previous sections, were not included in the current version of `RAT` since they are not used in actual physics phases.

hoods and derivatives for events interested by designating their event GTIDs in the database. By looking at the likelihood surfaces and derivatives of the event interested, the fit performance of that event can be checked to see whether the fitter finds the global or local maximum. Sect. A.5 shows an example of the dumped likelihood surfaces and derivatives for an ^{16}N event vertex reconstruction.

Once the reconstructed results are obtained, the fitter will send them to the classifiers for further analysis calculations.

4.7 Energy Reconstruction

The SNO+ energy reconstruction algorithms (energy fitters) were based on SNO[138, 156] and has been further developed and optimized[79, 123, 157].

The energy fitters mainly use lookup tables to convert the NHits of a triggered event into reconstructed energy. The energy fitters used in the water phase are mainly the energy response processor (`EnergyRSP fitter`)[138, 156, 123] and the energy Lookup fitter (`EnergyLookup fitter`)[79, 158]. The `EnergyRSP fitter` is used to reconstruct the events inside the AV (internal events). It considers the detailed detector effects, such as the asymmetric geometry of the detector, the optical response of each PMT (including the PMT detection efficiency, transmission probability, attenuation, etc.). It utilizes the reconstructed event positions, directions, and time residuals as inputs to convert the corresponding value of NHits to estimated energy based on simulation models and calibration data. The `EnergyLookup fitter` is simpler and is mainly used to reconstruct the events in the cavity water (external events). It mainly uses the lookup table of the NHits dependence on the event reconstructed position from simulations to calculate the energy of the event[79]. For the scintillator phase, a method using functional form based on simulations was developed by Ref. [158, 159] and is currently used in the `EnergyRThetaFunctional fitter`. All these fitters correct the actual number of online PMTs for a realistic physics run (or called "channel efficiency").

The resolutions and scales of the reconstructed energies in the water phase were derived from the ^{16}N calibration scans at certain detector points, which is shown in Chapter 5.

4.7.1 Energy Figure of Merit

The SNO+ Antineutrino working group developed three figure of merit (FoM) quantities for the energy fitters in the water phase to identify the poor reconstructed results which have significant biases to the truth energy values, especially for the low energy regions around 2.2 MeV, which helps the analysis of neutron capture[160, 161]. The following energy FoMs were applied to the energy reconstruction results during the water phase, which will be discussed in the next chapter. Brief descriptions are presented below, while more details can be found in Ref. [161].

- U-test (U_{test}): a Mann-Whitney quantity uses the channel hit probabilities calculated by the `EneryRSP` which are ordered and ranked. The `EneryRSP` calculates the N as the prompt NHits, and N_{active} as the total number of active channels. For each active channel, the smallest hit probability assigned rank 1 and largest N_{active}. S is a sum of assigned ranks and $S \equiv \sum_i^N \text{rank}_i$.

$$U_{test} \equiv \frac{S - N(N+1)/2}{N(N_{active} - N)}, \tag{4.17}$$

- G-test (G_{test}): a quantity uses the hit probabilities by `EnergyRSP` (E_i), which are normalized to the number of observed hits (N):

$$G_{test} \equiv \frac{1}{N} \sum_{i=1}^{N} \log(\frac{1}{E_i}), \tag{4.18}$$

- Z-factor (Z_{factor}): a quantity uses the medians and median absolute deviations of hit probabilities by `EnergyRSP`:

$$Z' \equiv 1 - \frac{3(\sigma_p + \sigma_n)}{\mu_p - \mu_n}, \tag{4.19}$$

  where μ_p is the median probability of all active PMT channels with hits; μ_n is the median probability of all active PMT channels; σ_p is the median absolute deviation of hit PMT probability distribution; and σ_n is median absolute deviation of PMT probability distribution.

4.7.2 Energy Reconstruction in Partial-fill Phase

Up till this thesis writing, there is no proper energy fitter for the partial-fill phase. I attempted two methods for energy reconstruction in the partial-fill phase: the NHits-scale method, based on Ref. [162] and the NHits-ratio method, based on Ref. [163]. Both of them use look up tables produced by simulations of e^- events in the partial-fill geometry, then compare with the case in the full-fill geometry and scale the energy. Both of these methods need further efforts to produce well-defined results[164, 165].

In the NHits-scale method, for an e^- event at (0,0,z) with a fixed energy (the 1 MeV and 2.5 MeV were tested), a scaling factor between its NHits value in the partial-fill (NHits$_{partial}$) with a water level Z_{water} set in the simulation and the NHits value in the full-fill (NHits$_{full}$) is found by $scale = (\mathrm{NHits_{partial}} - \mathrm{NHits_{full}})/\mathrm{NHits_{full}} = 0.33 \cdot a_0 \cdot (Z_{water} + 6005)^{2.76}$, where the last term is an empirical function and the fit parameter a_0 depends on the different event z positions in the simulations. Then the energy in the partial-fill is found by $E_{partial} = E/(1 + scaling)$[162, 164].

In the NHits-ratio method, the NHits of an e^- event at (0,0,0) mm in the full scintillator geometry was used as a reference (NHits$_{ref}$). By simulating 1 to 10-MeV (with a 1-MeV step) e^- events in the full-fill geometry with 0.5 g/L PPO, and fitting the NHits to the energies, a converting function between the energy and NHits is found by: $E_{full} = f(\mathrm{NHits}) = 0.051 + 0.003 \cdot NHits + 2.49 \times 10^{-7} \cdot \mathrm{NHits}$[165].

Then for the partial-fill geometry with a fixed Z_{water}, the e^- events were simulated at different $(\rho = \sqrt{x^2 + y^2}, z)$ positions in the AV, where ρ goes from 0 to 5500 mm by a step of 500 mm and z goes from -5500 to 5500 by a step of 500 mm to cover all the interested AV volume. The value of scaled NHits for an event at (ρ_0, z_0) is found by: $\mathrm{NHits}' = \mathrm{NHits_{partial}}/(\mathrm{NHits}(\rho_0, \mathrm{z}_0)/\mathrm{NHits_{ref}})$. Finally, the partial energy is found by $E_{partial} = f(\mathrm{NHits}')$[165].

4.8 Machine Learning and Deep Learning

Nowadays, the vast amount of data available to particle experiments make it feasible to implement machine learning and deep learning methods for data analysis. In Chapter 6, it will show a machine learning method applied to the solar neutrino analysis. At the time of this writing, a deep learning framework is being developed for the reconstruction[166, 167, 168]. This method investigates the relation between the hit PMT distributions and the event reconstruction, currently for the position and direction. It trains neural networks based on the MC simulation datasets (with $\mathcal{O}(10^6)$ events) as well as the calibration datasets to predict the event position and direction[167]. A few physics-based loss functions, such as the loss function checking the t_{res}, can be further included to improve the reconstruction performance[167].

Once the neural networks are trained, the reconstruction speed is expected to be 100 to 1000 times quicker than the traditional likelihood-fit method running on the CPU (Central Processing Unit). Since the deep learning method can also utilize the computing power of the GPU (Graphics Processing Unit), it is expected to be 10^4 times quicker[167, 168]. Such a fast speed reconstruction will be promising to be applied in the scintillator phase, where it is time-consuming for reconstructing the higher NHits events. The deep learning framework is also expected to aid the data analysis.

4.9 Conclusion

The Multi-path Fitter framework of event vertex reconstruction was developed for multiple SNO+ physics phases. Under this framework, the `MP water fitter` works as an alternative fitter to provide additional reconstruction information for the water data, and it gives proper position and direction resolutions for the water analysis. The `MP scint-water fitter` works as the prime fitter for the SNO+ partial-fill phase.

Chapter 5

Calibration

A detailed description of the SNO+ detector has been implemented in the `RAT` software package for Monte Carlo (MC) simulations, as mentioned in Chapter 3. However, when the simulations are compared to the real world, there always exist discrepancies. To make precise measurements, calibration sources were implemented in the SNO+ detector during the water phase and the partial-fill phase. During the water phase, the ^{16}N source (described in Sect. 3.5.1, Chapter 3) was used for the primary detector calibration. The ^{16}N calibration data (^{16}N runs) were mainly used for checking the performances of the reconstruction of the event position, direction, and energy.

In this chapter, the `MPW fitter` (described in Sect. 4.2, Chapter 4) was applied on both the data and simulations of the ^{16}N runs in the water phase. By comparing the differences between the data and MC, systematics of the position and direction reconstruction were extracted. The event energy was reconstructed by the SNO+ energy fitter for the water phase (described in Sect. 4.7, Chapter 4), which utilizes the `MPW fitter` fitted event vertex and direction. Also, based on the `MPW fitter` reconstructed vertex and direction results, the other parameters, such as the in-time-ratio (ITR) and the isotropic parameter (β_{14}) were calculated. By comparing the ^{16}N data and the MC simulations, the relevant systematics were also evaluated. These systematic results were used in the solar neutrino analysis in Chapter 6.

5.1 ^{16}N Calibration Scans in the Water Phase

During the water phase, the ^{16}N source was deployed at different positions inside the AV in June and in November 2017 to perform internal calibration scans. It was also deployed at different positions in the external water region between the AV and the PSUP in March 2018 to perform external scans. For each ^{16}N run, the source was placed at a fixed position, and the data were taken for about 20 minutes (for the central run-107055, it took 1 hour). The source was inside the AV for the internal scans, moving along x, y, and z-axes (called "X, Y, Z scans" in this thesis). It was also was moved diagonally across the AV and was placed at the corners of the inner AV ("corner scans"). For the external scans, the source was placed in the external water region but outside the AV. The source was moved along the z-axis with a fixed (x, y) position close to the AV at (-5861.0,-2524.0) mm. Fig. 5.1 shows the different positions of the source deployment. In this thesis, 79 internal scan runs were used. Details of the calibration runs are listed in the tables in Appendix. B.1.

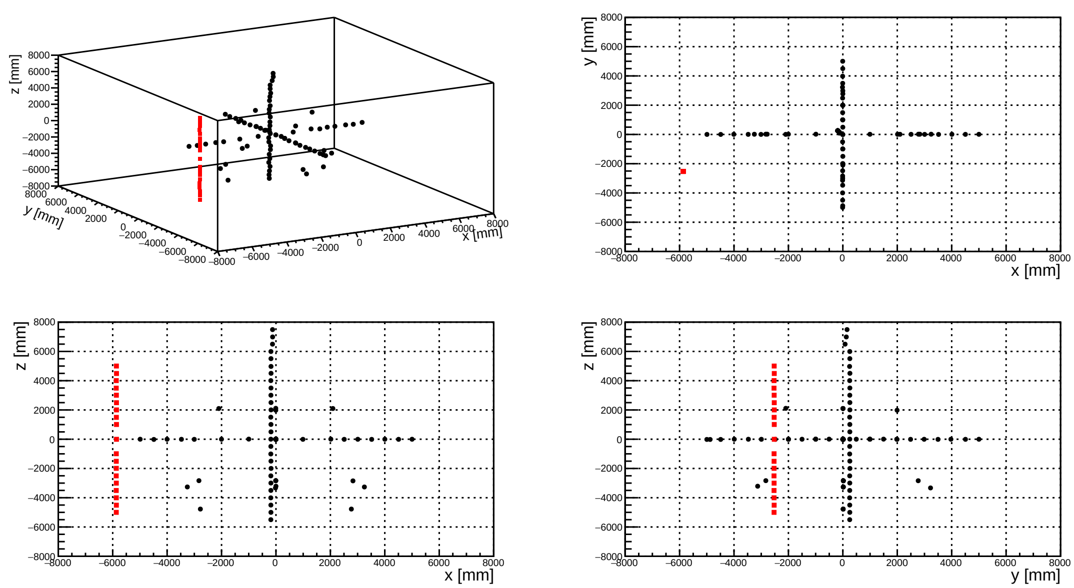

Figure 5.1: The deployed source positions of the ^{16}N scan runs used by this thesis. The black dots are internal runs while the red squares are external runs.

The ^{16}N calibration runs provide ideal tests for the fitter performance. From a comparison of reconstructions for data and MC, we can also extract the resolution and bias of the fitter. Here I worked out the vertex and the direction reconstruction performances for both of the `RAT water fitter` and the `MPW fitter`. The vertex shifts as well as the uncertainties were evaluated.

To tackle with the ^{16}N run data and simulations, an FECD tag cut ($FECD == 9188$) was applied during the data processing, to save the events only when the source trigger fired. A reconstruction threshold on NHits≥ 6 was applied to the MC and data. Besides these cuts, high-level cuts based on classifiers were used.

5.2 High Level Cuts for the Water Phase

A set of classifiers were developed by SNO analysis and been optimized for the SNO+ water analysis[169]. These classifiers utilized the reconstructed quantities, so they always require valid reconstructions.

- In time ratio (ITR) classifier

  For each event, this classifier loops the triggered PMTs (hits), calculates the t_{res}, and then finds the ratio of the number of hits in an optimized prompt time window. In the water phase, the time window was [-2.5,5.0] ns. If the ITR ratio is too low for an event, it indicates that most of the triggered PMTs are not caused by the prompt lights and thus the event probably does not originate from Cherenkov lights; it can be an instrumental noise, or caused by a large amount of lights reflecting off the detector components (called "late lights").

- β_{14} isotropy classifier

  This classifier uses Legendre polynomials to return the first (β_1) and the fourth (β_4) spherical harmonics of an event, where:

$$\beta_l = \frac{2}{N(N-1)} \sum_{i=1}^{N-1} \sum_{j=i+1}^{N} P_l(\cos\theta_{ij}), \tag{5.1}$$

  and $P_l(\cos\theta_{ij})$ are Legendre polynomials.

A combination of two β_l terms was chosen by the SNO collaboration to be: $\beta_{14} = \beta_1 + 4\beta_4$. This quantity gives a gaussian-like distribution for Cherenkov events[170]. In principle, any deviation from zero suggests some polarity or a deviation from a totally isotropic pattern.

- θ_{ij} isotropy classifier

  This classifier describes the angle subtended at an event vertex by PMT #i and PMT #j, which is calculated as:

$$\cos\theta_{ij} = \frac{(\vec{X}_{PMT\#i} - \vec{X}_{event}) \cdot (\vec{X}_{PMT\#j} - \vec{X}_{event})}{|\vec{X}_{PMT\#i} - \vec{X}_{event}||\vec{X}_{PMT\#j} - \vec{X}_{event}|}. \tag{5.2}$$

5.2.1 Effects of the High-level Cuts

As described above, the classifiers can help to distinguish the signals from Cherenkov events and backgrounds from non-Cherenkov events. To remove the non-Cherenkov backgrounds, cuts of $ITR > 0.55$ and $-0.12 < \beta_{14} < 0.95$ (called "high-level cuts") were suggested by the collaboration[161]. These cuts are based on the analyses of data cleaning, simulated physics events as well as the SNO experience[161, 171, 170].

The ^{16}N central run-107055 data and MC were used to check the effects of the high-level cuts. For the MC (data), the cut of $ITR > 0.55$ removed 0.69% (0.79%) of the total events; $-0.12 < \beta_{14} < 0.95$ removes 1.11% (0.93%) of the total events. Combining the ITR and β_{14} cuts, 1.69% (1.62%) of the total events were removed.

The poorly reconstructed events with large position biases (> 6000 mm) were counted. For the MC case, the position biases were taken as the distance between the reconstructed positions and the true positions generated by the MC: $|\vec{X}_{fit} - \vec{X}_{MC}|$; while for the data case, the biases were between the reconstructed positions and the source manipulation position: $|\vec{X}_{fit} - \vec{X}_{src}|$. The large biased events are 0.13% of the total events in both the MC and data. The high-level cuts removed 73.12% (66.82%) of them for the MC (data).

Fig. 5.2 shows the relations between the position biases and the ITR, β_{14} respectively, for the data and MC.

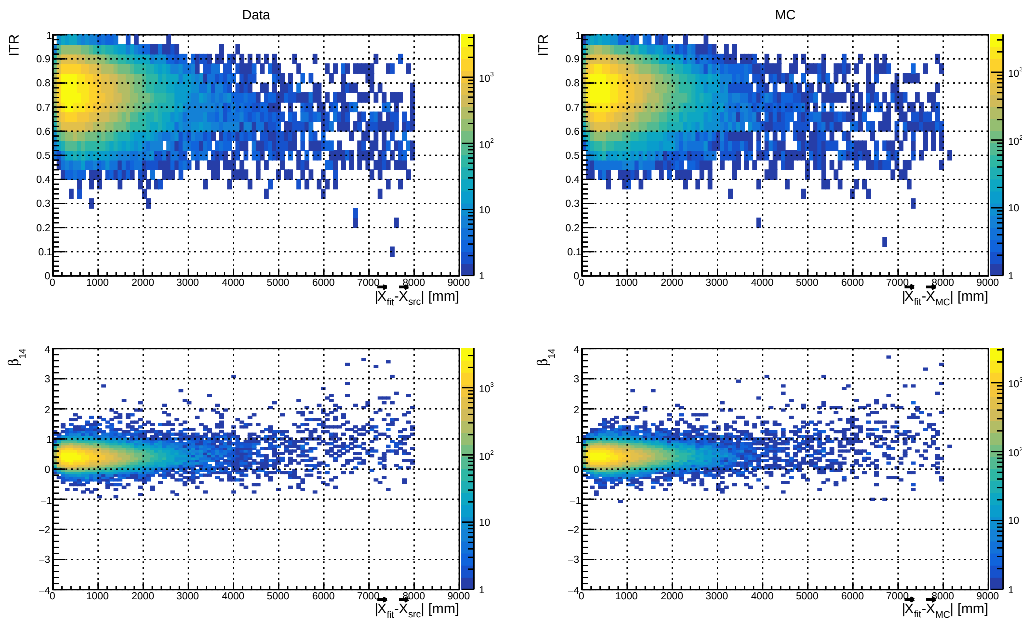

Figure 5.2: Position biases vs ITR (top) and β_{14} (bottom) for the ^{16}N central run-107055. Left is MC and right is data. For the data, the source position ($\vec{X}_{src}$) was compared.

As a summary, the high-level cuts remove more than half of the events with large position biases while removes about 1.6% of the total events.

5.3 Reconstruction Evaluations from ^{16}N Calibration Scans in the Water Phase

In this section, by analyzing the ^{16}N data and MC in the water phase, I extracted the reconstruction resolutions of the event position, direction, and energy respectively. Then by comparing the data with the MC, the reconstruction systematics were evaluated.

To do these evaluations, a few cuts were applied to both the data and MC. Firstly, the level cuts ($ITR > 0.55$, $-0.12 < \beta_{14} < 0.95$) were applied. For events with the position, direction and energy successfully reconstructed (i.e., the event has valid position, direction and energy reconstructions), further cuts on the reconstruction figure of merit (FoM) and source geometry (will be described in detail) were applied to ensure that the analyzed events were nicely reconstructed physics events caused by the source γ particles interacting with

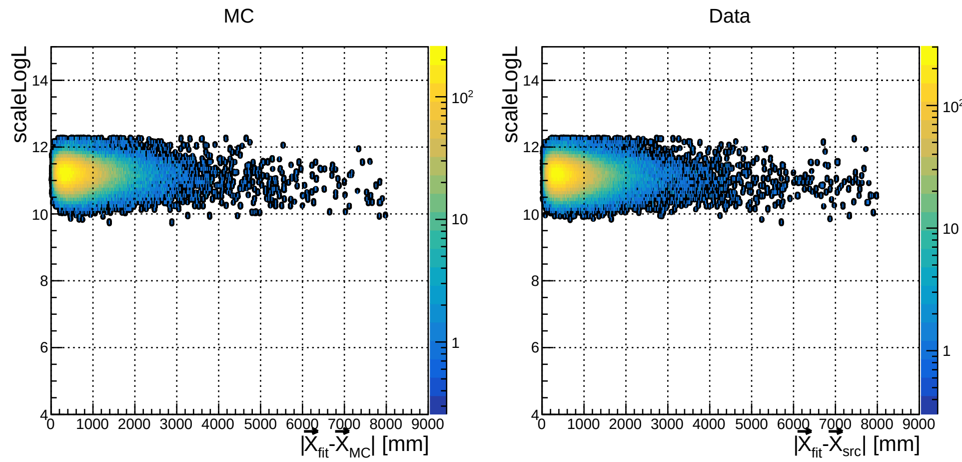

Figure 5.3: Position biases ($|\vec{X}_{fit} - \vec{X}_{MC}|$) vs *scaleLogL* for the ^{16}N central run-107055. Left is MC and right is data. For the data, the source position ($\vec{X}_{src}$) was compared.

the detector water.

5.3.1 Position Reconstruction Evaluation

The position figure of merit (posFoM) cuts mentioned in Sect. **??** were applied on the reconstruction results. Fig. 5.3 shows the *scaleLogL* with the position biases for the reconstructed events in ^{16}N central calibration run-107055. Both of the data and the MC simulations are shown. For the MC case, the position biases are between the reconstructed positions and the true positions generated by the MC: $|\vec{X}_{fit} - \vec{X}_{MC}|$; while for the data case, the biases are between the reconstructed positions and the source manipulation position: $|\vec{X}_{fit} - \vec{X}_{src}|$.

For the MC (data) case, about 0.035% (0.043%) of the total reconstructed events have large biases ($|\vec{X}_{fit} - \vec{X}_{MC}| > 6000$ mm). A cut of $scaleLogL > 10$ removes 96.0% (97.3%) of the events which have biases over 6000 mm, with a sacrifice of removing 0.012% (0.016%) of the total events.

Fig. 5.4 shows a relation between the *scaleLogL* and the reconstructed energy (E_{fit}).

For the events with reconstructed energies below the water solar neutrino analysis threshold 3.5 MeV ($E_{fit} < 3.5\ MeV$), they are mostly coming from the U/Th isotopes, decays of Potassium as well as instrumental noises[161]. Their lower energies or $NHits$ can affect the position reconstruction since there are fewer PMTs to be used, and thus their $posFoM$ can be worse. In the MC (data) case, there are about 13.04 % (12.89%) of the events with $E_{fit} < 3.5\ MeV$. By applying the cut of $scaleLogL > 10$, 0.10% (0.09%) of such events were removed.

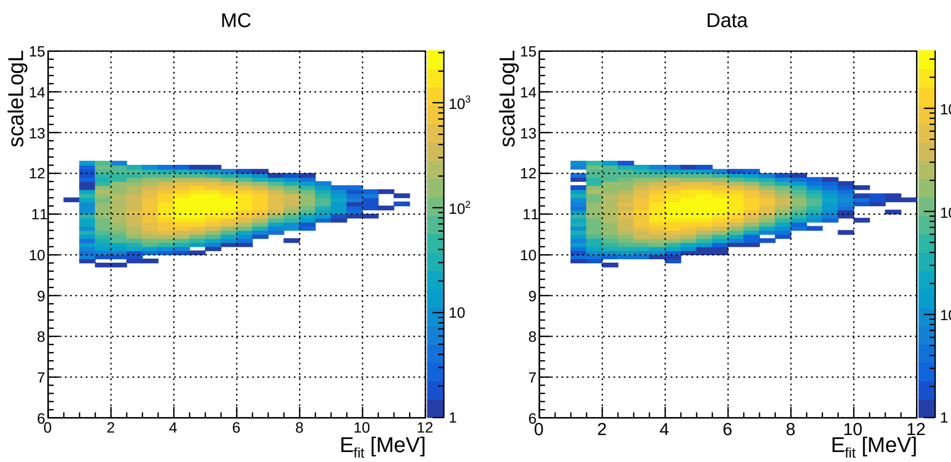

Figure 5.4: Reconstructed energy vs $scaleLogL$ for the ^{16}N central run-107055. Left is MC and right is data.

As a summary, there are about 0.04% of the reconstructed events which were poorly reconstructed (mis-reconstructed) by the `MPW fitter` with position biases over 6 meters. Applying a cut in $posFoM$ with $scaleLogL > 10$ can remove over 96% mis-reconstructed events. This $posFoM$ cut was used in the following direction and energy reconstruction evaluations.

5.3.1.1 Position Resolution

A position resolution function is defined for the reconstructed electron position distribution[138]:

$$R(x) = \frac{1-\alpha_e}{\sqrt{2\pi}\sigma_p} \exp\left[-\frac{1}{2}\left(\frac{x-\mu_p}{\sigma_p}\right)^2\right] + \frac{\alpha_e}{2\tau_p} \exp\left[\frac{-|x-\mu_p|}{\tau_p}\right], \tag{5.3}$$

where α_e is the fractional exponential component, σ_p is the Gaussian width (corresponding to the position resolution), μ_p is the Gaussian shift (corresponding to the position bias) and

τ_p is the exponential slope (corresponding to the position distributions in tails).

The γ-rays emitted from the ^{16}N source interact with the water in the detector mainly via Compton scattering, as shown in Fig. 5.5. The position distribution of the γ interaction vertices is peaked around the source container, spreading to about 2 meters.

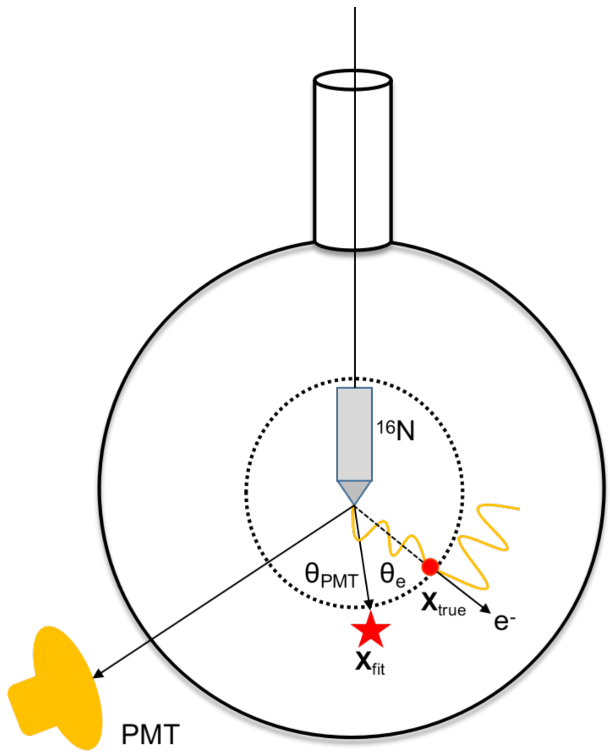

Figure 5.5: A cartoon shows the ^{16}N source.

Fig. 5.6 shows the spatial distributions $S(x)$ of the first γ-ray interaction positions projected on the x-axis obtained from MC simulation. Therefore, the ^{16}N source is considered as an electron source with a known spatial distribution[138]. For simplicity, in the following, we always discuss the x component of the position vector $\vec{X}$.

For electrons from the ^{16}N calibration source, their spatial distribution function $N_R(x)$ can be described by the position resolution function smeared by the convolution of $S(x)$ as[138]:

$$N_R(x) = \int_{-\infty}^{+\infty} S(x)R(x_{fit} - x)dx, \tag{5.4}$$

The values of $N_R(x)$ can be calculated bin by bin from the histograms of $S(x)$ and $R(x)$

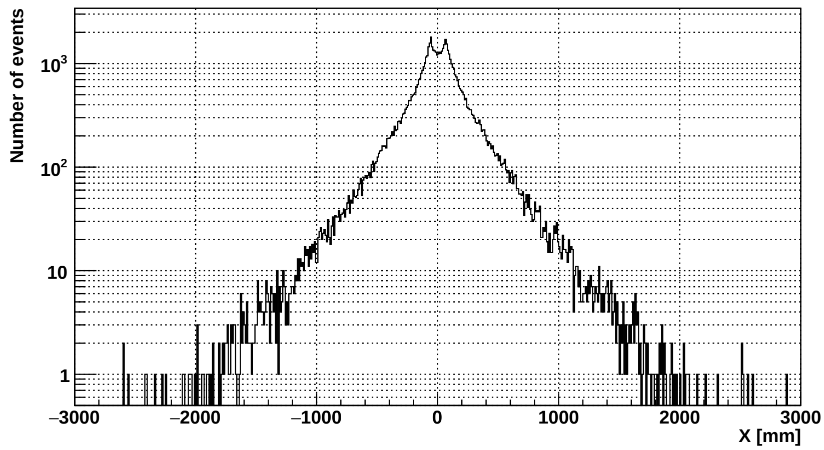

Figure 5.6: Spatial distributions of ^{16}N first γ-rays interaction position projected on x axis, obtained from the `RAT` simulations. The double-peak structure is due to the wall of the stainless steel container of the ^{16}N source.

extracted from the MC or data:

$$N_R(x_i) = \sum_{x_i=-\infty}^{+\infty} S(x_i) R(x^i_{fit} - x_i), \tag{5.5}$$

Then the χ^2 is calculated by:

$$\chi^2 = \sum_{i=0}^{N_{bins}} [\frac{N_R(x^i_{fit}) - N_R^{fit}(x^i_{fit})}{\sigma_i}]^2, \tag{5.6}$$

where N_R^{fit} is a trial fit to the N_R by tuning the $\{\alpha_e, \mu_p, \sigma_p, \tau_p\}$ and σ_i is taken as the bin width of the histograms.

By minimizing the χ^2, the parameters of the resolution function, $\{\alpha_e, \mu_p, \sigma_p, \tau_p\}$ and a best N_R^{fit} were obtained.

Fig. 5.7 shows a comparison of the reconstructed x position of ^{16}N events between data and MC. The reconstructed position distributions were fitted with N_R^{fit}.

Table. 5.1 summarizes the values of position resolution parameters (for x-axis) obtained from data and MC of ^{16}N calibration runs at the detector center.

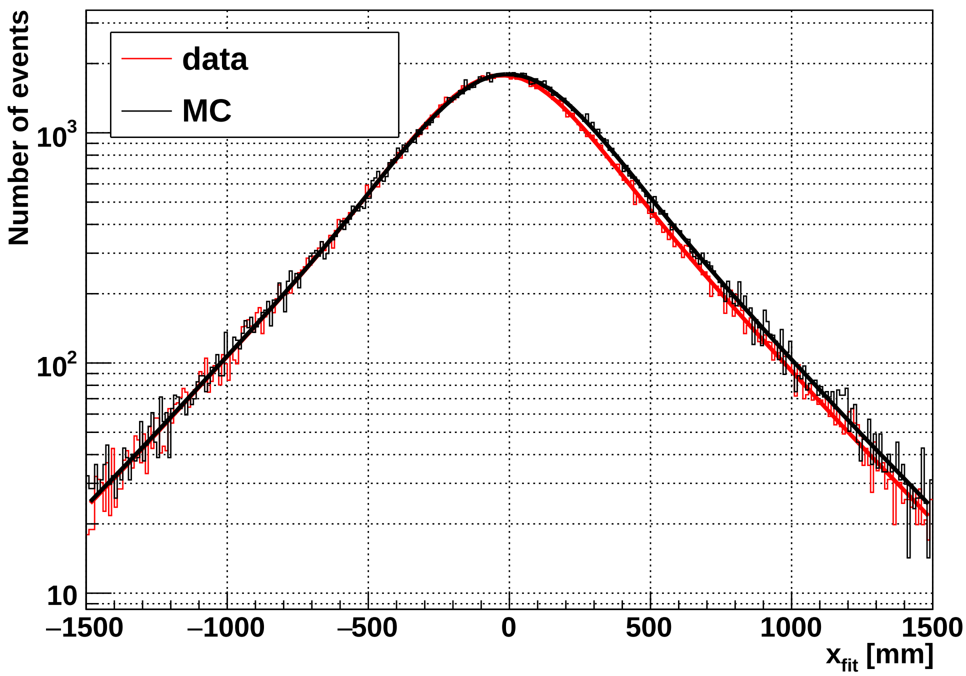

Figure 5.7: Distributions of the reconstructed position projected on x axis, obtained from SNO+ ^{16}N central run data (red) and MC (black). The distributions are fitted with N_R^{fit} (red and black lines).

Table 5.1: Position resolution parameters for the `MPW fitter` (x-axis).

MPW fitter	α_e	σ_P (mm)	τ_P (mm)	μ_P (mm)
data	0.58±0.04	175.8±3.8	288.0±5.7	-28.8±1.0
MC	0.51±0.05	195.2±3.3	298.4±6.1	-10.9±1.0

5.3.1.2 Position Systematics

To evaluate the position uncertainties, the MC and data runs of the ^{16}N internal scans along x, y, z axes were taken to evaluate the x, y, z position uncertainties respectively (the runs are listed in Table. B.1 to B.3. Three neck runs in z-scan were not used). The high-level cuts as well as the $E_{fit} > 3.5\ MeV$ and $scaleLogL > 10$ cuts were applied. fit range was set as $[-2000, +2000]\ mm$. If the lower range was smaller than -6000 mm, it was set to -6000 mm; if the upper range was larger than 6000 mm, it was set to +6000 mm. This was used to remove the effects caused by the AV.

The position resolution function was first fitted with 4 free parameters: α_e, μ_p, σ_p and τ_p. The the average values of the α_e and τ_p were calculated from all the scan runs used here. To simplify the calculation in propagating systematics, the α_e and the τ_p were fixed to the average value: $\alpha_e = 0.5288$ (0.5375) for the MC (data); $\tau_p = 271.738$ (263.735) for the MC (data). With the fixed values of α_e and τ_p, both the data and the MC were refit with μ_p and σ_p only. Using the fixed values of α_e and the τ_p is based on the reasons that these parameters in principle can be viewed as corrections to the γ distribution ($S(x)$) and they can be absorbed, which would not depend on position[161].

Fig. 5.8 shows the fitted results of μ_P and σ_P along the x, y, z-axes scans respectively. For the sake of simplicity, for the x-scan case, only the x-axis results ($\mu_{P,x}, \sigma_{P,x}$) are shown here. Similarly, only the $\mu_{P,y}$ and $\sigma_{P,y}$ ($\mu_{P,z}$ and $\sigma_{P,z}$) are shown for the y-scan (z-scan). The relative differences discussed later consider all the three axes.

It shows that the position resolutions of the MC are mostly better than the data, which is expected since the non-uniformities of the detector in realistic situations can cause a broader resolution in the data[161]. Also, when the source is close to the AV or at the edges of the axes, the Gaussian shift μ_P becomes large and the resolution worsens. Also,

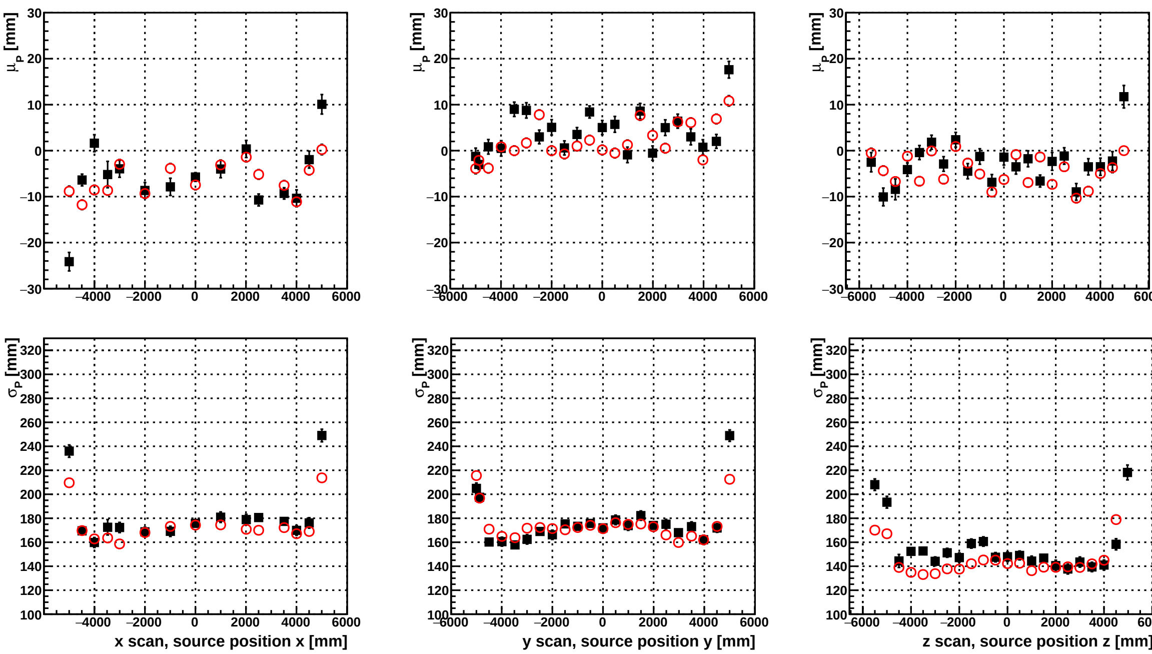

Figure 5.8: The fitted values of μ_P (top) and σ_P (bottom) along x (left), y (middle) and z (right) scans. The source positions in each set of scans are projected onto x, y and z axes respectively. The MC results (red circles) are compared with the data (black boxes).

the difference between the MC and data becomes large.

To quantify the discrepancies between the MC and data, a relative difference of σ_p between the MC and data is defined as[161]:

$$\sigma_{p,\delta} \equiv \sqrt{\sum_i |(\sigma_{P,i}^{data})^2 - (\sigma_{P,i}^{MC})^2|} \quad (i = x, y, z), \tag{5.7}$$

Fig. 5.9 shows the $\sigma_{p,\delta}$ changing along the internal x, y and z-axes scans respectively. All the differences are below 190 mm except the run-106979 with the source at $z = 4973.567$ mm. The neck effects can cause this worst resolution.

It goes worse when the source is close to the AV or at the edges of the axes. When the source is close to the AV center, the differences are below 100 mm.

The values of $\sigma_{p,\delta}$ were taken to represent the position resolution systematics.

As listed in Table. 5.2, the averages and the standard deviations of the $\sigma_{p,\delta}$ were taken as the resolution systematics for x, y and z-axes respectively. To smear the position results, a Gaussian distribution $\mathcal{N}(0, \delta)$ was convolved with positions. The upper values δ were used to smear the positions.

Table 5.2: The `MPW fitter` position resolution systematic uncertainties in x, y and z axes. Unit: mm.

axis	systematic uncertainties	systematic to be applied (δ)	smearing
x	73.89 ± 39.71	113.6	$x + \mathcal{N}(0, \delta)$
y	56.03 ± 34.96	90.99	$y + \mathcal{N}(0, \delta)$
z	75.47 ± 70.09	145.56	$z + \mathcal{N}(0, \delta)$

To quantify the vertex shifts between the MC and data, values of vertex shifts: $\mu_{P,\delta} \equiv \mu_P(data) - \mu_P(MC)$ were calculated for the x, y and z scans respectively. Fig. 5.10 shows these results.

In Table. 5.3, the averages and the standard deviations of the $\mu_{P,\delta}$ were taken as the vertex shifts for x, y and z-axes respectively. To smear the position results, the positions were simply shifted by the upper values δ were used to smear the positions.

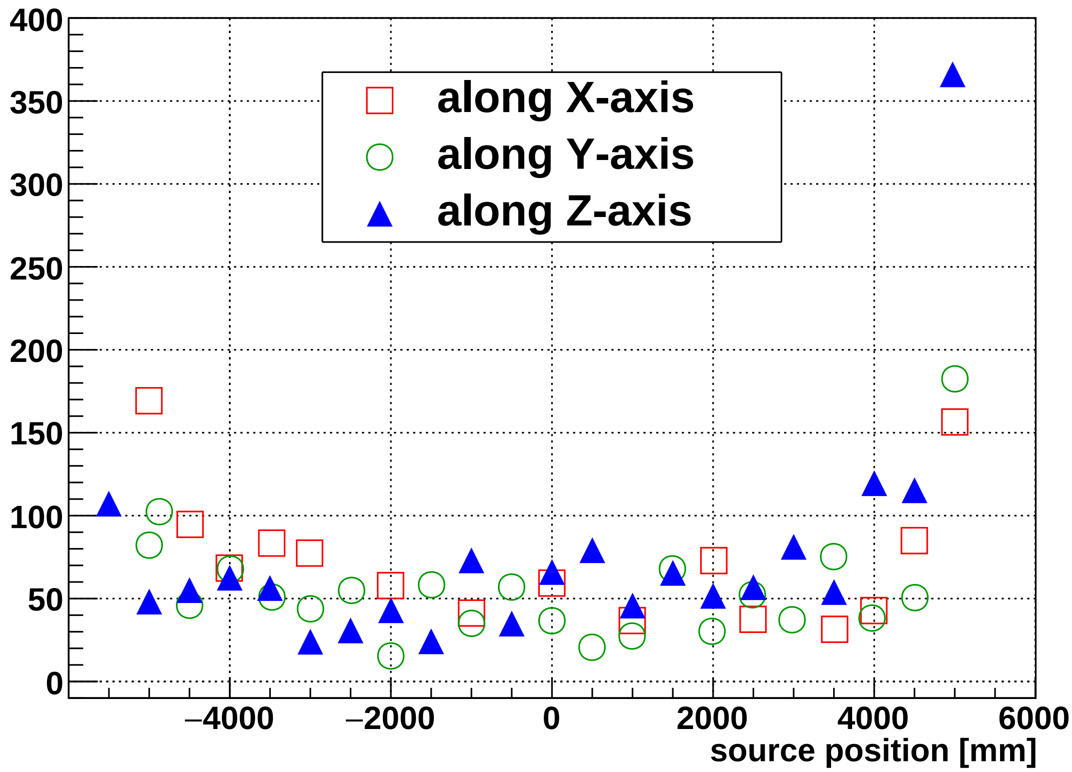

Figure 5.9: Relative differences of σ_P ($\sigma_{p,\delta}$) as a function of the ^{16}N source position. For simplicity, the corner scans are not shown in this figure. The red squares represent the results from the x-scan runs; green circles represent the y-scan runs and the blue triangles represent the z-scan runs.

5.3.1.3 Vertex Scale Uncertainties

In addition to the vertex shifts mentioned previously, the vertex scale is defined as a linear scale factor between the fitted positions of the data and the MC: $x^{data}_{fit} - x^{MC}_{fit} = \mu^{data}_{P,x} - \mu^{MC}_{P,x} = \Delta + \beta \cdot x^{MC}_{fit}$.

Since $x^{data}_{fit} = \Delta + (1+\beta) \cdot x^{MC}_{fit}$, if the vertex scale factor is defined as: $\alpha \equiv 1 + \beta$, then $x_{data} = \alpha x_{MC}$.

To obtain the α, the results in Fig. 5.10 were fitted with linear functions: $shifts = p_0 + p_1 \cdot x_{src}$ (where x_{src} is the source position), as shown in Fig. 5.11.

From the linear fits, the values of vertex shifts were obtained and listed in Table. 5.4.

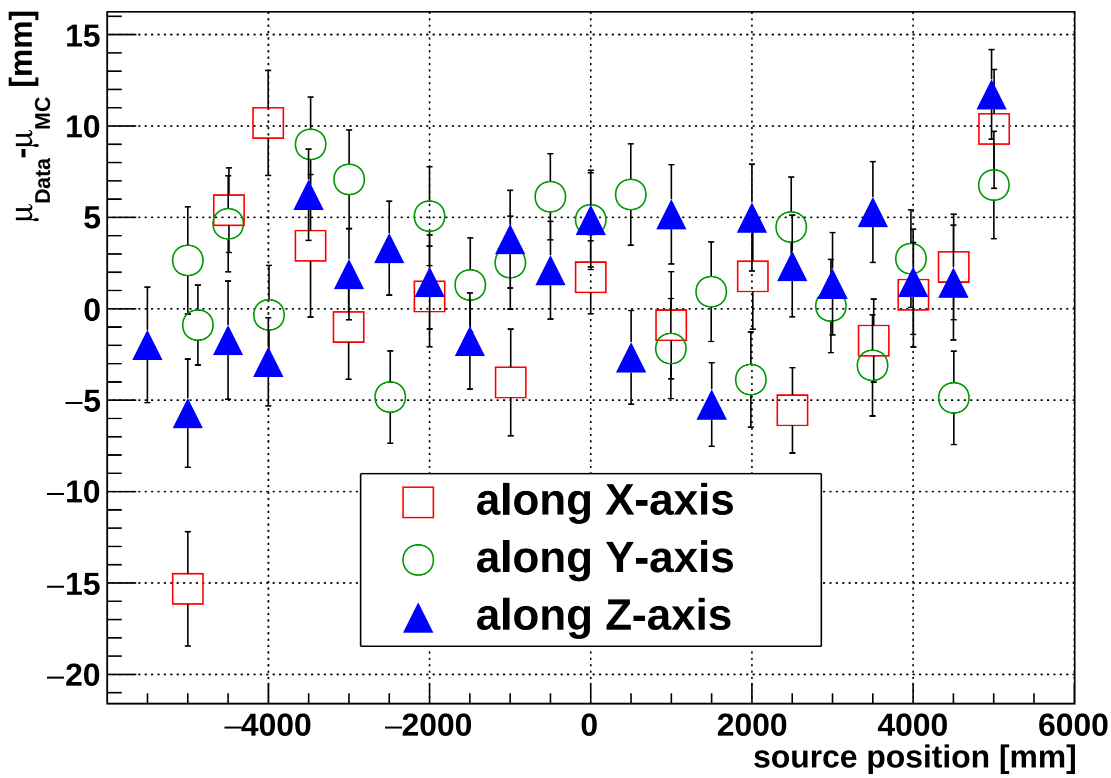

Figure 5.10: Vertex shifts of μ_P ($\mu_{p,\delta}$) as a function of the ^{16}N source position. For simplicity, the corner scans are not shown in this figure. The red squares represent the results from the x-scan runs; green circles represent the y-scan runs and the blue triangles represent the z-scan runs.

Since the χ^2/ndf values here were large, according to Refs. [161, 21], inflated errors were calculated as $S\times$(slope errors), where the error scale factor $S = \sqrt{\chi^2/(ndf-1)}$. The downward systematic was calculated as the slope minus the slop error as well as the inflated error. In contrast, the upward systematic was taken as the positivel inflated error, as suggested by [161]. For the z scan, the position at $(-185.037, 247.24, 4973.567)$ mm pulls the slope results to the positive due to the possible biases in simulation for the neck geometry effects and makes the slope positive. So this point was not used in the linear fit.

The vertex scale systematics is then transformed by: $x' = (1+\delta_x/100)x$, the same for y, z.

Table 5.3: Vertex shifts for the reconstructed positions in x, y and z axes. Unit: mm.

axis	vertex shift	systematic to be applied (δ)	smearing
x shift	0.50±5.98	+6.48/-5.98	$x+\delta$
y shift	2.02±4.11	+6.13/-4.11	$y+\delta$
z shift	1.89±4.82	+6.71/-4.82	$z+\delta$

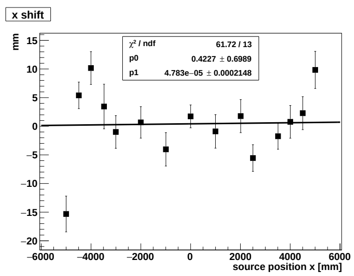

(a) ^{16}N x-scan runs.

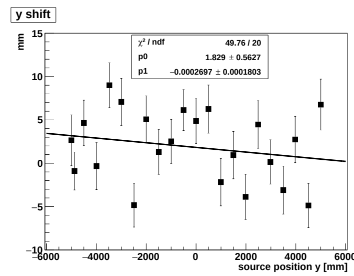

(b) ^{16}N y-scan runs.

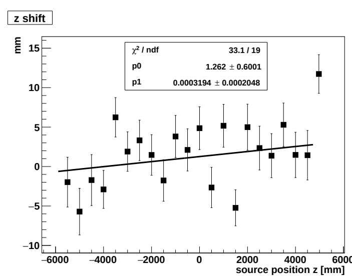

(c) ^{16}N z-scan runs.

Figure 5.11: Vertex shifts along x, y, z axes and fitted with linear functions.

The scale systematics also depends on the radius $r=\sqrt{x^2+y^2+z^2}$[161]. By the error propagation, for an event position (x,y,z), δ_r is calculated as[161]:

$$\delta_r = \sqrt{\sum_{i=1}^{3}(\frac{\partial r}{\partial x_i})^2\delta_{x_i}^2} = \sqrt{\frac{x^2\delta_x^2+y^2\delta_y^2+z^2\delta_z^2}{r^2}}, \tag{5.8}$$

where the δ_r^+ and δ_r^- are calculated by δ^+ and δ^- respectively.

Then the two-sided bounds of the radial r are calculated by: $r^+=(1+\delta_r^+/100)\cdot r$ and $r^-=(1+\delta_r^-/100)\cdot r$.

Table 5.4: Vertex shifts for the reconstructed positions in x, y and z axes. Unit: mm.

axis	fitted slope (%)	inflated error	systematic (δ^+/δ^-) (%)
x scale	0.005±0.021	0.048	+0.07/-0.06
y scale	-0.027±0.018	0.030	+0.02/-0.07
z scale	0.032±0.020	0.027	+0.08/-0.01

5.3.2 Direction Reconstruction Evaluation

5.3.2.1 Direction Resolution

For the reconstructed events in the ^{16}N calibration, assuming a γ particle emitted from the source and interacts with e^- at the reconstructed position, the "true" direction of an event is defined as the direction pointing from the source manipulation position to the reconstructed position: $\vec{u}_{true} = (\vec{X}_{fit} - \vec{X}_{src})/|\vec{X}_{fit} - \vec{X}_{src}|$. The angle θ is the displacement between the "true" and the reconstructed directions and $\cos\theta = \vec{u}_{true} \cdot \vec{u}_{fit}$.

The distribution of the $\cos\theta$ was fitted with the direction resolution function (Eqn. 4.9) mentioned in Sect. 4.2.8, Chapter 4. Before the fitting, a few cuts relating to the position and energy reconstruction were applied to the data or simulation results. As mentioned in Chapter 4, the direction reconstruction relies on the position. Therefore, the $posFoM$ cut: $scaleLogL > 10$ was applied before evaluating the direction reconstruction. Other cuts were suggested by the SNO+ analysis to remove the instrumental backgrounds and poor reconstructions for the events close to the source container or far away from the source. To remove the instrumental backgrounds, the cuts of $E_{fit} > 3.5$ MeV, $ITR > 0.55$ and $-0.12 < \beta_{14} < 0.95$ were used. To remove poorly reconstructed events which were close to the source container due to its shadow effect, and also the events far away from the source, a distance cut of $1000 < |\vec{X}_{fit} - \vec{X}_{src}| < 2300$ mm was applied. For the internal scans, a radius cut $R' < 5850$ mm was also applied. This radial cut was not applied on the external and neck scans[161].

Fig. 5.12 shows the fitted results of the angular distributions in a fit range of [0.3,1] after the cuts mentioned.

The resolution parameters are shown in Table. 5.5. It shows that the direction resolu-

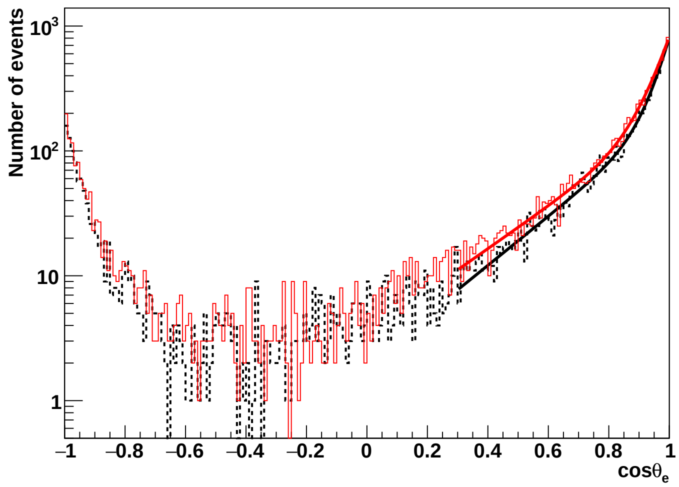

Figure 5.12: Angular distributions extracted from the data (red solid line) and MC (black dashed line); both are reconstructed by the `MPW fitter`. These distributions are fitted with the angular resolution functions ranging from 0.3 to 1.

Table 5.5: Direction resolutions.

107055	β_M	β_S	α_M	χ^2/ndf	$\cos\theta_{0.5}$	$\cos\theta_{0.8}$	$\cos\theta_{0.9}$
MPW data	4.15±0.18	19.08±0.94	0.58±0.02	77.1/66	0.964	0.744	0.410
MPW MC	4.42±0.19	20.41±1.01	0.56±0.02	83.8/66	0.974	0.768	0.454
`RAT` data	3.76±0.18	17.90±0.82	0.55±0.02	70.5/66	0.974	0.731	0.364
`RAT` MC	4.02±0.18	20.89±0.92	0.54±0.03	94.9/66	0.979	0.753	0.409

tions of the MC are always better than the data due to the ideal situations in the simulations. The reconstruction performance of the `MPW fitter` and the `RAT water fitter` are similar, while the β_M values of the `MPW` are about 10% higher than the `RAT` in both of the data and the MC. This indicates the direction resolution of the `MPW` is slightly better than the `RAT`.

5.3.2.2 Direction Systematics

For all the internal ^{16}N scans, the cuts mentioned in the last section were applied on both the data and simulations. Similar to the evaluation of the position uncertainties, the angular resolution function was first fitted with three free parameters: α_M, β_S, and β_M. To simplify the calculation in propagating systematics, an average value of the fitted α_M was calculated from all the internal scans (except the three neck scans), as 0.613 for data and 0.585 for

MC. With the fixed values of α_M, both the data and the MC were refit with β_S and β_M only. The default fit range is [0.3,1], while for some scans close to the AV, the events can be few after the cuts. For these situations, to ensure more than 5000 events were fitted, the fit range was enlarged by moving a 0.1 step to the left until the left value reaches -0.5: $[0.3 - 0.1 \cdot step, 1]$.

Fig. 5.13 shows the results of the fitted β_M and β_S values for the internal ^{16}N x, y and z-axes scans. It shows that for most of the scans, the MC results are better than the data. The three Z scans in the neck have the worst direction resolutions due to the asymmetry of the detector geometry.

The relative difference between data and MC of a fitted resolution quantity $q \pm \delta_q$ is defined as:

$$(\Delta q)_{rel} = \frac{q_{data} - q_{MC}}{q_{MC}} \times 100\%. \tag{5.9}$$

The error of the relative difference is defined as:

$$\delta_{(\Delta q)_{rel}} = \sqrt{(\frac{\delta_{q_{data}}}{q_{data}})^2 + (\frac{\delta_{q_{MC}}}{q_{MC}})^2} \times 100\%. \tag{5.10}$$

Fig. 5.14 shows the relative differences for the internal x, y, z scans (not using the neck scans).

Taking the internal scans except the neck scans (77 runs in total), the means and standard deviations of the relative differences are:

$\Delta(\beta_M)_{rel} = (-6.09 \pm 4.01)\%$, and $\Delta(\beta_S)_{rel} = (-3.09 \pm 4.39)\%$.

To be conservative, taking the largest and smallest values of the $\Delta(\beta_M)_{rel}$ and $\Delta(\beta_S)_{rel}$, the negative and positive values of the direction systematic (δ_θ) are obtained as $\delta_\theta = +0.013/-0.101$.

To propagate the uncertainties of β to the direction resolution, a first-order approximation function was derived by the SNO collaboration[172]:

$$\cos\theta' = 1 + (\cos\theta - 1)(1 + \delta_\theta). \tag{5.11}$$

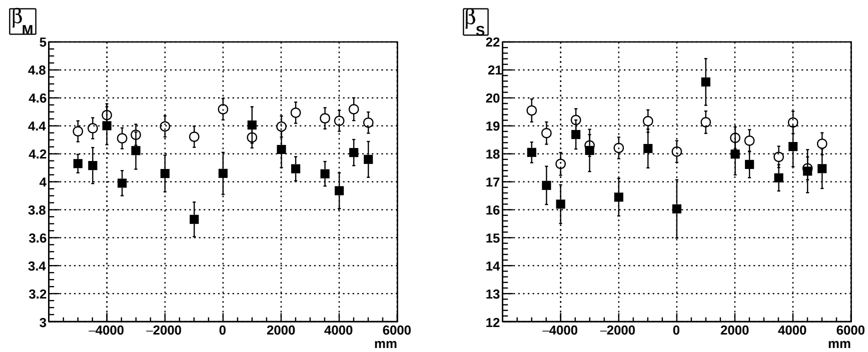

(a) ^{16}N x-scan runs.

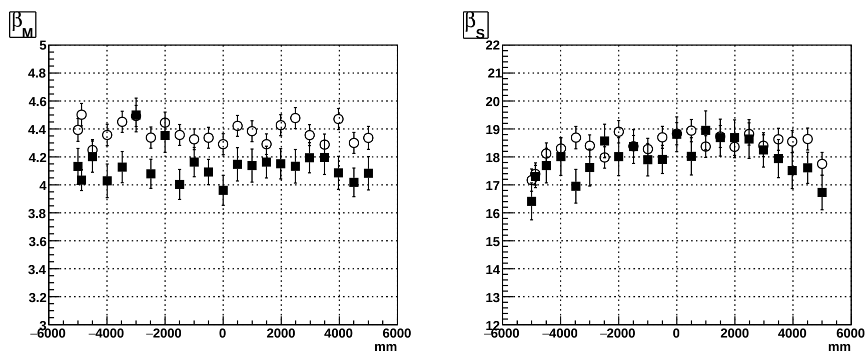

(b) ^{16}N y-scan runs.

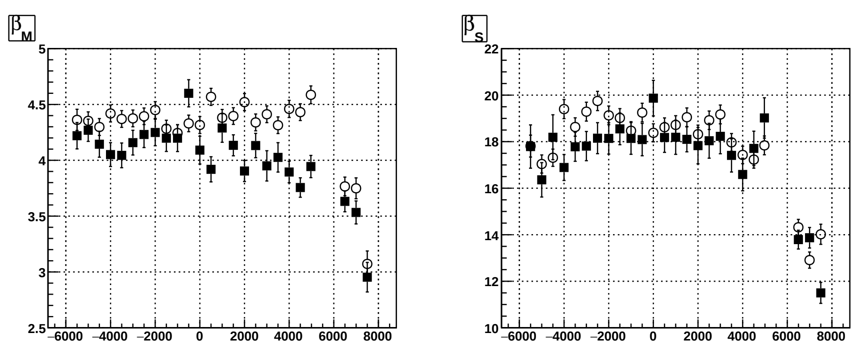

(c) ^{16}N z-scan runs.

Figure 5.13: Fitted direction resolution parameters β_M, β_S for the source scans in x, y, z-axes respectively.

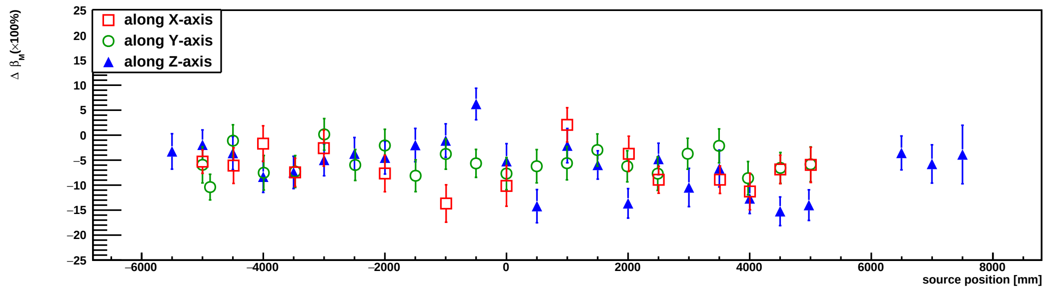

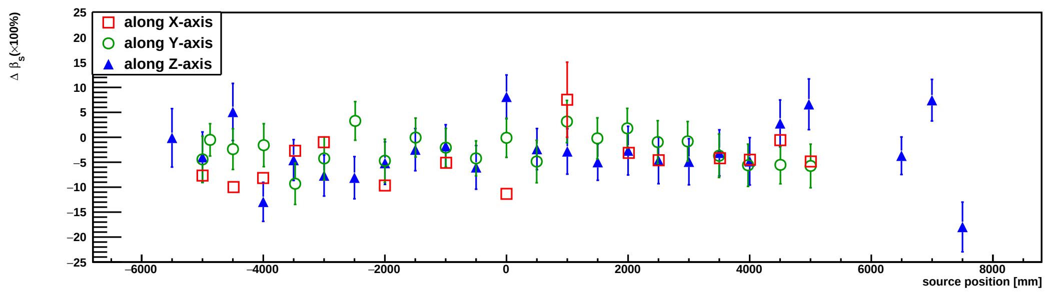

Figure 5.14: Relative differences of β_M and β_S as a function of the ^{16}N source position. For simplicity, the corner scans are not shown in this figure. The red squares represent the results from the x-scan runs; green circles represent the y-scan runs and the blue triangles represent the z-scan runs.

This angular remapping function is used to smear the angular distributions for systematic studies. In the next chapter, it will be applied on the angular distribution of solar neutrino data.

5.3.3 β_{14} and Its Systematic

Since β_{14} itself is used as the high-level cut, only the cuts of $ITR > 0.55$ and NHits> 5 were applied on the data and MC to extract the β_{14} distributions. Fig. 5.15 shows the β_{14} distributions of the central run-107055 data and MC, reconstructed by the `MPW fitter` and the official `RAT` fitter respectively. The β_{14} is calculated based on the reconstructed position, time, and direction of an event while the β_{14} distributions from the `MPW` and the `RAT` results are consistent. However, both of the two fitters show a discrepancy between the data and the MC. This discrepancy can be caused by inaccurate modeling of the Cherenkov process in the Geant4 simulation[170, 173]. Fig. 5.16 shows a comparison of the β_{14} for the data and the MC in run-107055. Both of the distributions are the MPW processed results and are fitted with Gaussian distributions in a region of $[-0.5, 1.5]$. The data shows a smaller Gaussian mean value, $\mu_{data} = 0.4157$, compared to the $\mu_{MC} = 0.4388$.

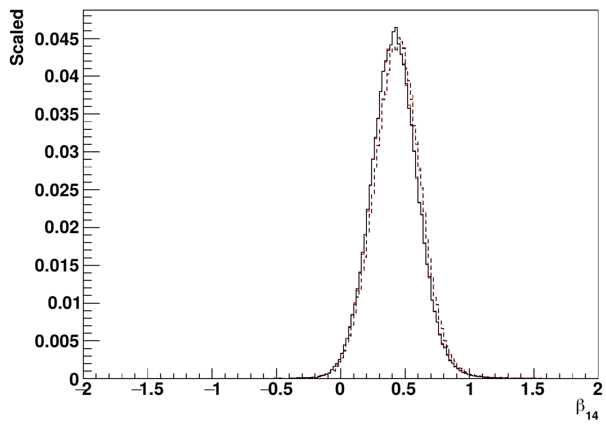

Figure 5.15: Distributions of β_{14} for the ^{16}N central run-107055. Dashed lines for the MC and solid lines for data; red for the `MPW fitter` processed results and black for the `RAT` results.

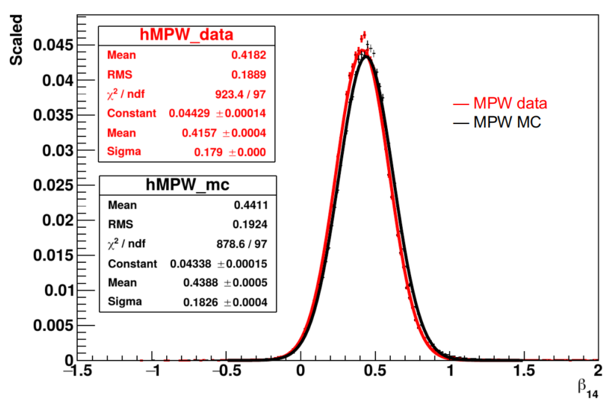

Figure 5.16: A comparison of the β_{14} for the data and the MC in run-107055.

Fig. 5.17 shows effects when the source moving along x, y and z axes. Taking all the 80 internal runs mentioned before, I calculated the $\Delta\beta_{14} \equiv \mu_{data} - \mu_{MC}$ for each run. The mean and standard deviation of these $\Delta\beta_{14}$ values were taken as the shift in β_{14}: -0.026 ± 0.010. Following the suggestion in Ref. [161], an asymmetric uncertain was taken: the upward shift was taken as $+0.010$ while the downward was taken as $-0.026 - 0.01 = -0.036$. Thus the shifts: $+0.010/-0.036$ were taken as the β_{14} systematics. It will be applied to the solar neutrino analysis in the next chapter.

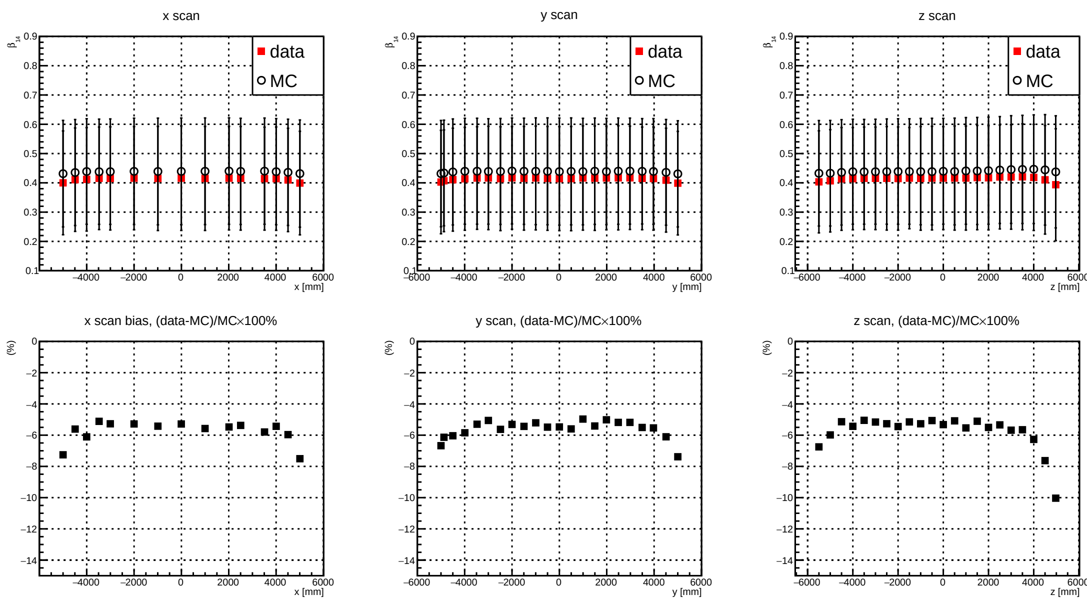

Figure 5.17: β_{14} systematic along x, y, z scans.

5.3.4 Energy Reconstruction Evaluation

5.3.4.1 Energy Figure of Merits

Three energy FoM quantities: G_{test}, U_{test} and Z_{factor} were introduced in Sect. 4.7.1. Here I used the MC simulations as well as the data of the ^{16}N central run-107055 to check the effects of the cuts on FoM quantities toreduce the energy biases. The sacrifices of the events were calculated.

- U_{test}: Fig. 5.18 shows U_{test} vs. energy biases. A cut of $0.61 < U_{test} < 0.95$ was suggested by the collaboration, to remove the events were mostly caused by the source encapsulation. This cut removes 0.38% of MC events and 0.34% of data events.

- G_{test}: Fig. 5.19 shows G_{test} vs. energy biases. A cut of $0 < G_{test} < 1.9$ was suggested by the collaboration, which removes 0.01% events for both MC and data.

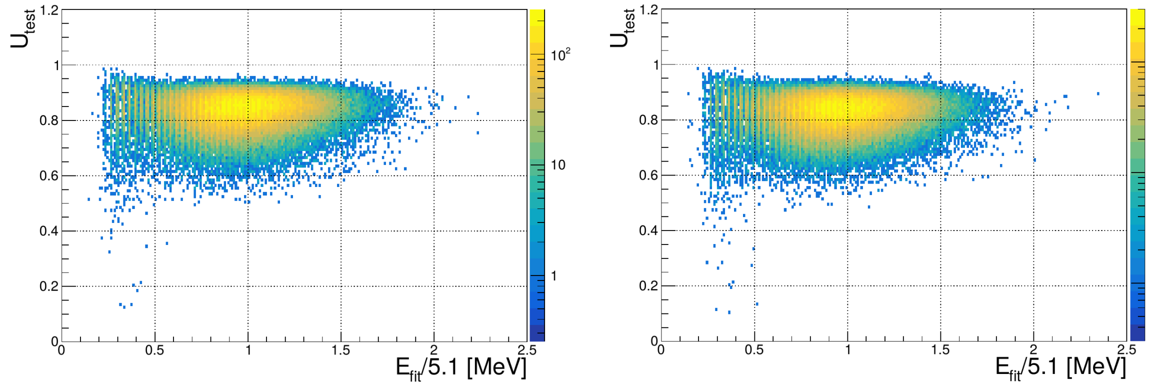

(a) MC (b) data

Figure 5.18: ^{16}N central-run 107055, U_{test} vs. $E_{fit}/5.1$ MeV.

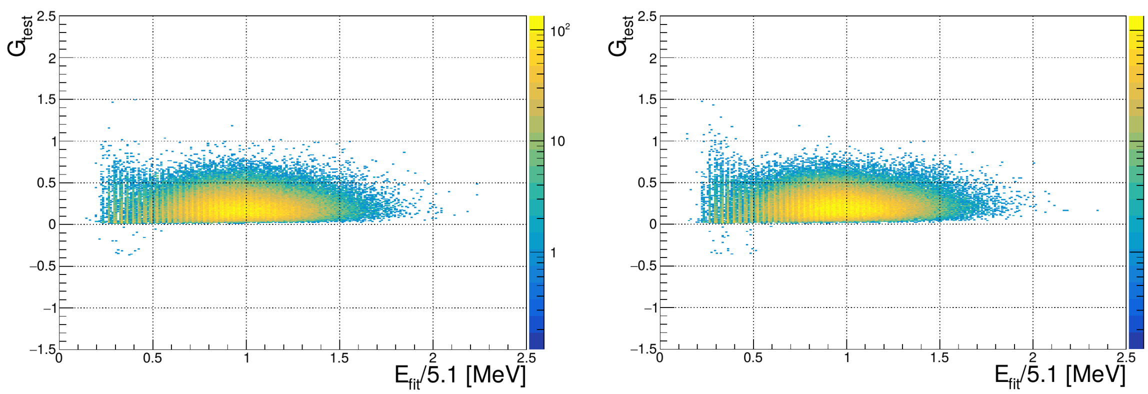

(a) MC (b) data

Figure 5.19: ^{16}N central-run 107055, G_{test} vs. $E_{fit}/5.1$ MeV.

- Z_{factor}: Fig. 5.20 shows Z_{factor} vs. energy biases. A cut of $-11 < Z_{factor} < 1$ was suggested by the collaboration, which removes 0.13% events for both MC and data.

All the cuts on the three energy FoM quantities remove 0.40% events from MC and 0.37% events from data. These cuts were also used in the water phase analysis in Chapter 6.

5.3.4.2 Energy Resolution and Systematics

The energy reconstruction algorithms for the water phase (mentioned in Sect. 4.7, Chapter 4) was applied on the ^{16}N MC simulations and data. The reconstructed energy of the ^{16}N

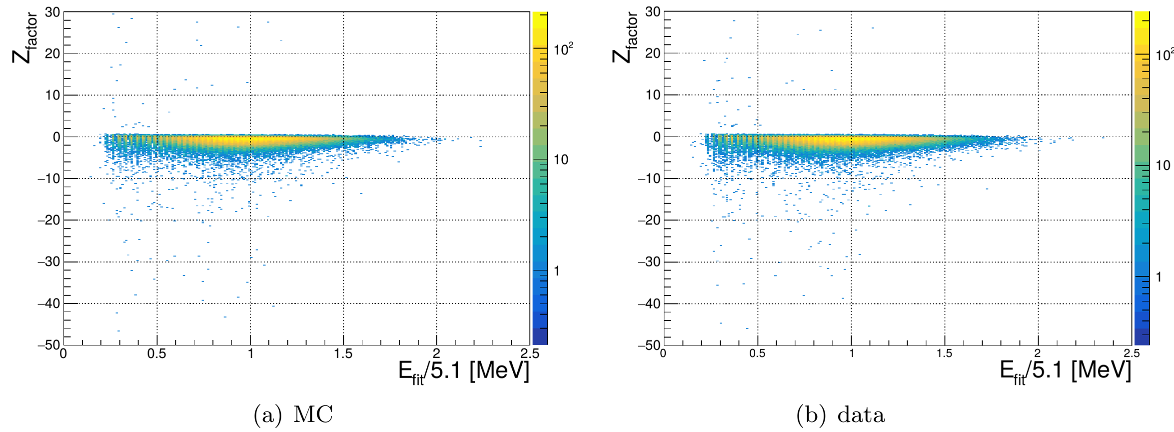

Figure 5.20: ^{16}N central-run 107055, Z_{factor} vs. $E_{fit}/5.1$ MeV.

events are shown in Fig. 5.21. The results from the MC and the data are compared.

5.3.4.3 Energy Resolutions

Following the methods described in Ref. [98, 161], a map that relates the number of Cherenkov photons to the electron energy is created by simulating mono-energetic electrons events with different energies at the detector center, as shown in Fig. 5.25 (a). By looking up the map and applying linear interpolation, the number of the photons created from the ^{16}N source is converted into an effective or apparent electron energy spectrum ($P_{source}(T_e)$)[161]. Fig. 5.25 (b) shows the effective electron spectrum of the ^{16}N central run-107055.

To obtain the energy reconstruction resolutions, the reconstructed energy spectrum $P(T_{eff})$ is fitted with the energy resolution function defined as[161]:

$$P(T_{eff}) = N \int P_{source}(T_e) \frac{1}{\sqrt{2\pi}\sigma_E} \exp\{-\frac{[(1+\delta_E)T_{eff} - T_e]^2}{2\sigma_E^2}\}, \tag{5.12}$$

where the predicted apparent energy spectrum, $P_{source}(T_e)$, is convolved with a Gaussian resolution function. In the Gaussian function, σ_E is the detector resolution and $\sigma_E = b\sqrt{T_{eff}}$, where b is the energy resolution parameter and δ_E is the energy scale parameter. The $P_{source}(T_e)$ is the apparent energy spectrum.

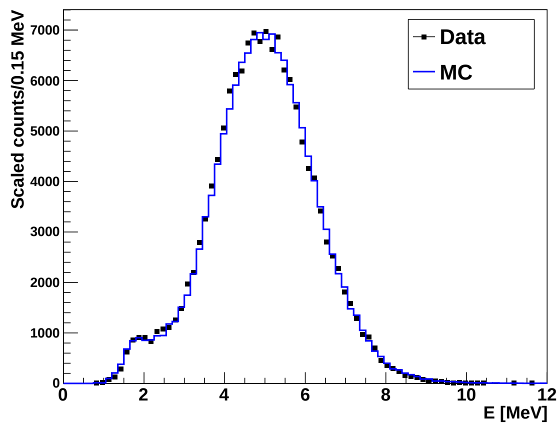

(a) ^{16}N run-106925

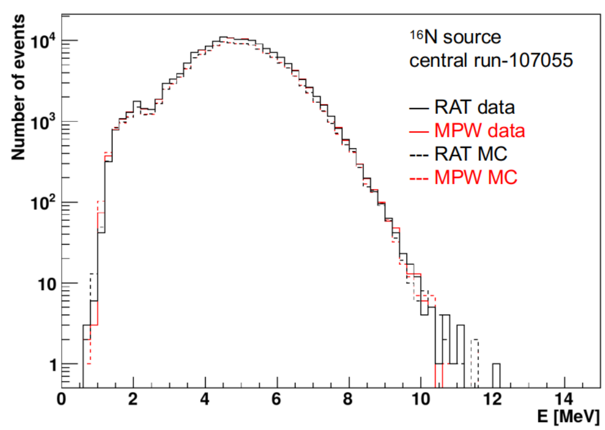

(b) ^{16}N run-107055

Figure 5.21: Reconstructed energy spectrum from the ^{16}N central run-106925 (top) and 107055 (bottom). For the run-106925 (top), the reconstructed data (black dots) are compared to the MC (blue line), both are `MPW fitter` results; for the run-107055 (bottom), the `MPW fitter` results and the `RAT` results are also compared. Dashed lines for the MC and solid lines for data; red for the `MPW fitter` results and black for the `RAT` results.

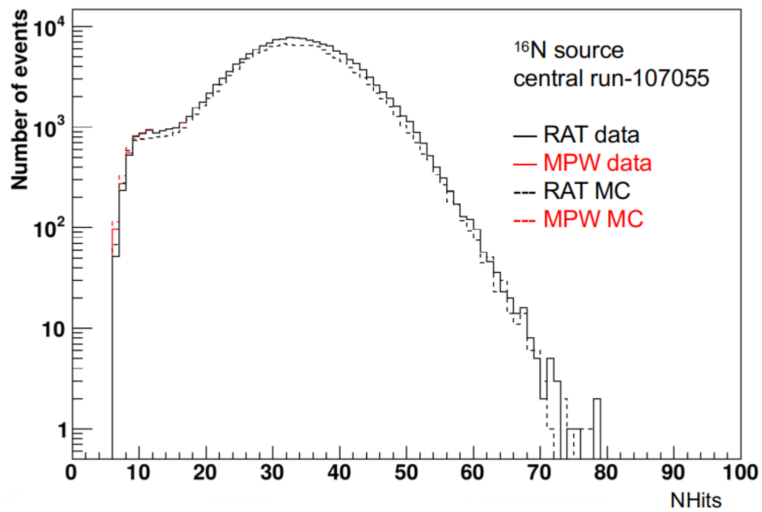

Figure 5.22: NHit spectrum for the ^{16}N central run-107055. Dashed lines for the MC and solid lines for data; red for the MPW fitter results and black for the RAT results.

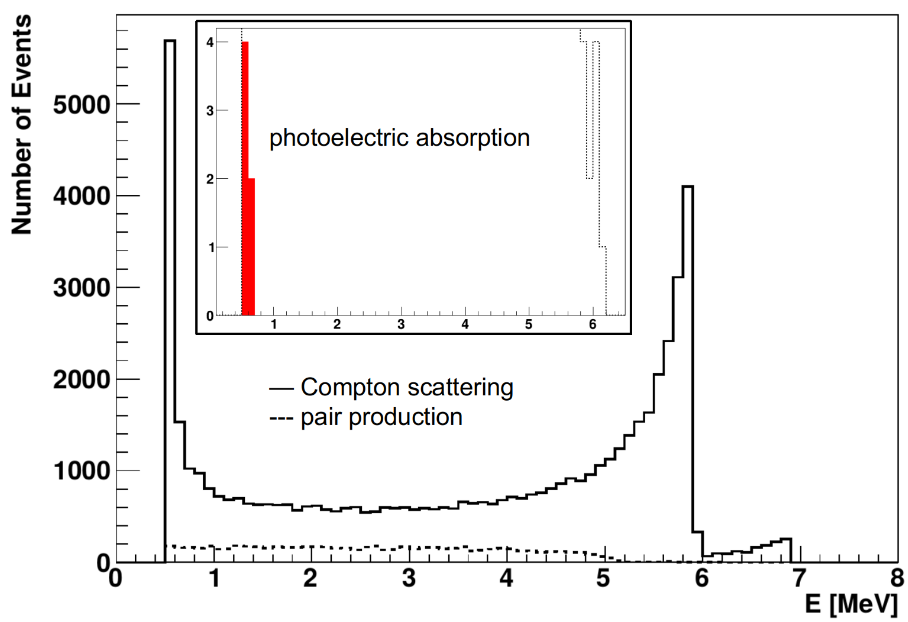

Figure 5.23: Simulated ^{16}N energy spectrum for different processes, extracted from 10^5 MC simulations.

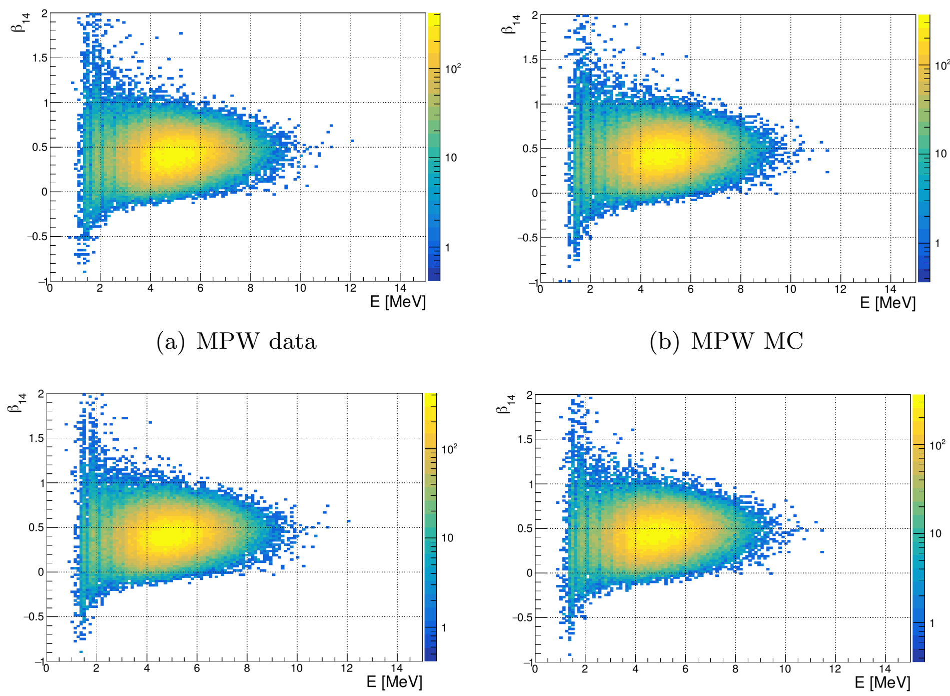

(a) MPW data

(b) MPW MC

(c) `RAT` data

(d) `RAT` MC

Figure 5.24: E_{fit} vs β_{14} for the data and MC. Both the `RAT` and the `MPW` results are shown.

Before fitting the reconstructed energy spectrum with the energy resolution function, a few cuts were applied on both the data and MC: the position FoM cut $scaleLogL > 10$ and the energy FoM cuts: $0 < G_{test} < 1.9$, $U_{test} < 0.95$ and $-11 < Z_{factor} < 1$ mentioned in the previous sections were used; the cuts of NHit> 5, $ITR > 0.55$ and $-0.12 < \beta_{14} < 0.95$ were used to remove instrumental backgrounds; a distance cut: $|\vec{X}_{fit} - \vec{X}_{src}| > 700\ mm$ was suggested by Refs. [174, 161] to remove the shadow effects when the events are close to the source container; for the event reconstructed within the 700 mm distance, if its direction $\vec{u}_{fit}$ is within 45° of the vector from the source to its vertex, i.e., if $\sqrt{2}/2 < \vec{u}_{true} \cdot \vec{u}_{fit} < 1$, its energy will also be kept.

A fit range of [3.5, 6.0] MeV was suggested by Ref. [161] to remove poorly reconstructed events due to the trigger inefficiency. Fig. 5.26 shows the energy resolution function fitted with the reconstructed energy spectrum of the ^{16}N central run-107055 data, after applying the cuts mentioned above.

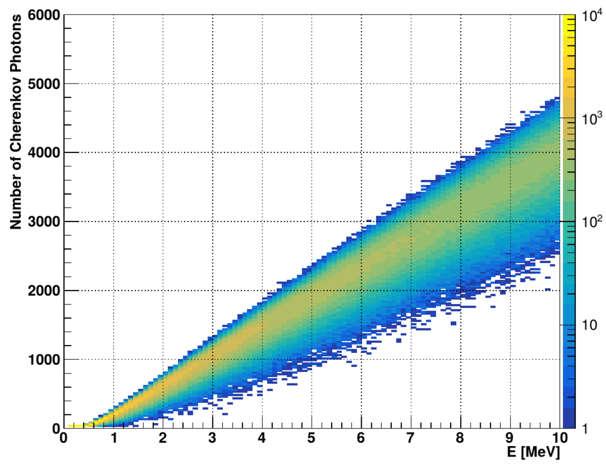

(a)

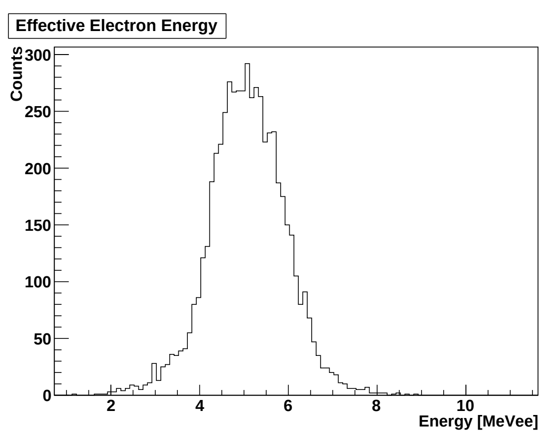

(b)

Figure 5.25: Converting number of photons to effective electron spectrum. (a): A 2D map of Electron energy vs number of Cherenkov photons. (b): Effective electron spectrum of ^{16}N central run-107055.

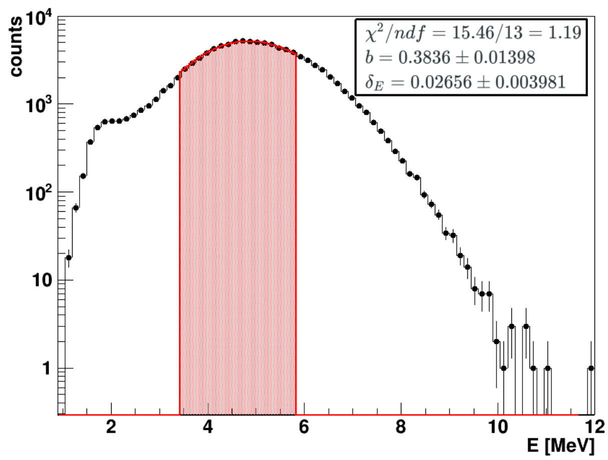

Figure 5.26: The reconstructed energy spectrum of central run-107055 data, fitted with the resolution function (red).

For all the internal scans, Fig. 5.27 and Fig. 5.28 show the energy scale (δ_E) and energy resolution (b) as a function of the radius of the source manipulation positions. Both the data and MC are shown.

5.3.4.4 Energy Uncertainties

By comparing the differences between data and MC, the uncertainties of the energy scale δ_E and resolution b are calculated as:

$$\Delta_\delta^2 = (\delta_{data} - \delta_{MC})^2 + \text{Error}^2_{\delta,data} + \text{Error}^2_{\delta,MC}, \tag{5.13}$$

where $\delta = b$ or δ_E, and $\Delta_b = \sqrt{\Delta_b^2}$ since the resolution is always positive; while $\Delta_{\delta_E} = \pm\sqrt{\Delta^2_{\delta_E}}$. The fit errors in data and MC were also included in the uncertainties.

Taking the ^{16}N scan runs within $r < 6$ m, the averaged uncertainties are: $\overline{\Delta_{\delta_E}} = 0.0107$ and $\overline{\Delta_b} = 0.0369$. For the ^{16}N scan runs within $r < 5.5$ m, which is the fiducial volume of the solar neutrino analysis mentioned in Chapter 6, $\overline{\Delta_{\delta_E}} = 0.0100$ and $\overline{\Delta_b} = 0.0320$.

To apply the energy scale systematics, the reconstructed energy E_{fit} is smeared by $E'_{fit} = (1 \pm \Delta_{\delta_E}) \cdot E_{fit}$, where the "+" sign is for scaling up the energy while "−" for scaling down. Fig. 5.29 shows the effects of smearing the energy scales on the reconstructed energy spectrum of the ^{16}N central run-107055. It is obvious that scaling up the E_{fit} widen the

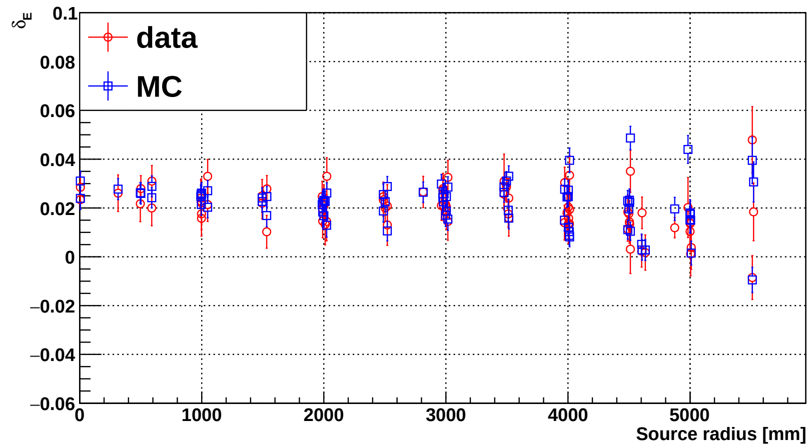

Figure 5.27: Fitted energy scales (δ_E) as a function of the source radial manipulation position. Red circles for data and blue squares for the MC.

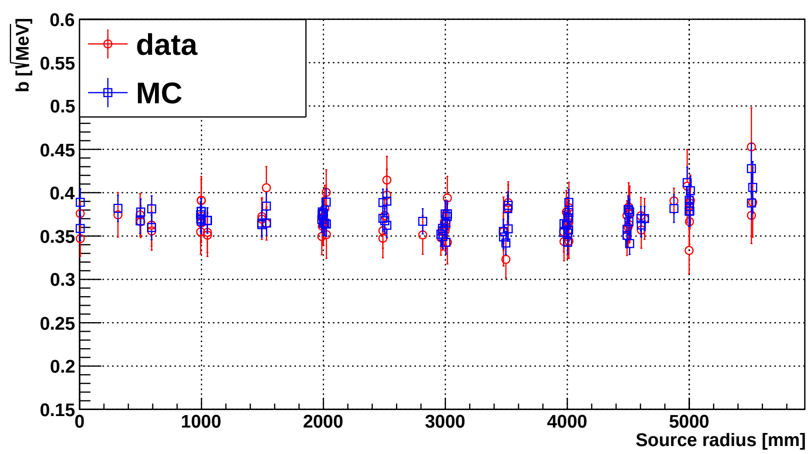

Figure 5.28: Fitted energy resolutions (b) as a function of the source radial manipulation position. Red circles for data and blue squares for the MC.

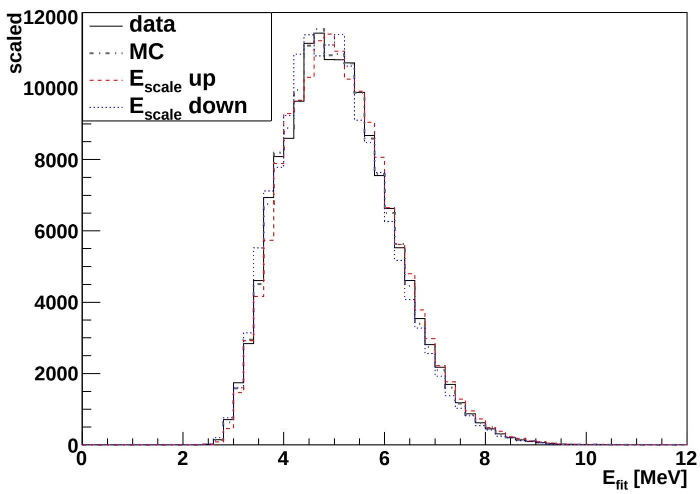

Figure 5.29: Smeared reconstructed energy spectrum of ^{16}N central run-107055. The solid black line is for data and the gray dash-dot line is for unsmeared MC; the red dash line is for scaling up the E_{fit} in MC; the blue dot line is for scaling down the E_{fit} in MC. Histograms are normalized to the total counts of the data.

E_{fit} spectrum while scaling down the E_{fit} narrows the spectrum.

To apply the energy resolution systematics, the spectrum of the reconstructed energy E_{fit} is convolved with an additional Gaussian resolution function $Gaus(0, \sigma_{smear})$, where $\sigma_{smear} = \sqrt{E_{fit}} \cdot \sqrt{(1+\Delta_b)^2 - 1}$. To smear the E_{fit} event by event, E_{smear} is randomly sampled from $Gaus(0, \sigma_{smear})$, and then $E'_{fit} = E_{fit} + E_{smear}$. Fig. 5.30 shows the effects of smearing the energy resolution on the E_{fit} spectrum of the ^{16}N central run-107055. It is obvious that smearing with the additional resolution coming from the uncertainties in b widen the E_{fit} spectrum. Because there is no unfolding procedure to improve or narrow the energy resolution, this energy resolution systematic is one-sided[171]. Therefore, in the analysis in Chapter 6, I simply took symmetric uncertainties with different signs.

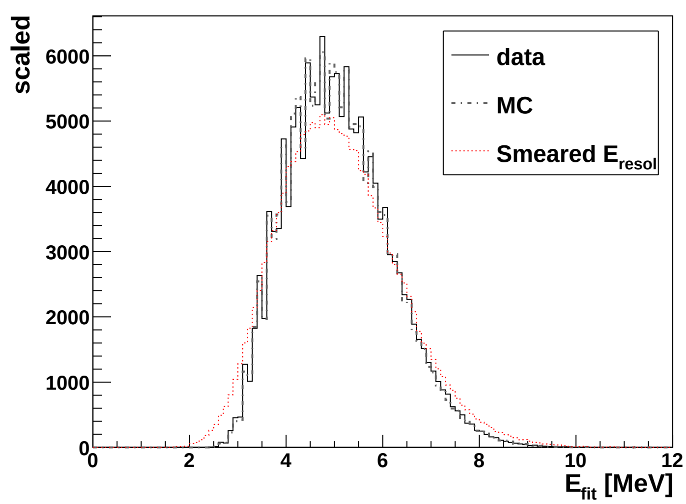

Figure 5.30: Smeared reconstructed energy spectrum of ^{16}N central run-107055. The red dash line is for smearing the E_{fit} with $Gaus(E_{fit}, \sigma)$. Histograms are normalized to the total counts of the data.

Chapter 6

Solar Neutrino Analysis in the SNO+ Water Phase

The SNO+ water phase data were taken from May 2017 to September 2018. The period from May 2017 to October 2018 is the first stage of the water phase. During this stage, several calibration runs were taken, including the ^{16}N calibration scans and the laserball scans. During the period from October 2018 to July 2019, over 20 tonnes of LAB (without PPO) was filled into the detector and the LAB mostly occupied the neck volume, slightly below the neck bottom. With the nitrogen cover gas on the top of the AV, the dataset taken during this period is called "low background dataset". The main analyses of this chapter are based on this low background dataset. The dataset was processed by the data cleaning procedure, and 4838 runs of data were used, which summed up a total live time of 190.33 days.

In this chapter, I applied the `MPW fitter` described in Chapter 4 to reconstruct the event vertex and direction for both the data and the run-by-run MC simulations. The run-by-run simulations simulated the full detector conditions for a specific run. The reconstructed event vertex and direction were further used by the `energy fitter`, the classifiers, and the high level cuts. Therefore, by using the alternative reconstruction framework which is different to the official SNO+ reconstruction (`RAT water fitter`), it provides alternative analyses on the data, which can bring helpful information, especially for the systematic uncertainties coming from the reconstruction.

First, a small amount of open dataset taken in 2017 was used to test the `MPW` results. The results from the `RAT water fitter` were compared. A new quantity called "Kullback–Leibler Divergence" was developed to evaluate the Cherenkov signals coming from the solar ν_e based on the simulations. After that, I mainly analyzed the low background dataset. I used sub-datasets of the run-by-run MC simulations to evaluate the ability of separating the solar ν_e signals from the backgrounds. The Toolkit for Multivariate Data Analysis with ROOT (`TMVA`) package[175, 176] was used to train and test on the MC simulations to obtain optimized discriminants. These optimized discriminants were applied on the whole dataset to remove the backgrounds.

The outputs from the data were fitted to obtain the number of signal events and the background events. Ensemble tests were performed on fake datasets to check the fit pull and bias. The systematics obtained from the ^{16}N calibration in Chapter 5 were applied on the results. Finally, the solar ν_e interaction rates and the ^{8}B solar neutrino flux were evaluated.

6.1 Backgrounds

6.1.1 Internal backgrounds

Most backgrounds come from natural radioactive isotopes inside or around the detector, such as the isotopes in the detection medium, detector materials and the PMTs. The major isotopes in the water phase are: ^{238}U, ^{232}Th, ^{40}K, and ^{222}Rn. These have been monitored by *in-situ* and *ex-situ* measurements and analyses.

The ubiquitous ^{238}U and ^{232}Th isotopes decay sequentially and form decay chains. The target level in the SNO+ water phase is 3.5×10^{-14} gram ^{238}U in per gram water (gU/gH$_2$O) and 3.5×10^{-14} gTh/gH$_2$O[161]. The rates of the background events caused by the decays from specific isotopes, especially the β-decays of ^{214}Bi (from the ^{238}U decay chain) and ^{208}Tl (from the ^{232}Th decay chain), were carefully calculated and were put into the simulations. In this chapter, the simulated background events from the ^{214}Bi and the ^{208}Tl β-decays were used to develop the multi-variable analysis to select solar neutrino events from the background events.

6.1.2 External backgrounds

As mentioned in Chapter 3, Sect. 3.1, since the depth of the SNO+, the cosmogenic backgrounds induced by the cosmic muons are very few, while there exist muon events and muon follower events. There are also instrumental backgrounds, such as the flashers from the PMTs, noises from PMT channels, etc. In order to remove these external backgrounds, a set of data cleaning cuts are applied to the actual data by using the analysis mask. In the following analyses, the data cleaning cuts were always applied to the actual data.

6.2 Solar neutrino Analysis in Open Dataset

The open dataset was taken in 2017 at the beginning of the water phase from run-100000 to 100399, which has a live time of 16.607 days. This open dataset was used to compare the reconstructed events by the `MPW fitter` and the `RAT water fitter`.

In the SNO+ water phase, solar ν_es are measured via elastic scattering: $\nu_e + e^- \rightarrow \nu_e + e^-$ ($\nu + e^-$ ES, see Sect. 2.2.1). The observable quantity is the solar angle θ_{sun}, the direction of the event relative to the Sun's location, which is defined as:

$$\cos\theta_{sun} \equiv \vec{u}_{event} \cdot \frac{\vec{X}_{event} - \vec{X}_{sun}}{|\vec{X}_{event} - \vec{X}_{sun}|}, \tag{6.1}$$

where $\vec{X}_{sun}$ is taken as the Sun's location relative to the SNOLAB location since the whole lab can be treated as a point regarding the long distance to the Sun.

For the open dataset, the data cleaning mask and high level cuts: $ITR > 0.55$ and $-0.12 < \beta_{14} < 0.95$ (mentioned in Sect. 5.2, Chapter 5) were applied to the actual data. These cuts were suggested by the collaboration, which were mostly based on the experiences for removing the instrumental backgrounds[161].

Table 6.1: Candidate events in the open dataset. Compared the fit results of the candidate events with different fitters.

Fitter	Run	GTID	$z - 0.108$(m)	R(m)	$(R/R_{av})^3$	$\cos\theta_{sun}$	SNO+ Day
Rat	100093	11108354	3.49	3.57	0.21	-0.954	2683.92
MPW	–	–	3.43	3.52	0.20	-0.906	–
Rat	100207	5079885	-2.61	4.60	0.45	0.816	2687.04
MPW	–	–	-3.63	**7.61**	2.03	**0.656**	–
Rat	100632	7882360	1.77	3.19	0.15	0.937	2696.93
MPW	–	–	1.67	3.11	0.14	0.911	–
Rat	100663	15767175	-4.33	4.96	0.56	0.978	2698.18
MPW	–	–	-4.45	5.07	0.60	0.980	–
Rat	100915	169700	-1.00	5.10	0.61	0.341	2701.23
MPW	–	–	-1.08	5.08	0.61	0.337	–

Table 6.2: Candidate events in the open dataset searched by the `MPW fitter`.

Run	GTID	E_{fit} (MeV)	$z - 0.108$ (m)	R (m)	$(R/R_{av})^3$	$\cos\theta_{sun}$
100093	11108354	5.83	3.43	3.52	0.20	-0.907
100632	7882360	6.18	1.67	3.11	0.14	0.915
100663	15767175	6.18	-4.45	5.07	0.60	0.981
100915	169700	5.68	-1.07	5.08	0.61	0.339
100984	8621621	5.70	0.76	4.75	0.502	-0.648
101075	11673714	5.67	4.43	5.18	0.64	0.587

First, all the solar neutrino candidate events found by the `Rat water fitter` were refit by the `MPW fitter`. The results are compared in Table. 6.1. For each events, their hit PMT distributions as well as the reconstructed positions and directions from the two fitters are compared in Fig. 6.1.

It shows that, for the candidate events, the results from the `MPW` are mainly consistent with the `RAT`, while the `MPW` disfavored one event in run-100207, with GTID=5079885, as its position is outside the AV and $\cos\theta_{sun}$ is away from $+1$.

Besides, instead of refitting the candidate events found by the `RAT`, the `MPW` results were used directly to search for the candidate events, as shown in Table. 6.2. From the table, the `MPW` also obtained alternative candidate events. Therefore, the `MPW` can provide an alternative analysis of the solar neutrinos.

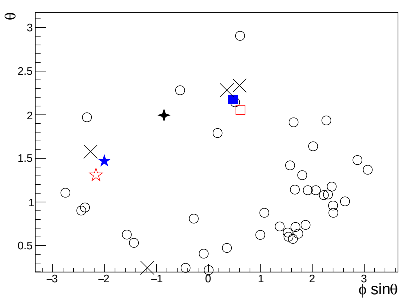

(a) Run 100093, GTID 11108354

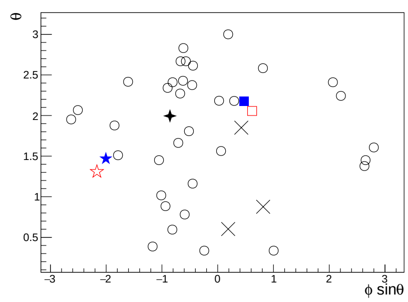

(b) Run 100207, GTID 5079885

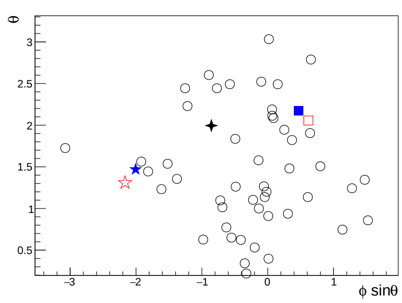

(c) Run 100632, GTID 7882360

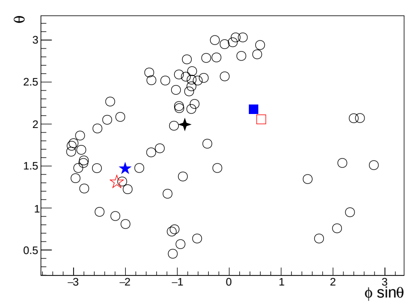

(d) Run 100663, GTID 15767175

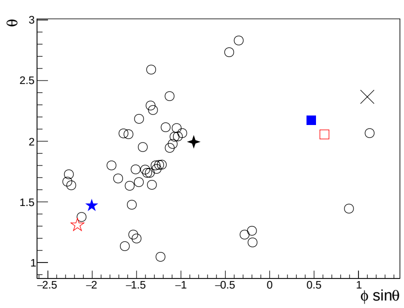

(e) Run 100915, GTID 169700

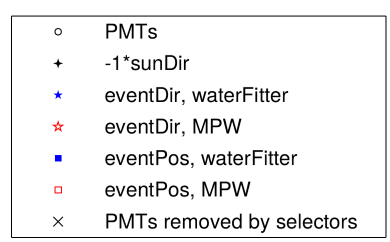

(f) Legends

Figure 6.1: Reconstruction results for the candidate events, projected onto PMT sinusoidal maps. Black circles stand for the hit PMTs used by the fitter; crosses stand for the hit PMTs removed by the selectors; blue full star stands for the event direction fitted by the `Rat water fitter`; red open star stands for the direction fitted by the `MPW fitter`; full double diamond stands for the solar direction*-1; blue full square stands for the event position fitted by the `Rat water fitter`; open square stands for the position fitted by the `MPW fitter`.

6.3 Likelihood Fits for Solar Neutrino Candidate Events

From this section, I focus on the 190.33 live-day low background dataset taken in the second stage of the water phase with the nitrogen cover gas on the top of the AV.

In this section, a maximum likelihood fit method for counting the number of the candidate solar neutrino events (N_{sig}) and background events (N_{bkg}) in a dataset is discussed. To check the method, the dataset from the run-200004 to 203602 was used. This dataset has a live time of 92.54 days, about a half of the whole 190.33 live-day dataset, so it is denoted as the "half-dataset". The actual data and the run-by-run MC simulations of this half-dataset were used for testing the analyses in this section and the next.

Before the analysis, a few "beforehand cuts" were applied: NHits$>$ 20, $R'_{fit} < 5500\,mm$, $ITR > 0.55$, and $-0.12 < \beta_{14} < 0.95$. Here NHits$>$ 20 is a reconstruction threshold set for the solar neutrino analysis, which means that only the events with NHits$>$ 20 were reconstructed by the `MPW fitter`. The R'_{fit} is the magnitude of the reconstructed event position $\vec{X}_{fit}$ after the AV coordinate correction: $R'_{fit} \equiv \sqrt{x^2_{fit} + y^2_{fit} + (z_{fit} - 108)^2}$ (the 108 mm offset in z was discussed in Chapter 3 and Chapter 4.). The cut on R'_{fit} defines a fiducial volume of 5500 mm for solar neutrino analysis. Finally, the high level cuts ITR and β_{14} cuts were mentioned previously.

6.3.1 Maximum Likelihood Fit

To prepare for the fit, the values of the solar angle, $\cos\theta_{sun}$ from the data were filled into a histogram in a range of [-1,1] with 40 bins. For each bin, the observed event number (n_{obs}) was considered as a sum of solar ν_e and background events. The n_{obs} in each bin was assumed to follow a Poisson distribution: $Poisson(n_{obs}, N_{bkg} \cdot P_{bkg} + N_{sig} \cdot P_{ES}(E))$, where P_{bkg} and $P_{ES}(E)$ are the assumed distribution of backgrounds and solar ν_e events respectively.

For the background events, a uniform distribution of $\cos\theta_{sun}$ was assumed. On the other hand, the $\cos\theta_{sun}$ distributions of solar ν_e were extracted from the realistic run simulations after applying the beforehand cuts, as shown in Fig. 6.2.

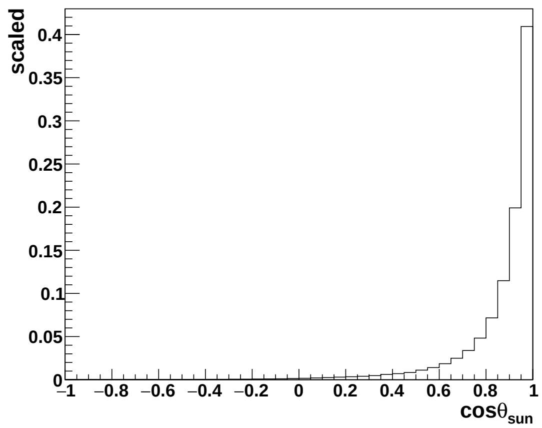

Figure 6.2: The $\cos\theta_{sun}$ distribution of solar ν_e extracted from the simulations, which is used as a PDF function. It is scaled to its integral.

Adding up each bin i and taking N_{bkg} and N_{sig} as the free parameters for fitting, the maximum likelihood function was built as[21]:

$$-2\ln\lambda(N_{sig}, N_{bkg}) = 2\sum_{i=0}^{N_{bins}}[\mu_i(N_{sig}, N_{bkg}) - n_i + n_i \ln\frac{n_i}{\mu_i(N_{sig}, N_{bkg})}], \tag{6.2}$$

where $\mu_i(N_{sig}, N_{bkg})$ is the expected number of events in each bin: $\mu_i(N_{sig}, N_{bkg}) = N_{sig} \cdot P^i_{ES}(E^i) + N_{bkg} \cdot 1/N_{bins}$; N_{bins} is the total number of the bins, usually taken as 40 (per 0.05 bins). This quantity also includes the cases when the bin contains zero ($n_i = 0$).

Fitting the data with (N_{bkg}, N_{sig}) by maximizing the quantity $-2\ln\lambda$, the best fit of the N_{bkg} and N_{sig} were obtained. In the next section, an ensemble test based on fake datasets was applied for testing the fit performances.

6.3.2 Ensemble Test

To check the uncertainty of the Poisson fit, 5000 fake datasets were generated. Here I used the method similar to the Ref. [174]. The MC dataset includes the run-by-run simulations from the 92.54 live-day half-dataset (run-200004 to 203602).

The fake data were taken from the run-by-run MC simulations of the half-dataset. The beforehand cuts were applied to these simulations.

The number of backgrounds in a fake dataset, N^f_{bkg}, was assumed to be two times of the event number in the $-1 < \cos\theta_{sun} < 0$ region while the number of signals $N^f_{sig} = N^f_{total} - N^f_{bkg}$. These numbers were determined by the actual data, rather than the simulations. Fig. 6.3 shows the actual data of the half-dataset, after the data-cleaning cuts and beforehand cuts. Reading from the actual data, it found $N^f_{bkg} = 38$ and then $N^f_{sig} = 109 - N^f_{bkg} = 71$. To do the ensemble test, for each fake dataset, two random numbers: N^r_{sig} and N^r_{bkg} were generated by the `ROOT TRandom3` random number generator class. Each of the two random numbers followed the random Poisson distribution: $e^{-\mu}\mu^{N^r}/N^r!$, where $\mu = 71$ or 38, and thus they fluctuated around N^f_{sig} or N^f_{bkg}.

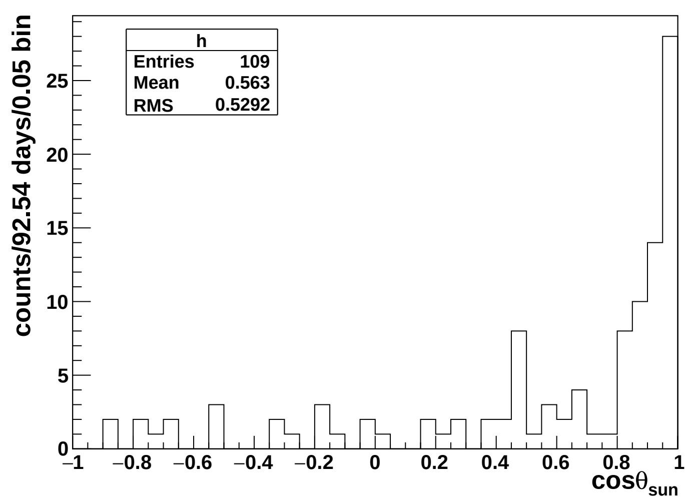

Figure 6.3: Real data from run-200004 to 203602 (half-dataset), after the beforehand cuts. The number of counts in the $-1 < \cos\theta_{sun} < 0$ region is 19.

To create the fake datasets, from the solar ν_e MC simulations, N^r_{sig} events which passed the cuts were randomly selected; similarly, from the merged background simulations, N^r_{bkg} events were randomly selected. These randomly selected events were merged into a fake dataset, and their values of E_{fit} and $\cos\theta_{sun}$ were recorded. By repeating the random selection, an ensemble of fake datasets were created. Each fake dataset was fitted with the maximum likelihood function described in Sect. 6.3.1. Fig. 6.4 shows an example of the fit results from a random fake dataset.

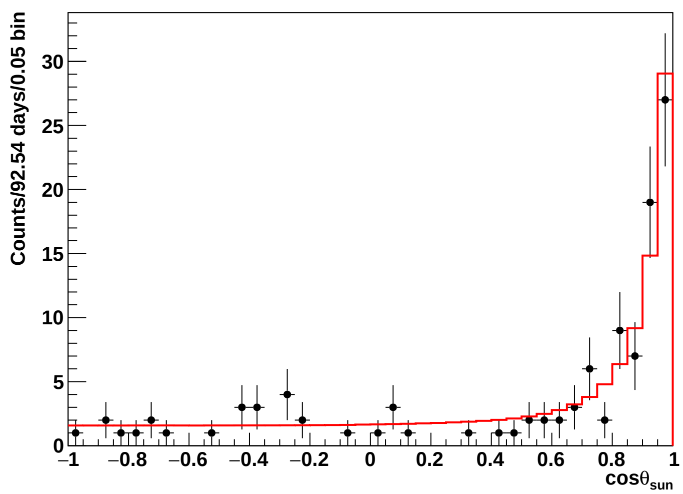

Figure 6.4: An example of the $\cos\theta_{sun}$ distribution from a fake dataset fitted with (N_{sig}, N_{bkg}). The black dots are data points and the red line shows the fit. For $N^r_{sig} = 73$ and $N^r_{bkg} = 44$, the fit results are $N_{sig} = 73.42 \pm 9.42$ and $N_{bkg} = 43.58 \pm 7.73$, with a $\chi^2/ndf = 60.19/40 = 1.50$.

The fit pull and the fit bias were defined by [174]:

$$bias = \frac{N_{sig} - N^r_{sig}}{N_{sig}}, \tag{6.3}$$

$$pull = \frac{N_{sig} - N^r_{sig}}{\sigma_{sig}}, \tag{6.4}$$

where N_{sig} is the fitted number of signal events, σ_{sig} is the statistical uncertainty of N_{sig}; N^r_{sig} is used as the true number of signal events in the fake dataset.

Fig. 6.6 and Fig. 6.5 show the fit pull and biases respectively. The histograms were fitted with Gaussians. For the fitted number of signal events, the Gaussian mean of the fit biases is -0.0044 ± 0.0008 for 5000 fake datasets while the Gaussian mean of the fit pulls is -0.026 ± 0.006. These pulls and biases will be applied on the data. Fig. 6.7 shows the distributions of the $-2\ln L$ returned by the best fit result ($-2\ln L_{best}$) for each fake dataset. The distribution, $f(-2\ln L_{best})$, follows the asymptotic χ^2 PDF with a degree of 40 and is used to compute the $p-values$[21]. For a best-fit set (N^i_{sig}, N^i_{bkg}) with a value of $-2\ln L^i_{best}$, the $p - value$ is calculated as $p = \int_{-2\ln L^i_{best}}^{-2\ln L^{max}_{best}} f(-2\ln L_{best}) d(-2\ln L_{best})$.

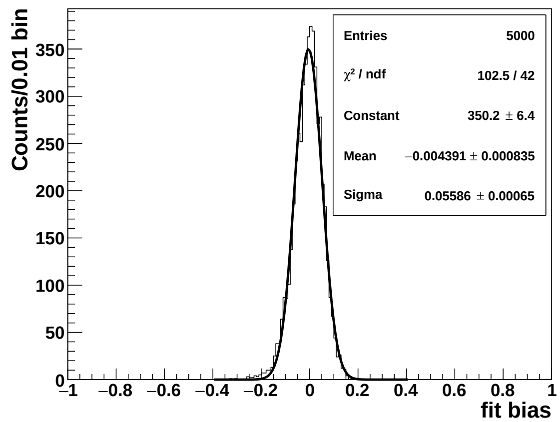

Figure 6.5: N_{sig} fit biases for 5000 fake datasets.

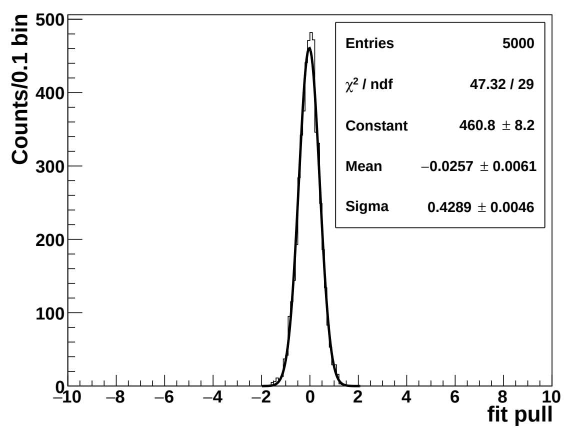

Figure 6.6: N_{sig} fit pulls for 5000 fake datasets.

6.3.3 Kullback–Leibler Divergence for High Level Cuts

For the solar neutrino analysis, I used a quantity called "Kullback–Leibler (KL) divergence" (also called "relative entropy") as a new quantity of classifier for checking the reconstruction of a possible solar neutrino event. The KL divergence is used to measure the dissimilarity of two probability distributions[177]. For an event, its reconstructed angular distribution to the PMT is: $\cos\theta_{Ch} = \vec{u}_{fit} \cdot (\vec{X}_{PMT} - \vec{X}_{fit})/|\vec{X}_{PMT} - \vec{X}_{fit}|$, and it is compared with the averaged angular distribution of solar ν_e events extracted from the MC simulations (with the reconstructed $\vec{u}$ and $\vec{X}$ from MC), which is set as the nominal distribution. It considers

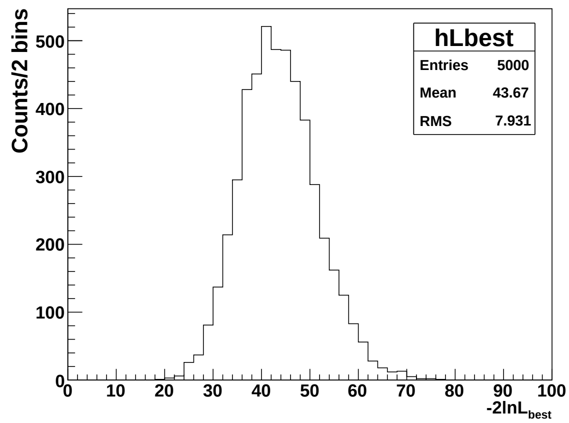

Figure 6.7: The $-2\ln L$ distribution of the best fit results from the 5000 fake datasets.

that the solar ν_e events produce nice Cherenkov angular distribution, which is peak around the Cherenkov angle ($\theta_{Ch} \sim 0.75$). On the other hand, background events with lower energies may have smeared distributions. The dissimilarity of the event distribution to be investigated and the nominal distribution is calculated. The quantity $klDiv(p||q)$ is calculated as:

$$klDiv(p||q) \equiv \sum_{i}^{N} p(x_i) \log \frac{p(x_i)}{q(x_i)}, \tag{6.5}$$

where $p(x_i)$ is the angular distribution after a time residual window cut: $-5 < t_{Res} < 1$ ns, to extract prompt Cherenkov lights. Both of the event and the MC distributions were filled into a histogram with 40 bins ranging from [-1,1] and the $klDiv$ values were calculated bin by bin except the empty bins (zero count). A small $klDiv$ value indicates a small dissimilarity.

These values were used for distinguishing the signal from backgrounds, which will be discussed in the Sect. 6.3.4. Fig. 6.8 shows an example of the $klDiv$ calculation. Two events are compared here: one is a randomly selected event from the solar ν_e run-by-run MC (E = 4.78 MeV), the other is from the ^{214}Bi MC (E = 2.18 MeV), with the same event GTID. Their $\cos\theta_{Ch}$ distributions were scaled to the nominal one. It can be seen that the background event with lower energy is more dispersive while the signal event has a peak around the Cherenkov angle, and thus its shape is more close to the PDF. The calculation of 6.5 gives $klDiv(solar\ \nu_e) = 11.78$ and $klDiv(^{214}Bi) = 22.69$, which verifies the observation.

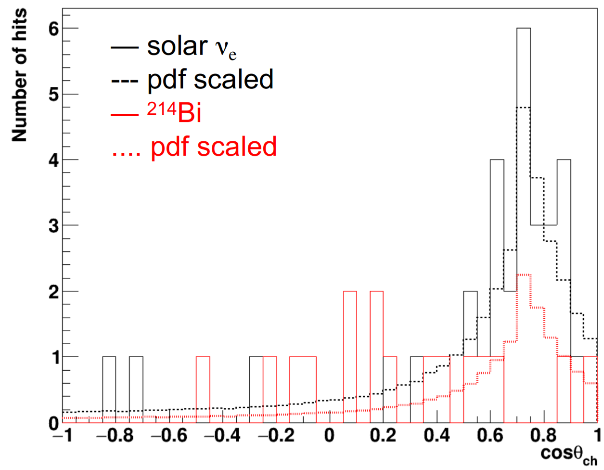

Figure 6.8: Angular distributions of the MC events in run-by-run simulations of run-206391, with the same event (GTID = 7). The black line is the MC solar ν_e distribution, while the red line is the MC ^{214}Bi distribution. The PDF is scaled to the number of the hits in solar ν_e event (dashed black line) and the ^{214}Bi event (dotted red line) respectively.

A symmetrical form of $klDiv$ can be taken as:

$$klDiv(p,q) \equiv \frac{1}{2}\sum_{i}^{N}(p\log\frac{p}{q} + q\log\frac{q}{p}), \tag{6.6}$$

Since $klDiv(p,q) = klDiv(q,p)$, it has a meaning of distance. This symmetric quantity is used in the TMVA method in Sect. 6.3.4.

6.3.4 Signal-background Discrimination Based on TMVA

To further reduce the background events, besides the beforehand cuts mentioned in the previous section, the cuts applied on the position and energy FoMs, as well as the $klDiv$, were also considered. The FoM cuts suggested by the collaboration are[178]: $-11 < Z_{factor} < 1$, $scaleLogL > 10.85$, $0 < G_{test} < 1.9$, $U_{test} < 0.95$, $ITR > 0.55$, $-0.12 < \beta_{14} < 0.95$[1] . These cuts are denoted as "default cuts".

[1]These cuts are mainly based on the ^{16}N analyses. There is also a suggested cut on the quantity of position error (position error< 525 mm). However, this quantity was not calculated by the `MPW fitter`, so it was not included here.

To optimize the cuts on the FoM and *klDiv* variables, the `TMVA` package was used. The run-by-run simulations of the solar neutrinos (as signals) and various backgrounds were used to train the machine learning methods in the TMVA. All these variables were used as inputs for training the signal-background discrimination.

For the MC dataset, two types of background isotopes, ^{208}Tl and ^{214}Bi were simulated in different detector regions. In this study, the background events simulated in the inner AV (internal backgrounds), in the AV, and in the external water region were checked. The solar ν_e events simulated in the inner AV were used as signals. Table. 6.3 summarizes the types of simulations used in this study.

Table 6.3: Datasets of MC simulations.

Simulations	Simulated positions in the detector
^{208}Tl	inner AV (internal ^{208}Tl)
–	AV
–	external water (external ^{208}Tl)
^{214}Bi	inner AV (internal ^{214}Bi)
–	AV
–	external water (external ^{214}Bi)
Solar ν_e	inner AV (internal ν_e)
–	AV
–	external water (external ν_e)

Different types of the simulations were merged into a mixed dataset. The simulated solar ν_e events are tagged as signals and mixed with ^{214}Bi and ^{208}Tl background events. The total dataset was divided into training and testing sets.

Fig. 6.9 shows the energy spectrum of simulated internal events with their fitted positions inside the 5.5-m fiducial volume, i.e., with a radial cut of $R'_{fit} < 5.5$ m.

From the simulations of the half-dataset, runs from run-200004 to 202516 were taken as the training set (about 67 live days and 72.4% of the half-dataset), and the rest 27.6% (run-202517 to 203602) were taken as the testing set[2] . The machine learning algorithms in the TMVA train the weights of the input variables by using the training set, while they apply

[2]For a more unbiased analysis, a bootstrap method[177] that randomly separates the training and testing datasets can be used, but it is not applied here.

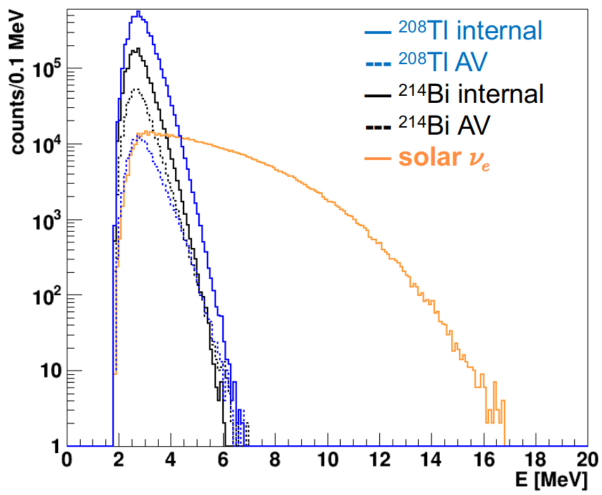

Figure 6.9: Energy spectrum of events from different simulations in the half-dataset: ^{214}Bi (black), ^{208}Tl (blue) and solar ν_e (orange). Solid lines show the internal events and dotted lines show the AV events.

the trained weights to the testing set for validations of the signal-background separation. Once the weights of the input variables were obtained, they were applied to the actual data.

Three ranges of E_{fit} were tested: $4 < E_{fit} < 15$ MeV, $5 < E_{fit} < 15$ MeV ($E > 5$ MeV region), and $4 < E_{fit} < 5$ MeV (low energy region).

After applying these beforehand cuts, for the different energy regions, the ratios of the signal event numbers (N_{sig}) to the background event numbers (N_{bkg}) are listed in Table. 6.4. It shows that, in the low energy region $4 < E_{fit} < 5$ MeV, the background events are dominant, while for the $E_{fit} > 5$ MeV, the background events are significantly reduced.

Table 6.4: Ratios of the signal event numbers to the background event numbers.

energy region (MeV)	N_{sig}	N_{bkg}	N_{sig}/N_{bkg}
$4 < E_{fit} < 15$	434830	166280	2.6
$5 < E_{fit} < 15$	317205	6359	49.9
$4 < E_{fit} < 5$	117625	159921	0.73

Three machine-learning algorithms/classification methods implemented in the `TMVA` package were applied to the training and testing datasets: the Fisher discriminants/linear discriminant analysis (Fisher/LD), the Boosted Decision Tree (BDT), and the Artificial Neural

Networks Multilayer Perceptron (ANN-MLP, or MLP in short)[176].

The Fisher discriminant $y_{F_i}(i)$ for classifying event i is defined by [175]:

$$y_{F_i}(i) = F_0 + \sum_{k=1}^{n_{params}} F_k x_k(i), \tag{6.7}$$

where n_{params} is the number of input variables, and the Fisher coefficients F_k is given by:

$$F_k = \frac{\sqrt{N_S N_B}}{N_S + N_B} \sum_{l=1}^{n_{params}} 1/W_{kl}(\bar{x}_{S,l} - \bar{x}_{B,l}), \tag{6.8}$$

where $N_{S(B)}$ are the number of signal (background) events in the training sample; $\bar{x}_{S(B),l}$ are the means of input variables for signal (background); W_{kl} is the covariance matrix[175].

For the settings in the TMVA, the BDT method was set with: (1) using the adaptive boosting (AdaBoost) algorithm; (2) training 400 trees with a maximum depth of 3; and (3) using gini index for the decision tree.

The MLP method was set with: (1) using sigmoid function as the activate function; and (2) using neural networks with 4 hidden layers and 200 training cycles.

There are 9 variables used as the TMVA inputs: ITR, β_{14}, E_{fit}, G_{test}, U_{test}, $scaleLogL$, Z_{factor}, $\vec{u} \cdot \vec{R}$ and $klDiv$ (in the symmetrical form: Eqn. 6.6). Among them, the beforehand cuts had been applied to the ITR and β_{14}, and the E_{fit} had been selected for different regions, as mentioned previously. Here the NHits and θ_{ij} were not used, since the NHits is correlated to the energy, while the θ_{ij} is anticorrelated to the β_{14}, which can be redundant inputs.

Using the $4 < E < 15$ MeV training dataset as an example, the distributions of these variables are shown in Fig. 6.10. The differences in distributions between the signal inputs (black solid lines) and background inputs (red dotted lines) can be observed.

The output signal/background distributions on the test sub-dataset are shown in Fig. 6.11.

As one of the essential TMVA output, the background rejection versus signal efficiency curve is denoted as a receiver operating characteristic (ROC) curve, which is usually used to test the performance of machine learning classifier. A quantity taking the integrals of

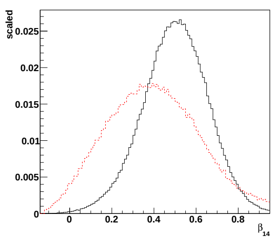

(a) β_{14}

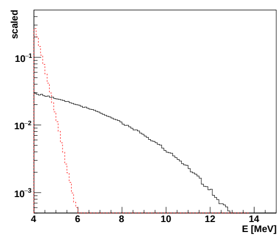

(b) E_{fit}

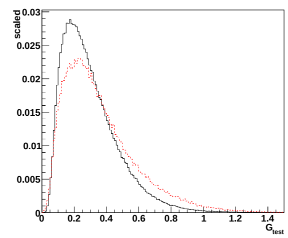

(c) G_{test}

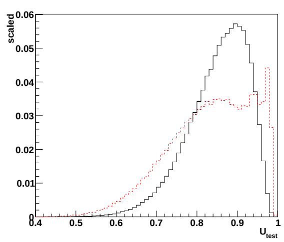

(d) U_{test}

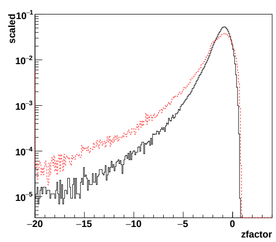

(e) Z_{factor}

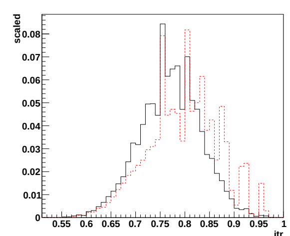

(f) ITR

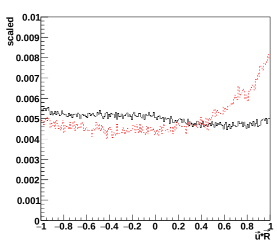

(g) $\vec{u} \cdot \vec{R}'$

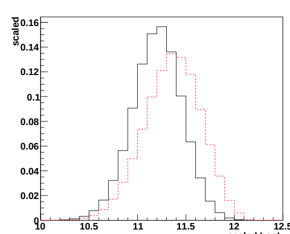

(h) $scaleLogL$

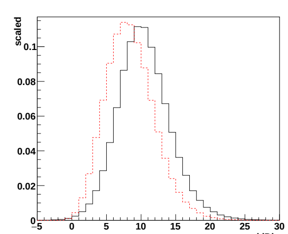

(i) $klDiv$

Figure 6.10: Multiple variables as the inputs for the TMVA analysis, for the $4 < E < 15$ MeV dataset. The distributions of the backgrounds are show in dotted red lines while the signals are shown in solid black lines. The distributions are normalized to their integrals.

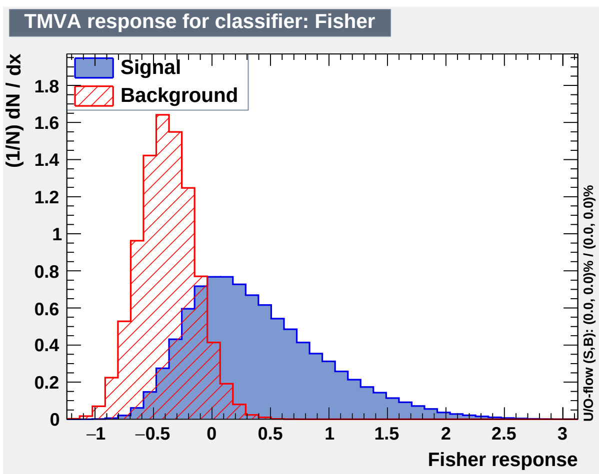

(a) Fisher/LD output.

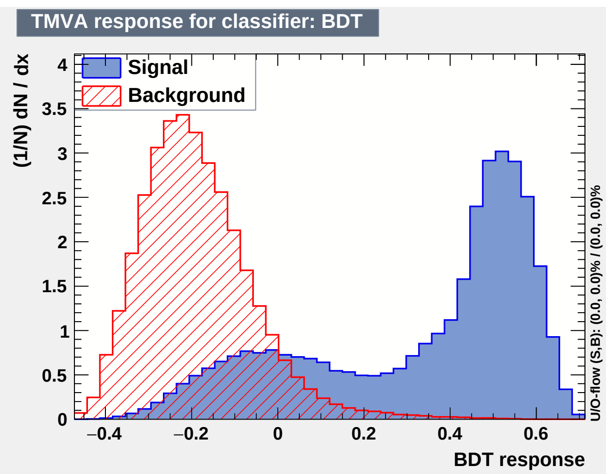

(b) BDT output.

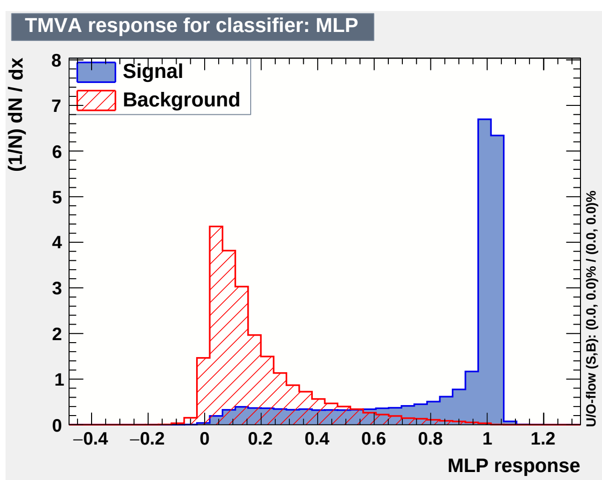

(c) MLP output

Figure 6.11: TMVA outputs for signal/background separations by different methods, for the $4 < E < 15$ MeV testing dataset.

the ROC curve: called the "area under the curve" (AUC) is often used to summarize the quality of a ROC curve[177]. Fig. 6.12 shows the ROC curves for three different methods and for the testing datasets with different energy regions.

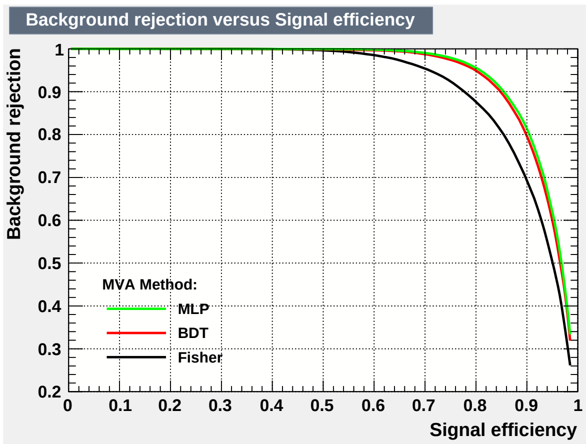

(a) $4 < E_{fit} < 15$ MeV.

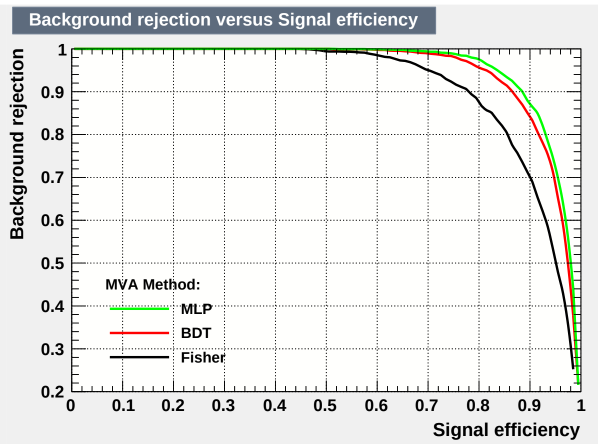

(b) $5 < E_{fit} < 15$ MeV (energy above 5 MeV).

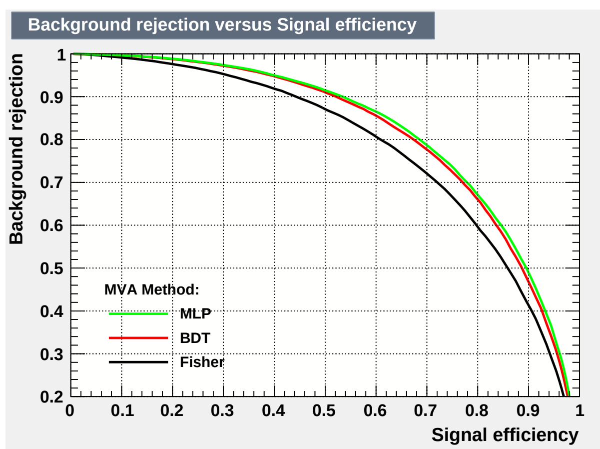

(c) $4 < E_{fit} < 5$ MeV.

Figure 6.12: TMVA outputs for signal/background separations by different methods, for the $4 < E < 15$ MeV, $5 < E < 15$ MeV, and $4 < E < 5$ MeV testing dataset.

A typical CPU time (t_{CPU}) for a certain method to train the dataset with different energy regions is listed in Table. 6.5.

It shows that, the Fisher/LD output gives the worst AUC. The BDT and MLP outputs are close to each other while the MLP gives the largest AUC values. However, the MLP was the most CPU-consuming method. For the energy in the lower region, it is more difficult

Table 6.5: Testing results from different TMVA methods.

Method	AUC	t_{CPU} (second/10^6 events)
$4 < E_{fit} < 15$ MeV		
Fisher/LD	0.915	0.81
BDT	0.940	249.53
MLP	0.944	1370.02
$5 < E_{fit} < 15$ MeV		
Fisher/LD	0.915	0.93
BDT	0.950	269.71
MLP	0.958	1450.90
$4 < E_{fit} < 5$ MeV		
Fisher/LD	0.782	0.84
BDT	0.816	280.1
MLP	0.823	1337.9

for all three methods to separate the signals from the backgrounds.

The distributions of the $\cos\theta_{sun}$ were used to show the performance of the solar ν_e event selection and background event discrimination. Here I applied the BDT and the MLP method on the test sub-dataset. For the real dataset from run-200004 to 207718, the trained weights and variables from the BDT and the MLP methods were applied event by event and the discriminator responses, D_{BDT} and D_{MLP} were calculated respectively. Cuts of $D_{BDT} > 0.0$ and $D_{MLP} > 0.5$ were applied to extract the solar ν_e signals from backgrounds.

6.3.5 TMVA Outputs

The trained weights were applied to both the simulations and the actual data from the 92.54 live-day half-dataset.

Fig. 6.13 shows a potential for the energy threshold down to 4 MeV. The outputs of the BDT and MLP selections for the $4 < E < 15$ MeV region. The BDT selection classifies about 80.8% of the total data as the backgrounds while the MLP classifies about 76.17%. Flat distributions of the $\cos\theta_{sun}$ can be seen obviously in the plots. Since the background events are overwhelming in the $4 < E < 5$ MeV region, the following analyses will focus only on the $5 < E < 15$ MeV region.

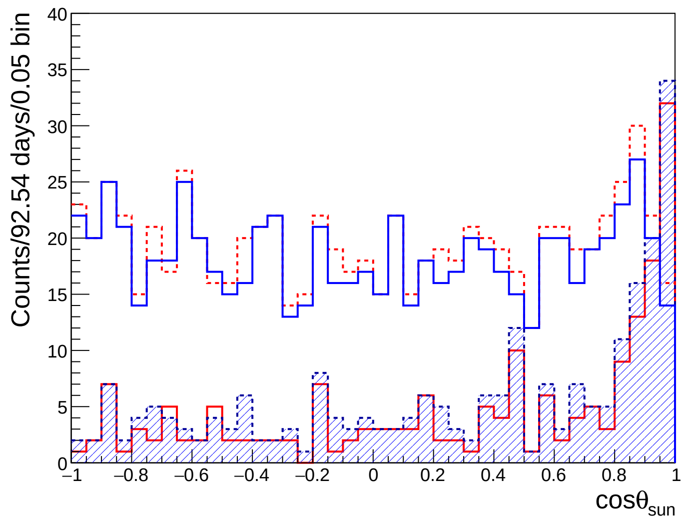

Figure 6.13: BDT and MLP outputs for the $\cos\theta_{sun}$, with $4 < E_{fit} < 15$ MeV. The solid red line shows the BDT selected candidate solar ν_e events, and the blue shaded histogram shows the MLP selected ones. The dotted red line is for BDT selected backgrounds, while the solid blue line is for the MLP selected backgrounds.

To test the outputs, the same fake datasets mentioned in Sect. 6.3.2 were used. Here just the energy region [5,15] MeV was checked. Fig. 6.14 shows the BDT output distributions of the $\cos\theta_{sun}$ for one random fake dataset, with $5 < E_{fit} < 15$ MeV. For this fake dataset, the true number of signal and background events are: $N_{sig}^{true} = 68$ and $N_{bkg}^{true} = 46$, while the BDT outputs are: $N_{sig}^{BDT} = 61$ and $N_{bkg}^{BDT} = 53$. It indicates an underestimate of the signal ($N_{sig}^{BDT} = 0.90 N_{sig}^{true}$) and also an overestimate of the background ($N_{sig}^{BDT} = 1.15 N_{sig}^{true}$).

As shown in Fig. 6.15, applying the TMVA BDT selection to each fake dataset, for 5000 fake datasets, the fractions of the event number selected by the BDT to the true event number are $(91.26 \pm 4.77)\%$ for the signal events, and $(117.1 \pm 10.46)\%$ for the background events (using the histogram mean and root mean square). The output after the default cuts is also shown here as a comparison.

In this case, though the number of signal events is underestimated, the TMVA methods can remove most of the background events. Also, for the Poisson fit, the TMVA methods were also applied to the MC simulations used as PDFs, these effects can be neutralized in fitting the events. In Sect. 6.3.7, it will show the fit of the TMVA outputs for the whole

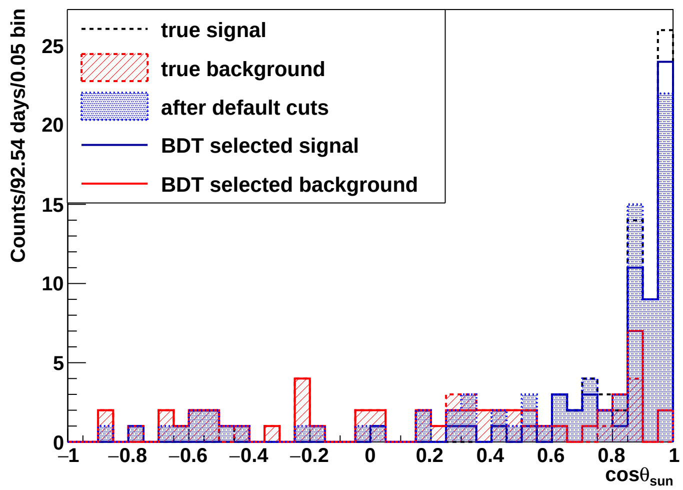

Figure 6.14: BDT outputs from one random fake dataset, with $5 < E_{fit} < 15$ MeV. The solid blue line and the solid red line are for the BDT output of the signal and background events, respectively; the dashed black line and the shaded red histogram are for the true signal and background events, respectively. Finally, the results after the default cuts are shown in the blue shaded area.

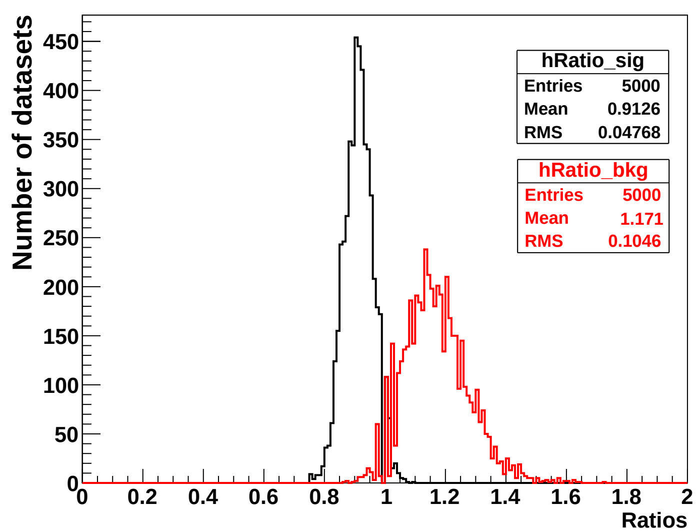

Figure 6.15: Event number ratios from BDT outputs on 5000 fake datasets, with $5 < E_{fit} <$ 15 MeV. The left black histogram is the distribution of the signal fractions and the right red histogram is the distribution of the background fractions.

dataset.

6.3.6 Discussions on TMVA Results

The TMVA methods optimize the cuts on more variables (FoMs and $klDiv$) and makes more stringent cuts to reduce the background events compared to the beforehand cuts. A more stringent radial cut (or tighter FV) can be applied on lower energy region $4 < E_{fit} < 5$ MeV to further remove the background events which are dominant in lower energy region. However, tighter cuts can also reduce the signal events.

Other packages developed for high energy particle physics, such as `StatPatternRecognition` (SPR)[179], can also be considered as an alternative tool or as a reference for results comparisons.

6.3.7 Fitting Whole Low Background Dataset

To combine the analyses in the previous two sections, the TMVA selection methods were applied to the actual data of the 190.33 live-day whole dataset and then a maximum likelihood fit was applied on the selected data.

For the whole dataset, the TMAV methods were applied to the whole MC datasets of the solar ν_e simulations as well as the background simulations[3] . Similarly, the training subset used 70.25% of the whole dataset (run-200004 to 205296), while the testing subset used the rest 29.75% (run-205297 to 207718). The trained BDT and MLP weights were applied to the whole dataset.

In the region of $5 < E_{fit} < 15$ MeV, the outputs from the BDT and MLP were fitted to obtain the N_{sig} and N_{bkg}. Fig. 6.16 show their results respectively. For comparisons, the results from applying the default cuts is also shown. The fit results are also summarized in Table. 6.6.

From the results, it shows that the results from the three outputs are consistent with each other. The estimated background rate in the [5,15] MeV energy region is about $\frac{1}{3}$

[3]The simulations of solar ν_μ were also trained with the background simulations separately to calculate the detected ν_μ from the oscillated solar neutrino flux mentioned in next section

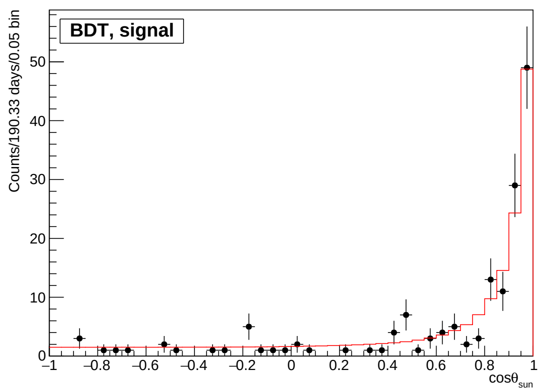

(a) BDT.

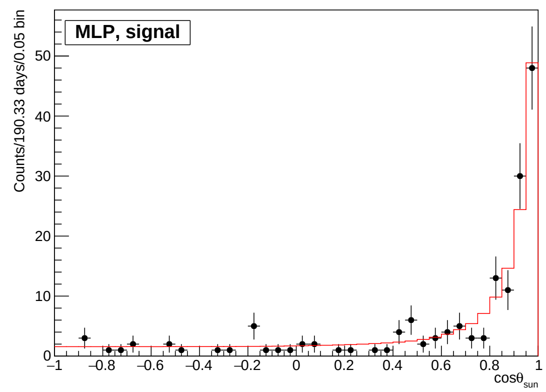

(b) MLP.

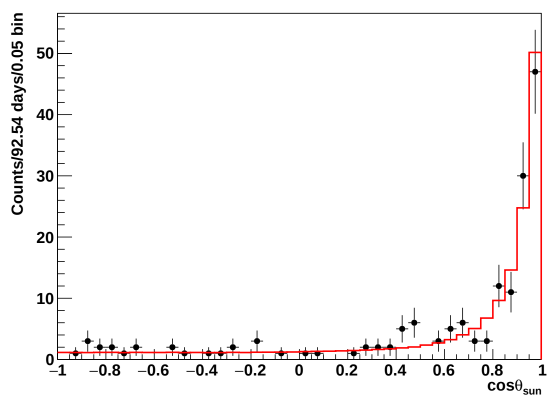

(c) Default cuts.

Figure 6.16: Poisson fit results for the $5 < E_{fit} < 15$ MeV, from the outputs of BDT (a), MLP (b), and default cuts.

of the signal rate, which indicates that a low background measurement is achieved for the solar neutrino analysis with the energy down to 5 MeV. For the sake of simplicity, since the output from the BDT selection gives a better $p - value$, the analyses in the following will just use the BDT output.

6.3.8 Evaluating ^{8}B Solar Neutrino Flux

A software called `PSelmaa` (Physics interpretation Sun-Earth Large Mixing Angle Adiabatic Approximation) was implemented in `RAT`[180]. The software uses the BS05(OP) SSM model.

Table 6.6: Fit results for the whole dataset ($5 < E < 15$ MeV).

Methods	N_{sig}	N_{bkg}	R_{sig}	R_{bkg}	$p-value$
BDT	119.57 ± 11.88	38.42 ± 7.75	0.90 ± 0.09	0.29 ± 0.06	0.14
MLP	118.77 ± 11.84	40.22 ± 7.85	0.90 ± 0.09	0.30 ± 0.06	0.18
Default Cuts	119.33 ± 11.96	42.67 ± 8.15	0.90 ± 0.09	0.32 ± 0.06	0.19

It assumes the normal mass hierarchy. It also applies the MSW effects from the Sun (see Chapter 2) but neglects the MSW effects from the Earth (i.e., the regeneration of coherence in the Earth). Fig. 6.17 shows the survival probability curve as a function of energies (in 0.1 MeV intervals) taken from the `PSelmaa`.

Since SNO+ can not discriminate ν_μ and ν_τ, only the ν_μ MC is included in the $P_{e\alpha}$.

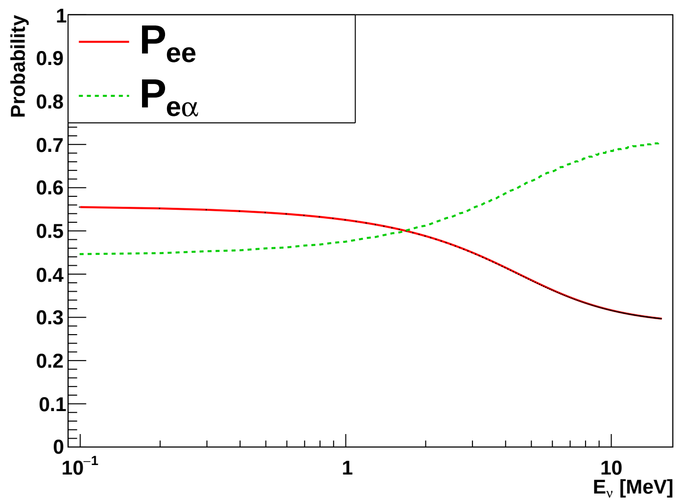

Figure 6.17: The MSW survival probability curves as functions of MC energies. The P_{ee} is in solid red line and $P_{e\alpha}(= 1 - P_{ee})$ is in dashed green line.

To gain more statistics of the MC simulations, the number of the simulated solar ν_e events is 1700 times the nominal ($flux\ scale = \frac{1}{1700}$); while the number of the solar ν_μ events is 9600 times the nominal ($flux\ scale = \frac{1}{9600}$). The two $flux\ scale$ factors are set according to the ratio of the ES cross-sections: $\sigma^{ES}(\nu_e + e^-)/\sigma^{ES}(\nu_{\mu,\tau} + e^-) \approx 6.5$, as mentioned in Sect. 2.2.1. A nominal ^{8}B solar ν_e flux $\Phi^{total}_{MC} = 5.46 \times 10^6$ cm^{-2}s^{-1} from the SSM prediction (see Refs. [181, 21]) is used by the simulation.

Since it is impossible for the SNO+ detector to discriminate between ν_μ and ν_τ via detecting the elastic scattering events, ν_τ is not generated separately[171]. Therefore, the generated solar ν_μ events are considered as a combination of ν_μ and ν_τ ($\nu_\mu \approx \nu_{\mu,\tau}$) in the solar neutrino flux. In addition, due to the data cleaning procedure, the actual live time of the data is slightly shorter than the raw live time used by the MC simulations. To compare the MC with the data, a live time fraction was applied to the MC: $f_{live\ time} = \frac{t_{data\ live\ time}}{t_{MC\ run\ time}} = \frac{190.33\ days}{198.17\ days} = 0.96$. Also, assuming a sacrifice of 1.7% from the data cleaning cuts on the data, a scale factor of $f_{dataClean} = (1 - \frac{1.7}{100})$ was applied to the MC simulations.

Therefore, the numbers of the MC generated ν_e and ν_μ events are scaled by the t_{frac} and $flux\ scale$, and then weighted by the oscillation probability P_{ee} and $P_{e\alpha} = 1 - P_{ee}$. Applying these weighting parameters as well as the BDT selections to the MC histograms, the MC $\cos\theta_{sun}$ distributions in the energy region $5 < E_{fit} < 15$ MeV with and without oscillations are shown in Fig. 6.18.

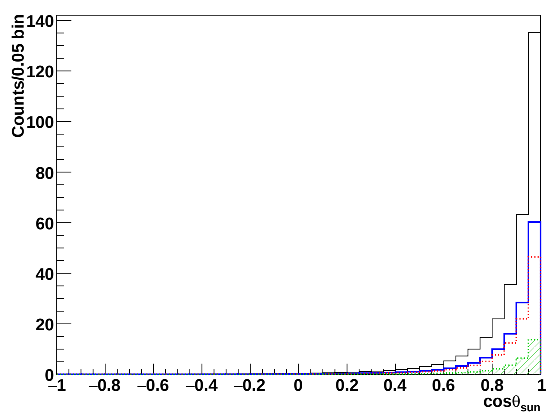

Figure 6.18: The MC $\cos\theta_{sun}$ distributions used as PDFs for the flux calculations, for $5 < E_{fit} < 15$ MeV after the BDT selections. The histogram in think black line is the ν_e flux without oscillation, denoted as $PDF(\nu_e, without\ oscillation)$. This histogram is used for fitting the elastic scattering flux. The histogram in dashed red line is the ν_e flux and the green shaded histogram is the ν_μ flux, both including the oscillation. These two histograms were combined to form the total flux including the oscillation, which is in blue line and is denoted by $PDF(\nu_e + \nu_\mu, oscillated)$. This histogram is used for fitting the total flux.

Reading from the above histograms, the expected event number for ν_e without the oscillation is $N_{\nu_e} = 314.679$[4] . While including the oscillations, the expected event number for ν_e and ν_μ are $N^{osci}_{\nu_e} = 109.494$ and $N^{osci}_{\nu_\mu} = 32.0757$ respectively, and the combined event number is $N^{osci}_{\nu_e+\nu_\mu} = 141.569$.

To fit for the total ^{8}B neutrino flux, the fit parameter used here is the flux scale f_s^{tot}, which is interpreted as the fraction of the observed ^{8}B flux to the expected flux. Using the same method in Sect. 6.3.1, and in the Eqn. 6.2, replacing the N_{sig} with $N_{sig} = f_s^{tot} \cdot N^{osci}_{\nu_e+\nu_\mu}$(where the estimated $N^{osci}_{\nu_e+\nu_\mu} = 141.57$), and then fitting the f_s^{tot} and the N_{bkg} with the $pdf(\nu_e + \nu_\mu, oscillated)$. The fit results are $f_s^{tot} = 0.8462 \pm 0.08398$ (corresponding to $N_{sig} = 119.8 \pm 11.89$ events) and $N_{bkg} = 38.20 \pm 7.731$ events, with a p-value of 0.1470. Fig. 6.19 shows the fit spectrum.

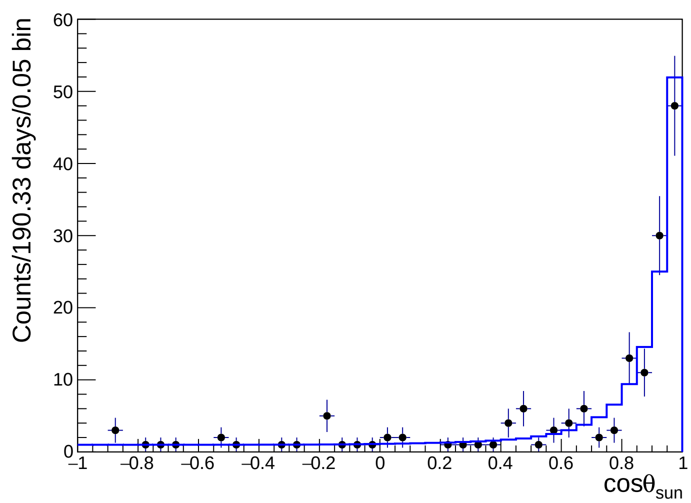

Figure 6.19: A fit on the total ^{8}B flux. The black dots are the data points and the blue histogram is the fit.

To fit for the ^{8}B flux corresponding to an observed flux of ES interactions, the same procedure was used, while the fit parameter was changed to $N_{sig} = f_s \cdot N_{\nu_e}(= 314.68)$ and the PDF was changed to $PDF(\nu_e, without\ oscillation)$. As shown in Fig. 6.20, the fit results are $f_s^{ES} = 0.3798 \pm 0.03772$ (corresponding to $N_{sig} = 119.5 \pm 11.62$ events) and $N_{bkg} = 38.48 \pm 7.751$ events, with a p-value = 0.140.

[4]Assuming a flux of ν_μ, the expected number of ν_μ is $N_{\nu_\mu} = 49.2741$, then $N_{\nu_e}/N_{\nu_\mu} \approx 6.4$, which is consistent with the ratio of the cross-sections mentioned before.

The N_{sig} and N_{bkg} results obtained by fitting flux fractions are consistent with

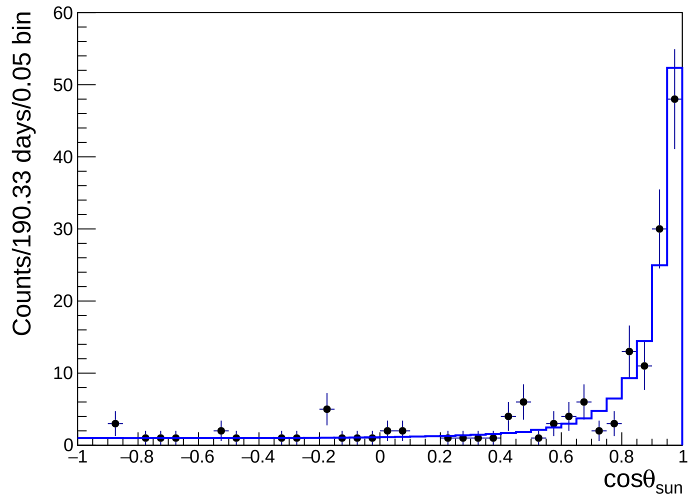

Figure 6.20: Fitting with the spectrum of elastic scattering. The black dots are the data points and the blue histogram is the fit.

The N_{sig} and N_{bkg} values obtained here by fitting the flux fractions are consistent with the values obtained in Sect. 6.3.7.

With the nominal ^{8}B solar neutrino flux Φ^{total}_{MC}, the estimated total flux is:

$$\Phi^{total}(^8\mathrm{B}) = f_s^{tot} \cdot \Phi^{total}_{MC} = (4.62 \pm 0.459(stats.)) \times 10^6 \ \mathrm{cm}^{-2}\mathrm{s}^{-1}, \tag{6.9}$$

and the estimated elastic scattering flux is:

$$\Phi^{ES} = f_s^{ES} \cdot \Phi^{total}_{MC} = (2.074 \pm 0.2061(stat.) \times 10^6 \ \mathrm{cm}^{-2}\mathrm{s}^{-1}. \tag{6.10}$$

The next section will evaluate the systematic uncertainties of the flux fractions.

6.3.9 Systematics Evaluation

In Chapter 5, the reconstruction systematics of the event position, direction and energy were obtained. The quantities of position scale, position shifts, direction resolution, β_{14} shifts, energy scale (E_{scale}) and energy resolution (E_{resol}) were used to evaluate the systematic uncertainties of the solar neutrino analysis. Table. 6.7 summarizes these systematics and their applications to transform the reconstructed results. In this thesis, only the systematics mentioned below were taken into account, and these systematics are considered uncorrelated.

Table 6.7: Systematics for the solar ν_e analysis in the water phase.

Systematics	values (positive/negative)	transformation
x shift (Δx)	+6.48/-5.98 mm	$x_{fit} \pm \Delta x$
y shift (Δy)	+6.13/-4.11 mm	$y_{fit} \pm \Delta y$
z shift (Δz)	+6.71/-4.82 mm	$z_{fit} \pm \Delta z$
x scale (Δs_x)	+0.07%/-0.06%	$(1 \pm \Delta s_x)x_{fit}$
y scale (Δs_y)	+0.02%/-0.07%	$(1 \pm \Delta s_y)y_{fit}$
z scale (Δs_z)	+0.08%/-0.01%	$(1 \pm \Delta s_z)z_{fit}$
direction δ_θ	+0.013/-0.101	$1 + \frac{\cos\theta_{sun} - 1}{1 \pm \delta_\theta}$
E_{scale} (Δ_{δ_E})	1.0%	$(1 \pm \Delta_{\delta_E})E_{fit}$
E_{resol} (Δ_b)	0.037 $\sqrt{\text{MeV}}$	$E_{fit} + Gaus(0, \sigma_{smear})$, $\sigma_{smear} = \sqrt{E_{fit}}\sqrt{(1+\Delta_b)^2 - 1}$
β_{14} shift ($\Delta\beta_{14}$)	+0.010/-0.036	$\beta_{14} \pm \Delta\beta_{14}$

Note that the position shifts were applied to the x_{fit}, y_{fit}, and z_{fit} respectively, while the position scales were applied simultaneously to the position vector:

$\vec{X'}_{fit} = ((1 \pm \Delta s_x)x_{fit}, (1 \pm \Delta s_y)y_{fit}, (1 \pm \Delta s_z)z_{fit})$.

For the δ_θ, since there is no physics meanings for the case when $\cos\theta_{sun} > 1$ or < -1, if the transformation causes $\cos\theta_{sun} > 1$, the smeared value is reset to 0.999; on the other hand, the $\cos\theta_{sun} < -1$ case happens more frequent and it is considered as mis-reconstruction. In this case, a random value is chosen by uniformly sampling in the [-1,1]. This procedure follows Ref. [161].

To evaluate the systematics of the solar neutrino analysis, the systematic transformations in Table. 6.7 were applied to the reconstructed quantities in MC simulations independently. The reconstructed quantities after the transformations are called “smeared” values. The smeared values of an event can affect whether the event will pass the cuts: the smeared positions of an event affect whether the event can pass the fiducial volume cut and then affect the results after the position cuts; the smeared energies affect the results after the energy cuts and the smeared β_{14} affect the results after the β_{14} cuts. Thus, for the solar ν_e

and ν_μ simulations, the shape of the $\cos\theta_{sun}$ distribution used as the PDF will be changed by the smeared values. In addition, the δ_θ transformation changes the PDF shape directly. Finally, the spectrum of the data was re-fit with the smeared PDFs to obtain the smeared physics quantity (specifically, the flux ratio f_s mentioned in the previous section), and the differences between the original value and the smeared value are used as the systematics of the physics quantity.

To obtain the smeared PDFs, first, only the cuts $5 < E_{fit} < 15$ MeV (for selecting energy region), NHit>20 (reconstruction threshold) and $ITR > 0.55$ (determined from the instrumental noises and its systematic uncertainty was not considered) were applied to the MC simulations of the solar ν_e and ν_μ. Then the systematic transformations were applied one by one and event by event. The positive ("smearing up") and negative ("smearing down") values were also applied, respectively. After the transformation, the whole beforehand cut was applied. At last, the TMVA BDT selection was applied. For a specific smeared quantity, the final output of the MC $\cos\theta_{sun}$ spectrum was used as the smeared PDF for that quantity. For example, if the E_{fit} is smeared by scaling up: $E'_{fit} = (1 + \Delta_{\delta_E})E_{fit}$, then the outputs of the $\cos\theta_{sun}$ after the beforehand cut and TMVA BDT selection is used as the "energy scale-up PDF".

Fig. 6.21 shows the effects of smearing the direction parameter, energy scale and energy resolution on the MC PDF. The original MC PDF is shown as black solid line histograms, overlaid by the smeared histograms.

Applying the systematic transformation in Table. 6.7 to the MC ES PDF, and then refitting the data with the smeared PDFs for each quantity, the smeared values of the flux fractions (f'_s) were found. The systematics of the f_s are calculated by $\Delta f_s = f'_s - f_s$. These results are listed in Table. 6.8.

It finds that the systematic uncertainties from the smeared position and β_{14} are negligible, while the direction and energy smearing give more significant uncertainties.

Using the quadrature sum ($\sigma_{tot}^2 = \sum_i \sigma_i^2$) which assumes that all the systematic variables are independent, the total systematic uncertainty of the total flux fraction f_s^{tot} is expected

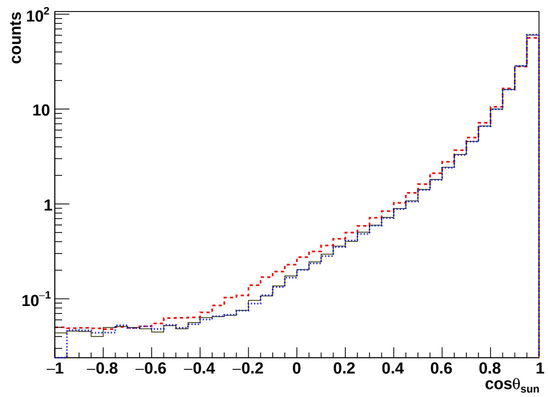

(a) Smearing direction parameter δ_θ.

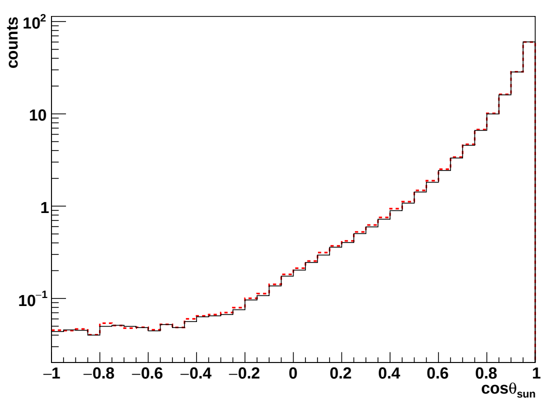

(b) Smearing energy resolution Δ_b.

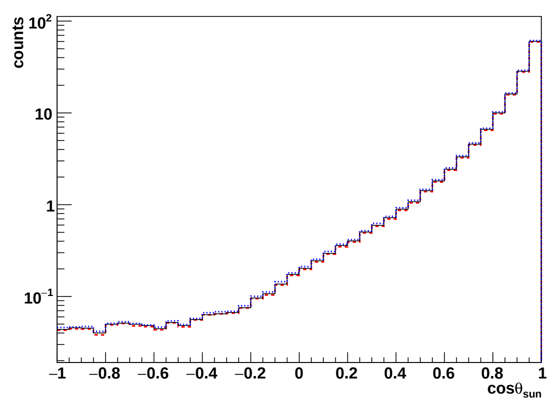

(c) Smearing energy scale Δ_{δ_E}.

Figure 6.21: Smearing effects on the $\cos\theta_{sun}$. The histogram with solid black line is the PDF before smearing. The dotted blue histogram is for smearing up the quantity (i.e., taking the positive values) and the dashed red is for smearing down (i.e., taking the positive values).

Table 6.8: Systematics for the fitted flux scale f_s.

Systematics	Δf_s (+/-)
x shift	$+0.001891/-0.001962$
y shift	$+0.001888/-0.001955$
z shift	$+0.002071/-0.001818$
position scale	$+0.000583/-0.00306$
δ_θ	$+0.01676/-0.004034$
E_{scale} (Δ_{δ_E})	$+0.01456/-0.01752$
E_{resol} (Δ_b)	$+0.003363/-0.003363$
β_{14} shifts	$+0.003968/-0.003285$

to be: $(f_s^{tot})^{+0.02306}_{-0.01912}$.

By using the same procedure to evaluate the systematics of the elastic scattering flux fraction f_s^{ES}, it gives $(f_s^{ES})^{+0.009655}_{-0.008305}$.

6.3.10 A Summary of Results

With the systematic uncertainties of the flux fractions obtained from the previous section, the total flux is:

$$\Phi_{fit}^{total}(^8\mathrm{B}) = f_s \cdot \Phi_{MC}^{total} = (4.62 \pm 0.459(stats.)^{+0.126}_{-0.104}(syst.)) \times 10^6\ \mathrm{cm}^{-2}\mathrm{s}^{-1}. \tag{6.11}$$

And the ES flux is:

$$\Phi_{\mathrm{ES}} = f_s \cdot \Phi_{MC}^{total} = (2.07 \pm 0.206(stat.)^{+0.0527}_{-0.0454}(syst.)) \times 10^6\ \mathrm{cm}^{-2}\mathrm{s}^{-1}. \tag{6.12}$$

A quadratic total uncertainty σ_{tot} is calculated by combining the larger uncertainties in statistics and systematics:

$$\sigma_{tot} = \sqrt{\sigma^2_{stat,larger} + \sigma^2_{sys,larger}}. \tag{6.13}$$

Fig. 6.22 shows a comparison of the Φ_{ES} results given here to the recent measurements from the other experiments (mentioned in Sect. 2.4, Chapter 2), including the SNO+ water phase measurement published in 2018[1], the Super-K phase-IV measurement (Super-K IV) and the combined four phases measurement (Super-K combined)[2], and the Borexino measurements published in 2020 (Borexino 2020)[48].

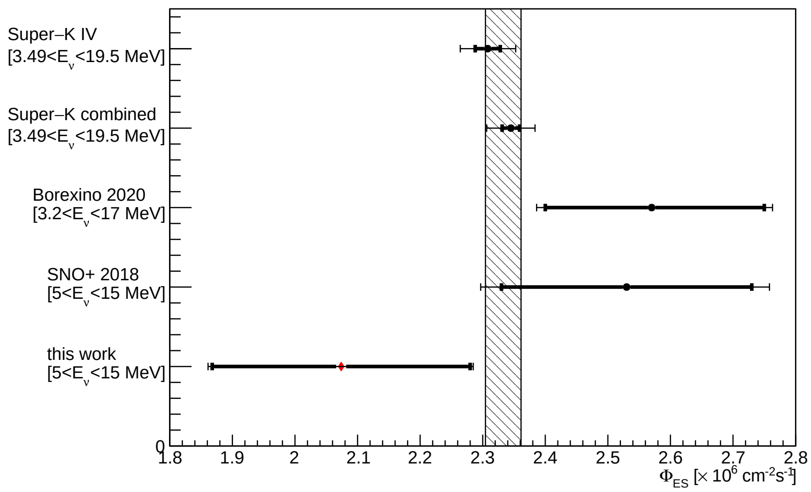

Figure 6.22: A comparison of the ES fluxes measured recently by three independent experiments (after BDT selection). The thick error bars include the statistical errors and the thin ones are quadratic errors including both the statistical and systematical errors. The shaded band is for the unconstrained average value and uncertainty of all the results: $\hat{\theta} \pm 1\sigma_{\hat{\theta}}$.

To combine the results from different experiments, an unconstrained average value $\hat{\theta}$ and its uncertainty $\sigma_{\hat{\theta}}$ are calculated by[21, 182]:

$$\hat{\theta} = \sum_{i=1}^{N} \left(\frac{x_i}{\sigma_i^2} \right) \Bigg/ \sum_{i=1}^{N} \left(\frac{1}{\sigma_i^2} \right), \tag{6.14}$$

$$\sigma_{\hat{\theta}} = \left[\sum_{i=1}^{N} \left(\frac{1}{\sigma_i^2} \right) \right]^{-\frac{1}{2}}, \tag{6.15}$$

where x_i is the measured Φ_{ES} value from each experiment, and the σ_i is the total uncertainty σ_{tot} calculated from each experiment.

Combined with the results from other experiments, the average results are listed in Table. 6.9. The Φ_{ES} result from this thesis is combined with the SNO+ 2018 result and then with all the other experiments' results. The average result without this work is also shown. All the three average results are consistent with each other.

From the average result including all the experiments mentioned, the region of $\hat{\theta} \pm 1\sigma_{\hat{\theta},tot}$ is plotted as the shaded band in Fig. 6.22.

Table 6.9: Average results.

Combinations	Φ_{ES} ($\times 10^6$ cm^{-2}s^{-1})
not including this work	2.338 ± 0.02868
this work and SNO+ 2018	2.281 ± 0.1571
all	2.333 ± 0.02843

6.3.11 Limitations of this Study

This study focuses on measuring solar neutrinos in the energy region [5,15] MeV with a fiducial volume of 5.5 m.

As listed in Table. 6.3, I used the ^{208}Tl and ^{214}Bi backgrounds simulated in three detector components , which were not complete. There are a few other backgrounds, such as the backgrounds in the other detector components (like the AV ropes, the PMTs, etc), the other isotopes such as the cosmic muon induced isotopes, etc. A more comprehensive study requires to include all possible background simulations.

To fit the background events, I assumed a flat distribution of $\cos\theta_{sun}$. A more realistic shape of the distribution can be investigated to describe the backgrounds more properly. In addition, the background levels can vary over time, so a more detailed analysis including different time periods can make the results more accurate.

The evaluation of the systematic uncertainties is not comprehensive. In particular, the uncertainties from the solar neutrino model used by the MC simulations to produce solar neutrinos and apply the oscillations are not included here. The uncertainties in the SSM model as well as the neutrino flavor transformation parameters can affect the MC simulations. In addition, the energy calibration used to mitigate the difference between data and simulations is not applied. This procedure can reduce the uncertainties from the energy reconstructions.

Since the dataset used here has a very low background level, it is also possible to probe the energy region down to 3.5 MeV and then enable the study of the solar neutrinos in a lower energy region. However, since the reconstruction threshold was set as NHit>20, so this part is not included in the thesis. It may be worthwhile to investigate the data with a lower NHit threshold down to NHit>6, and to apply a proper TMVA method selection for reducing the backgrounds in the lower energy region.

Chapter 7

Conclusions

In this thesis, a reconstruction algorithm framework was developed for multiple SNO+ physics phases. For the SNO+ detector with a diameter of 12 m, it achieves position resolutions of 300 mm for the water phase and 70 mm for scintillator phase. The position biases are within 100 mm for both phases. This framework has been applied to the SNO+ water phase and partial-fill phase analysis.

By utilizing the water phase reconstruction, this thesis provides an alternative analysis for the ^{8}B solar neutrino measurement during the SNO+ water phase. By looking at the low background dataset for 190.33 live days, a ^{8}B solar neutrino rate of 0.90 ± 0.09 $events/(kt \cdot day)$ with a background rate of 0.29 ± 0.06 $events/(kt \cdot day)$ in the energy region [5,15] MeV were obtained. As the energy threshold is pushed down to 5 MeV, this background rate is significantly low for the solar neutrino measurement in a water Cherenkov detector.

The result also gives an estimated ^{8}B solar neutrino flux as:

$\Phi_{^8\mathrm{B}} = (4.62 \pm 0.459(stats.)^{+0.126}_{-0.104}(syst.)) \times 10^6$ cm^{-2}s^{-1}, while the elastic scattering flux is measured as:

$\Phi_{\mathrm{ES}} = (2.07 \pm 0.206(stats.)^{+0.0527}_{-0.0454}(syst.)) \times 10^6$ cm^{-2}s^{-1}.

Appendix A

Details for the MultiPath Fitter

A.1 Create a Random Vertex

Four random seeds are generated from the uniform distribution function: `RandFlat` in Class Library for High Energy Physics library (`CLHEP`).

One random seed is used for generating the time of the vertex: t is a random variable following a uniform distribution in a range of $[100, 300]$ ns, say, $t \sim U(100, 300)$.

Three random seeds are used for generating the position of the trial vertex: $\texttt{ran0} \sim U(0, 1)$, $\texttt{ran1} \sim U(-1, 1)$ and $\texttt{ran2Pi} \sim U(0, 2\pi)$.

Let $r = \sqrt[3]{\texttt{ran0}} * 10000$ mm, $\phi = \texttt{ran2Pi}$, $\cos\theta = \texttt{ran1}$ and $\sin\theta = \sqrt{1 - \cos^2\theta}$, then the trial position can be built in Cartesian coordinate system: $\vec{x}_{trial} = (r\sin\theta\cos\phi, r\sin\theta\sin\phi, r\cos\theta)$. This procedure ensures that a proper random position is generated inside a sphere with a radius of 10 m.

For the trial direction, two random seeds are used. Each follows a uniform distribution: $\texttt{ranPi} \sim U(0, \pi)$ and $\texttt{ran2Pi} \sim U(0, 2\pi)$. Then the trial direction is built as: $\vec{u}_0 = (\cos\phi\sin\theta, \sin\phi\sin\theta, \cos\theta)$, with zenith angle $\theta = \texttt{ranPi}$ and azimuth angle $\phi = \texttt{ran2Pi}$.

Note that here the `ranPi` and `ran2Pi` are generated independently for the trial direction and they are not related to the vertex case.

A.2 Levenberg-Marquardt Method

This section is derived from Ref. [141]. Levenberg-Marquardt (MRQ) method is a common routine for non-linear fitting. Let $\mathbf{a} = [a_0, a_1, ..., a_{M-1}]^T$ be an M-dimensional vector with M unknown parameters to be fit, for example, $\mathbf{a}$ is an event vertex with 4 parameters: $\mathbf{a} = [x, y, z, t]^T$.

A χ^2 merit function with the unknown parameter vector $\mathbf{a}$ can be built and by minimizing the function, the best-fit $\mathbf{a}$ can be found.

The $\chi^2(\mathbf{a})$ can be approximately expanded into a quadratic form of Taylor-series:

$$\chi^2(\mathbf{a}) \simeq \gamma - \mathbf{d} \cdot \mathbf{a} + \frac{1}{2}\mathbf{a} \cdot \mathbf{D} \cdot \mathbf{a}, \tag{A.1}$$

where γ is a M-dimension constant vector around $\mathbf{a}$, $\mathbf{d}$ is a M-dimension vector and $\mathbf{D}$ is a $M \times M$ Hessian matrix.

To find a $\mathbf{a}_{min}$ so that a $\min \chi^2(\mathbf{a}_{min})$ is reached, in computing science we usually use iteration steps:

$$\mathbf{a}_{min} = \mathbf{a}_{cur} + D^{-1}[-\nabla\chi^2(\mathbf{a}_{cur})], \tag{A.2}$$

where $\mathbf{a}_{cur}$ is the current trial value of $\mathbf{a}$ and we assume matrix $\mathbf{D}$ is invertible. The $\mathbf{a}_{cur}$ thus jumps onto $\mathbf{a}_{min}$.

According to the definition of a χ^2 merit function, it can be written out explicitly as:

$$\chi^2(\mathbf{a}) = \sum_{i=0}^{N-1} \left[\frac{y_i - y(x_i|\mathbf{a})}{\sigma_i}\right]^2, \tag{A.3}$$

and with the same Taylor expansion, the quadratic form is written as:

$$\chi^2(\mathbf{a}) \approx \chi^2(\mathbf{a}_{cur}) + \sum_k \frac{\partial\chi^2(\mathbf{a}_{cur})}{\partial\alpha_k}\delta\alpha_k + \frac{1}{2}\sum_{kl}\frac{\partial^2\chi^2(\mathbf{a}_{cur})}{\partial\alpha_k\partial\alpha_l}\delta\alpha_k\delta\alpha_l, \tag{A.4}$$

where the first derivatives are:

$$\frac{\partial\chi^2}{\partial a_k} = -2\sum_{i=0}^{N-1}\left[\frac{y_i - y(x_i|\mathbf{a})}{\sigma_i}\right]\frac{\partial y(x_i|\mathbf{a})}{\partial a_k}, k = 0, 1, ..., M-1, \tag{A.5}$$

and the second derivatives are:

$$\frac{\partial^2\chi^2}{\partial a_k\partial a_l} = 2\sum_{i=0}^{N-1}\left\{\frac{\partial y(x_i|\mathbf{a})}{\partial a_k}\frac{\partial y(x_i|\mathbf{a})}{\partial a_l} - [y_i - y(x_i|a)]\frac{\partial^2 y(x_i|\mathbf{a})}{\partial a_k\partial a_l}\right\}, k = 0, 1, ..., M-1. \tag{A.6}$$

Let $\beta_k \equiv -\frac{1}{2}\frac{\partial \chi^2}{\partial a_k}, \alpha_{kl} \equiv \frac{1}{2}\frac{\partial^2 \chi^2}{\partial a_k \partial a_l}$, then the factor of 2 is removed. The α_{kl} is defined as the curvature matrix and $\alpha = \frac{1}{2}\mathbf{D}$, which implies that it is the half of the Hessian matrix.

From A.2, we have: $D(\mathbf{a}_{min} - \mathbf{a}_{cur}) = [-\nabla\chi^2(\mathbf{a}_{cur})] \implies 2\alpha\delta\mathbf{a} = 2\beta$. The A.2 is now transformed into a systems of linear equations:

$$\sum_{l=0}^{M-1} \alpha_{kl}\delta a_l = \beta_k, \tag{A.7}$$

where δa_l is a varying amount added to the current value of parameter for the next iteration.

The main task now is to calculate α_{kl} and β_k and then solve for δa_l in A.7. Once δa_l is solved, we can vary the current trial or approximate values of $\mathbf{a}_{cur}$ and let it go close to or reach the $\mathbf{a}_{min}$.

If we consider the method of steepest descent: $\mathbf{a}_{next} = \mathbf{a}_{cur} - \text{const} \cdot \nabla\chi^2(\mathbf{a}_{cur})$, where const is a constant, then the δa_l is solved by:

$$\delta a_l = \text{const} \cdot \beta_l, \tag{A.8}$$

where no Hessian matrix is needed.

In the MRQ method, in order to solve for δa_l, the detailed calculation of $\mathbf{D}^{-1}$ in A.2 and the simplified calculation of steepest descent in A.8 are combined and a smooth transition between A.2 and A.8 is considered.

In A.8, the const describes the distance or magnitude of how far the parameter should go along the gradient β_l. From dimensional analysis, since $\beta_k \equiv -\frac{1}{2}\frac{\partial \chi^2}{\partial a_k}$ and χ^2 is a non-dimensional number, $[\beta_l] = [1/a_l]$. Then from A.8, $[\text{const}] = [a_l^2]$. The const has the same dimension to the term $1/\alpha_{ll} = 1/(\frac{1}{2}\frac{\partial^2 \chi^2}{\partial a_l \partial a_l})$, i.e., the diagonal elements in the curvature matrix. A bridge between A.2 and A.8 is thus built. The diagonal elements in the curvature matrix can control the magnitude of the const, tells how far the parameter should go along the gradient.

Then A.8 can be written as:

$$\delta a_l = \frac{1}{\lambda\alpha_{ll}}\beta_l \textit{ or } \lambda\alpha_{ll}\delta a_l = \beta_l, \tag{A.9}$$

where α_{ll} is written in a form of $\alpha_{ll} = \sum_{i=0}^{N-1} \frac{1}{\sigma_i^2}[\frac{\partial y(x_i|\mathbf{a})}{\partial a_l}\frac{\partial y(x_i|\mathbf{a})}{\partial a_l}]$ to ensure that α_{ll} is always positive; a fudge factor λ can be set to $\lambda \gg 1$ to avoid the case when the value of const is taken too large.

Compare A.7 and A.9, if define a new curvature matrix α' as $\alpha'_{jj} \equiv (1+\lambda)\alpha_{jj}$ (for diagonal elements) and $\alpha'_{jk} \equiv \alpha_{jk} \quad (j \neq k)$ (for non-diagonal elements), these two equations can be combined into one:

$$\sum_{l=0}^{M-1} \alpha'_{kl}\delta a_l = \beta_k \tag{A.10}$$

From the definition of α', if λ takes a large value, α' is dominated by diagonal elements, then A.10 is close to A.9; while if $\lambda \to 0$, A.10 is close to A.7.

The algorithm of the MRQ method requires a reasonable start value (first guess) of the fitting parameter $\mathbf{a}$ and a reasonable preset value of λ (usually take $\lambda = 0.001$). The iteration loop of the algorithm is: calculate the value of $\chi^2(\mathbf{a})$, solve for $\delta\mathbf{a}$ from A.10 and then calculate $\chi^2(\mathbf{a}+\delta\mathbf{a})$. During this loop, the algorithm checks whether $\chi^2(\mathbf{a}+\delta\mathbf{a}) \geq \chi^2(\mathbf{a})$, if it is, λ is increased by $\lambda = 10 \cdot \lambda$; if not, λ is decreased by $\lambda = 0.1 \cdot \lambda$.

The iteration loop is terminated when the change amount of the χ^2 is negligible: if the loop calculates several χ^2 values which are close to each other within a fit tolerance (`fTolerance`): $|\chi^2_{curren} - \chi^2_{previous}| <$ `fTolerance`, the algorithm will consider the χ^2 is minimized with a set of best-fit parameters. Here the termination condition of iterating the χ^2 value to convergence to the machine accuracy or to the roundoff limit is not used, since χ^2 is a statistical quantity rather than a solution of an equation. It is not statistical meaningful to vary the value of $\mathbf{a}$ to vary χ^2 by a small amount $\ll 1$.

Once the minimum is reached, λ is set to 0 and then the estimated covariance matrix of the standard errors in the fitted $\mathbf{a}$ can be calculated as: $C \equiv \alpha^{\mathbf{-1}}$.

The MRQ method is the core algorithm in the `MP fitter` framework for likelihood fitting. A few fitter setting parameters relating to the method can be optimized in practice. These parameters are:

- `fTolerance`: the fit tolerance, which is set as $|\chi^2_{curren} - \chi^2_{previous}| <$ `fTolerance`.

- `nGood`: the number of good fits. The maximum number of the "good fits" required to be a valid result. This is to avoid the case when the MRQ minimizer finds a local minima instead of a global minima.

- `fMaxIter`: the maximum iteration. The allowed maximum number for looping the MRQ minimizer.

- `nStart`: the maximum number of start positions. If the start value does not give a valid result, the fitter will try another random start value. `nStart` is the maximum number of the start value the fitter is allowed to try.

Table. A.1 shows the optimized values of the fitter setting parameters for different phases.

Table A.1: Optimized fitter setting parameters for different physics phases.

SNO+ phase	`fTolerance`	`nGood`	`fMaxIter`	`nStart`
water phase	0.001	6	500	250
partial-fill phase	0.001	4	100	250
scintillator phase	0.001	4	100	250

A trade-off between the accuracy & precision of the reconstructed results and the CPU time is considered. If increasing the `fTolerance` while decreasing the number of `nGood`, `fMaxIter` and `nStart`, the CPU time will decrease at costs of the fitter accuracy & precision, and vice versa.

A.3 Calculations of Derivatives of Likelihood Functions

The MRQ method requires the derivatives of the likelihood function. These derivatives can be calculated analytically in explicit mathematical forms.

The position difference is defined as $\vec{X}_{\text{diffCh}} = \vec{X}_0 - \vec{X}_{\text{pmt}}$. Then the TOF for the prompt Cherenkov light is $t_{\text{Ch}} = |\vec{X}_{\text{diffCh}}|/v_g$ and $L_{\text{Ch}} = L(t_{\text{Ch}})$.

Then it comes out for the water vertex case,

$$\frac{\partial L}{\partial t_0} = \frac{dL_{\text{Ch}}}{dt_{\text{Ch}}}, \tag{A.11}$$

$$\frac{\partial L}{\partial x} = \frac{\partial L_{\mathrm{Ch}}}{\partial t_{\mathrm{Ch}}} \frac{dt_{\mathrm{Ch}}}{\partial x} = -\frac{dL_{\mathrm{Ch}}}{dt_{\mathrm{Ch}}} \frac{X_{\mathrm{diffCh}}}{|\vec{X}_{\mathrm{diffCh}}| \cdot v_g}, \tag{A.12}$$

$$\frac{\partial L}{\partial y} = -\frac{dL_{\mathrm{Ch}}}{dt_{\mathrm{Ch}}} \frac{Y_{\mathrm{diffCh}}}{|\vec{X}_{\mathrm{diffCh}}| \cdot v_g}, \tag{A.13}$$

$$\frac{\partial L}{\partial z} = -\frac{dL_{\mathrm{Ch}}}{dt_{\mathrm{Ch}}} \frac{Z_{\mathrm{diffCh}}}{|\vec{X}_{\mathrm{diffCh}}| \cdot v_g}, \tag{A.14}$$

where the derivative $\frac{dL_{\mathrm{Ch}}}{dt_{\mathrm{Ch}}}$ can be calculated numerically from the timing *pdf* saved as a binned histogram.

For the water direction case,

$$\frac{\partial L}{\partial \theta} = \frac{dL_{\mathrm{Ch}}}{d\cos\theta_{\mathrm{Ch}}} \frac{d\cos\theta_{\mathrm{Ch}}}{\partial \theta} = \frac{dL_{\mathrm{Ch}}}{d\cos\theta_{\mathrm{Ch}}} \frac{d\vec{u}_0}{d\theta} \cdot \frac{\vec{X}_{\mathrm{diffCh}}}{|\vec{X}_{\mathrm{diffCh}}|}, \tag{A.15}$$

where $d\vec{u}_0/d\theta = (\cos\phi\cos\theta, \sin\phi\cos\theta, -\sin\theta)$ and

$$\frac{\partial L}{\partial \phi} = \frac{dL_{\mathrm{Ch}}}{d\cos\theta_{\mathrm{Ch}}} \frac{d\cos\theta_{\mathrm{Ch}}}{d\phi} = \frac{dL_{\mathrm{Ch}}}{d\cos\theta_{\mathrm{Ch}}} \frac{d\vec{u}_0}{d\phi} \cdot \frac{\vec{X}_{\mathrm{diffCh}}}{|\vec{X}_{\mathrm{diffCh}}|}, \tag{A.16}$$

where $d\vec{u}_0/d\phi = (-\sin\phi\sin\theta, \cos\phi\sin\theta, 0)$. The derivative $\frac{dL_{\mathrm{Ch}}}{d\cos\theta_{\mathrm{Ch}}}$ can be calculated numerically from the PMT angular response *pdf* saved as a binned histogram.

A.4 Inversion of Hessian Matrix

Matrix inversion is a frequent calculation when applying the MRQ method. In the `MP fitter`, the inversion of a 2×2 Hessian matrix (usually used for direction reconstruction with two parameters) is calculated directly. For the higher dimension matrix, usually the 4×4 matrix for vertex reconstruction, a `SDecompQRH` class is called for calculating the inversion matrix by using QR decomposition method[141]. This class was introduced by Jeff Tseng and it was modified from the `ROOT TDecompQRH` class[183]. Compared to the ROOT version, its `Solve()` function was slightly modified for solving the matrix equation $Ax = b$, where $A = QR$ is composed of an orthogonal matrix Q and an upper triangular matrix R. If the diagonal element in R is too small, instead of returning failure, the modified algorithm simply sets the corresponding x component to be 0. This allows an optimization for the MRQ method to continue in frequent cases when the matrix is singular.

A.5 Likelihood Surfaces

Fig. A.1 shows vertex likelihood surfaces produced by the MRQ method in the `MP water fitter`, for an typical ^{16}N event (central run-100934, event GTID = 61836), projected on $X-Y$, $X-Z$ and $Y-Z$ planes. A clear global maxima gives the reconstructed vertex: $\vec{X}_{fit} = (-211.958, 503.399, 275.990)$ mm and $t_{fit} = 217.039$ ns.

A.6 Detailed Light Path Calculations in the `MP Partial Fitter`

The following algorithm shows the detailed calculations for evaluating the light path in the scintillator regions. Each check steps are marked by number and if-conditions are marked by Latin letters (a, b or c).

First check the ray-sphere intersection (Eqn. 4.14):
If $\Delta > 0$,
(step. 1a) if $|\vec{x}_0| < r_{AV}$ (and $a_+ > 0 > a_-$), check the ray-plane intersection:
(2a-a) if $a_3 > 0$, the ray-vector hits the interface plane:
(3a-a-a) if $z_0 < Z_{split}$ and $a_3 < a_+$: $d_{sp,AV} = a_+ - a_3$, see Fig. A.4 (a).
(3a-a-b) if $z_0 \geq Z_{split}$:
(4a-a-b-a) if $a_3 < a_+$: $d_{sp,AV} = a_3$, see Fig. A.4 (b).
(4a-a-b-b) if $a_3 \geq a_+$: $d_{sp,AV} = a_+$, see Fig. A.4 (c).
(2a-b) if $a_3 \leq 0$:
(3a-b) if $z_0 > Z_{split}$: $d_{sp,AV} = a_+$, see Fig. A.4 (d).
(step. 1b) if $|\vec{x}_0| \geq r_{AV}$ (and $a_+ > a_- > 0$), calculate the z position of the intersection point: $z_\pm = z_0 + a_\pm \cdot (z_{PMT} - z_0)/|\vec{X}_{PMT} - \vec{X}_0|$:
(1-b-a) if $z_- \geq Z_{split}$ and $z_+ \geq Z_{split}$: $d_{sp,AV} = a_+ - a_-$, see Fig. A.4 (e).
(1-b-b) if $z_- < Z_{split}$ and $z_+ > Z_{split}$ and $a_3 > 0$: $d_{sp,AV} = a_+ - a_3$, see Fig. A.4 (f).
(1-b-c) if $z_- > Z_{split}$ and $z_+ < Z_{split}$ and $a_3 > 0$: $d_{sp,AV} = a_3 - a_-$, see Fig. A.4 (g).

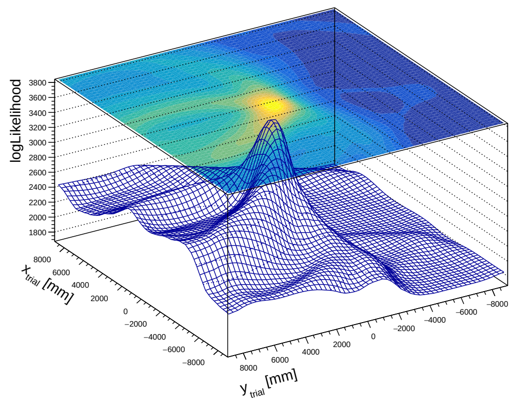

(a) X-Y plane.

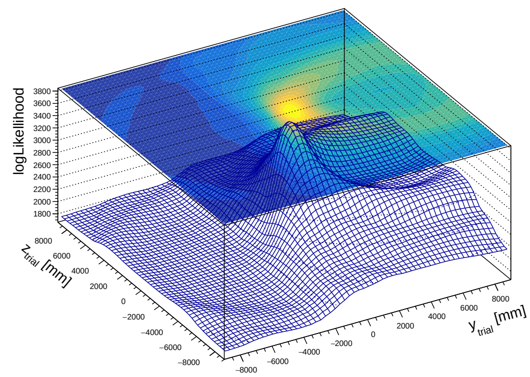

(b) Y-Z plane.

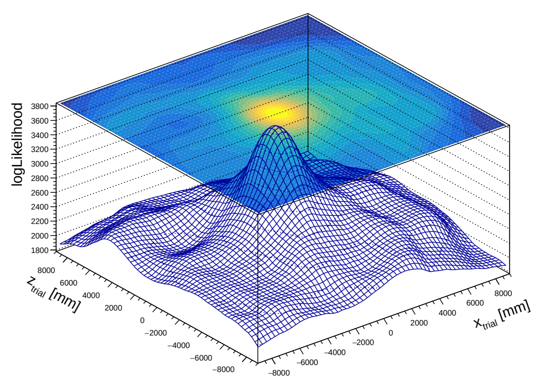

(c) X-Z plane.

Figure A.1: Likelihood surface of an ^{16}N event projected on X-Y, Y-Z, X-Z planes. A clear global maxima is reached for the fitted vertex.

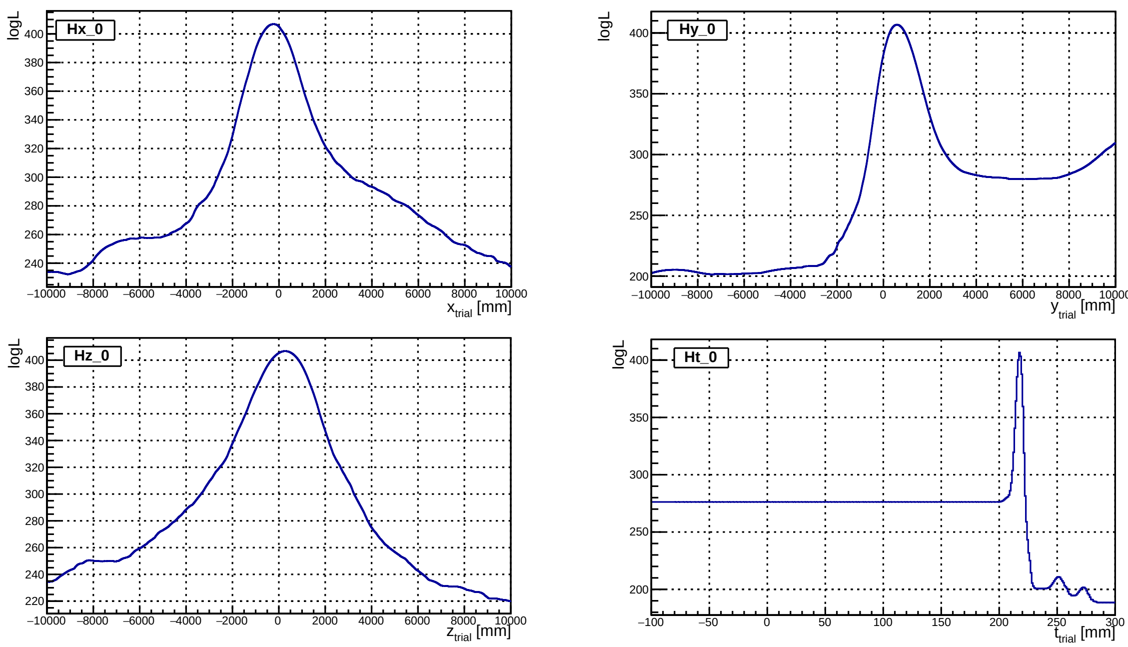

Figure A.2: Likelihood surface of an ^{16}N event projected on x, y, z, t-axis respectively.

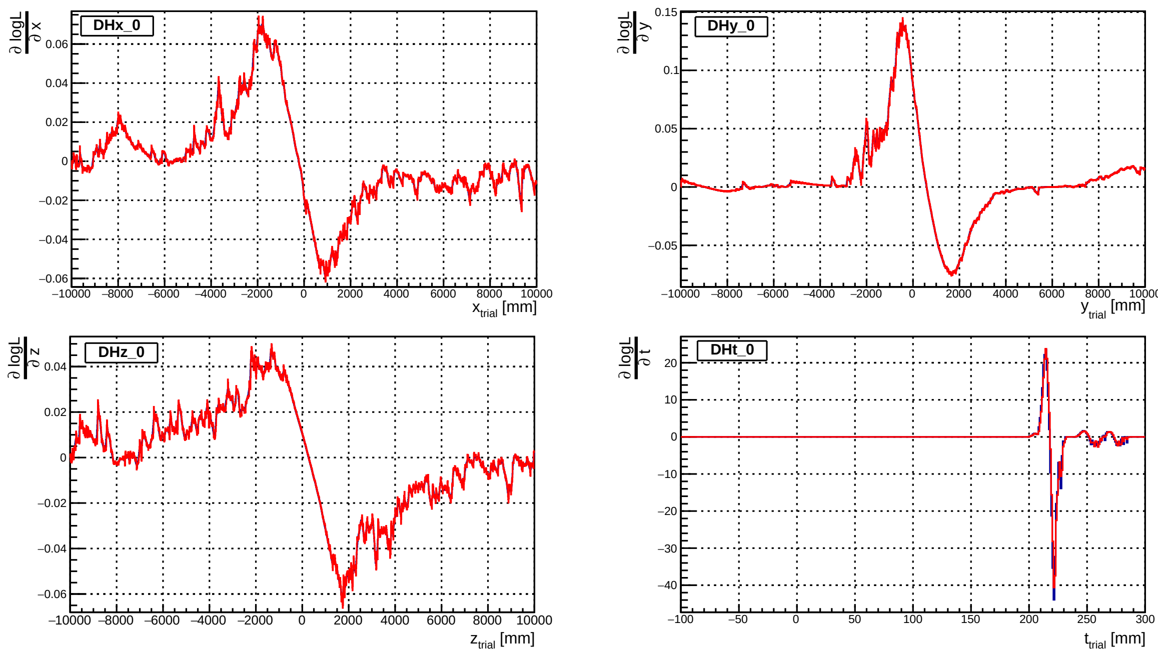

Figure A.3: Derivatives of $\ln L$ of an ^{16}N event projected on x, y, z, t-axis respectively. The analytical derivatives (blue) are overlaid with numerical derivatives (red). They basically match with each other.

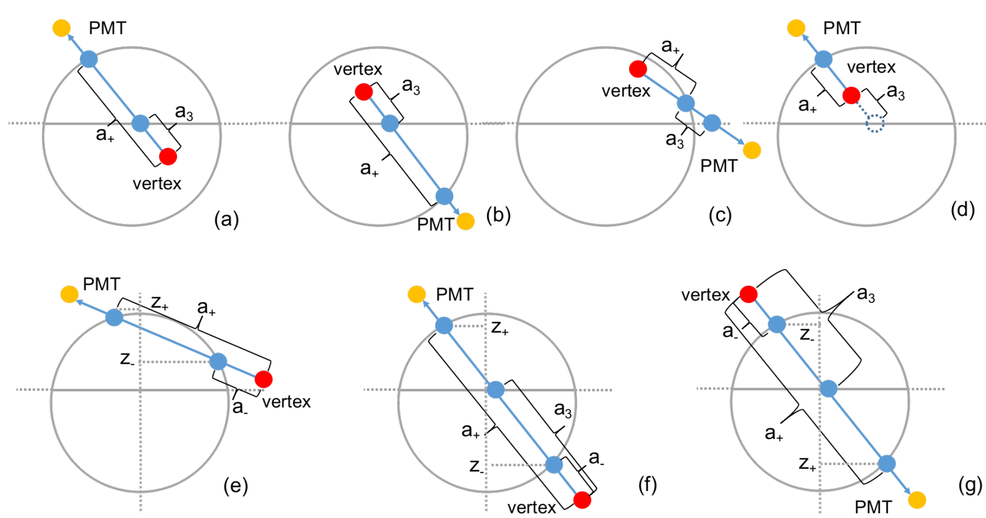

Figure A.4: Layouts for the scintillator light paths inside the AV sphere.

First check the ray-cylinder intersection (Eqn. 4.14):

If $\Delta_{neck} > 0$,

(step. 1a) if $a'_+ a'_- < 0$ (event position is inside the cylinder), check the z position of the intersection point on neck, $z_+ = z_0 + a'_+ u_z$:

(2a-a) if $6108 < z_+ < 8390$ mm (in the valid neck region), then check the AV sphere:

(3a-a-a) if $|\vec{X}_0| \geq r_{AV}$: $d_{sp,neck} = a'_+$, see Fig. A.5 (a).

(3a-a-b) if $|\vec{X}_0| < r_{AV}$ and $a_+ a_- < 0$: $d_{sp,neck} = a'_+ - a_+$, the light ray first hits the sphere inside the cylinder and then hits the cylinder, see Fig. A.5 (b).

(2a-b) if $z_+ < 6108$ mm:

(3a-b) if $|\vec{X}_0| \geq r_{AV}$ and $6108 < z_0 < 8390$ mm:

(4a-b) if $a_+ > a_- > 0$: $d_{sp,neck} = a_-$, see Fig. A.5 (c).

(step. 1b) if $a'_+ > a'_- > 0$ (event position is outside the cylinder), check the z position of the intersection point on neck, $z'_\pm = z_0 + a'_\pm \cdot u_z$:

(2b-a) if $6108 < z'_\pm - < 8390$ mm, check the AV intersection:

(3b-a-a) if $a_\pm$ do not exit (never passes through AV), $d_{sp,neck} = a'_+ - a'_-$, see Fig. A.5 (d).

(3b-a-b) if $a_+ > a_- > 0$, evaluate the z positions of the ray-sphere intersection points $z_\pm = z_0 + a_\pm \cdot u_z$:

(4b-a-a) if $z_\pm \geq 6108$ mm: $d_{sp,neck} = a'_+ - a'_- - (a_+ - a_-)$, see Fig. A.5 (e). The path inside the sphere is subtracted to avoid duplicated calculation.

(4b-a-b) if $z_+ < 6108$ and $6108 < z_- < 8390$ mm:

(5b-a-b-a) if $a_+ > a_- > 0$: $d_{sp,neck} = a_- - a'_-$, see Fig. A.5 (f).

(5b-a-b-b) if $z_- < 6108$ and $6108 < z_+ < 8390$ mm:

in this case, either the event position is inside the sphere ($a_+ a_- < 0$), shown in Fig. A.5 (g), or outside the sphere ($a_+ a_- < 0$), shown in Fig. A.5 (h)), the path in neck is same: $d_{sp,neck} = a'_+ - a_+$.

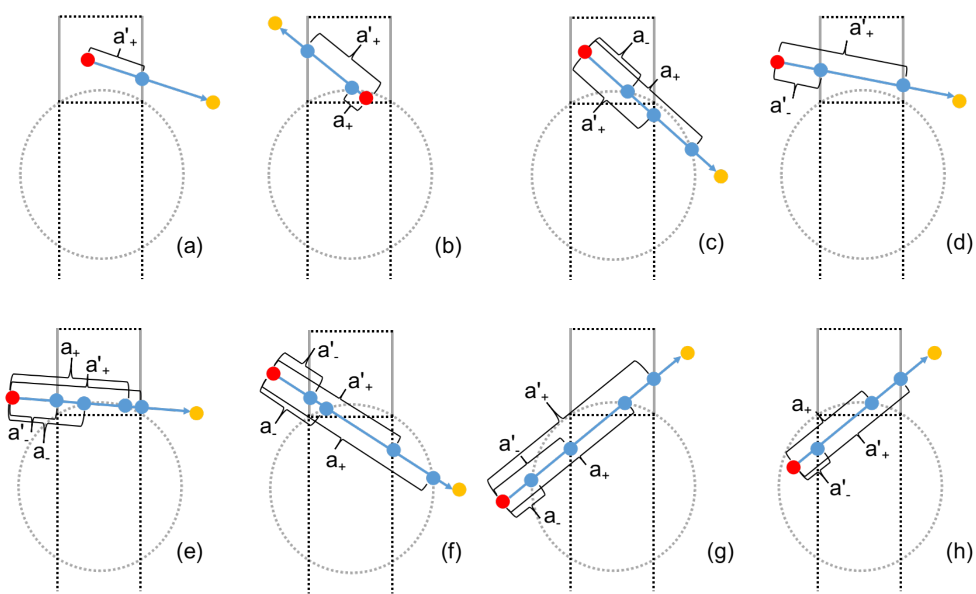

Figure A.5: Layouts of the scintillator light paths inside the neck cylinder.

Appendix B

Information for ^{16}N Scan Runs

B.1 Information for ^{16}N Scan Runs

The tables below show the ^{16}N runs used in this thesis. Table. B.1 to B.3 are the internal scans inside the AV along the detector z-axis, y-axis and x-axis respectively. Table. B.4 shows the runs when the source was at the detector corner. Table. B.5 shows the external scans.

Table B.1: ^{16}N internal z-axis scan runs. The last 3 scans were inside the AV neck (neck runs).

run number	nominal source position [mm]		
	x	y	z
100934	-186.0	256.0	1.0
106923	-186.0	254.0	-5501.2
106925	-186.0	254.0	-4999.899
106930	-186.0	254.0	-4500.2
106942	-186.0	254.0	-4001.0
106944	-186.0	254.0	-3501.399
106946	-186.0	254.0	-2999.7
106948	-186.0	254.0	-2500.399
106950	-186.0	254.0	-1998.499
106952	-186.0	254.0	-1499.5
106954	-186.0	254.0	-1000.099
106956	-186.0	254.0	-499.6
106958	-186.0	254.0	0.401
106960	-186.0	254.0	500.8
106962	-186.0	254.0	1000.3
106964	-186.0	254.0	1500.9
106967	-186.0	254.0	2000.001
106969	-186.0	254.0	2500.3
106971	-186.0	254.0	3000.3
106973	-186.0	254.0	3500.9
106975	-186.0	254.0	4000.5
106977	-186.0	254.0	4500.4
106979	-185.037	247.24	4973.567
107049	-121.599	81.021	6496.04
107051	-123.099	126.177	6997.52
107053	-124.4	153.386	7499.79

Table B.2: ^{16}N internal y-axis scan runs.

run number	nominal source position [mm]		
	x	y	z
106992	-5.995	-0.201	-1.107
106994	-7.761	-998.068	0.159
106996	-7.084	-2000.578	-0.716
106998	-5.491	-2998.017	-4.196
107000	-3.774	-3992.167	-7.374
107002	-1.624	-4999.882	-12.012
107004	-1.745	5002.057	-9.897
107006	-3.967	3973.021	-7.359
107008	-5.984	2980.035	-3.441
107010	-7.952	1986.669	-1.714
107012	-9.242	994.183	0.553
107014	-9.867	496.858	0.269
107016	-8.414	1494.71	0.634
107018	-6.835	2487.539	-1.126
107026	-4.949	3496.338	-5.971
107028	-2.539	4505.371	-7.453
107030	-7.711	-501.268	0.126
107033	-7.534	-1494.927	-0.096
107035	-6.349	-2487.912	-1.434
107043	-4.366	-3475.769	-6.019
107045	-2.799	-4498.62	-10.213
107047	-1.898	-4874.53	-11.077

Table B.3: ^{16}N internal x-axis scan runs.

run number	nominal source position [mm]		
	x	y	z
107055	-5.283	-0.209	-1.057
107075	-4999.043	2.46	-9.899
107077	-4002.525	5.269	-7.364
107079	-3004.229	8.101	-2.54
107081	-2000.155	10.637	-0.361
107083	-992.994	11.641	0.024
107085	998.133	10.897	-0.044
107087	2011.103	9.874	0.057
107091	4003.323	4.378	-5.974
107093	5004.868	2.262	-7.547
107095	4503.445	3.278	-7.0
107110	-4489.301	3.918	-10.545
107116	3511.147	5.742	-2.578
107118	2502.805	8.681	-2.803
107120	-3476.709	6.643	-4.886

Table B.4: ^{16}N corner scan runs.

run number	nominal source position [mm]		
	x	y	z
106981	-186.0	254.0	5500.9
106985	-186.0	254.0	5999.8
107058	-8.765	996.891	0.172
107060	-7.518	1990.663	-0.445
107062	-7.794	-997.865	0.155
107064	-7.083	-1990.651	-0.744
107089	3003.718	7.258	-0.69
107098	2091.016	6.312	2099.444
107020	-5.399	1991.04	1988.97
107022	-9.92	2776.47	-2839.41
107024	-10.44	3227.32	-3324.9
107037	-8.377	-2832.33	-2839.69
107039	-9.284	-3137.21	-3212.18
107041	-4.719	-2099.25	2110.71
107100	2824.56	13.507	-2840.13
107102	3245.74	13.681	-3264.76
107104	-3250.29	13.438	-3264.7
107106	-2834.05	13.893	-2839.43
107108	-2109.28	6.613	2098.57
107112	-2771.9	16.196	-4773.96
107114	2771.1	15.596	-4773.27

Table B.5: ^{16}N external scan runs.

run number	nominal source position [mm]		
	x	y	z
111211	-5861.0	-2524.0	-1.62
111213	-5861.0	-2524.0	-5000.525
111215	-5861.0	-2524.0	-4000.021
111217	-5861.0	-2524.0	-3000.151
111219	-5861.0	-2524.0	-1999.248
111221	-5861.0	-2524.0	-998.923
111223	-5861.0	-2524.0	1000.798
111225	-5861.0	-2524.0	2000.597
111228	-5861.0	-2524.0	3000.734
111230	-5861.0	-2524.0	4000.977
111232	-5861.0	-2524.0	5000.86
111234	-5861.0	-2524.0	4498.167
111236	-5861.0	-2524.0	3498.838
111238	-5861.0	-2524.0	2498.641
111240	-5861.0	-2524.0	1498.713
111242	-5861.0	-2524.0	-1501.717
111244	-5861.0	-2524.0	-2500.89
111246	-5861.0	-2524.0	-3500.764
111248	-5861.0	-2524.0	-4500.812

Appendix C

Bi-Po Analysis

C.1 Uranium chain and Bi-Po Analysis

A flowchart for picking up the Bi-Po event pairs is listed in Fig. C.1. The algorithm is based on Ref. [109].

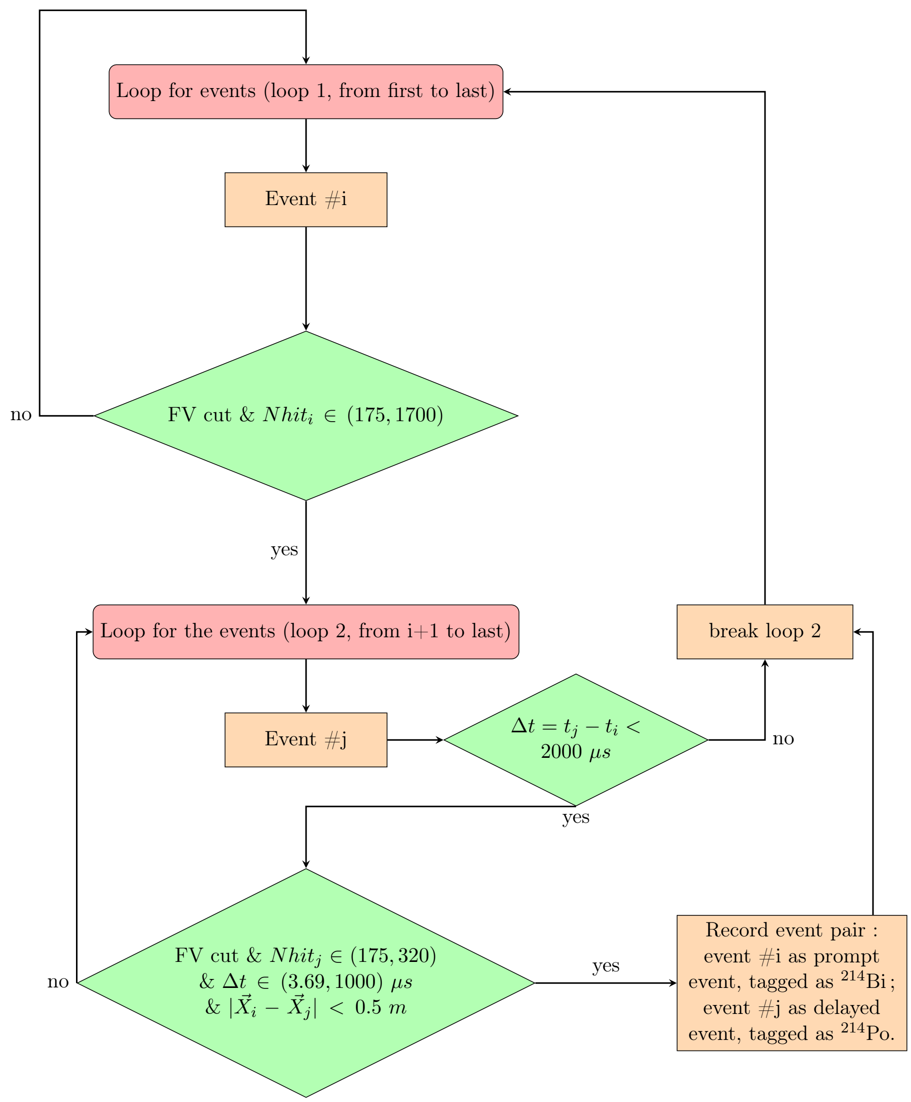

Figure C.1: A flow chart for Bi-Po tagging.

References

[1] M. Anderson, S. Andringa, S. Asahi, M. Askins, D. Auty, N. Barros, D. Bartlett, F. Barão, R. Bayes, E. Beier, *et al.*, "Measurement of the ^{8}B solar neutrino flux in SNO+ with very low backgrounds," *Physical Review D*, vol. 99, no. 1, p. 012012, 2019.

[2] K. Abe, Y. Haga, Y. Hayato, M. Ikeda, K. Iyogi, J. Kameda, Y. Kishimoto, L. Marti, M. Miura, S. Moriyama, *et al.*, "Solar neutrino measurements in super-kamiokande-iv," *Physical Review D*, vol. 94, no. 5, p. 052010, 2016.

[3] C. Giunti and C. W. Kim, *Fundamentals of neutrino physics and astrophysics.* Oxford university press, 2007.

[4] V. Albanese, R. Alves, M. Anderson, S. Andringa, L. Anselmo, E. Arushanova, S. Asahi, M. Askins, D. Auty, A. Back, *et al.*, "The SNO+ experiment," *arXiv preprint arXiv::2104.11687*, 2021.

[5] J. Paton, "Neutrinoless Double Beta Decay in the SNO+ Experiment," 2019.

[6] E. Antonio, *State Of The Art Of Neutrino Physics: A Tutorial For Graduate Students And Young Researchers*, vol. 28. World Scientific, 2018.

[7] E. Leming, "Oxford LAB + PPO timing and light yield measurements," *SNO+ Internal Document, docDB-6179-v1.*

[8] A. Hallin, "SNO+ director's review documentation," *SNO+ Internal Document, docDB-2888-v3.*

[9] A. Hallin, “Fitting partial fill data from december 2014,” *SNO+ Internal Document, docDB-2888-v3.*

[10] D. Auty and A. Hallin, “Partial water fitter,” *SNO+ Internal Document, docDB-2965-v2.*

[11] K. Singh, “Wavelength shifter: Carbostyril 124,” *SNO+ Internal Document, docDB-3351-v2.*

[12] K. Singh, “Wavelength shifter in water phase of SNO+,” *SNO+ Internal Document, docDB-3869-v2.*

[13] K. Singh, “Multipath fitter processor,” *SNO+ Internal Document, docDB-3849-v1.*

[14] J. Hu and J. Tseng, “Updates on the multipath water fitter 2018,” *SNO+ Internal Document, docDB-4936-v2.*

[15] J. Leite-Lopes, “Weak interaction physics: from its origin to the electroweak model,” tech. rep., SCAN-9607019, 1996.

[16] H. Bethe and R. Peierls, “The “neutrino”,” *Nature*, vol. 133, no. 3362, pp. 532–532, 1934.

[17] F. Reines, C. Cowan Jr, F. Harrison, A. McGuire, and H. Kruse, “Detection of the free antineutrino,” *Physical Review*, vol. 117, no. 1, p. 159, 1960.

[18] G. Danby, J. M. Gaillard, K. Goulianos, L. M. Lederman, N. Mistry, M. Schwartz, and J. Steinberger, “Observation of high-energy neutrino reactions and the existence of two kinds of neutrinos,” *Physical Review Letters*, vol. 9, no. 1, p. 36, 1962.

[19] K. Kodama, N. Ushida, C. Andreopoulos, N. Saoulidou, G. Tzanakos, P. Yager, B. Baller, D. Boehnlein, W. Freeman, B. Lundberg, *et al.*, “Observation of tau neutrino interactions,” *Physics Letters B*, vol. 504, no. 3, pp. 218–224, 2001.

[20] D. Decamp, B. Deschizeaux, J.-P. Lees, M.-N. Minard, J. Crespo, M. Delfino, E. Fernandez, M. Martinez, R. Miquel, M. Mir, *et al.*, "Determination of the number of light neutrino species," *Physics Letters B*, vol. 231, no. 4, pp. 519–529, 1989.

[21] P. D. Group, P. Zyla, R. Barnett, J. Beringer, O. Dahl, D. Dwyer, D. Groom, C.-J. Lin, K. Lugovsky, E. Pianori, *et al.*, "Review of particle physics," *Progress of Theoretical and Experimental Physics*, vol. 2020, no. 8, p. 083C01, 2020.

[22] Z. Xing and S. Zhou, *Neutrinos in particle physics, astronomy and cosmology.* Springer Science & Business Media, 2011.

[23] Y. Suzuki, "The sun, neutrinos and super-kamiokande," *Proceedings of the Japan Academy, Series B*, vol. 96, no. 6, pp. 204–233, 2020.

[24] E. Akhmedov, "Quantum mechanics aspects and subtleties of neutrino oscillations," *arXiv preprint arXiv:1901.05232*, 2019.

[25] Y. Fukuda, T. Hayakawa, E. Ichihara, K. Inoue, K. Ishihara, H. Ishino, Y. Itow, T. Kajita, J. Kameda, S. Kasuga, *et al.*, "Evidence for oscillation of atmospheric neutrinos," *Physical Review Letters*, vol. 81, no. 8, p. 1562, 1998.

[26] Wikipedia, *CP violation*, 2020 (accessed Mar 15, 2020). `https://en.wikipedia.org/wiki/CP_violation`.

[27] I. J. Aitchison and A. J. Hey, *Gauge theories in particle physics: A practical introduction, Volume 2: Non-Abelian Gauge theories: QCD and the electroweak theory*, vol. 2. CRC Press, 2012.

[28] S. Abe, T. Ebihara, S. Enomoto, K. Furuno, Y. Gando, K. Ichimura, H. Ikeda, K. Inoue, Y. Kibe, Y. Kishimoto, *et al.*, "Precision measurement of neutrino oscillation parameters with kamland," *Physical Review Letters*, vol. 100, no. 22, p. 221803, 2008.

[29] K. Abe, C. Bronner, Y. Haga, Y. Hayato, M. Ikeda, K. Iyogi, J. Kameda, Y. Kato, Y. Kishimoto, L. Marti, *et al.*, "Atmospheric neutrino oscillation analysis with exter-

nal constraints in super-kamiokande i-iv," *Physical Review D*, vol. 97, no. 7, p. 072001, 2018.

[30] F. P. An, A. Balantekin, H. Band, M. Bishai, S. Blyth, D. Cao, G. Cao, J. Cao, W. Cen, Y. Chan, *et al.*, "Measurement of electron antineutrino oscillation based on 1230 days of operation of the daya bay experiment," *Physical Review D*, vol. 95, no. 7, p. 072006, 2017.

[31] X. Qian and J.-C. Peng, "Physics with reactor neutrinos," *Reports on Progress in Physics*, vol. 82, no. 3, p. 036201, 2019.

[32] K. Abe, R. Akutsu, A. Ali, C. Alt, C. Andreopoulos, L. Anthony, M. Antonova, S. Aoki, A. Ariga, Y. Asada, *et al.*, "Constraint on the matter-antimatter symmetry-violating phase in neutrinooscillations," *arXiv preprint arXiv:1910.03887*, 2019.

[33] A. Y. Smirnov, "Solar neutrinos: Oscillations or no-oscillations?," *arXiv preprint arXiv:1609.02386*, 2016.

[34] A. Y. Smirnov, "The msw effect and matter effects in neutrino oscillations," *Physica Scripta*, vol. 2005, no. T121, p. 57, 2005.

[35] M. Fukugita and T. Yanagida, *Physics of Neutrinos: and Application to Astrophysics*. Springer Science & Business Media, 2013.

[36] H. A. Bethe, "Energy production in stars," *Physical Review*, vol. 55, no. 5, p. 434, 1939.

[37] W. C. Haxton, R. Hamish Robertson, and A. M. Serenelli, "Solar neutrinos: status and prospects," *Annual Review of Astronomy and Astrophysics*, vol. 51, pp. 21–61, 2013.

[38] L. Oberauer, A. Ianni, and A. Serenelli, *Solar Neutrino Physics: The Interplay Between Particle Physics and Astronomy*. John Wiley & Sons, 2020.

[39] J. W. F. Valle and J. Romao, *Neutrinos in high energy and astroparticle physics*. John Wiley & Sons, 2015.

[40] F. Suekane, *Neutrino oscillations: a practical guide to basics and applications*, vol. 898. Springer, 2015.

[41] J. N. Bahcall, "Solar neutrinos. i. theoretical," *Physical Review Letters*, vol. 12, no. 11, p. 300, 1964.

[42] R. Davis Jr, "Solar neutrinos. ii. experimental," *Physical Review Letters*, vol. 12, no. 11, p. 303, 1964.

[43] R. Davis Jr, D. S. Harmer, and K. C. Hoffman, "Search for neutrinos from the sun," *Physical Review Letters*, vol. 20, no. 21, p. 1205, 1968.

[44] Super-Kamiokande, "Solar neutrinos," 2020 (accessed 1-Jan-2020). `http://www-sk.icrr.u-tokyo.ac.jp/sk/sk/solar-e.html`.

[45] Q. R. Ahmad, R. Allen, T. Andersen, J. Anglin, J. Barton, E. Beier, M. Bercovitch, J. Bigu, S. Biller, R. Black, *et al.*, "Direct evidence for neutrino flavor transformation from neutral-current interactions in the sudbury neutrino observatory," *Physical review letters*, vol. 89, no. 1, p. 011301, 2002.

[46] B. Aharmim, S. Ahmed, A. Anthony, N. Barros, E. Beier, A. Bellerive, B. Beltran, M. Bergevin, S. Biller, K. Boudjemline, *et al.*, "Combined analysis of all three phases of solar neutrino data from the sudbury neutrino observatory," *Physical Review C*, vol. 88, no. 2, p. 025501, 2013.

[47] A. Gando, Y. Gando, K. Ichimura, H. Ikeda, K. Inoue, Y. Kibe, Y. Kishimoto, M. Koga, Y. Minekawa, T. Mitsui, *et al.*, "Constraints on θ 13 from a three-flavor oscillation analysis of reactor antineutrinos at kamland," *Physical Review D*, vol. 83, no. 5, p. 052002, 2011.

[48] M. Agostini, K. Altenmüller, S. Appel, V. Atroshchenko, Z. Bagdasarian, D. Basilico, G. Bellini, J. Benziger, D. Bick, D. Bravo, *et al.*, "Improved measurement of b-8 solar neutrinos with 1.5 kt· y of borexino exposure," *Physical Review D*, vol. 101, no. 6, p. 062001, 2020.

[49] M. Agostini, K. Altenmüller, S. Appel, D. Jeschke, B. Neumair, L. Oberauer, L. Papp, S. Schönert, F. von Feilitzsch, V. Atroshchenko, *et al.*, "Comprehensive measurement of pp-chain solar neutrinos," *Nature*, vol. 562, no. 7728, pp. 505–510, 2018.

[50] B. Collaboration *et al.*, "Experimental evidence of neutrinos produced in the cno fusion cycle in the sun," *Nature*, vol. 587, no. 7835, pp. 577–582, 2020.

[51] G. D. O. Gann, "Everything under the sun: A review of solar neutrinos," in *AIP Conference Proceedings*, vol. 1666, p. 090003, AIP Publishing LLC, 2015.

[52] T. Yano, "Solar neutrino physics at hyper-kamiokande," in *36th International Cosmic Ray Conference (ICRC2019)*, vol. 36, p. 1037, 2019.

[53] F. Capozzi, S. W. Li, G. Zhu, and J. F. Beacom, "Dune as the next-generation solar neutrino experiment," *Physical review letters*, vol. 123, no. 13, p. 131803, 2019.

[54] M. Askins, Z. Bagdasarian, N. Barros, E. Beier, E. Blucher, R. Bonventre, E. Bourret, E. Callaghan, J. Caravaca, M. Diwan, *et al.*, "Theia: an advanced optical neutrino detector," *The European Physical Journal C*, vol. 80, no. 5, pp. 1–31, 2020.

[55] A. Giaz, "Status and perspectives of the JUNO experiment," *arXiv preprint arXiv:1804.03575*, 2018.

[56] J. F. Beacom, S. Chen, J. Cheng, S. N. Doustimotlagh, Y. Gao, G. Gong, H. Gong, L. Guo, R. Han, H.-J. He, *et al.*, "Physics prospects of the jinping neutrino experiment," *Chinese physics C*, vol. 41, no. 2, p. 023002, 2017.

[57] M. Wurm, L.-L. working group, *et al.*, "Studying neutrino properties in the future lena experiment," *Nuclear Physics B-Proceedings Supplements*, vol. 237, pp. 314–316, 2013.

[58] L. Baudis, A. Ferella, A. Kish, A. Manalaysay, T. M. Undagoitia, and M. Schumann, "Neutrino physics with multi-ton scale liquid xenon detectors," *Journal of cosmology and astroparticle physics*, vol. 2014, no. 01, p. 044, 2014.

[59] J. Aalbers, F. Agostini, M. Alfonsi, F. Amaro, C. Amsler, E. Aprile, L. Arazi, F. Arneodo, P. Barrow, L. Baudis, *et al.*, "Darwin: towards the ultimate dark matter detector," *Journal of Cosmology and Astroparticle Physics*, vol. 2016, no. 11, p. 017, 2016.

[60] J. Aalbers, F. Agostini, S. A. Maouloud, M. Alfonsi, L. Althueser, F. Amaro, J. Angevaare, V. C. Antochi, B. Antunovic, E. Aprile, *et al.*, "Solar neutrino detection sensitivity in darwin via electron scattering," *The European Physical Journal C*, vol. 80, no. 12, pp. 1–10, 2020.

[61] N. Aghanim, Y. Akrami, M. Ashdown, J. Aumont, C. Baccigalupi, M. Ballardini, A. Banday, R. Barreiro, N. Bartolo, S. Basak, *et al.*, "Planck 2018 results-vi. cosmological parameters," *Astronomy & Astrophysics*, vol. 641, p. A6, 2020.

[62] C. Dvorkin, M. Gerbino, D. Alonso, N. Battaglia, S. Bird, A. D. Rivero, A. Font-Ribera, G. Fuller, M. Lattanzi, M. Loverde, *et al.*, "Neutrino mass from cosmology: Probing physics beyond the standard model," *arXiv preprint arXiv:1903.03689*, 2019.

[63] J. Lesgourgues, G. Mangano, G. Miele, and S. Pastor, *Neutrino cosmology.* Cambridge University Press, 2013.

[64] B. Povh, K. Rith, and F. Zetsche, *Particles and nuclei*, vol. 1. Springer, 2008.

[65] B. R. Martin and G. Shaw, *Nuclear and particle physics: an introduction.* John Wiley & Sons, 2019.

[66] E. Akhmedov, “Majorana neutrinos and other majorana particles: Theory and experiment,” *arXiv preprint arXiv:1412.3320*, 2014.

[67] E. Majorana and L. Maiani, *A symmetric theory of electrons and positrons*. Springer, 2006.

[68] W. H. Furry, “On transition probabilities in double beta-disintegration,” *Physical Review*, vol. 56, no. 12, p. 1184, 1939.

[69] K. Zuber, *Neutrino physics*. CRC press, 2020.

[70] M. J. Dolinski, A. W. Poon, and W. Rodejohann, “Neutrinoless double-beta decay: status and prospects,” *Annual Review of Nuclear and Particle Science*, vol. 69, pp. 219–251, 2019.

[71] A. Gando, Y. Gando, T. Hachiya, A. Hayashi, S. Hayashida, H. Ikeda, K. Inoue, K. Ishidoshiro, Y. Karino, M. Koga, *et al.*, “Search for majorana neutrinos near the inverted mass hierarchy region with kamland-zen,” *Physical Review Letters*, vol. 117, no. 8, p. 082503, 2016.

[72] C. Alduino, F. Alessandria, K. Alfonso, E. Andreotti, C. Arnaboldi, F. Avignone III, O. Azzolini, M. Balata, I. Bandac, T. Banks, *et al.*, “First results from cuore: A search for lepton number violation via $0\nu\beta\beta$ decay of te-130,” *Physical review letters*, vol. 120, no. 13, p. 132501, 2018.

[73] M. Agostini, G. Araujo, A. Bakalyarov, M. Balata, I. Barabanov, L. Baudis, C. Bauer, E. Bellotti, S. Belogurov, A. Bettini, *et al.*, “Final results of gerda on the search for neutrinoless double-β decay,” *Physical Review Letters*, vol. 125, no. 25, p. 252502, 2020.

[74] “Muons,” 2001 (accessed 19-July-2019). `https://cosmic.lbl.gov/SKliewer/Cosmic_Rays/Muons.htm`.

[75] V. Albanese, R. Alves, M. Anderson, S. Andringa, L. Anselmo, E. Arushanova, S. Asahi, M. Askins, D. Auty, A. Back, *et al.*, "The SNO+ experiment," *Journal of Instrumentation*, vol. 16, no. 08, p. P08059, 2021.

[76] J. Waterfield, *Optical calibration system for SNO+ and sensitivity to neutrinoless double-beta decay.* PhD thesis, University of Sussex, 2017.

[77] S. Andringa, E. Arushanova, S. Asahi, M. Askins, D. Auty, A. Back, Z. Barnard, N. Barros, E. Beier, A. Bialek, *et al.*, "Current status and future prospects of the SNO+," *Advances in High Energy Physics*, vol. 2016, 2016.

[78] M. Stringer, *Sensitivity of SNO+ to supernova neutrinos.* PhD thesis, University of Sussex, 2019.

[79] P. G. Jones, *Background rejection for the neutrinoless double beta decay experiment SNO+.* PhD thesis, University of Oxford, 2011.

[80] M. Anderson, S. Andringa, E. Arushanova, S. Asahi, M. Askins, D. Auty, A. Back, Z. Barnard, N. Barros, D. Bartlett, *et al.*, "Search for invisible modes of nucleon decay in water with the SNO+ detector," *Physical Review D*, vol. 99, no. 3, p. 032008, 2019.

[81] M. Anderson, S. Andringa, M. Askins, D. Auty, N. Barros, F. Barão, R. Bayes, E. Beier, A. Bialek, S. Biller, *et al.*, "Measurement of neutron-proton capture in the SNO+ water phase," *Physical Review C*, vol. 102, no. 1, p. 014002, 2020.

[82] M. Anderson, S. Andringa, M. Askins, D. Auty, F. Barão, N. Barros, R. Bayes, E. Beier, A. Bialek, S. Biller, *et al.*, "Optical calibration of the SNO+ detector in the water phase with deployed sources," *arXiv preprint arXiv:2106.03951*, 2021.

[83] J. D. Jackson, *Classical Electrodynamics.* John Wiley & Sons, 2007.

[84] L. D. Landau, J. Bell, M. Kearsley, L. Pitaevskii, E. Lifshitz, and J. Sykes, *Electrodynamics of Continuous Media*, vol. 8. elsevier, 2013.

[85] H. W. C. Tseung and N. Tolich, "Ellipsometric measurements of the refractive indices of linear alkylbenzene and ej-301 scintillators from 210 to 1000 nm," *Physica Scripta*, vol. 84, no. 3, p. 035701, 2011.

[86] W. R. Leo, *Techniques for Nuclear and Particle Physics Experiments: a How-to Approach*. Springer Science & Business Media, 2012.

[87] G. F. Knoll, *Radiation Detection and Measurement*. John Wiley & Sons, 2010.

[88] J. Birks and F. Firk, "The theory and practice of scintillation counting," *Physics Today*, vol. 18, p. 60, 1965.

[89] B. Von Krosigk, *Measurement of Proton and α Particle Quenching in LAB Based Scintillators and Determination of Spectral Sensitivities to Supernova Neutrinos in the SNO+ Detector*. PhD thesis, Technische Universitaet Dresden, 2015.

[90] A. Sörensen, "Temperature quenching in lab based liquid scintillator and muon-induced backgrounds in the sno+ experiment," 2016.

[91] J. Dunger, *Topological and time based event classification for neutrinoless double beta decay in liquid scintillator*. PhD thesis, University of Oxford, 2018.

[92] D. A. McQuarrie and J. D. Simon, *Physical chemistry: a molecular approach*, vol. 1. University science books Sausalito, CA, 1997.

[93] S. Collaboration, M. Anderson, S. Andringa, L. Anselmo, E. Arushanova, S. Asahi, M. Askins, D. Auty, A. Back, Z. Barnard, *et al.*, "Development, characterisation, and deployment of the SNO+ liquid scintillator," *arXiv preprint arXiv:2011.12924*, 2020.

[94] J. B. Birks, "Scintillations from organic crystals: specific fluorescence and relative response to different radiations," *Proceedings of the Physical Society. Section A*, vol. 64, no. 10, p. 874, 1951.

[95] PerkinElmer, "Liquid scintillation cocktails," 1998-2021 (accessed 20-Dec-2019). `https://www.perkinelmer.com/en-ca/`

`lab-products-and-services/application-support-knowledgebase/radiometric/liquid-scintillation-cocktails.html`.

[96] X. Dai, E. Rollin, A. Bellerive, C. Hargrove, D. Sinclair, C. Mifflin, and F. Zhang, "Wavelength shifters for water cherenkov detectors," *Nuclear Instruments and Methods in Physics Research Section A: Accelerators, Spectrometers, Detectors and Associated Equipment*, vol. 589, no. 2, pp. 290–295, 2008.

[97] J. Alonso, N. Barros, M. Bergevin, A. Bernstein, L. Bignell, E. Blucher, F. Calaprice, J. Conrad, F. Descamps, M. Diwan, *et al.*, "Advanced scintillator detector concept (asdc): a concept paper on the physics potential of water-based liquid scintillator," *arXiv preprint arXiv:1409.5864*, 2014.

[98] M. Askins, M. Bergevin, A. Bernstein, S. Dazeley, S. Dye, T. Handler, A. Hatzikoutelis, D. Hellfeld, P. Jaffke, Y. Kamyshkov, *et al.*, "The physics and nuclear nonproliferation goals of watchman: A water cherenkov monitor for antineutrinos," *arXiv preprint arXiv:1502.01132*, 2015.

[99] Wikipedia, "Linear alkylbenzene," 2020 (accessed 1-Jan-2020). `https://en.wikipedia.org/wiki/Linear_alkylbenzene`.

[100] S. W. Wunderly and J. M. Kauffman, "New quench-resistant fluors for liquid scintillation counting," *International Journal of Radiation Applications and Instrumentation. Part A. Applied Radiation and Isotopes*, vol. 41, no. 9, pp. 809–815, 1990.

[101] Y. Xing-Chen, Y. Bo-Xiang, Z. Xiang, Z. Li, D. Ya-Yun, L. Meng-Chao, D. Xue-Feng, Z. Xuan, J. Quan-Lin, Z. Li, *et al.*, "Preliminary study of light yield dependence on lab liquid scintillator composition," *Chinese Physics C*, vol. 39, no. 9, p. 096003, 2015.

[102] T. Kaptanoglu, M. Luo, and J. Klein, "Cherenkov and scintillation light separation using wavelength in lab based liquid scintillator," *Journal of Instrumentation*, vol. 14, no. 05, p. T05001, 2019.

[103] V. Novikov, "Scintillator development for sno+," *SNO+ Internal Document (2009).*

[104] S. Grullon, "Light yield and scintillation decay time constants of te-loaded liquid scintillator for the sno+ experiment," in *Proceedings of the 26th International Conference on Neutrino Physics and Astrophysics (Neutrino'14)*, 2014.

[105] S. D. Biller, E. J. Leming, and J. L. Paton, "Slow fluors for highly effective separation of cherenkov light in liquid scintillators," *arXiv preprint arXiv:2001.10825*, 2020.

[106] A. LaTorre, "New measurements for the timing spectrum of electrons and alphas in LAB+PPO," *SNO+ Internal Document, docDB-4081-v1.*

[107] T. Kaptanoglu, "Measurements of light yield and timing of 0.5 g/l lab+ppo," *SNO+ Internal Document, docDB-5997-v1.*

[108] T. Kaptanoglu, "Penn light yield measurements of Te+DDA samples," *SNO+ Internal Document, docDB-5997-v1.*

[109] J.-S. Wang, "Bipo analysis using partial fill data," *SNO+ Internal Document, docDB-5950-v3.*

[110] M. C. Helen O'Keeffe, Valentina Lozza, "Lab backgrounds expected numbers," *SNO+ Internal Document, docDB-507-v42.*

[111] S. T. L. working group, "Te loading," *SNO+ Internal Document, planned to be submitted.*

[112] S. Biller, S. Manecki, S. collaboration, *et al.*, "A new technique to load 130te in liquid scintillator for neutrinoless double beta decay experiments," in *Journal of Physics: Conference Series*, vol. 888, p. 012084, IOP Publishing, 2017.

[113] S. Biller, "DDA synthesis model," *SNO+ Internal Document, docDB-5364-v3.*

[114] S. Biller, "DDA vs SOP," *SNO+ Internal Document, docDB-5437-v1.*

[115] Hamamatsu-Photonics, "Photomultiplier tube r580," 2020 (accessed 1-Jan-2020). `www.hamamatsu.com/eu/en/product/type/R580/index.html`.

[116] CAEN, "DT5751 - CAEN - tools for discovery.," 2020 (accessed 1-Jan-2020). `hwww.caen.it/products/dt5751`.

[117] CAEN, "CoMPASS multiparametric DAQ software for physics applications," 2020 (accessed 1-Jan-2020). `https://www.caen.it/products/compass/`.

[118] *National Nuclear Data Center*, 2019 (accessed Oct 30, 2019). `https://www.nndc.bnl.gov/`.

[119] J. Boger, R. Hahn, J. Rowley, A. Carter, B. Hollebone, D. Kessler, I. Blevis, F. Dalnoki-Veress, A. DeKok, J. Farine, *et al.*, "The sudbury neutrino observatory," *Nuclear Instruments and Methods in Physics Research Section A: Accelerators, Spectrometers, Detectors and Associated Equipment*, vol. 449, no. 1-2, pp. 172–207, 2000.

[120] K. Hamamatsu Photonics, "Photomultiplier tubes: Basics and applications, 2007," 2018.

[121] G. O. Gann, "Dealing with time in RAT," *SNO+ Internal Document, docDB-481-v2.*

[122] R. Bonventre, *Neutron multiplicity in atmospheric neutrino events at the Sudbury Neutrino Observatory.* PhD thesis, University of Pennsylvania, 2014.

[123] J. M. Walker, *Study of Invisible Mode Nucleon Decay in the SNO+ Detector.* PhD thesis, University of Liverpool, 2016.

[124] K. Singh, P. Gorel, A. Hallin, C. Krauss, and Z. Petriw, "Underwater photometry system of the SNO+ experiment," in *Journal of Physics: Conference Series*, vol. 1342, p. 012130, IOP Publishing, 2020.

[125] M. R. Dragowsky, *Sudbury Neutrino Observatory energy calibration using gamma-ray sources.* PhD thesis, Oregon State University, 1999.

[126] M. Dragowsky, A. Hamer, Y. Chan, R. Deal, E. Earle, W. Frati, E. Gaudette, A. Hallin, C. Hearns, J. Hewett, *et al.*, "The ^{16}N calibration source for the sudbury neutrino observatory," *Nuclear Instruments and Methods in Physics Research Section A: Accelerators, Spectrometers, Detectors and Associated Equipment*, vol. 481, no. 1-3, pp. 284–296, 2002.

[127] A. S. Hamer, *Energy calibration of SNO for measurement of the charged-current neutrino reaction.* PhD thesis, Queen's University, 2001.

[128] R. F. MacLellan, *The energy calibration for the solar neutrino analysis of all three phases of the Sudbury Neutrino Observatory.* PhD thesis, Queen's University, 2009.

[129] M. Mottram, "N16 source update," *SNO+ Internal Document, docDB-1769-v1.*

[130] Z. Barnard, "Update to N16 geometry," *SNO+ Internal Document, docDB-4414-v1.*

[131] R. Bayes, "Analysis of N16 scan," *SNO+ Internal Document, docDB-4482-v2.*

[132] S. Agostinelli, J. Allison, K. a. Amako, J. Apostolakis, H. Araujo, P. Arce, M. Asai, D. Axen, S. Banerjee, G. . Barrand, *et al.*, "Geant4—a simulation toolkit," *Nuclear instruments and methods in physics research section A: Accelerators, Spectrometers, Detectors and Associated Equipment*, vol. 506, no. 3, pp. 250–303, 2003.

[133] R. Brun, F. Rademakers, P. Canal, *et al.*, "Root: An object oriented data analysis framework, 2007," *See Also http://root.cern.ch.*

[134] *RAT Overview*, 2020 (accessed Mar 15, 2020). `https://rat.readthedocs.io/en/latest/overview.html`.

[135] G. Horton-Smith *et al.*, "Introduction to GLG4sim," 2006.

[136] T. Caldwell, "Simulation of noble liquid detectors using rat," in *AARM Meeting at Fermilab*, 2014.

[137] J. Dittmer and M. Meyer, "Topological track reconstruction with the sno+ experiment," *SNO+ Internal Document, docDB-5749-v1.*

[138] M. G. Boulay, *Direct Evidence for Weak Flavour Mixing with the Sudbury Neutrino Observatory.* PhD thesis, Queen's University, 2004.

[139] C. Jillings, R. Ford, A. Hallin, P. Harvey, R. MacLeod, H. Mak, P. Skensved, and R. Stevenson, "The photomultiplier tube testing facility for the sudbury neutrino observatory," *Nuclear Instruments and Methods in Physics Research Section A: Accelerators, Spectrometers, Detectors and Associated Equipment*, vol. 373, no. 3, pp. 421–429, 1996.

[140] P. Gregory, *Bayesian Logical Data Analysis for the Physical Sciences: A Comparative Approach with Mathematica® Support.* Cambridge University Press, 2005.

[141] W. H. Press, S. A. Teukolsky, W. T. Vetterling, and B. P. Flannery, *Numerical recipes 3rd edition: The art of scientific computing.* Cambridge university press, 2007.

[142] E. Turner, "A water scattering scaling factor for rat," *SNO+ Internal Document, docDB-5864-v2.*

[143] I. T. Coulter, *Modelling and Reconstruction of Events in SNO+ related to Future Searches for Lepton and Baryon Number Violation.* PhD thesis, University of Oxford, 2013.

[144] F. Barao and J. Maneira, "Group velocity measurement, plot for approval," *SNO+ Internal Document, docDB-5071-v1.*

[145] P. Skensved and B. Robertson, "Miscellaneous effects," *SNO Techinical Report, SNO-STR-90-28.*

[146] S. J. Brice, *Monte Carlo and Analysis Techniques for the Sudbury Neutrino Observatory.* PhD thesis, University of Oxford, 1996.

[147] L. Lebanowski, "Improved mode cut," *SNO+ Internal Document, docDB-5488-v1.*

[148] P. Mekarski, *Electron Antineutrinos in the Water Phase of the SNO+ Experiment.* PhD thesis, University of Alberta, 2018.

[149] E. Leming, "LAB + PPO timing measurements at Oxford," *SNO+ Internal Document, docDB-6161-v1.*

[150] J. Hu, "Partial fitter re-coordination with various PPO concentrations based on Oxford measurements," *SNO+ Internal Document, docDB-6186-v2.*

[151] J. Hu, "Test the PPO concentration effect on the partial fitter reconstruction," *SNO+ Internal Document, docDB-6230-v1.*

[152] J. Hu, "Use multipath fitter to fit water level," *SNO+ Internal Document, docDB-6062-v1.*

[153] E. Leming and J.-S. Wang, "Partial fill time residuals," *SNO+ Internal Document, docDB-5957-v1.*

[154] E. Morton-Blake, "Partial fill: Bipo214 time residuals + energy data/mc comparison," *SNO+ Internal Document, docDB-6796-v1.*

[155] Wikipedia, *JSON*, 2020 (accessed Mar 15, 2020). `https://en.wikipedia.org/wiki/JSON`.

[156] B. A. Moffat, *The optical calibration of the Sudbury Neutrino Observatory.* PhD thesis, Queen's University, 2001.

[157] M. Mottram, "Note on RSP fitter," *SNO+ Internal Document, docDB-3939-v1.*

[158] K. Majumdar, "Functional form energy reconstruction," *SNO+ Internal Document, docDB-2782-v2.*

[159] M. Mottram, "Updated functional form energy reconstruction: Energyrthetafunctional," *SNO+ Internal Document, docDB-3488-v1.*

[160] L. Lebanowski, "Water reconstruction errors and fom," *SNO+ Internal Document, docDB-6190-v2.*

[161] W. P. Group, "Water physics unidoc," *SNO+ Internal Document.*

[162] M. Mottram, “Energy reconstruction in partial scintillator fill,” *SNO+ Internal Document, docDB-3133-v1.*

[163] Y. Zhang, “Performance of qenergy based on q,” *SNO+ Internal Document, docDB-6065-v1.*

[164] J. Hu, “Updates on the multipath fitter and partial energy,” *SNO+ Internal Document, docDB-5765-v1.*

[165] J. Hu, “Switch the charge-ratio partial energy fitter to nhit-ratio,” *SNO+ Internal Document, docDB-6495-v1.*

[166] M. Anderson, “Water phase ml fitter: status and updates, direction fitter,” *Canadian AI Conference 2020 - Talk.*

[167] M. Anderson, “Deep learning to reconstruct particle interaction properties for the SNO+ neutrino physics experiment,” *Canadian AI Conference 2020 - Talk.*

[168] M. Anderson, “Status and updates on neural network fitter,” *SNO+ Internal Document, docDB-6298-v1.*

[169] J. Klein, “Leta high level cuts (including qpdt and itr),” *SNO+ Internal Document, docDB-2512-v1.*

[170] J. A. Dunmore, *The separation of CC and NC events in the Sudbury Neutrino Observatory.* PhD thesis, University of Oxford, 2004.

[171] E. Marzec, “Measurement of 8B solar neutrinos in the sno+ water phase and a model of vacuum-enhanced neutrino mixing,” 2019.

[172] P.-L. Drouin, *Three-phase extraction of the electron neutrino survival probability at the Sudbury Neutrino Observatory.* PhD thesis, Carleton University, 2012.

[173] B. K. Ryan Bayes, “Beta 14 discrepancy in sno+,” *SNO+ Internal Document, docDB-6613-v2.*

[174] L. W. Group, "Low energy threshold analysis (leta) unidoc v. 0.1," *SNO+ Internal Document, docDB-4322-v1.*

[175] *TMVA*, 2020 (accessed Mar 30, 2020). `https://root.cern.ch/tmva`.

[176] K. Albertsson, S. Gleyzer, A. Hoecker, L. Moneta, P. Speckmayer, J. Stelzer, J. Therhaag, E. von Toerne, H. Voss, and S. Wunsch, "Tmva 4," *arXiv preprint physics/0703039*, 2007.

[177] K. P. Murphy, *Machine learning: a probabilistic perspective.* MIT press, 2012.

[178] M. Askins, "Water phase figures of merit selection," *SNO+ Internal Document, docDB-6560-v1.*

[179] *StatPatternRecognition and Machine Learning in HEP*, 2020 (accessed Mar 30, 2020). `http://www.hep.caltech.edu/~narsky/spr.html`.

[180] F. Shaker, "PSelmaa a solar neutrino tool," *SNO+ Internal Document, docDB-6013-v1.*

[181] N. Vinyoles, A. M. Serenelli, F. L. Villante, S. Basu, J. Bergström, M. Gonzalez-Garcia, M. Maltoni, C. Peña-Garay, and N. Song, "A new generation of standard solar models," *The Astrophysical Journal*, vol. 835, no. 2, p. 202, 2017.

[182] O. Behnke, K. Kröninger, G. Schott, and T. Schörner-Sadenius, *Data analysis in high energy physics: a practical guide to statistical methods.* John Wiley & Sons, 2013.

[183] ROOT, *TDecompQRH Class Reference*, 2020 (accessed Mar 15, 2020). `https://root.cern.ch/doc/master/classTDecompQRH.html`.